R-14-11

Bentonite Rock Interaction Experiment

Characterisation of rock and installation, hydration and dismantling of bentonite parcels

Åsa Fransson, Chalmers University of Technology

Mattias Åkesson, Linus Andersson
Clay Technology

April 2017

Svensk Kärnbränslehantering AB
Swedish Nuclear Fuel
and Waste Management Co

Box 3091, SE-169 03 Solna
Phone +46 8 459 84 00

ISSN 1402-3091
SKB R-14-11
ID 1462218
April 2017

Bentonite Rock Interaction Experiment

Characterisation of rock and installation, hydration and dismantling of bentonite parcels

Åsa Fransson, Chalmers University of Technology

Mattias Åkesson, Linus Andersson
Clay Technology

Abstract

Construction of a nuclear waste repository requires information about and an understanding of the fractured rock and proposed engineered barriers. The Swedish concept for nuclear waste deposition that is currently being developed by the Swedish Nuclear Fuel and Waste Management Co (SKB) includes a natural barrier in the form of crystalline rock, and engineered barriers in the form of bentonite and a copper canister (SKB, 2011).

The Bentonite Rock Interaction Experiment, BRIE, that started in 2010 and that is presented in this report was focused on the hydraulic interaction between the system components of compacted bentonite and the near-field host rock composed of hard and fractured bedrock. The main objectives of BRIE were:

- An increased scientific understanding of the exchange of water across the bentonite-rock interface.
- Better predictions of the wetting of the bentonite buffer.
- Better characterisation methods of the deposition holes.

The experiment was performed at –420 m at Äspö Hard Rock Laboratory, Sweden. Site investigations included three rock characterisation phases: Selection of site; Characterisation of site; and Characterisation of two central boreholes. A conceptual model, see Table 5-1 was used to identify processes, geometric framework, material properties, spatial assignment method and boundary conditions. Based on the conceptual model, investigations were designed to obtain data and concluding remarks considering e.g geometry and hydraulic properties were given following each investigation phase. Based on investigations, main rock types were diorite (gabbroid-dioritoid) with occurrences of fine-grained granite and pegmatite.

The central boreholes KO0017G01 – Hole 17 and KO0018G01 – Hole 18, had a diameter of 300 mm and a length of approximately 3.5 m and 3.0 m respectively. Following characterisation, bentonite was installed using a total number of 28.5 cylindrical blocks with a height of approximately 100 mm for the parcel in Hole 18. For Hole 17, 33.5 blocks of similar height were used. For installation, a central tube was welded to a bottom plate and was thereafter mounted in upright vertical position. The bentonite blocks were threaded, one by one, on the central tube. Instruments were installed in the holes and slots of the machined bentonite blocks. Relative humidity, axial- and total radial total pressure as well as pore pressure were monitored in bentonite during the experiment. Focus was on investigating one section expected to be wet for each of the central holes (close to a water-bearing fracture), and one section expected to be (comparatively) dry (not being close to a fracture).

The bentonite parcels in both holes were installed in September 2012 and finally Hole 17 was dismantled in November 2013 and Hole 18 in the end of February 2014. Dismantling was carried out using stitch drilling and wire-line sawing and bentonite and rock in contact with bentonite (wall of central boreholes) were investigated to obtain water content, density and relative humidity. These investigations and measurements were performed in the laboratory. Besides these investigations, additional laboratory tests were performed providing hydraulic conductivity and water retention curves for the rock matrix and a water up-take test provided data for bentonite. In addition, photography of bentonite was used for documentation of traces of fractures.

The experiment included valuable investigation steps and characterisation methods for rock and bentonite and provides a unique data set for a heterogeneous, low hydraulic conductivity rock (10^{-15} to 10^{-11} m/s from 60 mm diameter cores cut into 10 mm thick specimens) intersected by low-transmissive water-bearing fractures (for Hole 17 e.g. 10^{-11} m^2/s). A de-saturated zone around the borehole was identified and it is likely that both minor fractures as well as differences in rock type results in different ability to transmit water.

Sammanfattning

Byggandet av ett kärnavfallsförvar kräver information om och en förståelse för såväl den sprickiga bergmassan som de föreslagna ingenjörsbarriärerna. Det svenska konceptet för kärnavfallslagring som för närvarande utvecklas av Svensk Kärnbränslehantering (SKB) innefattar en naturlig barriär i form av kristallint berg och ingenjörsbarriärer i form av bentonit och en kopparbehållare (SKB, 2011).

BRIE, Bentonite Rock Interaction Experiment, som inleddes 2010 och som presenteras i denna rapport hade sitt fokus på hydraulisk samverkan mellan komprimerad bentonit och den angränsande sprickiga bergmassan. De främsta målen för BRIE var:

- En ökad vetenskaplig förståelse för utbytet av vatten över gränssnittet bentonit-berg.
- Bättre förutsägelser av bentonitens bevätning.
- Bättre karakteriseringsmetoder för deponeringshålen.

Experimentet utfördes på djupet –420 m vid Äspölaboratoriet och undersökningarna av berget inkluderade tre olika faser: Val av plats; Karaktärisering av plats; och Karaktärisering av två centrala borrhål. En konceptuell modell, se Tabell 5-1, användes för att identifiera processer, geometriskt ramverk, materialegenskaper, rumslig fördelning och randvillkor. Den konceptuella modellen användes sedan för att utforma undersökningar och för att ta fram data. Varje undersökningsfas avslutades med sammanfattande slutsatser angående exempelvis geometri och hydrauliska egenskaper. Baserat på undersökningarna var de viktigaste bergarterna diorit (gabbroid-dioritoid) med förekomster av finkornig granit och pegmatit.

De centrala borrhålen KO0017G01 – hål 17 och KO0018G01 – hål 18 hade en diameter på 300 mm och en längd av ca 3,5 m respektive 3,0 m. Efter karakterisering installerades bentonit i hål 18 (totalt 28,5 cylindriska block med en höjd av ca 100 mm). För hål 17 användes 33,5 block med samma höjd. Inför installationen svetsades ett centralt rör till en bottenplatta som sedan placerades vertikalt. Bentonitblocken monterades sedan, ett efter ett, på det centrala röret och instrument installerades i hål och slitsar i de bearbetade bentonitblocken. Relativ fuktighet, axiellt- och radiellt totaltryck såväl som portryck övervakades sedan i bentoniten under experimentet. Fokus var på att undersöka en sektion som förväntades vara våt (nära en vattenbärande spricka) och en sektion som förväntades vara (relativt) torr (på avstånd från en vattenförande spricka) för vart och ett av de två centrala borrhålen.

Bentonitpaketen installerades i båda hålen i september 2012. Upptaget för Hål 17 genomfördes i november 2013 och för hål 18 i slutet av februari 2014. Upptaget utfördes med sömborrning och vajersågning och både bentonit och berg i kontakt med bentonit (bergblock inklusive borrhålsvägg för centrala borrhål) undersöktes för att ta fram vattenhalt, densitet och relativ fuktighet. Dessa undersökningar och mätningar utfördes i laboratorium. Förutom detta utfördes ytterligare laboratorietester som gav hydraulisk konduktivitet och vattenretentionskurvor för bergmatris och ett vattenupptagsförsök gav motsvarande data för bentonit. Vidare användes fotografier av bentonit för dokumentation av sprickspår.

Experimentet inkluderade värdefulla undersökningsfaser och karaktäriseringsmetoder för berg och bentonit och ger ett unikt dataset för en heterogen, låggenomsläpplig bergmassa (konduktivitet från 10^{-15} till 10^{-11} m/s för kärnor med 60 mm diameter sågade i 10 mm tjocka prov) med vattenförande sprickor med låg transmissivitet (för hål 17 till exempel 10^{-11} m^2/s). En omättad zon identifierades i bergmassan runt borrhålen och det är troligt att både mindre sprickor och skillnader i bergarter ger olika förmåga att överföra vatten.

Contents

1 Introduction

1.1 Background and objectives

Construction of a nuclear waste repository requires information about and an understanding of the fractured rock and proposed engineered barriers. The Swedish concept for nuclear waste deposition that is currently being developed by the Swedish Nuclear Fuel and Waste Management Co (SKB) includes a natural barrier in the form of crystalline rock, and engineered barriers in the form of bentonite and a copper canister (SKB 2011). The canister and the bentonite should be placed in 1.75 m diameter deposition holes drilled to a depth of approximately 8 meters in the floor of the deposition tunnels. Important geo-scientific issues include the location and possible deformation (shearing) of fractures and deformation zones that could influence the localisation of canisters, and the distribution (amount and location) of fluid flow resulting in hydration of the bentonite, but may also, at high flowrates, cause piping and erosion

The Bentonite Rock Interaction Experiment, BRIE, presented in this report was focused on the hydraulic interaction between the system components of compacted bentonite and the near-field host rock composed of hard and fractured bedrock. The main objectives of BRIE were:

- An increased scientific understanding of the exchange of water across the bentonite-rock interface.
- Better predictions of the wetting of the bentonite buffer.
- Better characterisation methods of the deposition holes.

The experiment was subdivided into two main parts. The first part handled characterisation of rock including the selection and characterisation of a test site and two central boreholes. The second part handled the installation, hydration and dismantling of bentonite parcels installed in the two central boreholes. In addition to the field experiment a laboratory water uptake test was performed. BRIE is addressed in a joint modeling task (Task 8) of the SKB Task Force on Engineered Barrier Systems (EBS) and Groundwater Flow and Transport of Solutes (GWFTS). It was necessary to identify flowing fractures, wet sections, and sections that were “dry” to investigate wetting of the bentonite and exchange of water across the interface at these differing conditions.

1.2 Scope of work

The experiment was performed stepwise in successive activities:

- Selection of site: choice of an experiment area based on Äspö hydrogeological conditions and five investigation boreholes.
- Site characterisation including additional cored boreholes, borehole logging and hydraulic tests. Laboratory tests on rock.
- Characterisation of two central boreholes for installation of bentonite parcels. Drilling and testing of each central borehole and surrounding boreholes. Laboratory tests on rock and structural model of the experiment area.
- Design and installation of bentonite parcels.
- Monitoring of hydration and dismantling of the bentonite parcel.

Finally, analyses of water content for the bentonite parcels were performed and a compilation of results from the characterisation of rock bentonite analyses was made. A general timeline for the major activities are shown in Figure 1-1.

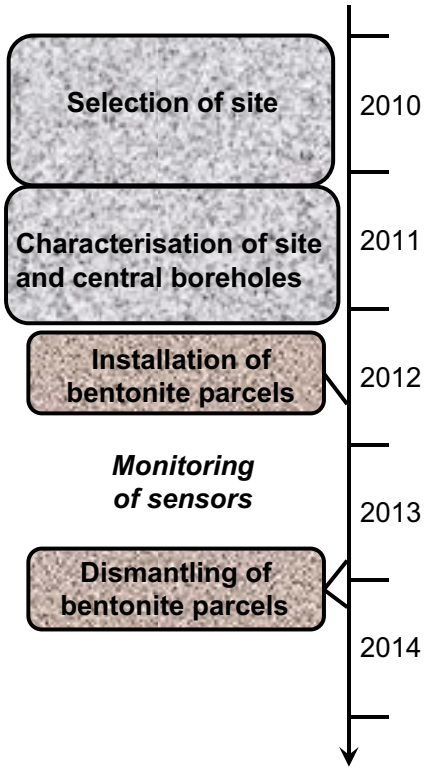

Figure 1-1. *Time-line for major activities in BRIE. Summary of main events for characterisation in the field and installation and dismantling of bentonite parcels are presented in Table 3-1 and Table 4-1.*

1.3 Outline of report

This report presents the work that has been performed within the BRIE project. An introductory description of investigation methodology and an initial, more general conceptual model is presented in Chapter 2. This chapter gives a brief overview of methods for deposition hole excavation and bentonite installation. Further it shows the investigation stages performed within BRIE and identifies parameters and processes that were expected to be of importance for the experiment. Chapter 3 describes the three different phases for characterisation of rock: 3.1 Selection of site; 3.2 Characterisation of site; and 3.3 Characterisation of central boreholes. The bentonite parcels were installed in the central boreholes characterised in the last investigation phase. For each of the three rock investigation phases, brief concluding remarks were given. These remarks were the basis for decisions before initiating the following phase. Work related to the bentonite parcels (design, installation, monitoring, dismantling, analyses and results) is presented in Chapter 4. In addition, this chapter presents results from a water-uptake test performed in the laboratory. Chapter 5 suggests a conceptual model of the BRIE site based on the investigations performed. Here, key features identified at the BRIE site are compiled (5.1.2) and an overview of data sets and references to previous chapters are given. Further, in the end of Chapter 5, results from rock characterisation and bentonite investigations are compiled to give a picture of the bentonite-rock interaction. Finally a list of concluding remarks for BRIE is presented, see Chapter 6. Results and data sets for different investigations are presented in the appendices.

2 Investigation methodology and conceptual model

This chapter includes an introductory description of investigation methodology and an initial, more general conceptual model. It gives a brief overview of methods for deposition hole excavation and bentonite installation. Further it shows the investigation stages performed within BRIE and identifies parameters and processes that were expected to be of importance for the experiment.

The overview of methods for deposition hole excavation and bentonite deposition is presented here to give a background for the experiment work, not to give a complete picture of the design premises.

2.1 Overview of methods from reference design

2.1.1 Selection of deposition hole positions

The acceptance of deposition hole positions is related to the fracture geometry and the hydraulic properties. Fracture size, water inflow and the transmissivity are of importance.

Deposition holes are drilled vertically in the floor of a deposition tunnel and based on current experience, the maximum distributed inflow to the deposition tunnel is set to be less than or equal to 5 l/min per deposition tunnel (300 m, or 1.7 l/min per 100 m) and the maximum point inflow less than or equal to 0.1 l/min (SKB 2010a).

Considering *fracture geometry* the following should be considered:

- Distance to deformation zones (with trace length longer than 3 km) should not be less than 100 m (SKB 2009).
- Considering shearing of fractures, deposition positions should be selected so that they do not intersect extensively large fractures. Currently, the Full Perimeter Intersection Criterion (FPC) and the Extended Full Perimeter Intersection Criterion (EFPC) should be satisfied (Munier 2006).
- The deposition holes should be located in solid or sparsely fractured rock.

An additional comment related to geology is that placing a deposition hole in rock with a very low thermal conductivity is not permitted. However, BRIE was a hydraulic experiment under iso-thermal conditions and no source of heating was included during the experiment.

Regarding inflow and transmissivity no more than 100 kg of the initially deposited buffer material should be lost (due to piping and erosion) from the time when the buffer is exposed to inflowing water to saturation. According to present knowledge the water flowing into an accepted deposition hole must be less than 150 m^3 (SKB 2009). In addition, the connected effective transmissivity along the full length of the deposition hole wall, and as averaged around the hole, must be less than 10^{-10} m^2/s.

2.1.2 Excavation of deposition holes

Deposition holes are excavated with a full-phase down-hole drilling technique and excavation of a level at top of hole is made using wire sawing (SKB 2010a). The diameter of the deposition hole should be 1.75 m and the depth approximately 8 meters. When drilling is finalised, levelling of bottom of hole should be made and loose rock debris should be removed. Further, removal of water, cleaning and inspection (inspection of inflow to deposition hole, inspection of fractures intersecting the deposition hole) are important.

Before deposition of the bentonite buffer, installation of a bottom plate of low-pH concrete combined with a copper plate is made.

2.1.3 Deposition of bentonite buffer

Prior to the installation of the buffer, canister and back-fill it shall be verified that the connected effective transmissivity in the excavation-induced damage zone is acceptable. Further, the deposition hole should not be intersected by a discriminating fracture.

Before deposition, a protection sheet is placed in the deposition hole (attached to border of copper plate) and a drainage system (pipe, an ejection pump and an alarm system) is placed between the sheet and the wall of the deposition hole.

In all, the installed buffer consists of one bottom block, six ring-shaped blocks and three solid blocks on top. The gap between the blocks and the rock surface will be filled with pellets (SKB 2010b). The minimum distance from tunnel floor to bentonite buffer is 1.25 m and the hole depth approximately 8 meters.

The installation of the pellets commences when the backfilling of the deposition tunnel has reached the section of the deposition hole. The drainage system, the protections sheet and sensors are removed before doing so.

Tests and inspections of the installed buffer geometry and density should be made. Important inputs are deposition hole volume, deposition hole radii and cross section area along its centre axis. Further, weight, dimensions and positions of installed blocks and weight and volume of installed pellets are used.

2.2 Investigation stages for BRIE

In the previous section, a brief overview of the principal steps including selection of deposition holes position, excavation of the deposition holes and deposition of bentonite were presented. Based on the above, the following stages were suggested and also performed for the field experiment, BRIE:

a) Selection of site.

b) Site characterisation.

c) Drilling and characterisation of two central boreholes.

d) Draw-down (very limited since borehole was kept wet and only emptied just before installation).

e) Installation of bentonite parcels.

f) Recovery and saturation, Monitoring of sensors.

g) Dismantling and analysis of (partly) saturated bentonite parcels and rock.

2.3 Initial/general conceptual model

Given one of the main objectives of BRIE, *an increased scientific understanding of the exchange of water across the bentonite-rock interface*, the focus of the experiment was on the water transport between the rock and the bentonite. As an example, a water supply from the rock that is larger than the ability of the bentonite to adsorb the water is expected to result in a situation where the inflow into the bentonite would mainly depend upon the bentonite properties. The opposite, a water supply that is smaller than the ability of the buffer to adsorb the water would result in a possible de-saturation of the rock. Of importance for BRIE was therefore to describe the evolution in space and time of:

- The rock: the water pressure and water flow in the rock matrix and fractures.
- The bentonite: the water pressure, total pressure (swelling pressure), density and water content.
- The interface: Exchange of water over the interface between the bentonite and a sparsely fractured rock. The interface as a mutual boundary.

As a basis for the experimental work, an initial conceptual model was made. According to Rhén et al. (2003) a conceptual model defines the geometric (or structural) framework in which the problem is to be solved and the size of the modeled volume (scale). Further, it defines the constitutive equations

(mathematical model) for the processes included in the model and the boundary conditions. Of importance to reach the objectives of the experiment was to characterise the site and the two central boreholes and the stages a) and c) with their differing geometries, see Figure 2-1, were therefore assumed to be of most importance. Figure 2-2 presents principle drawings of these two investigation stages to show the changes in the system. The figure also includes important parameters and processes. Of particular interest was to describe the geometry of the fracture system and the ability of the fractures, rock matrix and the excavation disturbed zones (EDZ) to transmit fluid flow. Considering important processes influencing the behavior of the system, induced damage to the rock from excavation methods (EDZ) was taken into account as a part of the geometrical description. Drilling of the central boreholes could result in a disturbed zone and a change in the hydraulic properties (Autio 1997, Andersson and Martin 2009, Andersson et al. 2009). Further, the pressure draw-down was expected to cause changes in hydraulic properties due to groundwater degassing and deformation (Jarsjö et al. 2001). Degassing results in unsaturated (or two-phase) flow. Following deposition of the bentonite, fluid flow results in wetting of the bentonite and may also cause piping and erosion. Deformation was treated to a limited extent and erosion and piping were not explicitly within the scope of this study.

Of interest was to identify flowing fractures, wet sections, and sections that were “dry” to investigate wetting of bentonite and exchange of water across the interface at these differing conditions. To conclude, parameters expected to be important were:

- Fracture: orientation, intensity, size (and location).
- Fracture: transmissivity, hydraulic aperture (based on cubic law) and storativity.
- Rock matrix hydraulic conductivity and EDZ transmissivity (and geometry).
- Pressure draw-down and hydraulic boundary conditions.
- Inflow to central borehole: total and point inflows (locations).
- Geometry (x, y, z) of tunnel, cored boreholes and central borehole(s).

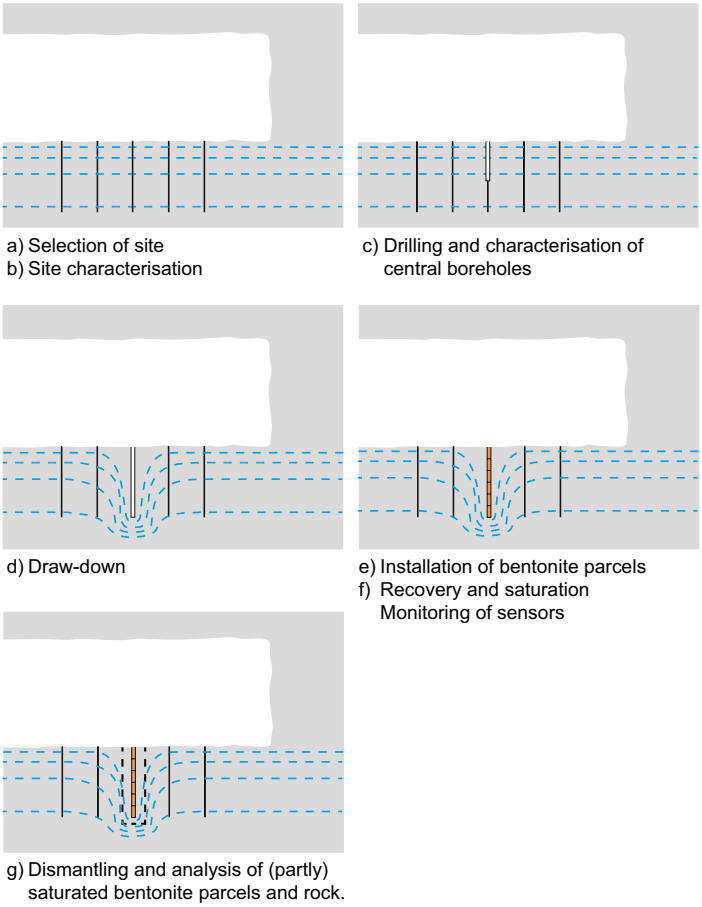

Figure 2-1. *Investigation stages for BRIE.*

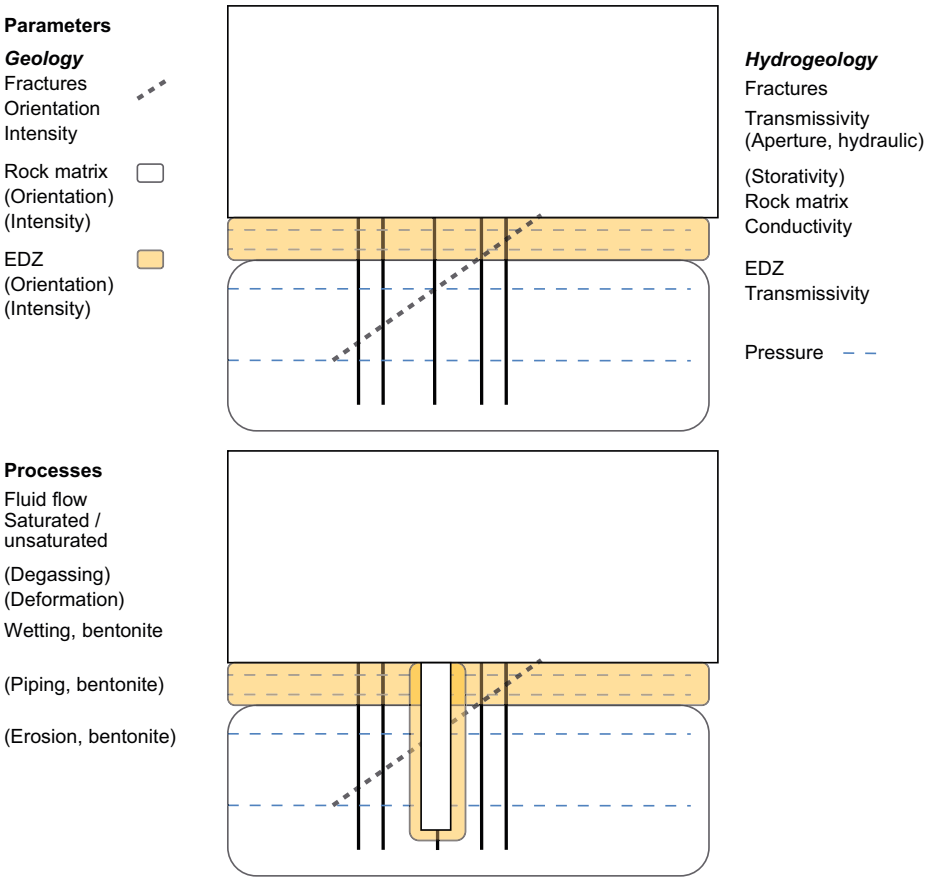

Figure 2-2. *Principle drawings of boreholes and tunnel. Investigation stages a) and c) were of most importance for the site characterisation. Parameters and processes included in the drawing were used as a basis for a conceptual model and design of investigations.*

Processes suggested to be relevant were:

- Fluid flow (saturated, unsaturated).
- Degassing (due to pressure loss).
- Deformation (due to change in stresses close to tunnel).
- Wetting, erosion and piping of bentonite (locations and size of inflows).

Parameters and processes included in Figure 2-2 formed the basis for the design of investigations for the experiment. The parameters are further described in the next section.

2.3.1 Geology

Fracture: orientation, intensity, size and location

Beside the geometry of tunnels and boreholes, the geometric or structural framework is determined by the geometry of the fracture system. Important parameters are *fracture orientation* and *fracture intensity*. Orientation can be presented using a stereoplot showing strike and dip of individual fractures along a tunnel or borehole. The fracture intensity is commonly described by the number of fractures identified per meter along a cored borehole (or scan-line) (Dershowitz and Herda 1992). Fractures found parallel or sub-parallel to the tunnel or borehole have to be taken into account. Sources of error in joint surveys is the topic of Terzaghi (1965).

Fracture size is important when considering shearing. Deposition positions should be selected so that they do not intersect extensively long fractures. Currently, the *Full Perimeter Intersection Criterion* (FPC) and the *Extended Full Perimeter Intersection Criterion* (EFPC) should be satisfied (Munier 2006).

The orientation, intensity and size will influence the positions selected for deposition holes. Further, the intersection between fractures and between fractures and boreholes (tunnel) will influence both pressure and flow. The microstructural geometry of fractures will influence fluid flow including transmissivity, saturation, storage coefficient etc.

Investigations are mainly performed using geological mapping and a tool referred to as BIPS (Borehole Image Processing System e.g. Carlsten et al. 2001). Identification of inflows during drilling as a function of borehole depth is an additional source of information. Further isolation and pressure logging of interesting sections in boreholes drilled early on can be used to identify larger intersecting fractures and to describe the fracture system.

2.3.2 Hydrogeology

Fracture: transmissivity and hydraulic aperture

The capacity of a fracture to transmit water, the transmissivity, is determined using hydraulic tests. Either steady state or transient (time-dependent) tests are used where pressure (head) and flow are central parameters for estimates of transmissivity. In this report, transmissivity, T, is used to describe the ability of a fracture to transmit water whereas hydraulic conductivity, K, as defined by Darcy's law, is used to describe the ability of the rock matrix to transmit water. The transmissivity can be expressed by the cubic law:

$$T = \frac{\rho g b_h^3}{12\mu} \tag{2-1}$$

which assumes fluid flow between two parallel surfaces, e.g. a fracture, with the distance (and hydraulic aperture) b_h (Snow 1968). The density and viscosity of the fluid, ρ and μ, and the acceleration due to gravity, g, are also included in the equation. Hydraulic aperture (based on the cubic law) is useful since it gives a physical representation of a fracture and relates to work performed for e.g. grouting of fractures and hydromechanical behavior.

Zimmerman and Bodvarsson (1996) concluded that the effective hydraulic aperture, b_h, is less than the mean aperture, $\langle b \rangle$, which was expressed by the use of the standard deviation, σ_b, and the contact area, c:

$$b_h^3 = \langle b \rangle^3 \left[1 - \frac{1.5\sigma_b^2}{\langle b \rangle^2} \right] (1 - 2c) \tag{2-2}$$

The transmissivity will be influenced by the degree of saturation. Pressure draw-down, caused by drilling and pumping, possible degassing and the fracture aperture variations are important. Aperture variations facilitate trapping of bubbles (Jarsjö et al. 2001).

The fracture geometry is influenced by the situation of stress. Rutqvist and Stephansson (2003) comment that results from field tests may show a general decrease in hydraulic conductivity (permeability) with depth (the most pronounced in the upper 100–300 meters). At greater depth fractures are closed to a residual hydraulic conductivity (transmissivity) meaning that further compression will not decrease the hydraulic aperture, but fractures that are locked-open by hard mineral fillings or by large shear dislocation may exist. Considering the small apertures at high effective stress, hydromechanical experiments show that residual void- and hydraulic aperture exist even at very high compressive stress since rock fractures do not close completely (Rutqvist et al. 1998). Change in stress and permeability may occur close to a tunnel due to redistribution of stresses (Hökmark et al. 2006, Rutqvist and Tsang 2008).

Hydraulic tests may include measurement of inflow along investigation boreholes using e.g. a method referred to as Posiva Flow Logging (PFL). The method allows identification of flow location and flow. Transient hydraulic tests can be used to estimate transmissivity. Performing tests at different pressures (e.g. above and below bubble pressure) could help identifying the occurrence of degassing, deformation and turbulent flow through the observed flowrate – pressure drawdown relation (Jarsjö et al. 2001, p 39). In Jarsjö et al. (2001, p 39) constant pressure tests (CPT) were used.

Rock matrix hydraulic conductivity and EDZ transmissivity (and geometry)

Rock matrix hydraulic conductivity is in principle estimated using the transmissivity of a section divided by the length of that section. Since hydraulic conductivity for good quality rock can be expected to be very low, hydraulic conductivity measurements in BRIE were performed in the laboratory. Hydraulic conductivity was investigated on cores originating from the 76 mm boreholes (cores approximately 60 mm) meaning that any (micro) fractures in the rock matrix are expected to be smaller than this size. Packers isolating sections including the excavation disturbed zones (EDZ) could however be used for estimate of its transmissivity.

Using mechanical excavation methods (TBM) it is possible to achieve a damage zone (EDZ) that is limited to a few centimeters (elastic rock conditions) (Bäckblom 2008). Further, for excavation using drill and blast, the damage zone will extend several decimeters (elastic rock conditions) (Bäckblom 2008).

Possible investigations methods could be ultrasonic measurements to determine depth of EDZ, laboratory measurements on rock cores, multi-packers for determining transmissivity, ground penetrating radar, refraction seismic and hydraulic interference testing. None of these methods were used in this experiment (BRIE). Focus in BRIE was on the hydraulic properties and the geometry of fractures and not on the detailed geometry of EDZ. Being aware of the above is however important when discussing the hydraulic behavior at the interface.

Pressure

Draw-down associated with tunnels and deposition holes

Figure 2-1 presents the most important investigation stages, from site characterisation to the short duration draw-down during installation of bentonite followed by pressure stabilization. Surrounding the deposition tunnel, the pressure in principal increases with increasing distance from the tunnel wall.

Drilling of investigation and central boreholes disturbs the pressure and sections with different transmissivity should therefore as far as reasonable be isolated. Total stress, pore water pressure and relative humidity (water content) was expected to be of importance for the bentonite. Of interest would also be to measure the pore water pressure and relative humidity close to the rock wall for investigation of behavior at the interface.

Hydraulic boundaries

When developing a conceptual model and designing an experiment, processes and parameters are of importance but so are also the boundary conditions. Depending upon the geometry of the site selected for BRIE different situations were expected to occur. Locating the test in the middle of a tunnel would possibly allow a 2D simplification, since there would be limited influence from tunnel front (spherical flow).

Inflow into central borehole

Inflows along a deposition hole could result in piping and erosion of the bentonite buffer. Visual inspection of inflows as a function of time (and pressure in surrounding boreholes) were therefore suggested. Locations as well as the size of inflows were important. Over-coring of previously investigated boreholes was expected to help in the identification of fracture orientation and intensity.

Table 2-1 presents important parameters, comments on related processes and investigation methods.

Discrete fracture network models (DFN) demand descriptions of individual features. DFN-modeling and included parameters are described in e.g. Dershowitz et al. (2003) and Svensson et al. (2008). Important parameters of a DFN model are: orientation, intensity, size, transmissivity and spatial pattern (e.g. Dershowitz et al. 2003).

Table 2-1. Important parameters, comments on related processes and investigation methods.

Parameter	Comments on related processes	Investigation methods
Geology		
Fracture orientation	Influences position of deposition holes.	Geological mapping (core and tunnel), BIPS.
Fracture intensity	Influences position of deposition holes.	Geological mapping (core and tunnel), BIPS.
(Fracture size)	Influences position of deposition holes.	Geological mapping (core and tunnel).
Hydrogeology		
Fracture transmissivity	Saturated flow.	Hydraulic tests: Short duration tests, Posiva Flow Logging (PFL), Transient hydraulic tests.
Fracture hydraulic aperture	Saturated flow.	Based on transmissivity.
Rock matrix hydraulic conductivity	Saturated flow.	Hydraulic laboratory tests.
Relative humidity (rock matrix)	Unsaturated flow: water content as a function of relative humidity, relative humidity profiles.	Hydraulic laboratory tests.
Pressure	Flow, boundary condtion.	Pressure logging (sections/full length).
Inflow central borehole: Total and point inflows	Flow, (wetting, piping and erosion). Flow, (wetting, piping and erosion).	Hydraulic tests, visual observations. Nappy test. Developed within project, see later sections.
Inflow tunnel Geometry	Flow, boundary condition.	Sorbing mats. Developed within project, see later sections.
Tunnel Cored boreholes Central borehole (s)		Coordinates for tunnel and all boreholes. Coordinates and volume of central borehole.

2.3.3 Bentonite

This section gives a brief overview of descriptions of bentonite material and of different experimental work which are of relevance for the BRIE project.

Mineralogy

Bentonite consists mainly of montmorillonite, which is responsible for the swelling ability of bentonite in contact with an aqueous solution. The montmorillonite mineral belongs to the smectite group, in which all the minerals have an articulated layer structure. Each layer is composed of a central sheet of octahedrally coordinated cations, which on both sides is linked through shared oxygens to sheets of tetrahedrally coordinated cations, as pictured in Figure 2-3. The thickness of an individual mineral layer is around 1 nm and the extension in the two other directions is often several hundred nanometres. The octahedral sheet has aluminium as central ion, which is partly substituted principally by magnesium and iron. The tetrahedral sheet has silicon as central ion, which partly may be substituted principally by aluminium. The substitutions result in a net negative charge of the montmorillonite layer. The negative layer charge is balanced by cations located between the individual layers (interlayer space). The structure leads to a water affinity in the interlayer space. It is the mechanisms of hydrating the interlayer cations and osmotically transporting water into the interlayer solution that are the causes for bentonite swelling. See Karnland et al. (2006) for a more detailed account on bentonite mineralogy.

The swelling ability is strongly dependent on what type of charge compensating cation is dominating in the interlayer. Montmorillonites dominated by either sodium or calcium, therefore exhibit very different properties in general. However, these differences appear to be fairly small for buffer densities (see below). Apart from the montmorillonite, bentonites contain other minerals as well (so-called accessory minerals), for instance quartz and gypsum. The content of montmorillonite and the composition of accessory minerals vary between different quarries. MX-80 is a commercial designation of a sodium dominated Wyoming bentonite produced by the American Colloid Company with a montmorillonite content of approximately 0.8.

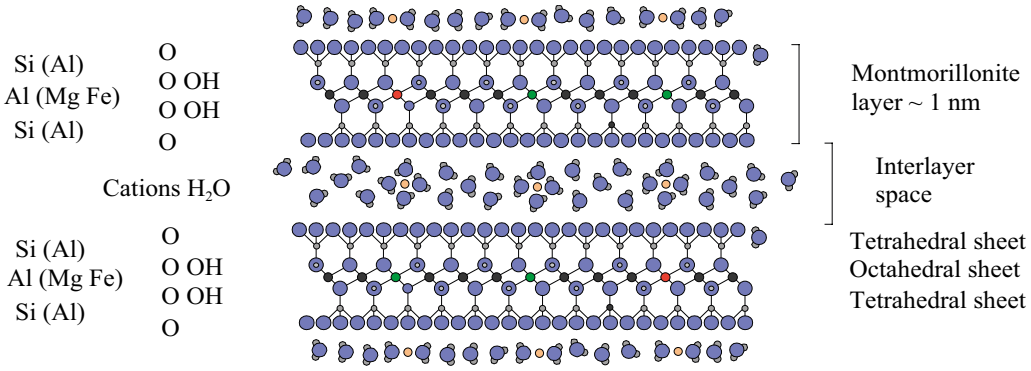

Figure 2-3. *Edge view cartoon of two montmorillonite layers with interlayer cations and water molecules (from Karnland et al. 2006). Colors: blue (O), gray (H, or Si in tetrahedral sheet), orange (cation e.g. Na), black (Al), green (Mg), red (Fe).*

Bulk variables

To be able to describe the conditions of a bentonite material, several parameters and definitions are used in this report. The bentonite material consists of solid particles and voids which can be partly filled with water (see Figure 2-4). The volume of the material can be divided into the volume of the porous system ($V_p = V_w + V_g$) and the volume of the solid particles (V_s) and corresponding masses, m_w and m_s. From these definitions several other parameters describing the condition of the bentonite can be defined. Some of the most common are listed in Table 2-2 and Table 2-3.

The requirement for the buffer density at saturation is 2 000 kg/m^3. For a particle density of 2 780 kg/m^3 for MX-80, and a water density (ρ_w) of 1 000 kg/m^3 this corresponds to a dry density of 1 562 kg/m^3 (see SKB 2010b).

Swelling pressure and water retention properties

The swelling pressure (P_{sw}) is the pressure exerted by a water saturated bentonite at free access of water, and this pressure display a strong relationship with the dry density (or any equivalent quantity). The water retention property, on the other hand, is the relationship between the water content and the external relative humidity (RH) at equilibrium and for unconfined (i.e. free swelling) conditions. These two properties both reflect the chemical potential of the clay water which can be described through the definition of suction (s):

$$s = -\frac{\rho_w \cdot RT}{M_w} \cdot \ln(RH) \qquad (2\text{-}3)$$

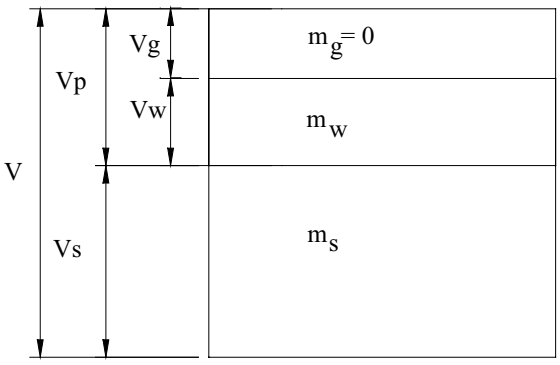

Figure 2-4. *Definition of masses and volumes for different phases.*

Table 2-2. Definitions for different densities.

Bulk density	Density of solid particles	Dry density	Density at saturation
$\rho_b = \frac{m_s + m_w}{V}$	$\rho_s = \frac{m_s}{V_s}$	$\rho_d = \frac{m_s}{V}$	$\rho_m = \frac{(\rho_w \times V_p + m_s)}{V}$

Table 2-3. Definitions for other bulk quantities.

Water content	Degree of saturation	Void ratio	Porosity
$w = \frac{m_w}{m_s}$	$S_l = \frac{V_w}{V_p}$	$e = \frac{V_p}{V_s}$	$n = \frac{V_p}{V}$

where R is the universal gas constant; T is the absolute temperature; and M_w is the molar mass of water. The suction value can be described as a function of the water content and the pressure (P):

$$s(w, P) = s_{free}(w) - \alpha \cdot P \tag{2-4}$$

where s_{free} is the suction at unconfined conditions; and α is a compressibility factor which usually is assumed to be equal to unity, especially at saturated conditions (Dueck 2004). Free access of water is equivalent with $s = 0$, which means that swelling pressure is equal to the suction at unconfined conditions ($P_{sw} = s_{free}$). The suction value can be equated with the difference between the external gas and liquid pressure ($s = P_g - P_l$). This means that a suction value can be treated as a negative pore pressure, although this should not be interpreted literally.

It should be noted that the actual behavior is more complex since the $s_{free}(w)$ relation also display a path dependence, and that the stress state in general is anisotropic which means that one cannot denote this a pressure. For modeling purposes it is usually convenient to define a water retention curve which describes a relation between suction and the degree of saturation, $S_l(s)$.

Hydraulic conductivity and moisture diffusivity

The mobility of the clay water can be described and measured in terms of hydraulic conductivity and moisture diffusivity. The hydraulic conductivity (K) is quantified by applying a hydraulic gradient (I) over the sample with section area (A), and by measuring the flow (Q). This is described by Darcy's law:

$$Q = -K \cdot I \cdot A \quad (m^3 / s) \tag{2-5}$$

The conductivity is equivalent to an intrinsic permeability, $k = K \cdot \mu / \gamma_w$, where μ is the dynamic viscosity and γ_w is the specific weight of water. The Darcy's law can be generalized to unsaturated conditions by introduction of a relative permeability (k_r), usually defined as a function of the degree of saturation, which gives the flux ($q = Q/A$) as:

$$q = -\frac{k \cdot k_r}{\mu} \cdot \frac{dP_l}{dx} \quad (m / s) \tag{2-6}$$

Note that $dP_l/dx = I \cdot \gamma_w$. This relative permeability function has to be indirectly evaluated, for instance from water uptake tests, after the adoption of an intrinsic permeability and a water retention curve.

The moisture transport in bentonite can also be describes as a diffusion processes following Fick's law:

$$\frac{\partial w}{\partial t} = D \cdot \frac{\partial^2 w}{\partial x^2} \tag{2-7}$$

where D is the moisture diffusivity. This can be directly evaluated from water uptake test, without adoption any other quantities. For a material with a homogenous porosity it can be shown that the diffusivity corresponds to the permeability and the retention properties according to the following expression:

$$D(S_l) = \frac{k \cdot k_r(S_l)}{n \cdot \mu} \cdot \frac{dP_l}{dS_l} \tag{2-8}$$

A compilation of the main parameters and the related processes and investigation methods are given in Table 2-4.

Apart from these parameters there are other bentonite properties of major interest although not for the BRIE projekt, such as the shear strength (e.g. Börgesson and Hernelind 2006) and the thermal conductivity (Hökmark et al. 2009).

Field experiments

The BRIE experiment can be put into perspective by comparing it with previously performed field experiments. On one hand there are a number of *large–scale tests* which either have represented a specific concept or have been largely generic. These tests can in turn be divided in tests with natural wetting: such as the Febex in-situ (Enresa 2006), the Kamaishi mine experiment (Chijimatsu et al. 2001), the Isothermal Test (Dixon et al. 2001), Buffer Container Experiment (Graham et al. 1997) and Prototype repository (Svemar et al. 2016); and those with artificial wetting: Canister retrieval test (Kristensson and Börgesson 2015) and Temperature Buffer Test (Åkesson 2012). On the other hand there are a number of *enhanced tests* with the focus on chemistry and mineralogy: such as the Long term tests of buffer materials (Karnland et al. 2009) and the Alternative buffer materials (Svensson et al. 2011). Among the large scale test, the BRIE experiment is most comparable to the ones with natural wetting and thus with localized water entry through fractures. The Isothermal Test resembles the BRIE experiment in terms of the absence of any heater. The enhanced tests, on the other hand, resemble the BRIE experiment in terms of dimensions (diameters ~ 0.3 m) and the dismantling method.

Table 2-4. Important parameters, related processes and examples of investigation methods.

Material parameter	Main process	Investigation methods
Water content	Description of state	Drying*
Density	Description of state	Paraffin oil submerging*
Swelling pressure	Homogenization of buffer and backfill	Swelling pressure device**
Water retention properties	Hydration of buffer and backfill	Jar method**
Hydraulic conductivity	Hydration of buffer and backfill	Swelling pressure device**
Moisture diffusivity	Hydration of buffer and backfill	Water uptake test***

* Section 4.4.3.
† Åkesson et al. 2012.
‡ Börgesson 2001.

2.4 Site selection criteria

Table 2-5 presents a list of the site selection criteria that were used. The BRIE specific criteria (first three rows including depth, fracture/rock geometry and borehole/test site geometry) were considered the most important. A limited (low) inflow was also suggested. The time expected for the field experiment was 3–5 years.

Table 2-5. Site selection criteria.

Location, geometry	Comment
	BRIE
”Large” depth	The rock stresses influence the hydraulic aperture.
	Aperture variations influence saturation.
	The water pressure influences the hydraulic gradient (degassing).
	Suggested depth > 300 meters (more relevant hydraulic head and rock stresses).
Fracture/rock geometry	The central borehole should include a few fractures with different transmissivity and also a significant part of unfractured rock.
Borehole/test site geometry	Central hole(s) size of the LOT and ABM holes (Long term test of buffer material, Karnland et al. (2000) and Alternative Buffer Material, Eng et al. (2007)). Diameter approx. 300 mm, depth 3–5 m.
	76 mm cored boreholes drilled to find most appropriate place.
	Suggested length of test site: 5–10 boreholes, 3 meters distance, approximately 20–40 meters of tunnel needed.
At “a distance” from tunnel front	Allows 2D simplification when modelling.
	General.
Fracture size	Distance to deformation zones (with trace length longer than 3 km) should not be less than 100 m.
	Considering shearing of fractures, deposition positions should be selected so that they do not intersect extensively long fractures. Currently, the Full Perimeter Intersection criterion (FPC) and the Extended Full Perimeter Intersection criterion (EFPC) should be satisfied (Munier 2006).
	The deposition holes should be located in solid or sparsely fractured rock.
Fracture distance from tunnel wall	Natural fractures parallel to the tunnel and within 0.8 m are critical.
Tunnel inflow	The maximum distributed inflow to the deposition tunnel is set to be less than or equal to 5 l/min per deposition tunnel (300 m) and the maximum point inflow less than or equal to 0.1 l/min.

Based on the site selection criterias above the TASO-tunnel was selected as a potential site for BRIE. Characterisation of rock at this site follows in the next chapter.

3 Characterisation of rock

This chapter describes the three different phases for characterisation of the rock in TASO in the following sections: 3.1 Selection of site; 3.2 Characterisation of site; and 3.3 Characterisation of central boreholes. The bentonite parcels, described in Chapter 4, were installed in the central boreholes that were characterised during the last rock investigation phase. For each of the three rock investigation phases, brief concluding remarks were given, see Sections 3.1.4, 3.2.5 and 3.3.5. These remarks formed the basis for decisions before initiating the next investigation phase. Chapter 5 is based on all three investigation phases and suggests a conceptual model of the BRIE site including identified key features and an overview of data sets with reference to the characterisation of rock that follows below, see compilation in Table 5-2 and Table 5-3.

It was of interest to identify flowing fractures, wet sections, and sections that were "dry" to enable investigations of the wetting of bentonite and the exchange of water across the interface under these differing conditions.

The following investigations were selected based on what was identified as important investigation stages, parameters and processes, see Chapter 2:

- Drilling.
  - Pressure Logging.
  - Flow measurements.
- BIPS, core mapping (and tunnel mapping).
- Posiva Flow Log or similar.
- Hydraulic tests (short duration and transient tests).
- Nappy test measurements.
- Tunnel inflow.
- Laboratory investigations of the rock matrix (hydraulic conductivity, retention curve and RH-profile at the time of dismantling).
- Scanning of fracture surface geometry (not a key parameter, but interesting from a mechanical perspective).

Dates for the main events during the course of work with the characterisation are compiled in Table 3-1.

Table 3-1. Summary of main events for characterisation in the field.

Time (date)	Event
2010-10-04	Drilling of five boreholes. Phase 1: Selection of site
2010-11-30	Hydraulic testing. Phase 1
2011-03-02	Concrete slab removed
2011-03-15	Drilling. Phase 2: Characterisation of site
2011-06-09	Difference flow logging. Phase 2
2011-09-08	Hydraulic testing. Phase 2
2011-11-16	Drilling. Phase 3: Characterisation of central boreholes
2012-02-23	Hydraulic testing. Phase 3
2012-04-26	Nappy test, KO0017G01
2012-08-21	Tunnel flow measurement

Figure 3-1 shows the boreholes drilled in the tunnel floor including the five primary boreholes drilled during the site selection (Phase 1, red) and the additional 14 drilled during the site characterisation (Phase 2, black). Phase 2 also included drilling of boreholes in the tunnel wall, see Figure 3-2. In Phase 3 boreholes KO0017G01 and KO0018G01 had their diameters increased from 76 to 300 mm.

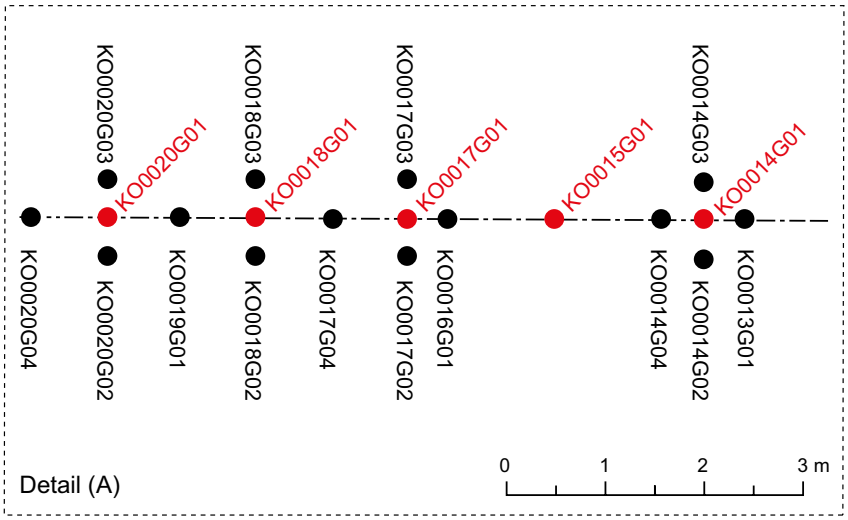

Figure 3-1. *Boreholes Phase 1 (red) with an individual distance of 1.5 m, and boreholes Phase 2 (black) at a distance of 0.4 m or 0.75 m. In Phase 3 boreholes KO0017G01 and KO0018G01 had their diameters increased from 76 to 300 mm. Tunnel front is found to the left in the figure.*

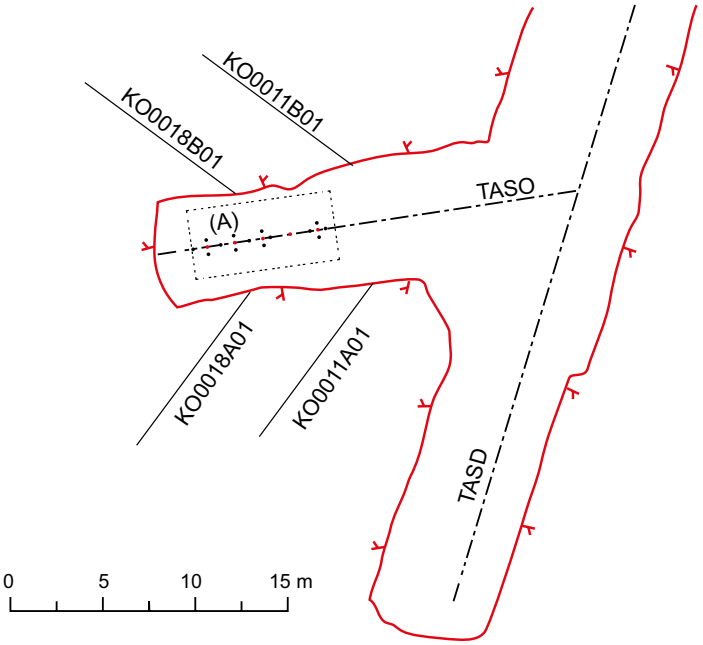

Figure 3-2. *Boreholes in tunnel wall, Phase 2: KO0011A01 and KO0018A01 (left wall). KO0011B01 and KO0018B01 (right wall). Boreholes in tunnel floor are seen as red and black dots along the tunnel axis.*

3.1 Selection of site

3.1.1 Drilling, pressure logging and flow

The purpose of this activity was to drill the first phase investigation boreholes and obtain pressure and flow for the individual boreholes. Sections with flowing fractures as well as “dry” sections were of main interest.

The initial five vertical 76 mm boreholes used in Phase 1 were positioned at an individual distance of 1.5 meters along the centre of the TASO-tunnel (KO0014G01, KO0015G01, KO0017G01, KO0018G01 and KO0020G01, see Figure 3-1). The group of five boreholes were positioned between the tunnel front and a deformation zone. During this phase, the tunnel floor was covered by a concrete slab, see Figure 3-3, so borehole location was selected based on borehole distance

only and was not influenced by the local geological or structural conditions. The concrete slab was cut and taken away before initiating Phase 2. In Phase 1, selection of site, the instruction concerning borehole length was an approximate length of 3.5 m (3.0 m in rock). Following drilling, the rock cores were placed in core boxes for core mapping.

Before starting the drilling, clocks were synchronized (to an SKB-computer) and during drilling, time when reaching specific depths should be documented. Depth and pressure responses aimed at identifying water-bearing fractures (location and approximate orientation). Once a borehole was drilled a packer was mounted 0.5–0.8 m from the rock surface to investigate the full length borehole properties and if the borehole did not exhibit natural flow the borehole was filled with water before closing the packer valve. In Phase 1 documentation of time and depth was made to a very limited extent. In Phase 2, see Section 3.2, documentation was made and found useful to identify connecting fractures.

Pressure monitoring was performed using pressure gauges on the wall, see Figure 3-4. The picture shows gauges for the five initial boreholes. Gauges were added during the experiment and the drilling of new boreholes. For flow measurements performed during drilling, flow was measured opening the packer valve right by the packer itself, see e.g. Figure 3-3. The pressure measurement mode employed was gauge measurements where the pressure is positive in relation to the varying atmospheric pressure.

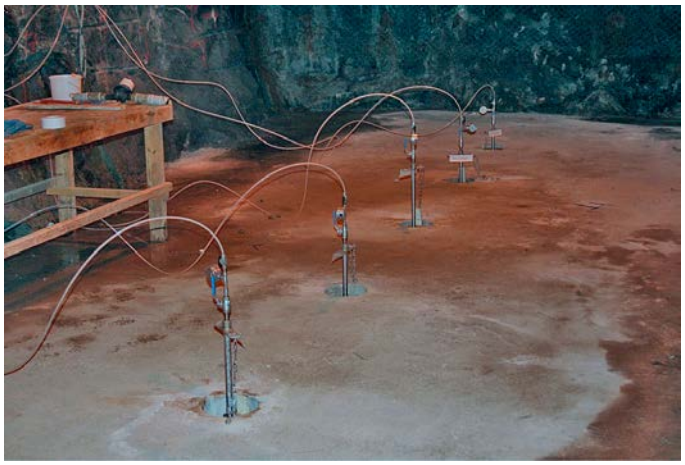

Figure 3-3. *TASO-tunnel (Phase 1) and the five boreholes (borehole distance 1.5 m) used for initial characterisation and selection of site. Picture includes the packers and the concrete slab.*

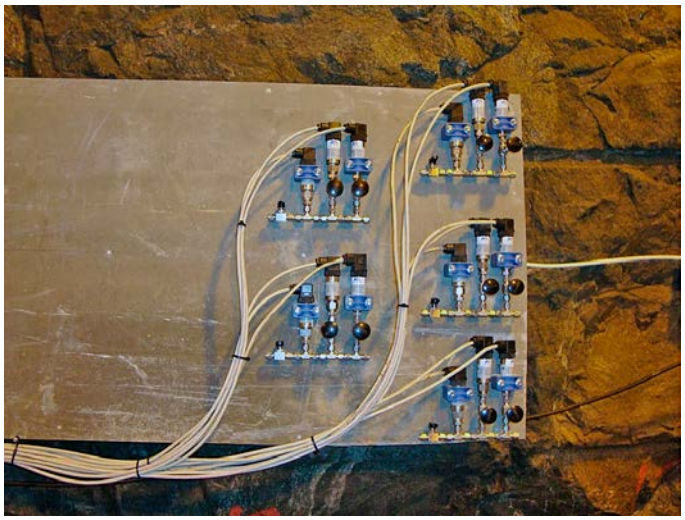

Figure 3-4. *Pressure gauges on tunnel wall during Phase 1. Three gauges for each borehole. During the experiment, packers and gauges were added when drilling new boreholes.*

Results

The purpose of this activity was to drill the boreholes and to obtain pressure and flow to indicate where fractures and "dry" sections could be identified. Pressure monitoring allowed for observation of pressure responses and identification of formation pressures (hydraulic head) in boreholes. Pressure was monitored using pressure gauges on the wall (see Figure 3-4) and flow was measured opening the packer valves (see Figure 3-3). Figure 3-5 shows an overview of the monitored pressure during drilling of the Phase 1 boreholes. Once one borehole was drilled, a packer was installed and the pressure was monitored. Among the five primary boreholes, KO0017G01 (yellow) had the highest pressure. Drilling was performed in October 2010.

Table 3-2. Pressure and flow, z-levels initial measurements.

Measurement	z-level
Pressure	Pressure gauges on wall (gauge)
	z: approximately –418.3 m*
Flow	Flow from packer valves above concrete slab, see Figure 3-3)

* Floor D-tunnel: −420 m; upper level area with gauges: −417.9; lower level: −418.7 m, see Figure 3-4.

Based on initial full-length flow measurements performed during Phase 1 the result was the following:

- Borehole KO0014G01 had a total flow of 0.001 l/min (0.01 l in 10 min), 2010-10-08, section 0.5–3.0 m.
- Borehole KO0017G01 had a total flow of 0.0005 l/min (0.005 in 10 min), 2010-10-11, section 0.5–2.97 m.
- Boreholes KO0015G01 (2010-10-15, section 0.75–3.03 m) and KO0018G01 (2010-10-15, section 0.55–3.06 m) had "no" flow in 30 min (1 800 s), only few drops.
- Borehole KO0020G01 had in total 19 ml in 30 min (almost all water immediately then only drops), 2010-10-15, section 0.82–3.1 m).

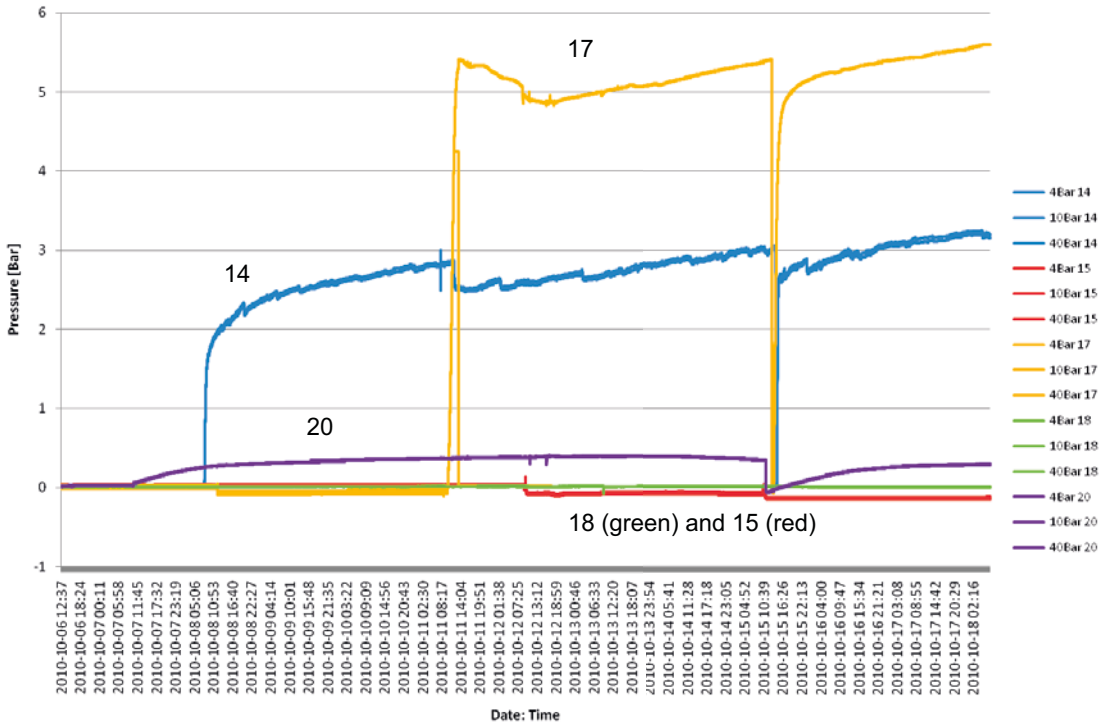

Figure 3-5. *Overview of natural pressure during drilling Phase 1 (five primary boreholes: KO0014G01, KO0015G01, KO0017G01, KO0018G01 and KO0020G01, here identified by the numbers 14, 15, 17, 18 and 20). Packers were installed immediately after a borehole was drilled and before drilling the next borehole.*

Additional single packer tests were performed for the flowing boreholes KO0014G01 and KO0017G01 to identify where flow was located. Flow was measured using a single packer which was installed at different borehole depths during the measurements. The pressure for the full length test was approximately 3 bars (see Figure 3-5). Figure 3-6 presents flow, *Q*, (blue lines and upper x-axis in figure) and specific capacity, *Q/dh* (red line and lower x-axis, approximately 5×10^{-10} m^2/s) for KO0014G01. For the full length test (solid line), the packer was installed at a depth of 0.5 m (thus measuring a section between 0.5 m and 3.0 m). For the dashed lines, the packer was installed at 1.0 m, 1.5 m and 2.0 m, thus measuring the section below these depths. If comparing the flow for the full length test, 0.001 l/m, to the other tests, lower than 0.0003 l/min, the largest flow seemed to be located in the upper part of the borehole (0.5–1.0 m).

Figure 3-7 presents flow, *Q*, (blue lines and upper x-axis in figure), specific capacity, *Q/dh* (red line and lower x-axis) and borehole depth intervals for borehole KO0017G01 in a similar way as for KO0014G01 above. Pressure for the full length borehole was approximately 6 bars (see Figure 3-5).

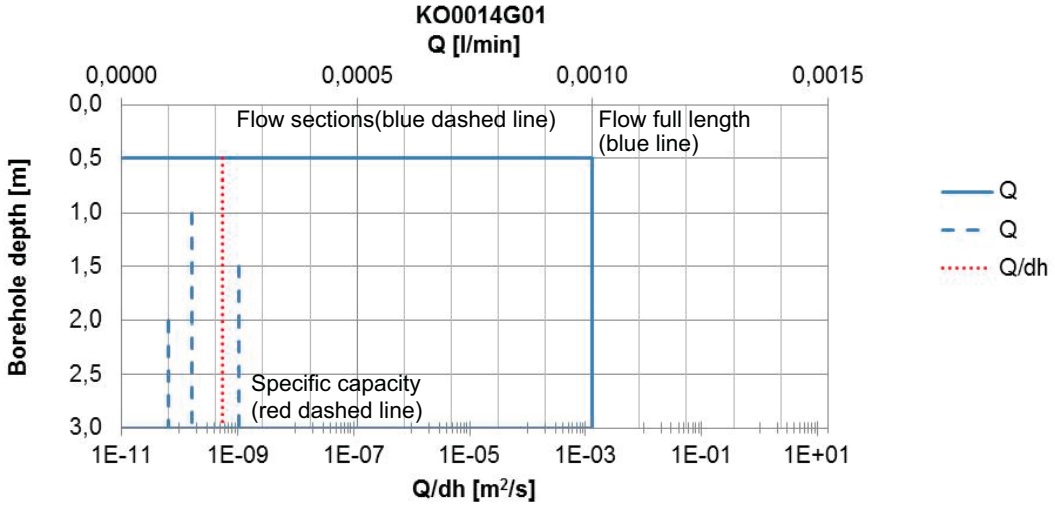

Figure 3-6. *Flow, Q, (blue lines and upper x-axis), specific capacity, Q/dh, (red line and lower x-axis) and borehole depth intervals where flow was measured for KO0014G01. Flow presented for full length (section 0.5 m to 3 m borehole depth) and shorter sections (dashed lines). Pressure for the full length borehole was approximately 3 bars (see Figure 3-5). Largest flow found in upper part of the borehole (0.5–1.0 m).*

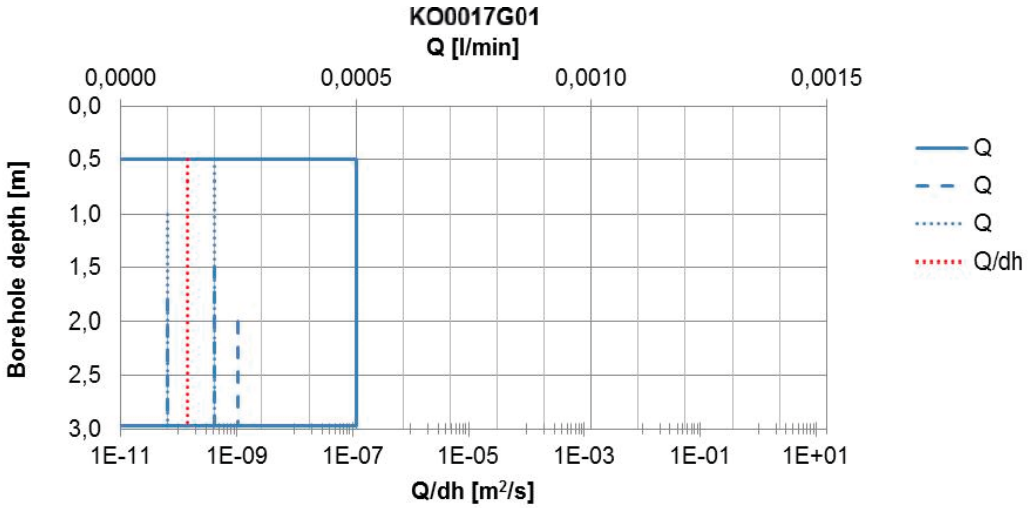

Figure 3-7. *Flow, Q, (blue lines and upper x-axis), specific capacity, Q/dh, (red line and lower x-axis) and borehole depth intervals where flow was measured for KO0017G01. Flow presented for full length (section 0.5 m to 3 m borehole depth) and shorter sections (dashed lines). Pressure for the full length borehole was approximately 6 bars (see Figure 3-5). Flow for a second full length test was lower than the first flow measurement. Largest flow thus identified in the lowest part of the borehole (2.0–3.0 m).*

The largest flow identified for the full length test was later found to be lower (long duration hydraulic test). The largest flow was identified in the lowest part of the borehole (2.0–3.0 m). Since flow often decrease as a function of time, this might be a reason for the difference.

Specific capacities based on natural flow of about 10^{-10} m^2/s were estimated for KO0014G01 and KO0017G01. Initial flow tests following drilling indicate that a major part of the flow for KO0014G01 is found at a shallow borehole depth. For KO0017G01 the difference between two full length measurements might be due to the smaller one being performed when the borehole had flown for a longer duration.

Even though no natural flow was measured in a borehole there may still be fractures connected to e.g. the tunnel floor. Consequently injection tests are also of interest and included in later sections.

3.1.2 BIPS and Core mapping

Information concerning rock type, fracture orientation, fracture filling etc was obtained by BIPS measurement (Borehole Image Processing System, see e.g. Gustafsson 2013) followed by core mapping. Initially an overview core mapping was performed. This was followed by BIPS measurements and finally a detailed core mapping using BOREMAP (see e.g. Sigurdsson 2013). Reference (level) was given both to the surface of the concrete slab (Phase 1, see Figure 3-3) and the rock surface.

Figure 3-8 presents a compilation of BIPS-images for the five primary boreholes (the depth is correct but the orientation has not been adjusted in this picture).

Main rock types are diorite, fine-grained granite and pegmatite. Further, based on core mapping, Figure 3-9 shows fracture frequencies (open and partly open). The higher number of fractures in the uppermost meter is probably due to an excavation damaged zone (EDZ), since a significant number of the fractures (21 out of the 28 open or partly open fractures) that were mapped as “no detectable fracture mineral” are situated in the first 0.5 meters. The higher fracture frequency and the absent fracture minerals was assumed to reflect new fractures being part of an EDZ.

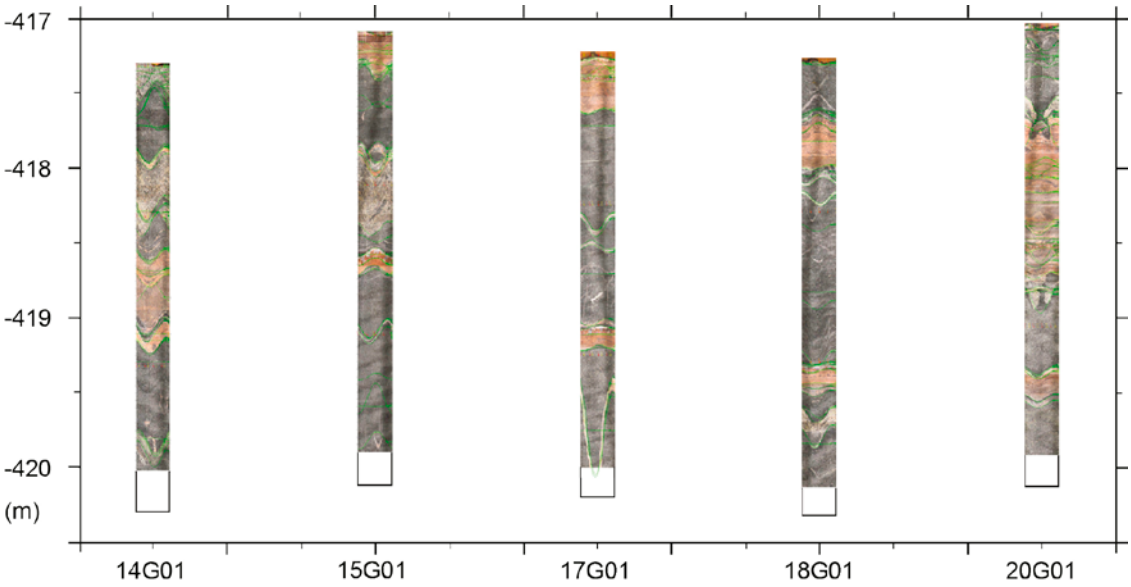

Figure 3-8. *Compilation of BIPS-images (orientation is not adjusted in this picture). Main rock types are diorite, fine-grained granite and pegmatite. Detailed images of KO0017G01 and KO0018G01 are presented in Appendix A.*

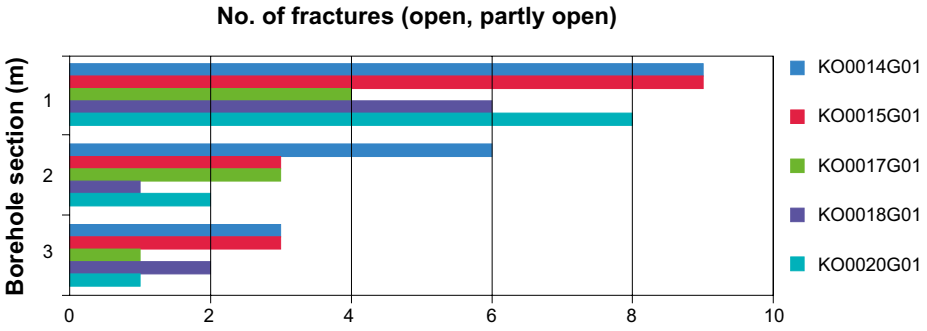

Figure 3-9. *Fracture frequencies of open and partly open fractures for the five primary boreholes. The higher number of fractures in the uppermost meter was assumed to reflect an excavation damaged zone, since 21 out of the 28 open or partly open fractures mapped as "no detectable fracture mineral" are situated in the first 0.5 meters.*

3.1.3 Hydraulic tests

The purpose of this activity was to obtain pressure and flow that served as a basis for evaluation of hydraulic properties of the boreholes/fractures. Further the activity aimed at giving a picture of the interference and connectivity between boreholes/fractures.

Equipment, execution and analyses

Flow was measured in two different ways. In measurements of the entire borehole that was sealed off at the upper part of a borehole, a measurement glass and a watch were usually used. Most of the other tests were performed with an equipment presented below and referred to as a "flow organ". Using this equipment, water level drawdown in tubes were read manually and based on this flow was calculated, see photo in Figure 3-10 and a principal sketch in Figure 3-11. The flow organ was combined with a mass flow meter and the water flow into the boreholes were measured with the automatic registration flow meter (Micro Motion) in series with the flow organ consisting of seven vertical polyamide tubes (Tecalan 8/6), see Figure 3-10 and Figure 3-11.

Flow rates down to 1 mL/min were measured with high resolution and accuracy with the Micro Motion flowmeter. Lower flow rates were measured using the vertical 1 500 mm long tubes, see Figure 3-10. Before each test, the tubes were filled so that the water levels were high without being hidden. With constant pressure water was then forced out of the system and into the boreholes. Water level drawdown was read manually and based on this flow was calculated. The system can measure flow down to 20 ml/h with a time resolution of about 10 seconds. Lower flows give poorer resolution in time and higher flows give a better resolution. One consequence is that the injection pressure will vary up to 1.5 m water column during the flow phase when water is forced down in the hoses.

Figure 3-11 shows a principal sketch of the equipment and pressure was controlled by gas pressure from a gas cylinder (N_2) in which a gas regulator was mounted. Based on experience this provides a stable pressure. At flows greater than 1 ml/min water was forced from two parallel 12-liter pressure vessels through the flow meter into the boreholes, see left, lower part of Figure 3-11. At lower flows, water was injected from the vertical tubes, in the middle of the sketch, into the boreholes with the aid of nitrogen gas. With the help of valves and the tubes in sequence, the injection could last a longer time. Valves at the gas cylinder and pressure vessels made it easy to switch between the two options for flow measurement. The injection pressure (P_{in}) was measured by a pressure sensor (gauge) with display. The pressure in section (P_{sec}) was also measured with a pressure sensor (gauge). Water levels in the vertical tubes were recorded manually and then converted into flow. Flows from the flow meter and pressure from sensors (gauges) were recorded by a data logger/PC.

Pressure was measured either by the gauges on the wall or by the level in the tubes of the flow organ (varied with the level of water). Flow was measured at a level of approximately 0.2 m above the concrete slab.

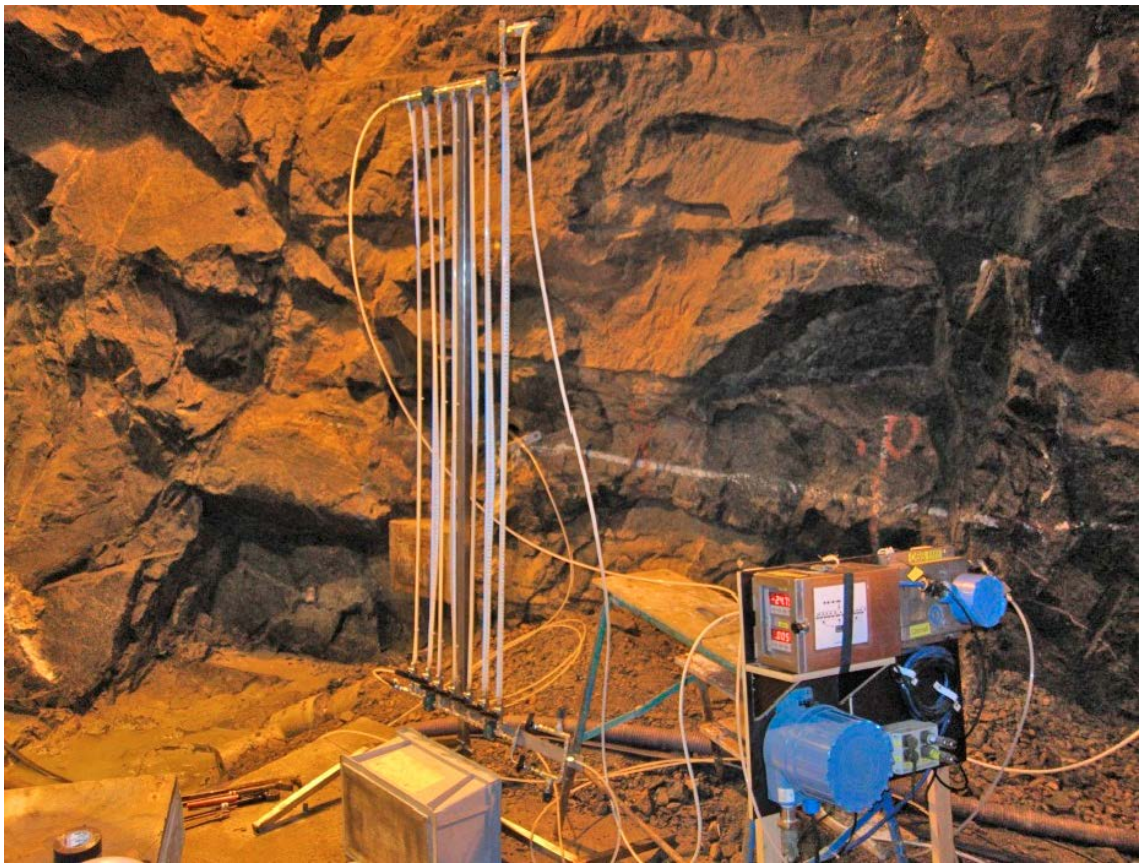

Figure 3-10. *Photo of equipment referred to as a "flow organ" used for transient hydraulic tests. See also principal sketch in Figure 3-11. Using this equipment, water level drawdown in tubes could be read manually and based on this flow was calculated.*

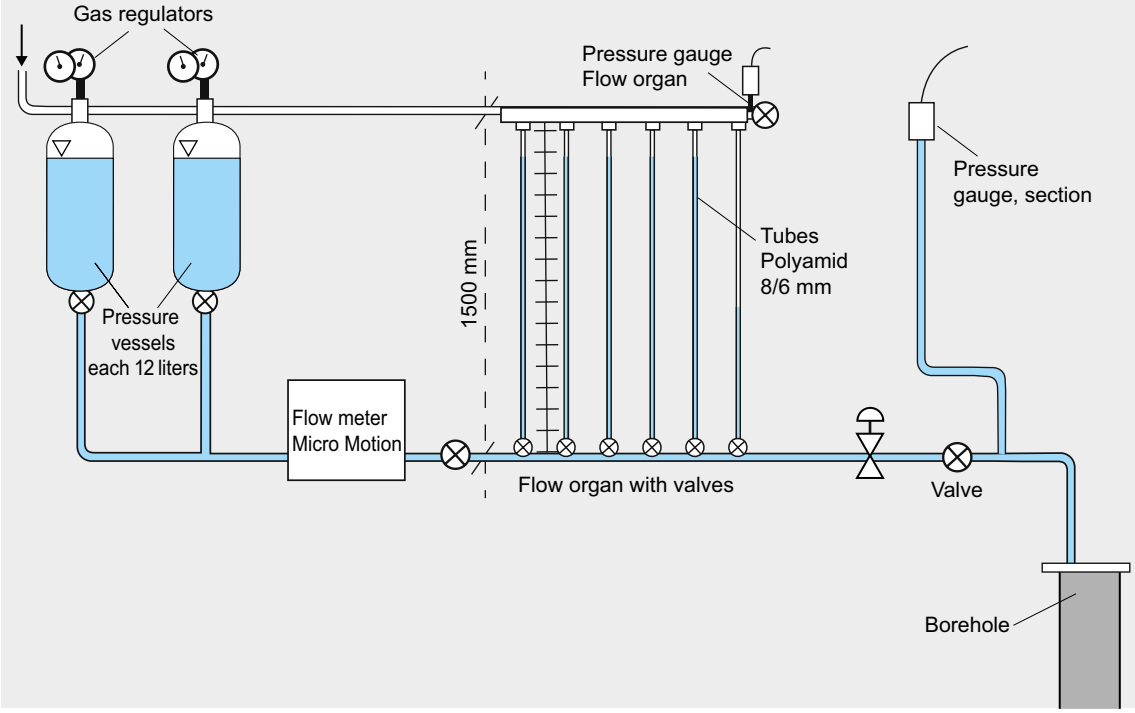

Figure 3-11. *Principal sketch of equipment, flow organ, for transient hydraulic tests.*

Hydraulic properties were presented either as a specific capacity, Q/dh or in terms of the transmissivity, T. An estimate of the hydraulic aperture, b, was obtained using the cubic law:

$$Q/dh \approx T = \frac{\rho g b^3}{12\mu} \quad (3\text{-}1)$$

To estimate transmissivity based on the injection or pumping (flow) phase, the increase in head, s and time, t, is often plotted in a lin-log plot. For the recovery phase, s_e and an equivalent time t_e was used.

$$t_e = t' \cdot t_p / (t' + t_p) \quad (3\text{-}2)$$

Pumping test were evaluated using the recovery data and a method referred to as Dougherty-Babu, see Dougherty and Babu (1984) and Appendix B.

Results Phase 1

The following hydraulic tests were performed during Phase 1:

- Full length (long duration) injection tests
- Injection tests
- Flow tests

Type of hydraulic test, date: start and stop, and sections tested are compiled in Appendix B. Pressure monitoring was performed in all boreholes.

The equipment presented in Figure 3-10 was used for these tests and pressure was as described earlier measured either by the gauges on the wall (Figure 3-4) or by the level in the tubes of the flow organ (varied with the level of water), Figure 3-10. Flow was measured at a level of approximately 0.2 m above the concrete slab.

Table 3-3. Pressure and flow, z-levels during hydraulic tests Phase 1.

Measurement	z-level
Pressure	Pressure gauges on wall (gauge) or by the level in the tubes of the “flow organ”
	z: approximately –418.3 m*
Flow	Flow using equipment or hose
	Concrete slab + 0.2 to 1.95 m

* Floor D-tunnel: −420 m; upper level area with gauges: −417.9; lower level: −418.7 m, see Figure 3-4.

Pressure logging

Figure 3-12 presents pressure monitored during the initial part of the hydraulic tests. Dashed grey lines indicate hydraulic testing the most water-bearing (flowing) boreholes (KO0014G01 and KO0017G01).

Noticeable is that the pressure in KO0017G01 has increased to approximately 12 bars (6 bars and increasing in Figure 3-5) and to 4 bars in KO0014G01 (previously 3 bars). Injection tests were performed at an excess pressure of about 2 bars and indications of interference is seen in borehole KO0014G01 when testing KO0015G01 (red) and in KO0017G01, KO0015G01 and KO0014G01 when testing KO0018G01 (green).

Injection tests

Long duration injection tests (full length)

Results from full length long duration injection tests performed during Phase 1 are presented in Table 3-4. Test duration was between 2.5 and 7 hours. Injection pressure, dh, was between 20–30 m (or 2–3 bars). Flow originates from the late part of the tests.

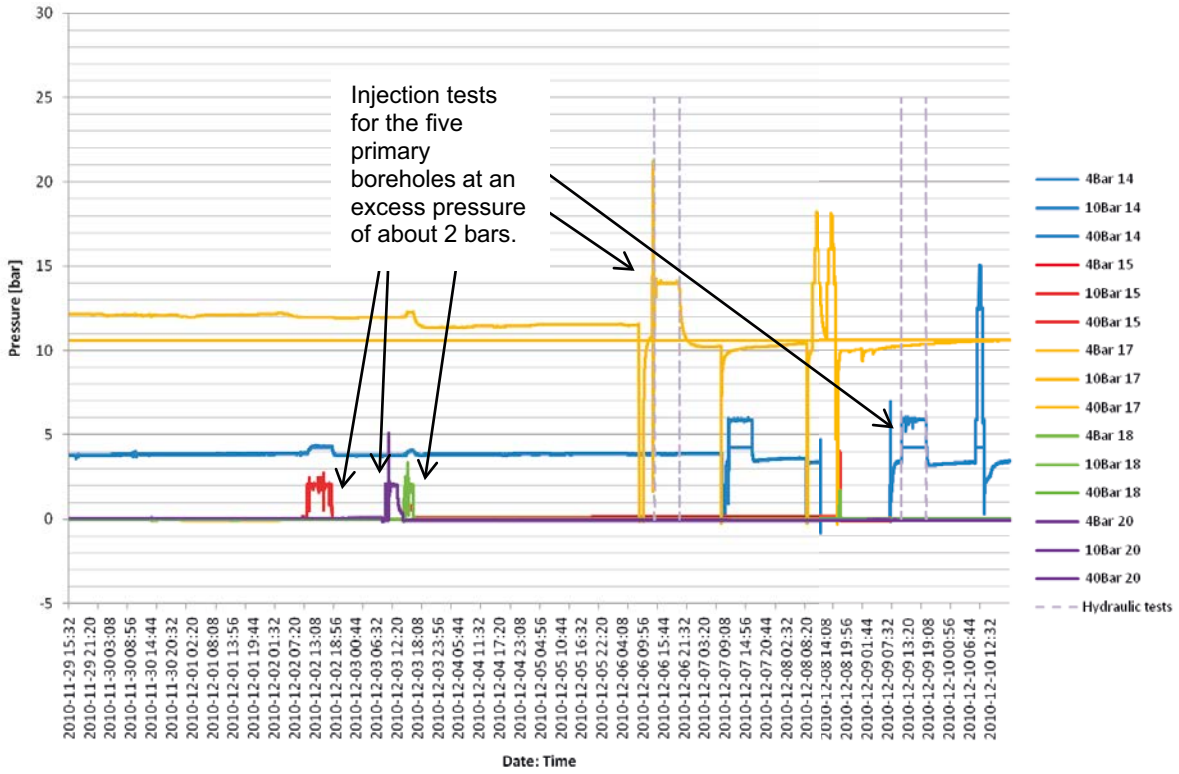

Figure 3-12. *Overview of pressure during the initial part of hydraulic tests Phase 1 (five primary boreholes: KO0014G01, KO0015G01, KO0017G01, KO0018G01 and KO0020G01, here identified by the numbers 14, 15, 17, 18 and 20). Injection tests were performed at an excess pressure of about 2 bars and indications of interference is seen in borehole KO0014G01 when testing KO0015G01 (red) and in KO0017G01, KO0015G01 and KO0014G01 when testing KO0018G01 (green). Grey dashed lines indicate tests in the most water-bearing (flowing) boreholes (KO0014G01 and KO0017G01).*

Table 3-4. Long duration full length injection tests performed during Phase 1.

	Section [m]	Start Stop	Q [ml/min]	dh [m]
14G01 ID9	0.5–3.0	2010-12-09 11:39-18:39	0.9	25
15G01 ID3	0.75–3.03	2010-12-02 11:01-18:01	200	20
17G01 ID5	0.5–2.97	2010-12-06 13:23-20:24	0.15	30
18G01 ID2	0.55–3.06	2010-12-01 15:56-18:57	540*	20
20G01 ID4	0.82–3.1	2010-12-03 10:05–12:36	0.5	20

*1 000 times higher than short duration 0.2–0.5 ml/min.

Short duration injection tests (sections) ID10x

To further identify location of fractures and estimate specific capacity, *Q/dh*, short duration section injection tests (10 minutes) were performed. Even though no natural flow was measured in a borehole there may still be fractures connected to e.g. the tunnel floor. Figure 3-13 to Figure 3-15 present flow during injection (10 min**,** blue lines and upper x-axis) and estimated specific capacity, *Q/dh*, (red line and lower x-axis) for KO0017G01, KO0018G01 and KO0020G01. For KO0018G01 and KO0020G01 the smallest flow was identified in the lowest part of the boreholes (2.0–3.0 m) making them interesting as representatives for investigations of "dry" sections and behavior of rock matrix.

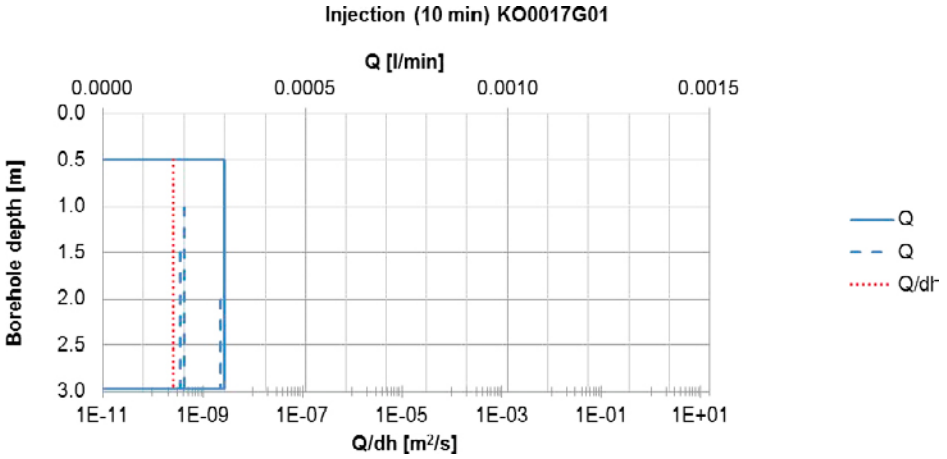

Figure 3-13. *Flow (injection), Q, (blue lines and upper x-axis), specific capacity, Q/dh, (red line and lower x-axis) and borehole depth intervals for KO0017G01. Flow presented for full length (0.5 to 3.0 m) and sections (dashed lines). Excess pressure during injection was approximately 2 bars. Largest flow identified in the lowest part of borehole (2.0–3.0 m).*

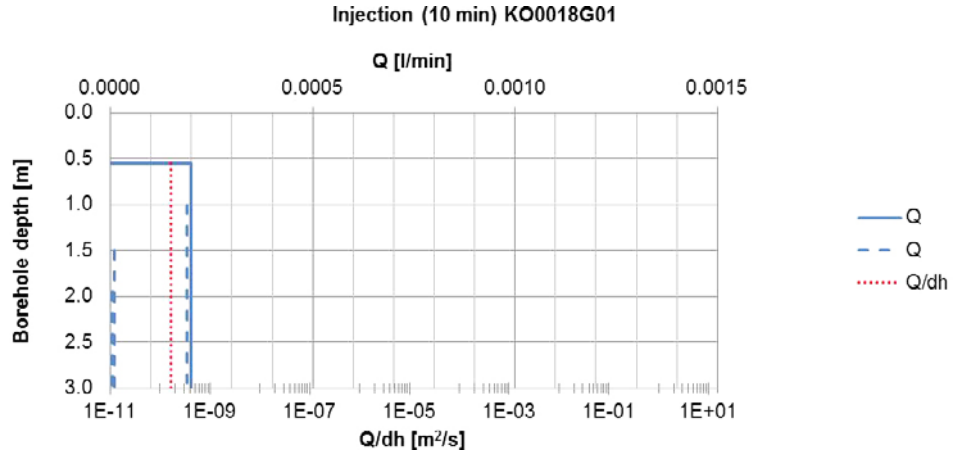

Figure 3-14. *Flow (injection), Q, (blue lines and upper x-axis), specific capacity, Q/dh, (red line and lower x-axis) and borehole depth intervals for KO0018G01. Flow presented for full length (0.5 to 3.0 m, solid line) and sections (dashed line). Excess pressure during injection was approximately 2 bars. Smallest flow identified in the lowest part of borehole (2.0–3.0 m). The section was interesting for investigation of rock matrix behavior.*

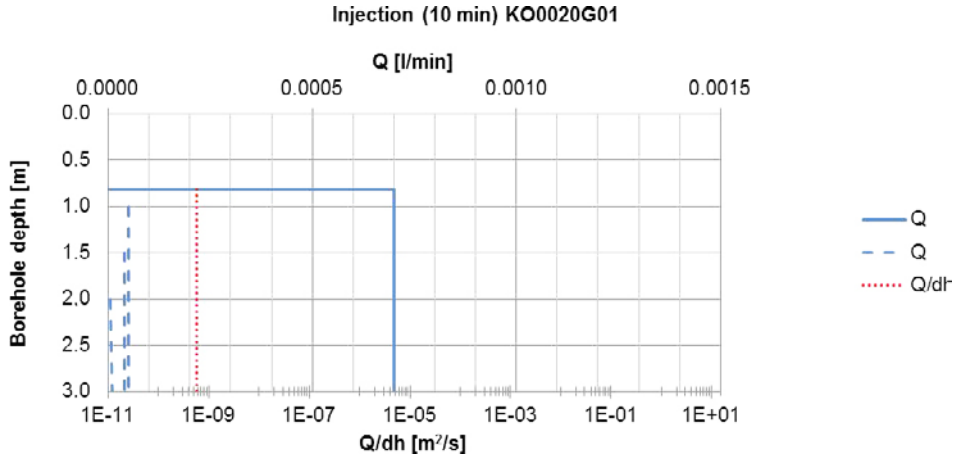

Figure 3-15. *Flow (injection), Q, (blue lines and upper x-axis), specific capacity, Q/dh, (red line and lower x-axis) and borehole depth intervals for KO0020G01. Flow presented for full length (0.5 to 3.0 m) and sections (dashed lines). Excess pressure during injection was approximately 2 bars. Smallest flow identified in the lowest part of borehole (2.0–3.0 m). The section was interesting for investigation of rock matrix behavior.*

Injection tests (constant pressure step tests)

Injection tests with different pressure steps allowed for a presentation of flow as a function of hydraulic head, *Q(h)* which may indicate e.g. deformation or movement of fracture filling. Further, hydraulic tests and deformation measurements was carried out by Johan Thörn, Chalmers. Deformation was not the main focus of BRIE and these tests were not further evaluated as a part of this report. Results from these tests are presented in e.g. Fransson et al. (2012) and Thörn and Fransson (2014).

Flow tests

Long duration flow tests

Long duration hydraulic tests (here 400 min and 60 min) allowed for evaluation of specific capacity and transmissivity. Flow data and specific capacity were evaluated for KO0014G01 and KO0017G01, see Table 3-5, Figure 3-16 and Figure 3-17. The two figures presents flow, *Q*, (blue lines and upper x-axis), specific capacity, *Q/dh*, (red line and lower x-axis) and borehole depth intervals. Flow presented in the table originate from the late part of the tests. Observe the higher pressure identified in KO0017G01 compared to Figure 3-5 and Figure 3-12 (approximately 17 bars or 170 m head likely to be due to the deeper and more isolated section tested).

Transmissivity was evaluated for KO0017G01 (section 0.5 to 2.97 m, presented in Appendix B) and was estimated to 4.5×10^{-11} m^2/s (close to the specific capacity of 4.6×10^{-11} m^2/s in the same section). Measured pressure for the full length borehole was 9 bars and for the lower section 17 bars. Flow decreased as a function of time which is one reason why the 60 min tests had a larger flow.

Table 3-5. Long duration flow tests performed during Phase 1.

	Section [m]	Start Stop	Q [ml/min]	dh [m]
14G01	0.5–3.0	2010-12-16	0.2	37
ID14		07:53-14:53		
17G01	0.5–2.97	2010-12-13	0.25	90
ID11		13:46-20:46		
17G01	2–2.97	2010-12-15	0.4	170
ID12		15:54–16:54		

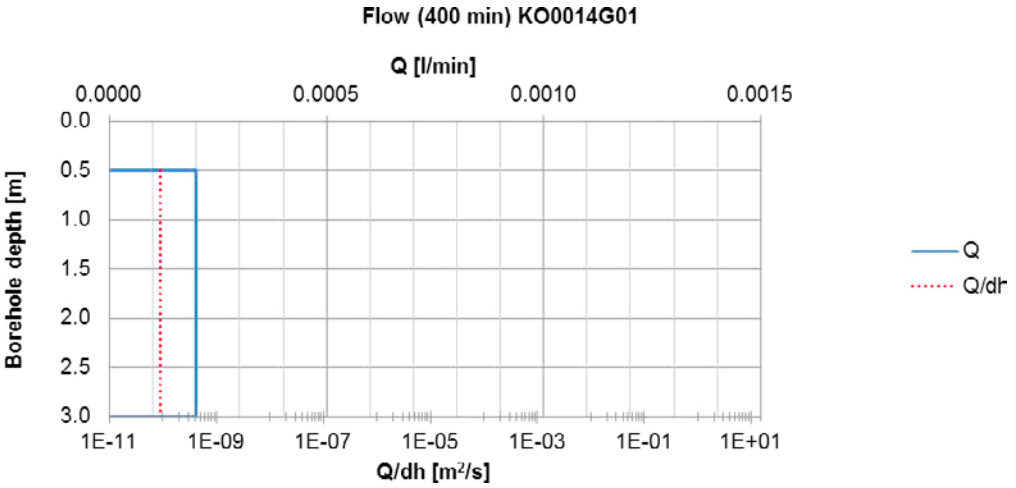

Figure 3-16. *Flow, Q, (blue lines and upper x-axis), specific capacity, Q/dh, (red line and lower x-axis) and borehole depth intervals for KO0014G01. Pressure for full length borehole (0.5 to 3.0 m) is approximately 3.7 bars. Specific capacity, Q/dh, estimated to 9.0×10^{-11} m^2/s.*

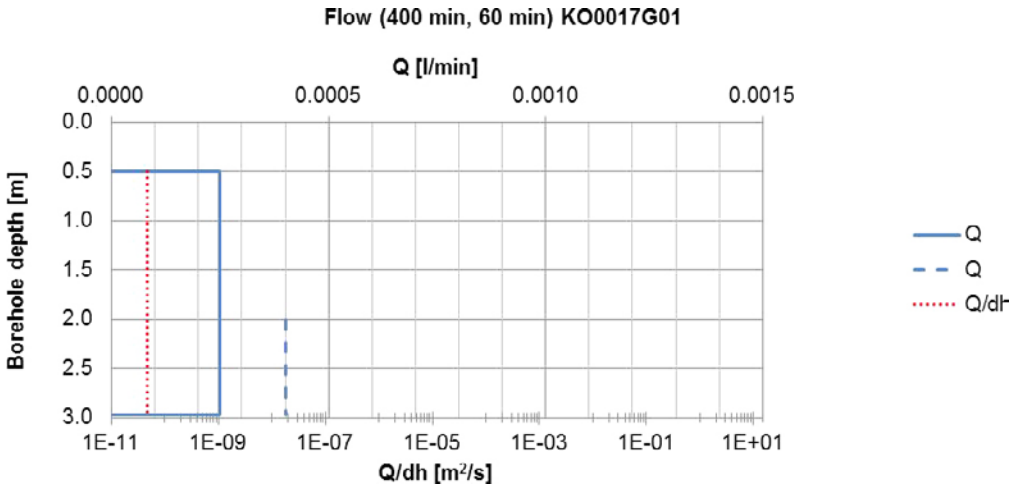

Figure 3-17. *Flow, Q, (blue lines and upper x-axis), specific capacity, Q/dh, (red line and lower x-axis) and borehole depth intervals for KO0017G01. Flow presented for full length (solid line, 0.5 to 3.0 m, 400 min) and section (dashed line, 2.0–3.0 m, 60 min). Measured pressure for the full length borehole was 9 bars and for the lower section 17 bars. Specific capacity, Q/dh, estimated to 4.6×10^{-11} and 3.9×10^{-11} m^2/s. Flow decreased as a function of time which is one reason why the 60 min tests had a larger flow.*

Flow tests (constant pressure step tests)

Examples of data from constant pressure step tests are presented in Figure 3-18 and Figure 3-19. The pressure measured is the natural pressure that was lowered according to the steps presented in the figures. In addition to pressure, flow for the different steps is also presented (blue and grey dots). Flow tests with different pressure steps allows for a presentation of flow as a function of hydraulic head, *Q(h)* which may indicate e.g. deformation or movement of fracture filling. This can also be a way to indicate possible de-gassing. As expected, flow increases when the natural pressure is lowered (increasing *dh*) and decreases when pressure is increased (decreasing *dh*). Tests are presented to illustrate this type of data but were not further evaluated as a part of this report.

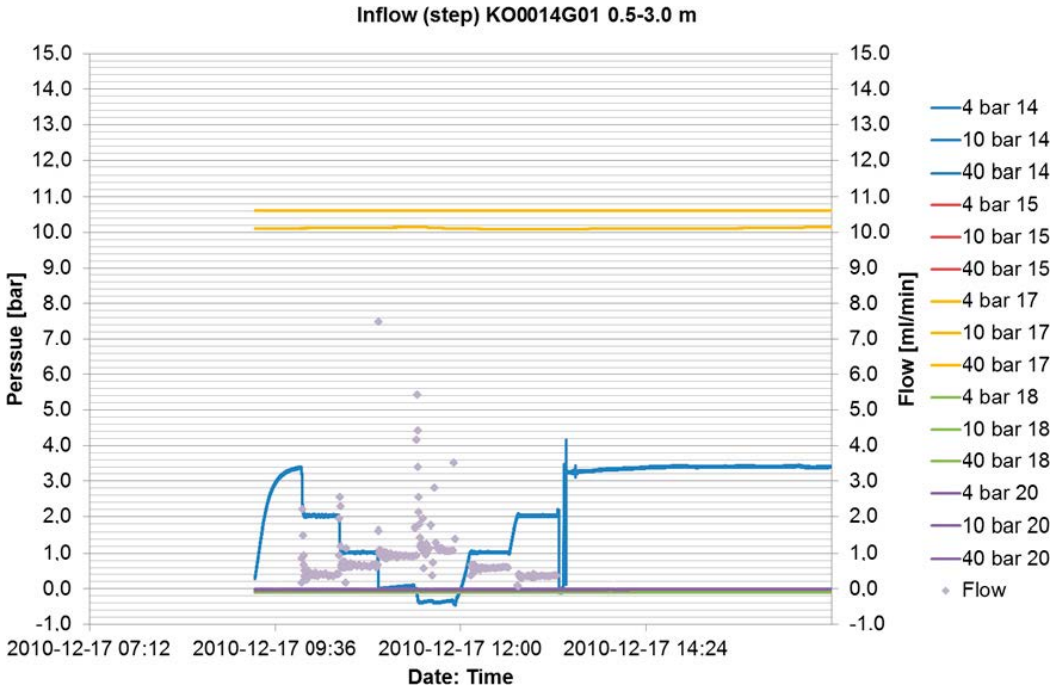

Figure 3-18. *Flow test (constant pressure step tests) for KO0014G01 (pressure shown with blue line), section 0.5–3.0 m (as previously, five primary boreholes: KO0014G01, KO0015G01, KO0017G01, KO0018G01 and KO0020G01, identified by the numbers 14, 15, 17, 18 and 20). In addition to pressure, flow for the different pressure steps is also presented (grey dots).*

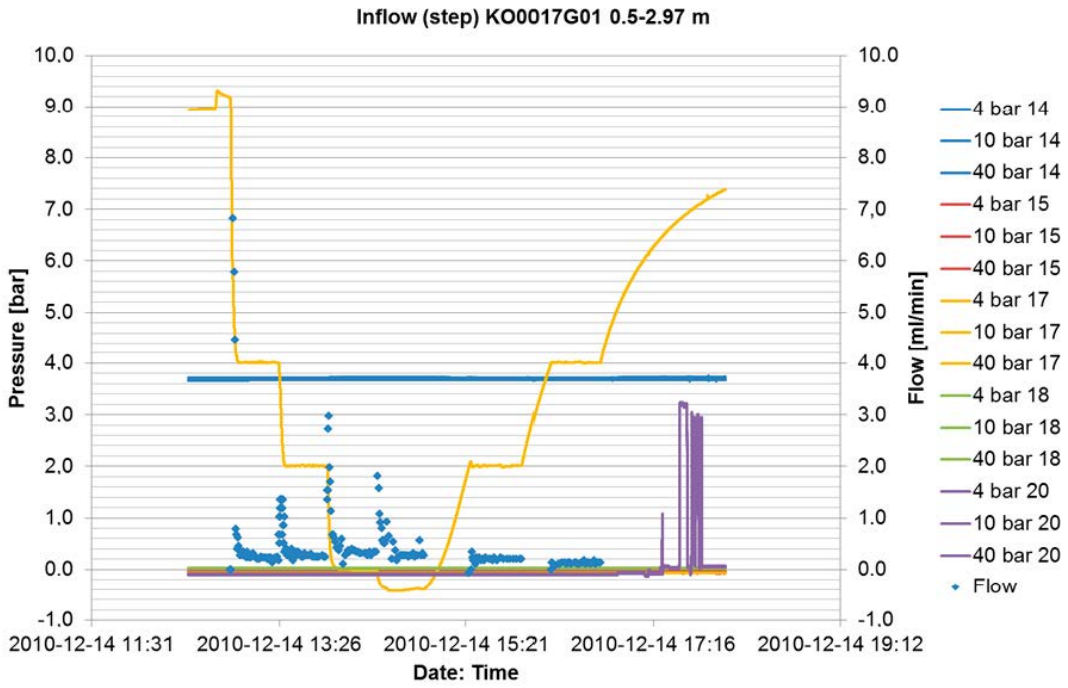

Figure 3-19. *Flow test (constant pressure step tests) for KO0017G01 (pressure shown with yellow line), section 0.5–2.97 m (as previously, five primary boreholes: KO0014G01, KO0015G01, KO0017G01, KO0018G01 and KO0020G01, identified by the numbers 14, 15, 17, 18 and 20). In addition to pressure, flow for the different pressure steps is also presented (blue dots).*

3.1.4 Concluding remarks Phase 1

Based on the five primary investigation boreholes, the main rock type was diorite. In addition, two types of granite were found (Ävrö granite and fine-grained granite). The frequency of open and partly open fractures was highest between the rock surface and a depth of one meter (4–9 fractures/m) and lowest at a depth of 2–3 meters. The higher number of fractures in the uppermost meter was probably due to an excavation damaged zone, since 21 out of the 28 open or partly open fractures mapped as "no detectable fracture mineral" were situated in the first 0.5 meters. The highest fracture frequencies among the boreholes were found in boreholes KO0014G01 and KO0015G01. This was also the location of a conductive deformation zone intersecting the tunnel. Based on tunnel mapping and the fractures mentioned above, three major units could be identified: An almost vertical deformation zone, individual water-bearing fractures, and an excavation damaged zone (EDZ).

Based on injection and flow (constant pressure) tests, boreholes KO0017G01 and KO0014G01 were suggested candidates for investigations of interaction between bentonite and individual water-bearing fractures. These boreholes had measurable natural flow of about 0.5 to 1 ml/min, see compilation in Table 3-6.

Table 3-6. Compilation of test results, Phase 1. The symbol √ indicates where flow was identified.

	KO0020G01	KO0018G01	KO0017G01	KO0015G01	KO0014G01
Flow	(√)	"no"	√ Q ≈ 0.5 ml/min p ≈ 6 bar ≈ 2–3 m	"no"	√ Q ≈ 1 ml/min p ≈ 3 bar ≈ 0.5–1 m
Injection	√	√ above 1 m "no" below 1 m (then revised to 1–1.5 m)	√	√	√

Estimated fracture hydraulic aperture based on the cubic law and results from the full length test in KO0017G01 was 4-5 µm, see, Table 3-7. Fracture hydraulic aperture is used here as a mean to illustrate a physical representation of the fracture. The fracture of most interest was located below 2 m depth. Estimated fracture aperture based on the full length test in KO0014G01 was 5-10 µm. The precise location of the most interesting fracture was more uncertain, possibly in the upper part of the borehole but there could be several features. Due to the uncertainty in location of fractures in KO0014G01, KO0017G01 might be the best candidate indicating an interesting water-bearing fracture below 2 m depth. Transient test evaluation for KO0017G01 is presented in Appendix B. The transmissivity was estimated to 4.5×10^{-11} m^2/s (close to the specific capacity of 4.6×10^{-11} m^2/s in the same section, 0.5–2.97 m).

Table 3-7. Estimates of specific capacity, Q/dh, and hydraulic aperture, b (Q/dh).

	Injection test				Flow test			
	Q [ml/min]	dh [m]	Q/dh [m^2/s]	b(Q/dh) [µm]	Q [ml/min]	dh [m]	Q/dh [m^2/s]	b(Q/dh) [µm]
KO0014G01	0.9 ID9 0.5–3 m	25	6.0E–10	10	0.2 ID14 0.5–3 m	37	9.0E–11	5
KO0015G01	200 ID3 0.75–3.03	20	1.7E–07	64				
KO0017G01	0.15 ID5 0.5–2.97	30	8.3E–11	5	0.25 ID11 0.5–2.97	90	4.6E–11	4
KO0018G01	540 ID2 0.55–3.06	20	4.5E–07	89				
KO0020G01	0.5 ID4 0.82–3.1	20	4.2E–10	9				

Borehole KO0018G01 was suggested the main candidate for investigation of interaction between bentonite and rock matrix. Low ("no") flow during injection tests was found below the depth of 1 to 1.5 m. A low ("no") flow during injection was also found in KO0020G01 below 2 m of depth. Full length borehole specific capacities of boreholes KO0015G01 and KO0018G01 were high. In KO0018G01 shallow fractures were expected to be the important conductors. The shallow part of KO0018G01 is suggested an example of the transmissivity of EDZ. The specific capacity, *Q/dh,* was estimated to approximately 10^{-7} m^2/s.

The text above mainly presents a compilation of results from hydraulic tests, concluding remarks for Phase 1 can be formulated as follows:

- Based on investigations performed boreholes KO0017G01 and KO0014G01 were suggested candidates for investigations of interaction between bentonite and individual fractures. These boreholes had natural flows.
- Estimated fracture aperture based on the full length test in KO0017G01 was 4-5 µm. The fracture of most interest was located below 2 m depth.
- Estimated fracture aperture based on the full length test in KO0014G01 was 5-10 µm. The location of the most interesting fracture was more uncertain, possibly in the upper part of the borehole but there might have been several features.
- Due to the uncertainty in location of fractures in KO0014G01, KO0017G01 was chosen the best candidate with an interesting fracture below 2 m depth.
- Borehole KO0018G01 was suggested the main candidate for investigation of interaction between bentonite and rock matrix. Low ("no") flow during injection tests was found below the depth of 1 to 1.5 m.

The objective of *Phase 1 Selection of site* was to perform investigations and compile data as a basis to decide whether the TASO-tunnel is a suitable location for BRIE. The conclusion was that TASO was a suitable location for the field experiment.

3.2 Characterisation of site

The objective of Phase 2 was to characterise the site, to further investigate and confirm that the site was a suitable location for the experiment and if so to suggest in what boreholes bentonite parcels could be installed.

3.2.1 Drilling and pressure logging

14 vertical boreholes were added in Phase 2 Site Characterisation, see Figure 3-1 and Figure 3-20. The distance was selected to conform to the future stitch-drilling for the extraction of the bentonite-rock parcels. In Phase 2, lengths of boreholes differ, short boreholes were drilled surrounding borehole KO0014G01 and long boreholes (approximately 3 meters) drilled for the others.

In addition to boreholes in the tunnel floor, four boreholes were drilled into the tunnel wall, see Figure 3-2. These boreholes were approximately 10 meters long and drilled at an angle of 45 degrees from the tunnel center line. Two of the boreholes aimed at intersecting the deformation zone identified in the beginning of the tunnel for monitoring of hydraulic head. The other two aimed at investigating the hydraulic head around the deeper part of the tunnel.

In Phase 2, the time when reaching 0.5 m, 1.0 m, 1.5 m, 2.0 m, 2.5 m, 3.0 m and approximately 3.5 m were documented. Pressure response as a function of borehole depth (during drilling of an adjacent, new borehole) was of interest to indicate the depth of connected fractures. Figure 3-21 presents pressure response in KO0017G01 while drilling the adjacent borehole KO0017G03, see borehole locations in Figure 3-1. Grey lines represent the time when starting and when reaching the different 0.5 m sections. The main response was observed at 3–3.5 m depth. This is in line with a suggested flowing fracture in the deep part of borehole KO0017G01.

Figure 3-22 presents pressure response in KO0017G01 while drilling borehole KO0016G01. The main response was observed at 2–2.5 m depth.

Figure 3-20. *TASO-tunnel (Phase 2) and the ongoing drilling of the additional 14 boreholes (tunnel floor), see geometry in Figure 3-1. The photo shows that the concrete slab has been removed.*

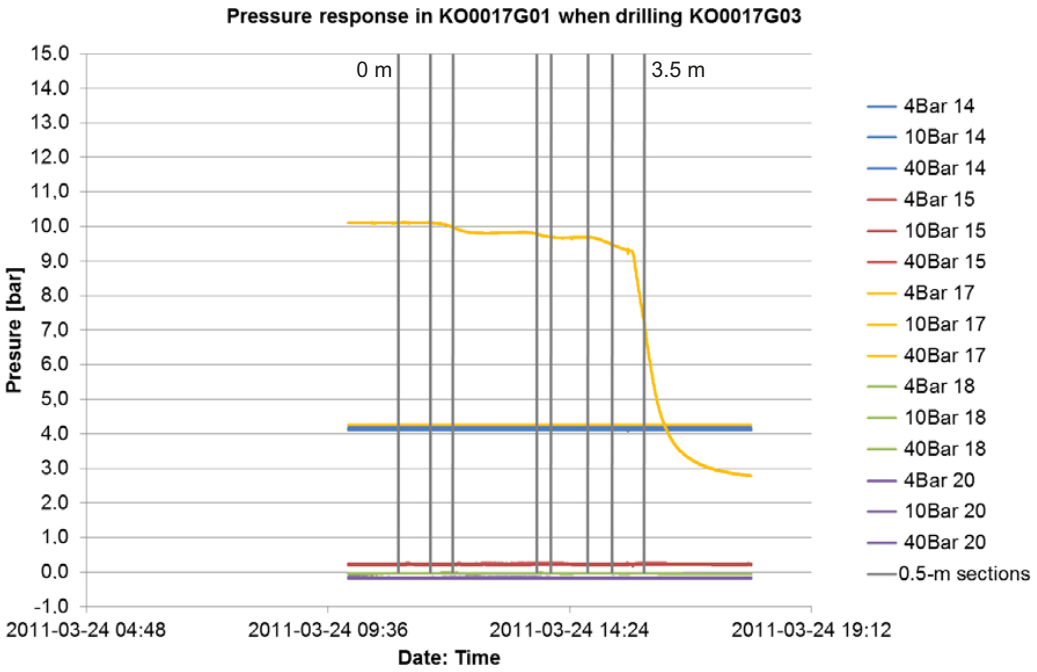

Figure 3-21. *Pressure response in KO0017G01 (one section special packer down to 2.1 m was installed in the borehole) when drilling KO0017G03: Grey lines represent time when starting (0 m) and when reaching the different 0.5 m sections. Main response identified at 3–3.5 m depth.*

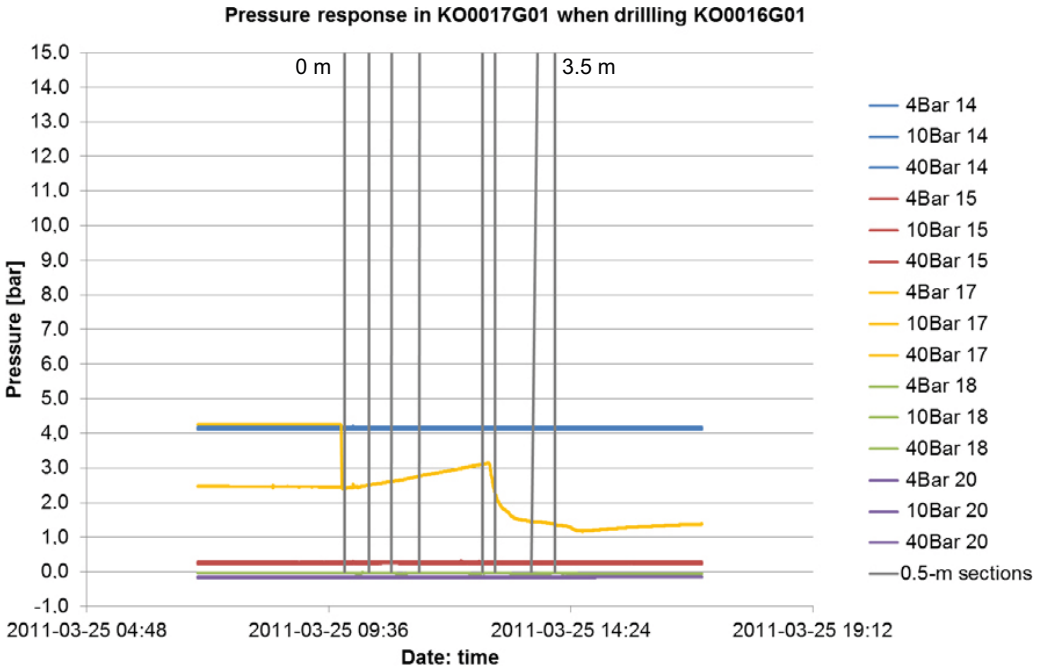

Figure 3-22. *Pressure response in KO0017G01 when drilling KO0016G01 (4 section special packer installed in KO0017G01). Grey lines represent time when starting (0 m) and reaching the different 0.5 m sections. Main response at 2–2.5 m. Section 1.71–2.215 m of packer deflated.*

3.2.2 BIPS, core and tunnel mapping

Fractures

The fracture of main interest in KO0017G01 was located at the bottom of the borehole (a pegmatite vein that has been subjected to shearing), see Figure 3-23. A fracture was also identified in e.g. KO0017G03, see Figure 3-24. For strike and dip of the fracture of main interest in borehole KO0017G01, see Table 5-5.

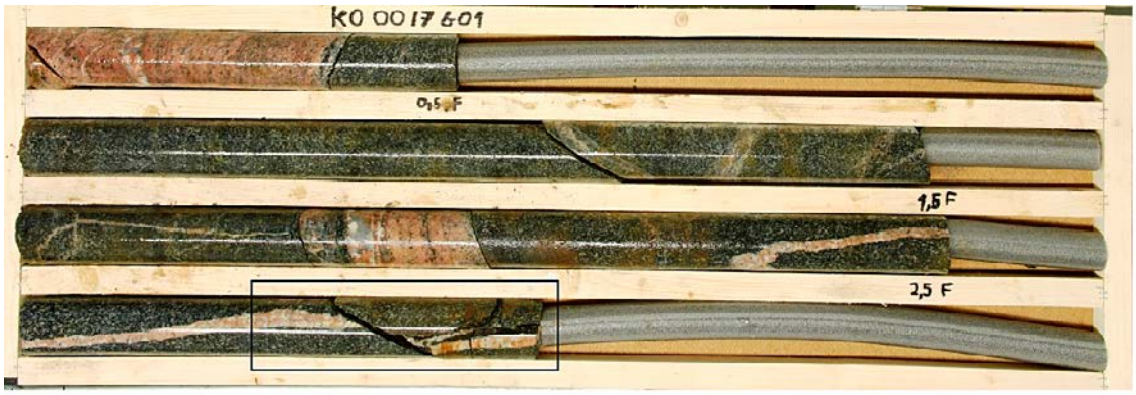

Figure 3-23. *Core from borehole KO0017G01. Fracture of main interest at the bottom of the borehole (black square, showing a pegmatite vein that has been subjected to shearing).*

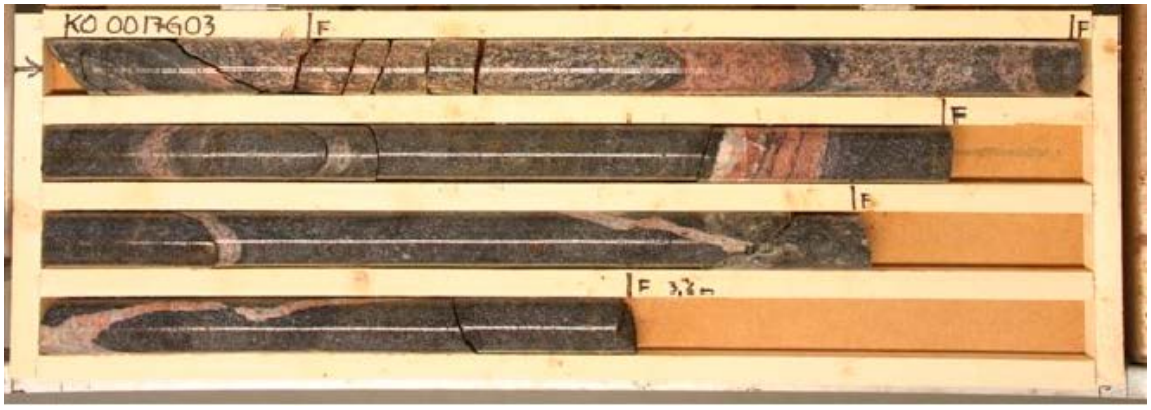

Figure 3-24. *Core from borehole KO0017G03. Fracture of main interest in the lower part of the borehole identified with the pegmatite vein (that has been subjected to shearing).*

Deformation zone

As mentioned in the beginning of the selection of site-section, the group with five initial boreholes were positioned between the tunnel front and a deformation zone. The location and orientation of the deformation zone identified in the tunnel was approximated by and based on the average orientation of two fractures, fractures 10 and 12 (from tunnel mapping, see Figure 3-25 and Figure 3-26). Similar fracture orientations were identified in the cored borehole KO0011AO1 drilled in the left hand wall of the tunnel with the expectation to intersect the deformation zone, see Figure 3-26. To geometrically represent the deformation zone by some of the fractures was of interest as a basis for a mechanical description where information about both orientation and stress-field is important, see Section 5.1.8 for some comments on mechanics and hydromechanics of the main water-bearing features.

Table 3-8. Strike and dip of deformation zone (here represented by fractures 10 and 12).

Fracture no.	Strike (deg) Äspö96	Dip (deg) Äspö96	Average orientation Strike (deg)	Average orientation Dip (deg)
12	310	80	315 (318 RT90)	75
10	320	70		

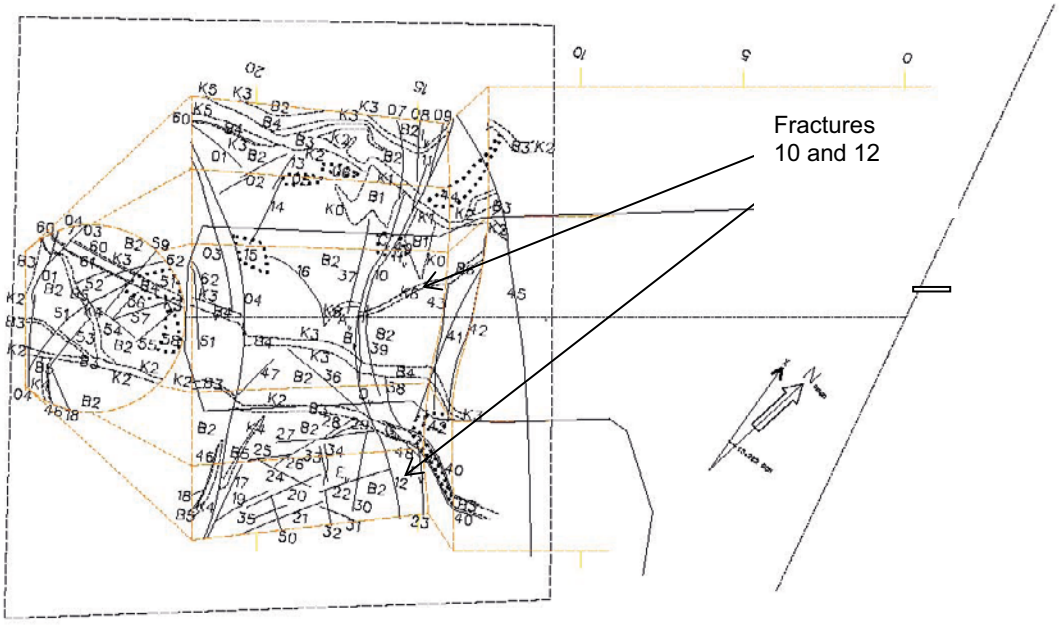

Figure 3-25. *Tunnel mapping (wall and roof) of TASO. Deformation zone in tunnel was based on (represented by) the average orientation of fractures 10 and 12.*

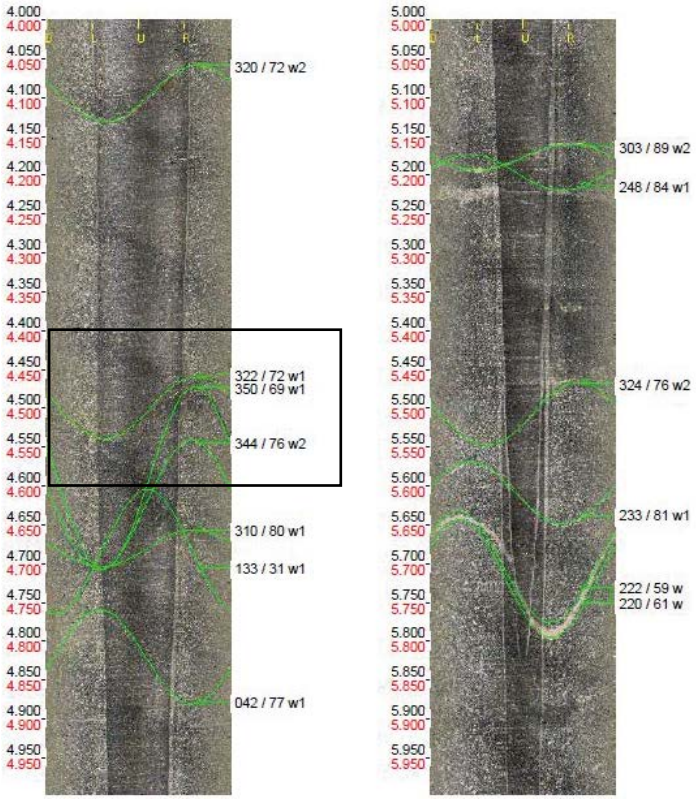

Figure 3-26. *BIPS-image of borehole KO0011A01, left tunnel wall. Orientation of fractures at approximately 4.4 m was similar to orientation of fractures 10 and 12 in the tunnel. This was also the location of major flow identified by Posiva Flow Log, see Table 3-9.*

3.2.3 Posiva Flow Log

Equipment and execution

The Posiva Flow Log, Difference Flow Method (PFL DIFF), see Figure 3-27, uses a flowmeter that can be used for relatively quick determination of flow and hydraulic head in cored boreholes. Measurements were carried out in boreholes KO0011A01, KO0014G01, KO0015G01, KO0016G01, KO0017G01, KO0017G02, KO0017G03 and KO0017G04, see Figure 3-1 and Figure 3-2. Measurements were not performed in all boreholes due to the detection limit (30 ml/h).

Measurements were made by moving the measurement tool in 0.1 m steps. Since a short interval at the bottom remains unmeasured with the DIFF flow guide and that it was important to capture also this section, flow along the borehole was measured for all boreholes. This means that an accumulated flow was actually measured.

Evaluation

The processing of measured data was made according to Hurmerinta (2015). Length corrected data files and plots were produced and hydraulic parameters calculated from steady state analysis. Table 3-9 presents length to flow anomaly, L, hydraulic head, h, and evaluated transmissivity, T.

Table 3-9. Inferred flow anomalies from flow logging (Hurmerinta 2015).

Borehole ID	Length to flow anom. L (m)	Q_0 (m^3/s)	h_{0FW} (m.a.s.l.)	Q_1 (m^3/s)	h_{1FW} (m.a.s.l.)	T_D (m^2/s)	h_i (m.a.s.l.)	Q_{min} (m^3/s)	Comments
KO0011A01	4.4	–	0.00	2.00E–06	415.90	4.8E–09	–	8.33E–09	
KO0011A01	5.4	–	0.00	2.14E–08	415.90	5.1E–11	–	8.33E–09	
KO0014G01	1.1	–	0.00	1.11E–08	417.31	2.6E–11	–	8.33E–09	*

* Uncertain = The flow rate is less than 30 mL/h or the flow anomalies are overlapping or they are unclear because of noise.

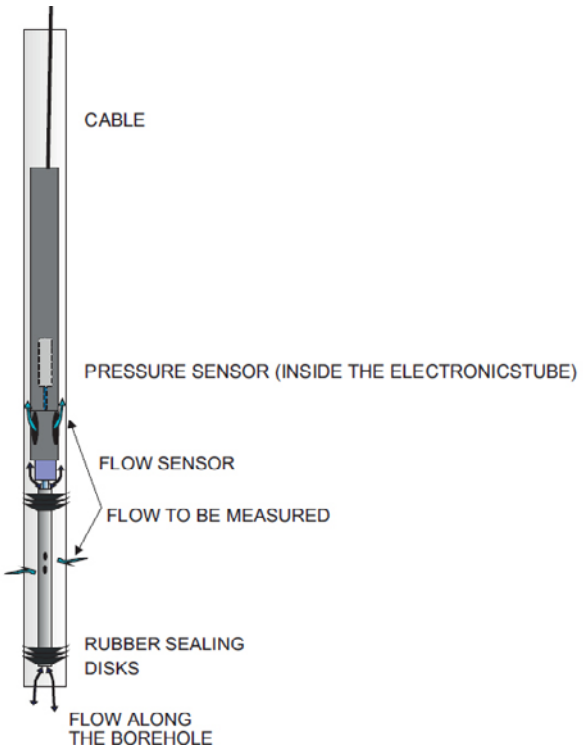

Figure 3-27. *Posiva Flow Log measurement tool measuring flow along the borehole (figure taken from Hurmerinta 2015).*

Borehole KO0011A01 (left wall) had a flow of 2.0×10^{-6} m^3/s (about 0.1 l/min) at about 4.4 meters depth and a smaller flow at 5.4 meters. Borehole KO0014G01 had a flow of 1.0×10^{-8} m^3/s at 1.1 m. Further, KO0017G01 had a flow below (but close to) the detection limit (30 ml/h). Two different packer set ups were used for the adjacent boreholes during logging of KO0017G01, first with several packed off sections using special packers and secondly with only the uppermost sections inflated. The one with packed-off sections indicated an outflow from the borehole between 1.8 and 2.0 m. Possibly, this is due to a lower pressure in the packed-off sections and the intersecting fracture influencing the flow in KO0017G01.

Orientation of fractures at the flowing section at approximately 4.4 m is similar to the orientation of fractures 10 and 12 in tunnel, see Figure 3-25 and Figure 3-26.

3.2.4 Hydraulic tests

The purpose of this activity, as for the hydraulic tests during the site selection, was to obtain pressure and flow that served as a basis for evaluation of hydraulic properties of the boreholes/fractures. Further the activity aimed at giving a picture of the interference and connectivity between boreholes/fractures.

The following hydraulic tests were performed during Phase 2:

- Short duration injection tests.
- Short duration flow tests (constant pressure tests).
- Injection tests and flow tests (constant pressure) in 14G01, 17G01 and boreholes at the wall.

Type of hydraulic test, date: start and stop, and sections tested are compiled in Appendix B. Pressure monitoring was performed in all boreholes. Equipment, execution and analyses are presented in Section 3.1.3.

Short duration flow tests: Flow distribution

Table 3-10 presents the results from short duration flow tests. Table 3-10 compiles section length and flow (at approximately 15 minutes) for boreholes KO0013G01 to KO0020G04. Noticeable is the differences in pressure, see e.g. KO0017G01 with a pressure of 5 bars in Table 3-10 compared to the highest pressure measured, 17 bars presented in Table 3-5. Location of packers as well as new boreholes interconnecting the fractures influence the pressure, this is a reason why pressure is not compiled for all boreholes in the table.

Table 3-10. Borehole, section length and flow (at approximately 15 minutes) for boreholes KO0013G01 to KO0020G04. Pressure based on Figure 3-28.

Borehole	Section	Q [ml/min]	Pressure [bar]
KO0013G01	0.53–1.5	0.4	
KO0014G01	1.33–3	0.1	1
KO0014G02	0.57–1.5	0.2	
KO0014G03	0.57–1.5	0.55	
KO0014G04	0.52–1.5	4	
KO0015G01	2.1–3.03	0.6	5
KO0016G01	2.21–3.5	1	
KO0017G01	2.11–2.97	1	5
KO0017G02	1.42–3.5	0.0001 (0)	
KO0017G03	2.1–3.5	1.5 (1–1.5)	
KO0017G04	2.21–3.5	0.0001 (0)	
KO0018G01	1.42–3.06	0.0001 (0)	”0”
KO0018G02	1.42–3.5	0.02	
KO0018G03	1.42–3.5	0.01 (0–0.01)	
KO0019G01	1.42–3.5	0.03	
KO0020G01	1–3.1	0.01	
KO0020G02	2–3.5	0.04	
KO0020G03	2–3.5	0.3	8
KO0020G04	1.42–3.5	0.03	

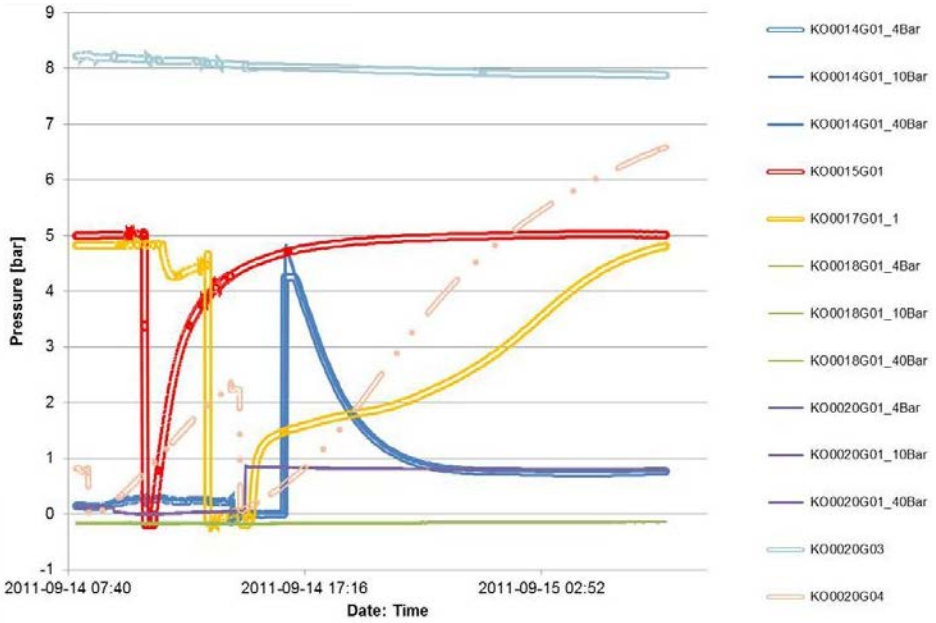

Figure 3-28. *Pressure for some of the boreholes (2011-09-14) before short duration flow tests (Table 3-10). KO0020G03 approximately 8 bars, KO0015G01 and KO0017G01 both 5 bars. Pressures included in Table 3-10.*

In Figure 3-28 and Table 3-10, "no" flow was measured and no pressure was registered in borehole KO0018G01. A few days later, 2011-09-19 at 10:52:26 there was a sudden loss in pressure in KO0020G03 followed by a slow increase in pressure in KO0018G01. The same day, at 19:23 to 19:43, an injection test was performed in section 2.0–3.06 m and at 20:05 to 20:25 another test was performed in section 1.5–3.06 m. Reasons for changes in head could be e.g. packers or fractures moving that may result in a low rate flow to the borehole. In case fractures did move, three fractures, two parallel and fairly steep, and one sub-horizontal fracture would be possible candidates, see Figure 3-39. These are interesting from a hydromechanical perspective.

Long duration flow tests

Long duration hydraulic tests allows for evaluation of transmissivity. Flow data and specific capacity were evaluated for KO0011A01, KO0018A01 and KO0017G01, see Table 3-11, Figure 3-29 and Figure 3-30. Flow values come from the late part of the tests where the flow starts to stabilise. Transmissivity was evaluated for borehole 11A01 (section 1.01 to 10 m, presented in Appendix B). The transmissivity was estimated as approximately 4.0×10^{-9} (3.5×10^{-9}) m^2/s.

Table 3-11. Long duration flow tests performed during Phase 2.

	Section [m]	Start Stop	Q [ml/min]	dh [m]
KO0011A01	1.01–10	2011-09-09	105	270
ID5		09:45-11:45		
KO0018A01	1.11–10	2011-09-09	11	260
ID6		13:40-16:10		
KO0017G01	2.11–2.97	2011-09-12	0.25	50
ID7		10:50–17:51		

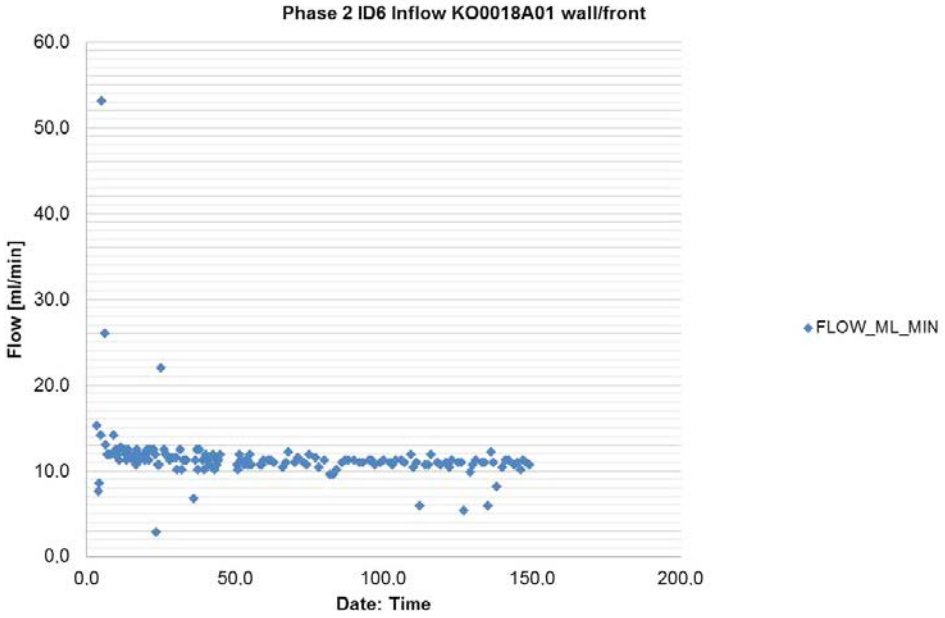

Figure 3-29. *Flow from long duration flow test, KO0018A01, wall.*

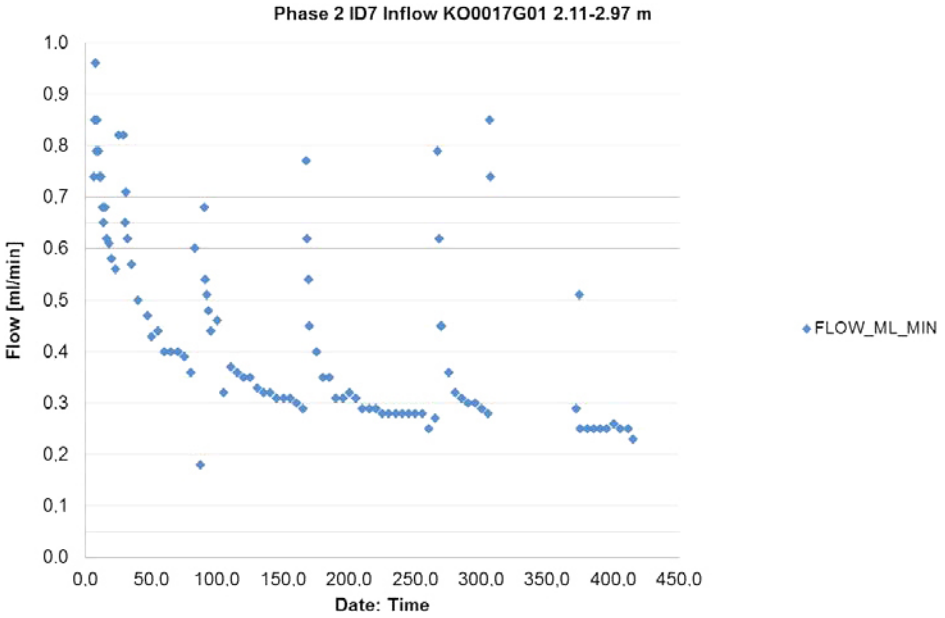

Figure 3-30. *Flow from long duration flow test, KO0017G01 76 mm.*

3.2.5 Concluding remarks Phase 2

Based on borehole and tunnel mapping, the main geometrical features of the system were identified, see the concluding remarks in Phase 1. These were the deformation zone perpendicular to the tunnel, natural fractures and increased fracturing close to the tunnel floor. The latter was assumed to be an excavation damaged zone (EDZ). Figure 3-31 shows an illustration of tunnel mapping (roof and walls) including the deformation zone (black box) as well as one of the most interesting flowing fractures identified in the lower part of borehole KO0017G01.

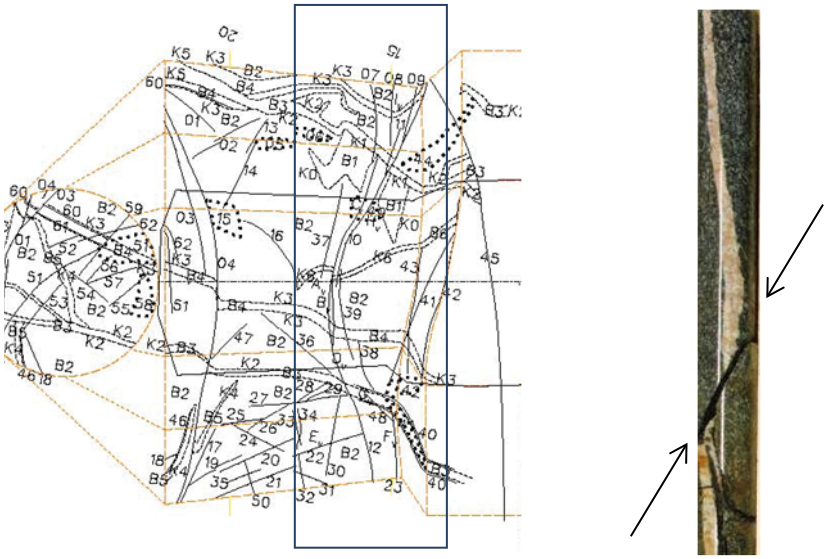

Figure 3-31. *Illustration of two of the main geometrical features, the deformation zone (black box in tunnel mapping, roof and walls) and the flowing fracture in the lower part of borehole KO0017G01.*

Logging of natural hydraulic heads in boreholes, pressure responses during drilling and hydraulic tests in combination, helped in identifying the location and the orientation of fractures as well as estimating the hydraulic properties for some of the most conductive ones. The deformation zone had, based on the test in KO0011A01, a transmissivity, *T,* of approximately 10^{-9} m^2/s. In addition, there was a number of conductive fractures with transmissivities of approximately 10^{-11} m^2/s. The two most interesting fractures were located in the upper part of borehole KO0014G01 and at a depth of 2.9 m in borehole KO0017G01, see Figure 3-31. An example of the transmissivity of EDZ originated from the shallow part of KO0018G01, where the specific capacity, *Q/dh,* was estimated to approximately 10^{-7} m^2/s.

Boreholes that were finally selected for over-coring and installation of bentonite were KO0017G01 and KO0018G01. The motivation for selecting these boreholes is found in Table 3-12.

Table 3-12. Motivation for selecting 17G01 and 18G01 based on characterisation of the site. Text in table has been translated from Swedish to English.

Motivation KO0017G01	Motivation KO0018G01
• Both KO0014G01 and KO0017G01 have water-bearing fractures. The investigated fracture in KO0014G01 is however relatively shallow (1.4 m). The fracture in KO0017G01 is found at 2.9 m. • Less influence of blasting at greater depths (see percentage of open fractures as a function of depth), • Less risk of contact with the surface (the tunnel). • Relevant depth of fractures considering depth of deposition holes. • Interesting fracture with respect to deformation. • Potential problem: distance between fracture and hole bottom may lead to the wetting not being from the fracture only (influence from bottom of borehole). Should still be interesting to study the upper parts of the fracture.	• Primarily objective is to study the transport from the rock matrix to the bentonite. • Pressure has increased in this borehole, and an "inflow" of about 5 drops were measured for 30 minutes. • The borehole thus contains both matrix and water-bearing fractures (very limited water discharge). • It should be possible to stop the test earlier so that wetting can be investigated in sections with matrix without (with limited) interference from possibly higher flows. • If it turns out that sections with rock matrix are too short, one option is not to install the bentonite in the borehole. The information obtained during drilling will still be interesting for the characterisation.

As a comment to the selection of KO0018G01 for investigation of a “dry” section and the objective to study the transport from the rock matrix to the bentonite. KO0020G01 could have been a potential candidate. Reasons not to select KO0020G01 was that during the early measurements had shown a flow of 19 ml in 30 min (almost all water immediately then only drops in section 0.82–3.1 m)

compared to “no” flow for KO0018G01. Further, injection tests in KO0018G01 indicated a longer section (1.5 m compared to 1 m) with flow close to zero compared to KO0020G01, see injected flow, *Q*, (blue lines and upper x-axis) in Figure 3-14 and Figure 3-15**.** One thing that made the decision somewhat more difficult was that an increase in pressure in KO0018G01 was observed during hydraulic testing in Phase 1 (see bullet two in Table 3-12, Motivation KO0018G01). Reasons for a change in head could be e.g. packers or fractures moving that may result in a low rate flow to the borehole. According to bullet four, one suggestion was to stop the test earlier so that wetting could be investigated in sections with matrix without (with limited) interference from possibly higher flows.

3.3 Characterisation of central boreholes

The objective of Phase 3 was to drill (over-core) and characterise the two central boreholes, KO0017G01 and KO0018G01, for installation of bentonite parcels.

3.3.1 Drilling and pressure logging

In Phase 3, the diameters of boreholes KO0017G01 and KO0018G01 were increased from 76 mm to 300 mm using over-coring. KO0017G01 had a final length of 3.5 m (76 mm borehole was 2.97 m) and borehole 18G01 had a final length of approximately 3.0 m (76 mm borehole 3.06 m). Figure 3-32 shows drilling of one of the two 300 mm boreholes.

Since pressure logging during drilling was performed and presented during Phase 2, no additional pressure logging is presented here.

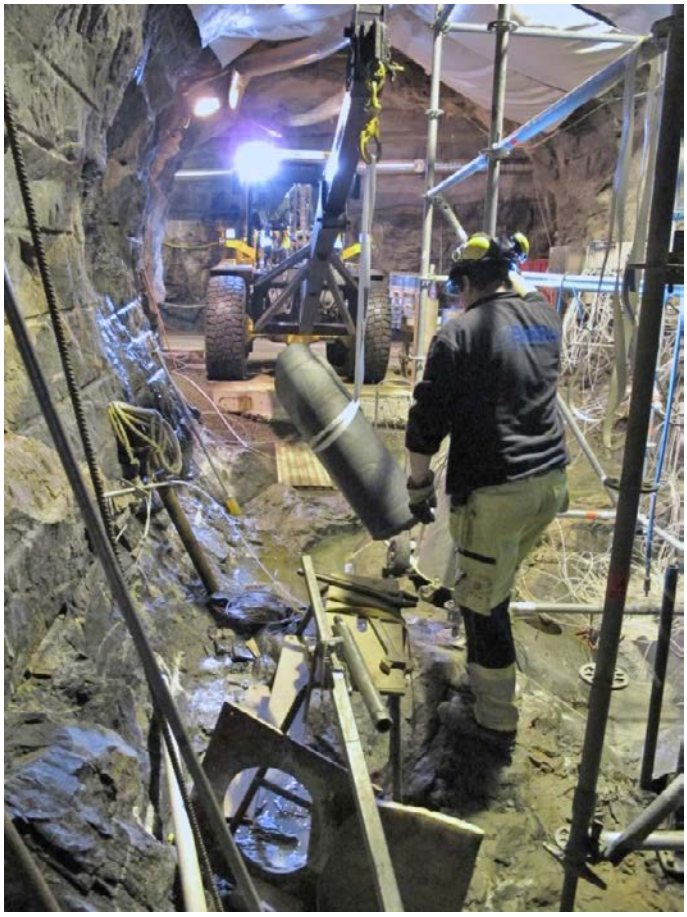

Figure 3-32. *TASO-tunnel (Phase 3) and the ongoing drilling of one of the central 300 mm boreholes.*

3.3.2 BIPS and core mapping

BIPS and core mapping were performed for both boreholes. Figures presented here show the lower part of the boreholes. Figure 3-33 to Figure 3-36 present KO0017G01 and include diorite and fine-grained granite that was intersected by the borehole at a right angle. The fracture of main interest has sheared a pegmatite vein.

Figure 3-37 to Figure 3-40 present KO0018G01 and include diorite and fine-grained granite that was also intersected by the borehole at a right angle. The fracture assumed to be of main interest in this borehole is seen in the lower rock core, see Figure 3-40. Evaluation of position and orientation of the main two fractures is presented in Table 5-5.

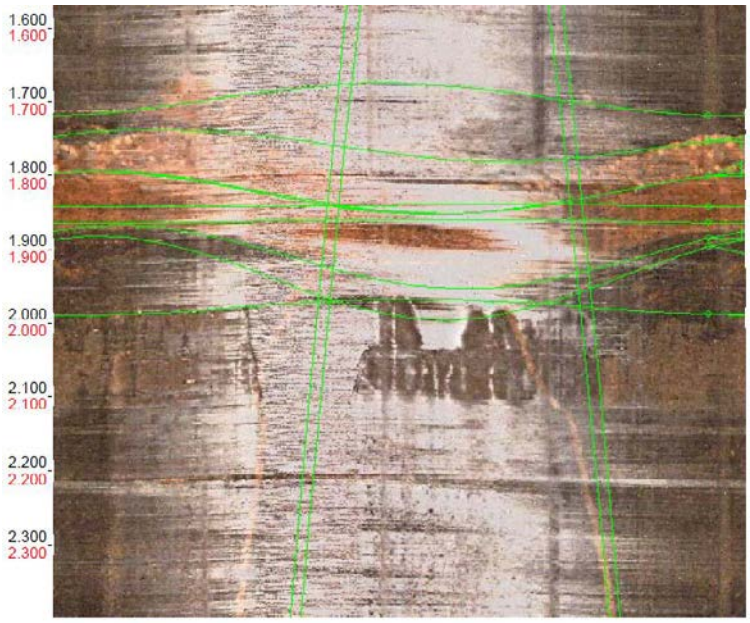

Figure 3-33. *BIPS KO0017G01, section 1.6–2.4 m, 300 mm (orientation not adjusted).*

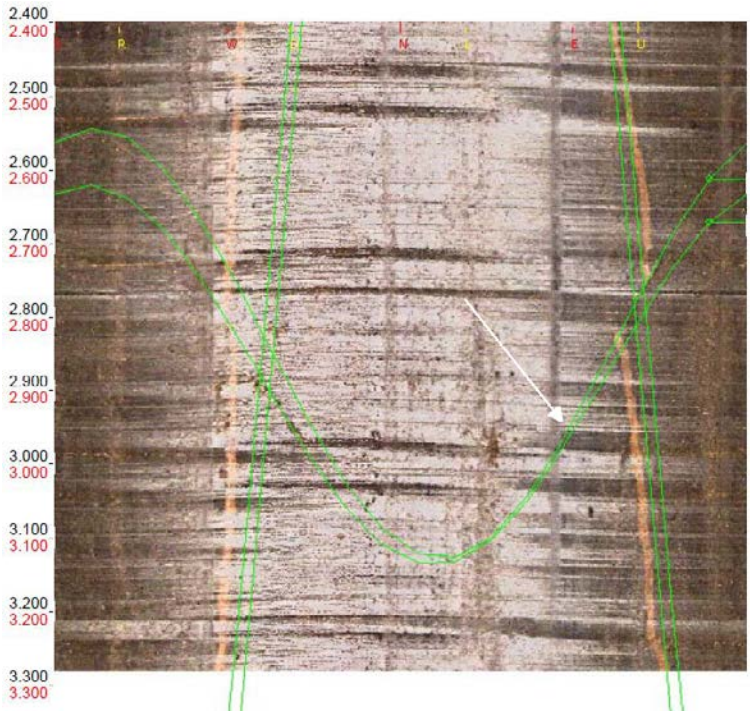

Figure 3-34. *BIPS KO0017G01, section 2.4–3.3 m, 300 mm (orientation not adjusted). Evaluation of position and orientation of the main fracture, indicated by an arrow in the image, is presented in Table 5-5.*

Figure 3-35. *KO0017G01, section 1.8–2.6 m, 300 mm.*

Figure 3-36. *KO0017G01, section 2.6–3.5 m, 300 mm.*

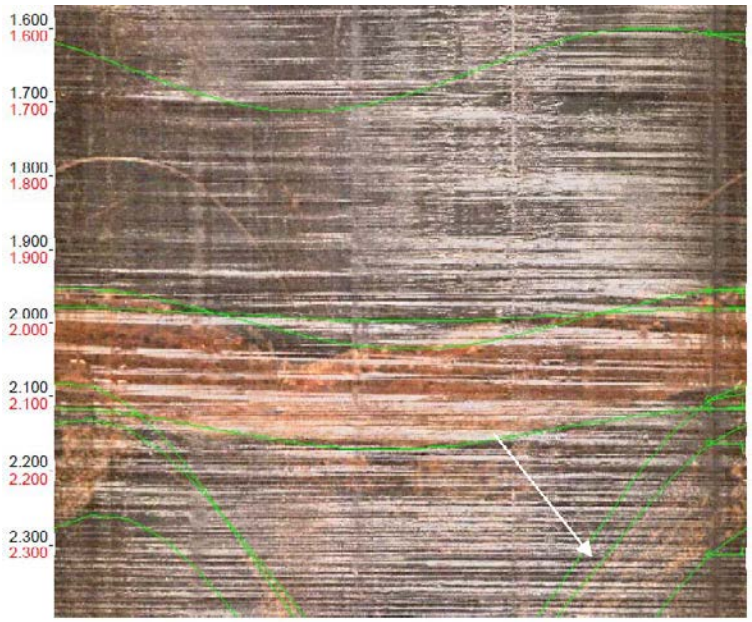

Figure 3-37. *BIPS KO0018G01, section 1.6–2.4 m, 300 mm (orientation not adjusted). Evaluation of position and orientation of the main fracture, indicated by an arrow in the image, is presented in Table 5-5.*

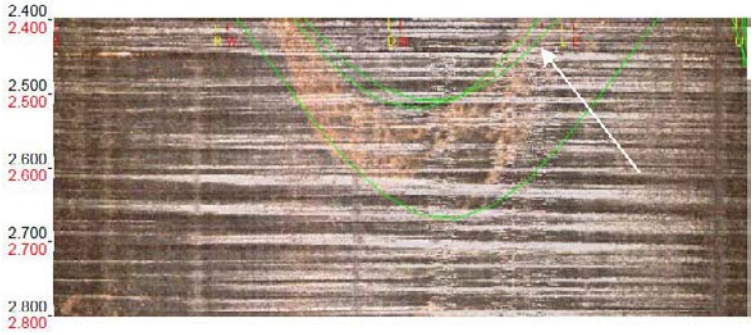

Figure 3-38. *BIPS KO0018G01, 2.4–2.8 m, 300 mm (orientation not adjusted). Evaluation of position and orientation of the main fracture, indicated by an arrow in the image, is presented in Table 5-5.*

Figure 3-39. *KO0018G01, 1.6–2.3 m, 300 mm. Main fracture of interest is indicated.*

Figure 3-40. *KO0018G01, 2.3–3.1 m, 300 mm. Main fracture of interest is indicated (deepest part of the core).*

3.3.3 Hydraulic tests, water chemistry sampling and gas volume measurement

The following hydraulic tests were performed in Phase 3:

- Short duration injection tests.
- Injection tests and flow tests (constant pressure tests).

In addition to these tests, water chemistry was sampled and gas volume measurements performed. Type of hydraulic test, date: start and stop, and sections tested are compiled in Appendix B. Pressure monitoring was performed in all boreholes. Equipment, execution and analyses are presented in Section 3.1.3.

Hydraulic tests were performed as short duration injection tests and flow tests. Tests in KO0017G01 and KO0018G01 used a special packer, Figure 3-41. Of main interest was to measure the flow from these larger dimension (300 mm diameter) boreholes and compare to flow for the 76 mm boreholes.

Figure 3-41. *Single packer for hydraulic testing in 300 mm boreholes.*

Flow for the lower sections of the 300 mm boreholes KO0017G01 and KO0018G01 are presented in Table 3-13 and Figure 3-42 to Figure 3-44. Two different ways of measuring the flow were used: a measuring glass and a watch; and the "flow organ" where levels in tubes are used to calculate the flow, see Figure 3-10 and Figure 3-11. Flow in KO0017G01 was measured with the two different methods thus resulting in two different values (approximately 0.12 ml/min for "flow organ" and 0.2 to 0.25 ml/min using a measuring glass). For KO0018G01, only the "flow organ" was used resulting in a flow between 0.01 and 0.02 ml/min.

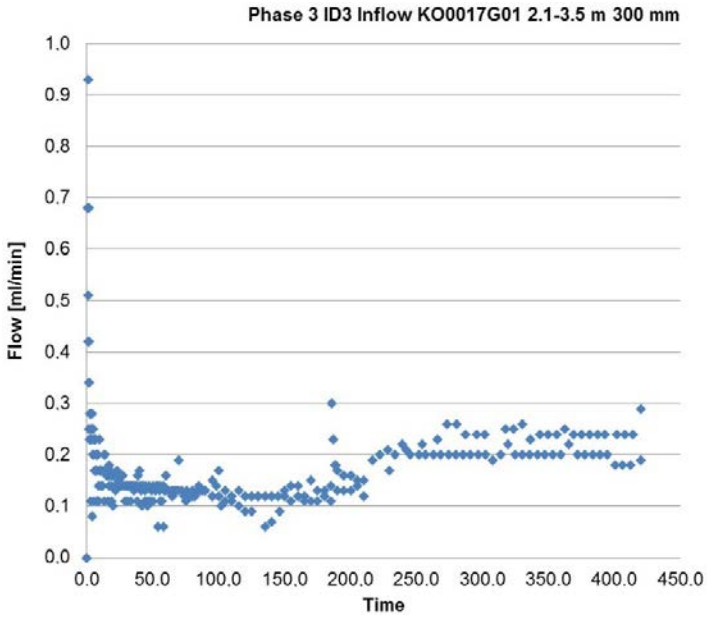

Figure 3-42. *Flow KO0017G01, section 2.1–3.5 m, 300 mm. Two different measurement methods (initially 0.12 ml/min based on levels in tubes using the "flow organ", followed by measuring glass from 211 min, 0.2–0.25 ml/min, change in flow assumed to be due to different measurement techniques).*

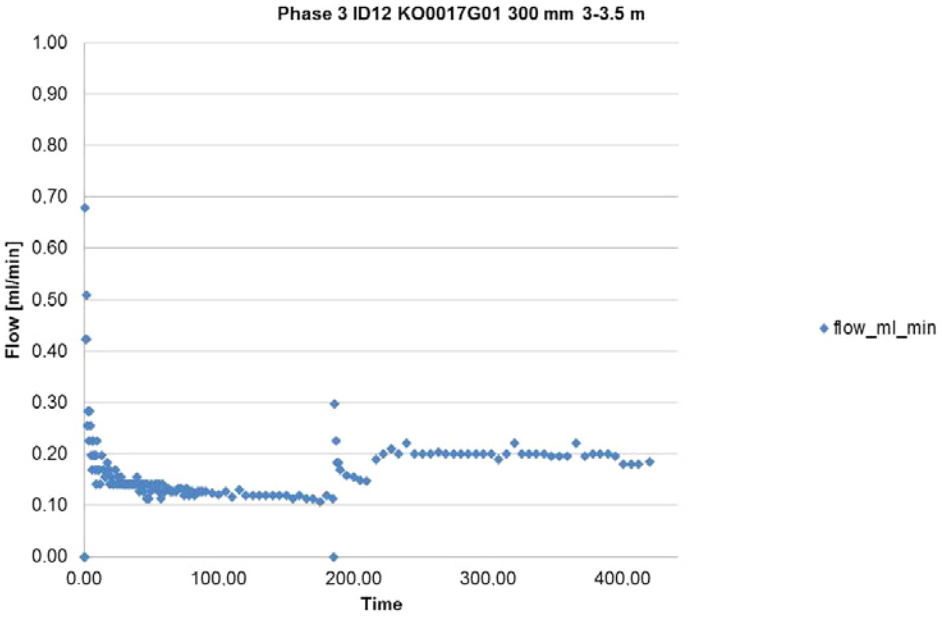

Figure 3-43. *Flow KO0017G01, section 3.0–3.5 m, 300 mm. Two different measurement methods (initially 0.12 ml/min based on levels in tubes using the "flow organ", followed by measuring glass, 0.2 ml/min, change in flow assumed to be due to different measurement techniques).*

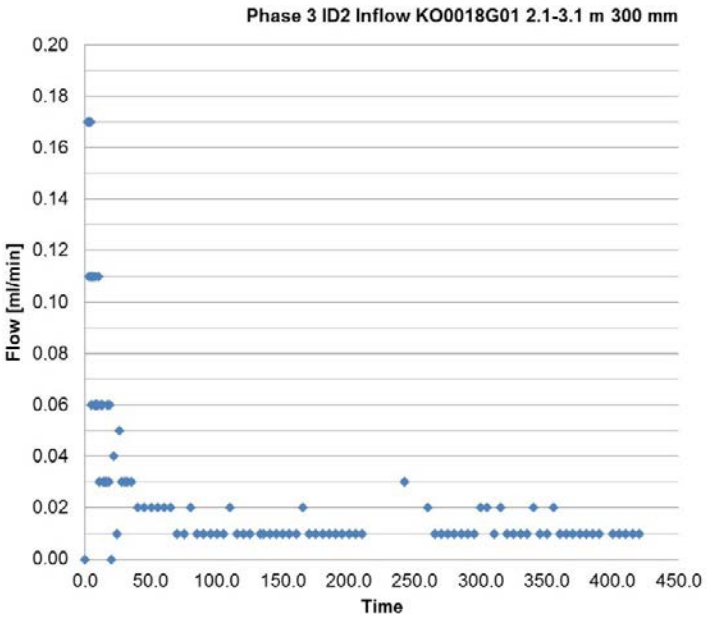

Figure 3-44. *Flow KO0018G01, section 2.1–3.1, 300 mm. Flow based on levels in tubes using the "flow organ", 0.01 to 0.02 ml/min.*

Table 3-13. Flow to 300 mm-boreholes KO0017G01 and KO0018G01 (400 min) using two different measurement methods (levels in tubes using the "flow organ" or measuring glass and watch).

	KO0017G01	KO0018G01
Inflow (300 mm) borehole	0.12 or 0.2–0.25 ml/min (2.1–3.5 m), Two different methods: Lower value based on levels in tubes using the "flow organ" and; higher value using measuring glass. 0.12 or 0.2 ml/min (3.0–3.5 m).	0.01–0.02 ml/min (2.1–3.1 m) "flow organ"

Water chemistry sampling in KO0011A01

Water sampling was performed 2012-02-15 in borehole KO0011A01 (long borehole found in left tunnel wall) and results are presented in Table 3-14 and Table 3-15. Flow was estimated to 0.1 l/min, pH measured in the field was 7.41 and temperature of water was 15.4 °C.

Table 3-14. Composition of groundwater 2012-02-15, borehole KO0011A01.

Na (mg/l)	K (mg/l)	Ca (mg/l)	Mg (mg/l)	HCO_3 (mg/l)	Cl (mg/l)	SO_4 (mg/l)	SO_4-S (mg/l)
1920.0	13.70	1410.0	75.20	73.30	5182.0	347.21	131.00

Table 3-15. Composition of groundwater 2012-02-15, borehole KO0011A01.

Br (mg/l)	F (mg/l)	Sl (mg/l)	Fe (mg/l)	Mn (mg/l)	Ll (mg/l)	Sr (mg/l)	PH (pH unit)	COND (mS/m)
25.480	1.53	7.14	0.4260	0.62200	1.0500	24.500	7.51	1556.0

Gas volume measurement during the hydraulic flow tests of the TASO tunnel in February 2012, a "gas trap" was designed and used to measure the volume of gas released when the groundwater pressure decreases. An inverted conical flask (50 mL) served as a gas trap, see Figure 3-45. The flask was mounted on a tripod which in turn was secured against a pole positioned at the boreholes. The

piston downward opening was closed with a rubber stopper and the location of the rubber stopper was marked. Further, two cannula tubes of predetermined lengths were intersected into the rubber stopper. A longer tube was connected to the valve of the borehole and a shorter connected to the flow meter, In order to prevent the rubber stopper to move by the pressure surge that may occur when the flow starts, the stopper was taped firmly against the flask. The whole system, including the borehole, was filled with water and carefully vented/de-aired from the borehole to the flowmeter. During a flow test, water was flowing from the borehole through the gas trap to the flow meter and the outlet and released gas was collected in the bottom of the inverted conical flask.

Following the flow test, the trapped gas volume was measured in the following way:

- The flask was turned right side up.
- The rubber stopper with the cannula tube was gently removed from the flask. If gas was released during the flow phase, the water level in the flask would be below the mark.
- The water was filled up to the mark using a measuring glass.

The gas volume, V_{gas}, was estimated based on the water volume, V_{filled}, subtracted by the volume of the cannulas in the flask, $V_{cannulas}$.

$$V_{gas} = V_{filled} - V_{cannulas}$$

Table 3-16 compiles the estimated gas volumes. Further comments on the tests are found in Appendix B.

Table 3-16. Compilation of air volume using a "gas trap". Performed during hydraulic testing in February 2012.

Date	Borehole	from_length	to_length	Flow start (hh:mm)	Flow end (hh:mm)	Volume of air in "gas trap" (ml)	Comment
2012-02-23	KO0018G01	2.1	3.1	05:57	12:57	0	Very low flow
2012-02-24	KO0017G01	2.1	3.5	05:26	12:26	31.25	High value!
2012-02-27	KO0015G01	2.1	3.03	05:32	12:46	0.3	
2012-02-28	KO0014G04	0.535	1.5	06:13	13:13	0.7	

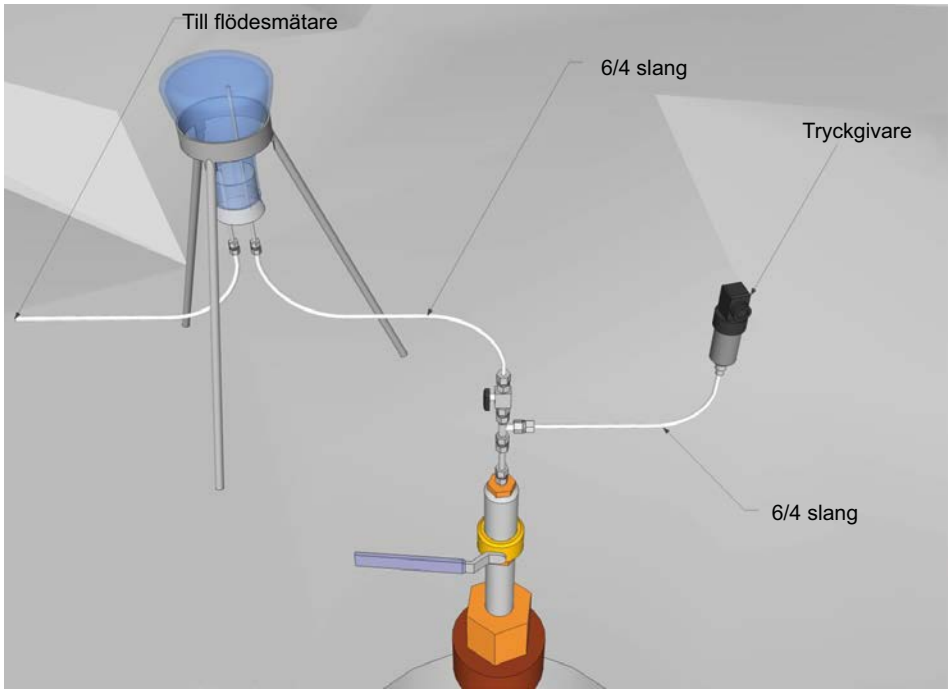

Figure 3-45. *Schematic sketch of the equipment for gas volume sampling in BRIE (figure used with courtesy of Geosigma AB).*

3.3.4 Nappy tests

The purpose of this activity was to obtain flow and flow distribution at the borehole wall of the 300 mm boreholes. Flow at the interface is an important input to the understanding of the exchange of water across the bentonite-rock interface and could hopefully allow for better predictions of the wetting of the bentonite buffer.

Nappy test measurements were performed in both KO0017G01 and KO0018G01.The equipment consists of a cylinder of approximately 1 m length and 0.3 m diameter covered by rubber that can be inflated using gas pressure to fit the borehole, see Figure 3-46. Nappies (15 around and 5 in height) were attached to the cylinder to measure the flow distribution over the borehole surface. Due to the low hydraulic conductivity of the rock matrix, only "larger" flows along fractures were expected to be identified.

Execution of the Nappy test included the following steps:

- Borehole was emptied.
- The nappies were numbered, weighed and attached to the cylinder, see Figure 3-46.
- Installation (lowering) of equipment into the borehole (check orientation).
- Rubber around cylinder was inflated and time registered (hh:mm). Since walls were still wet, this resulted in a slight increase in weight for the nappies.
- Sorbing mats were added above the cylinder (since there was flow in the upper sections of the borehole).
- Measurement.
- Rubber around cylinder deflated (time registered) followed by up-lift of the equipment.
- Nappies weighed.

Figure 3-46. *Equipment for borehole wall inflow measurements, also referred to as a "Nappy" test. The equipment consists of a cylinder of approximately 1 m length and 0.3 m diameter covered by rubber that can be inflated using gas pressure to fit the borehole. Nappies (15 around and 5 in height) were attached to the cylinder to measure the flow distribution over the borehole surface. Photo Christian Butron.*

Flows were estimated based on the change in weight divided by water density (1 gram approximated by 1 ml) and the time of measurement for each "nappy". The results were flows and their approximate location at the borehole wall. Only a test in KO0017G01 is presented in this report since the flow in KO0018G01 was too low (in combination with a large flow in the upper section of the borehole influencing the measurement at the lower section).

Figure 3-47 shows flow for individual "nappies" in ml/min (15 by 5), see data in Appendix C (with one table including and one table subtracting an estimated background value). In Figure 3-48 a background value based on the first row data (2.25–2.45 m) was subtracted from each nappy. This was done because the walls were wet when starting the measurement. Main flows identified in a north-easterly direction and at a depth between 2.45 to 2.65 m. Slightly lower flows were also indicated to the south below a depth of 2.45 m.

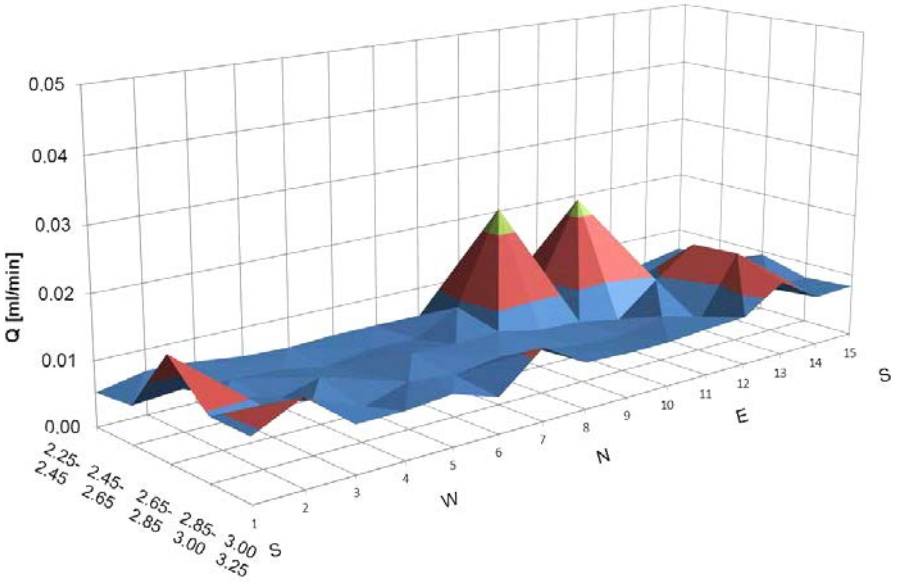

Figure 3-47. *Flow for individual "nappies" in ml/min. Main flows at approximately 2.45–2.65 m depth in a north-easterly direction. Total flow approximately 0.57 ml/min, see Appendix C.*

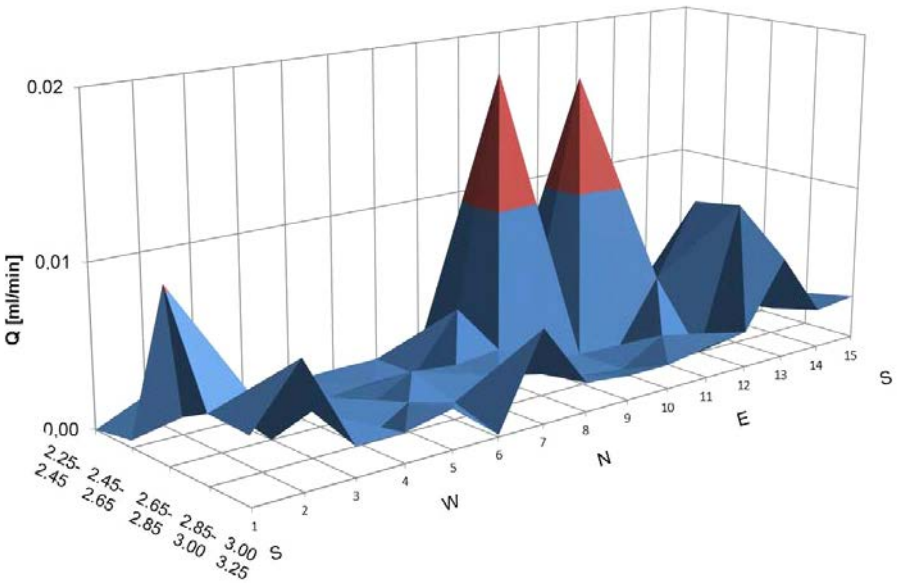

Figure 3-48. *Flow for individual "nappies" in ml/min. An approximate background value based on the first row data (2.25–2.45 m) was subtracted from data in Figure 3-47. Main flows at approximately 2.45–2.65 m depth in a north-easterly direction. Total flow approximately 0.16 ml/min, see Appendix C.*

3.3.5 Concluding remarks Phase 3

Hydraulic tests are compiled using flows measured during packer and nappy tests for the 300 mm boreholes, see Table 3-17. As a comparison, the table also includes measurements for the 76 mm boreholes. Figure 3-49 shows an approximate distribution of flows in the lower section of borehole KO0017G01 based on both packer and nappy tests (see Appendix C).

Flow for the section of most interest in KO0017G01 was about 0.1 to 0.25 ml/min for all tests except for Posiva Flow Log where the flow was below the detection limit (30 ml/h or 0.5 ml/min) and therefore uncertain. Results from Phase 3 confirm that the fracture in the lower part of KO0017G01 is the most conductive. The most water-bearing part of the fracture is found in a north-easterly direction which is in agreement with photos taken in the borehole where this flow is found in the upper part of the fracture, see Figure 3-49. This is opposite the dip direction presented in Figure 4-13 and Table 5-5.

During Phase 3, a flow of 0.01–0.02 ml/min was identified for KO0018G01 even though "no" flow was measured during Phase 1 (76 mm borehole). Both decrease and increase in head were however observed in KO0018G01 during hydraulic testing of the 76 mm borehole (Phase 2). Packers or fractures moving that may result in a low rate flow to the borehole could be two possible reasons for the increase in head. In case fractures did move, three fractures, two parallel and fairly steep, and one sub-horizontal fracture would be possible candidates, see Figure 3-39. These are interesting from a hydromechnical perspective.

Table 3-17. Compilation of flow for boreholes 17G01 and 18G01.

	17G01	18G01
Flow (76 mm) borehole	0.25 ml/min (0.5–2.97 m, 400 min), Phase 1.	–
Flow PFL	~ 0.5 ml/min (< 30 ml/h or 0.5 ml/min, uncertain).	–
Flow (300 mm) borehole	0.12 or 0.2–0.25 ml/min (2.1–3.5 m, 400 min), Phase 3. 0.12 or 0.2 ml/min (3.0–3.5 m, 400 min). Two different methods: Lower value based on levels in tubes using the "flow organ" and; higher value using measuring glass.	0.01–0.02 ml/min (2.1–3.1 m, 400 min), Phase 3.
Flow nappy test	~ 0.15 ml/min (2.25–3.25 m). (green: approx. 0.06–0.09 ml/min. Incl. backgr. value ~ 0.57 ml/min). Possibly water was entering in the lower part of the borehole (along pegmatite vein).	–

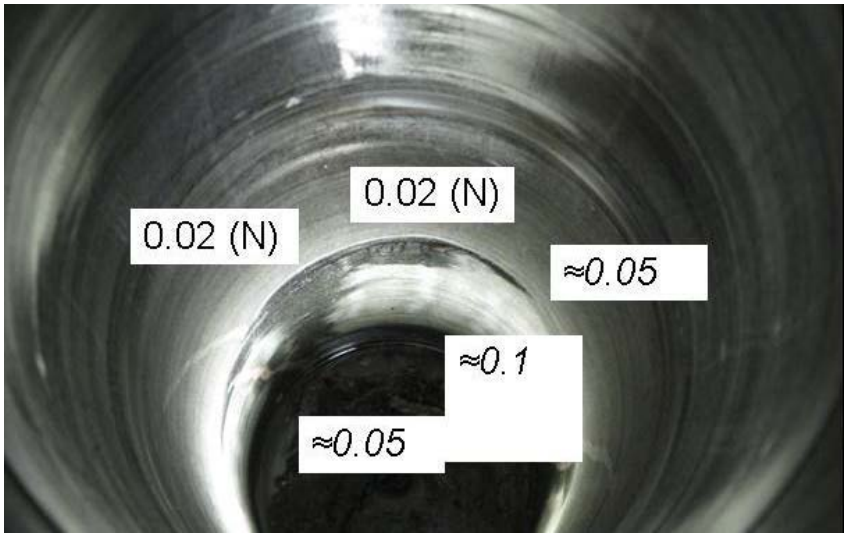

Figure 3-49. *Photo of the lower part of KO0017G01 including approximate distribution of flows based on packer (2.1–3.5 m) and nappy tests (2.25–3.25 m), see Appendix C.*

Following investigations it was decided that bentonite should be installed in both boreholes with main focus on fracture flow for KO0017G01 and rock matrix for KO0018G01. To increase the chance of identifying matrix flow, the dismantling should be initiated as soon as changes in relative humidity for the bentonite in contact with dry sections (matrix) were seen to decrease possible influence from fracture flow.

3.4 Tunnel flow measurement using sorbing mats

The purpose of this activity was to provide tunnel flow data for the description of the TASO tunnel.

Tunnel flow measurements were performed on the tunnel floor using sorbing mats (see Figure 3-50). An initial attempt was made to construct a weir but the presence of fracturing and a remaining concrete slab made this difficult since fractures were connected below the weir. Sorbing mats have (to our knowledge) not been used for this purpose before and a comparative study using both a weir and sorbing mats would be interesting to further evaluate the usefulness.

Before placing the mats, the floor was cleaned and water was pumped from wet (low) areas to obtain as dry conditions as possible. The mats were placed at lower locations (where wet spots had been identified). The locations of mats are shown in Figure 3-51.

Execution of the tunnel flow measurements included the following steps:

- Sorbing mats were numbered and weighed.
- Before placing each mat, its location should be dry (an extra mat was used to dry up).
- The first sorbing mat was placed and time (hh:mm) registrered. The mat was in contact with the rock surface.
- The other mats were placed using the same steps as described above.
- The mats were left to sorb water (larger expected flows by the deformation zone – shorter duration, here 1 hour for grey mats and approximately 3 hours for white mats, see Figure 3-51).
- Mats were removed, weighed and time (hh:mm) registrered. If floor was still wet (standing water, not only humid), remaining water was sorbed using an extra mat (add weight).

Figure 3-50. *Sorbing mats used for tunnel flow measurements (mats 3-4 close to KO0018G01, see Figure 3-51). Mats located on the floor where wet spots were identified. Photo Åsa Fransson.*

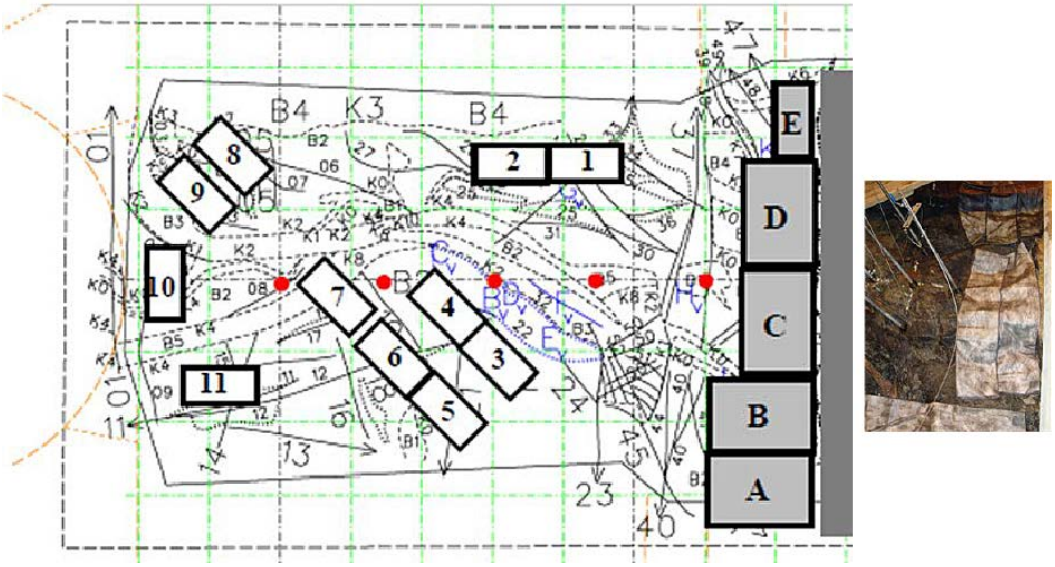

Figure 3-51. *Tunnel floor mapping, location of the five primary boreholes and location of sorbing mats, TASO-tunnel. The photo includes mats B, C, D and boreholes surrounding KO0015G01. To the far right in the photo, the edge of the concrete slab can be identified.*

Flows were estimated based on the change in weight divided by the time for each sorbing mat. The result (location of flows) is likely to be influenced by the excavation damaged zone (redistributing the flow) and should not be considered a description of the undisturbed rock. Further, one can expect water being transported from the tunnel by the ventilation. Locations of the sorbing mats (including tunnel floor mapping and the five primary boreholes) are shown in Figure 3-51 and the results from the measurements are presented in Table 3-18. Measurements for grey mats (A–E), see Figure 3-51, were about one hour (larger flows expected by the deformation zone). For low flows (white mats) measurements were performed for about three hours. The maximum capacity of the mats to sorb water was about 12 liters for 0.4 m^2.

Table 3-18. Tunnel flow data measured with sorbing mats.

Mat no. (Def. zone)	Q [ml/min]	Mat no. (HRD)	Q [ml/min]
A	12	3	7
B	7	4	< 1
C	57	5	1
D	3	6	8
E	< 1	7	1
E (extra)	< 1	8	< 1
		9	< 1
Zone left wall (extra)	1	10	2
1	1	11	1
2	2	3 (extra)	1
		Below KO0018A01	1

3.5 Scanning of fracture surfaces

Hydraulics as well as mechanics and hydromechanics are influenced by the fracture- and fracture surface geometry. To investigate the mechanical (and hydromechnical) behavior, surface geometry, fracture orientation and rock stresses are key aspects. The purpose of the fracture surface scanning was to further describe one aspect, the roughness, of the mechanical and hydromechanical fracture behavior.

Scanning of the fracture surfaces of main interest in KO0017G01 and KO0018G01, see Table 5-5, were made through photogrammetry. An example of the procedure is presented in Thörn and Fransson (2013).

The equipment set-up consists of a camera and a surface scanner. For execution of the measurements a series of photographs were initially taken on the surface of the different parts of the core, see example in Figure 3-52, (Thörn and Fransson 2013), this is not a necessary step to determine the undulation or roughness of each of the surfaces but of interest to relate the fracture surfaces to each other. In Thörn and Fransson (2013) photographs were processed by computer software that utilized code markings and dots that were placed on the surface for determining the relative positions of the sample halves, putting them in a common coordinate system (1). When this was done, the core was taken apart along the fracture (2). The dots on the upper surface of the core were supplemented with dots on the fracture surface (see green dots on the "computer screen" in Figure 3-52). Photographing was conducted again, one core half at a time before scanning the surface geometry of each surface (3, Figure 3-52). The dots that were attached to the sample before the photographing for enabling construction of a coordinate system were identified by the scanning software, which aligned the scanned surfaces into the established coordinate system (4). The point clouds obtained from the scans were converted to meshes. The meshes of the halves were then compared, and a high resolution map of the surfaces and the distance between the surfaces, i.e. the mechanical (or physical) aperture, was obtained (Figure 3-52) looking at the distance between the surfaces. For BRIE the surface geometry (undulation or roughness of the surface, step 3 in Figure 3-52 was the main focus since the original relationship between surfaces was not maintained when drilling and handling the cores.

The result from the fracture scanning is presented by Figure 3-53 and Figure 3-54.

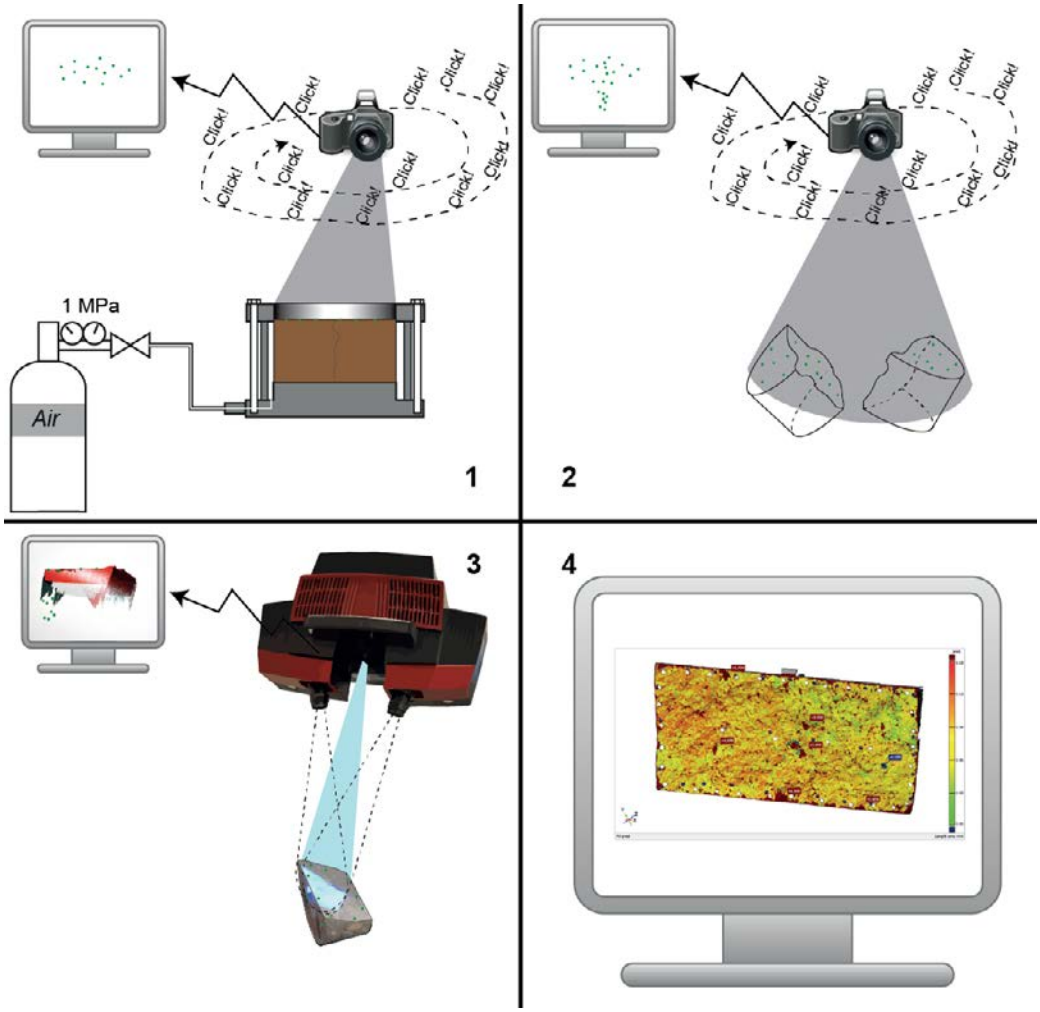

Figure 3-52. *Scanning of fracture surfaces, camera set-up. Example from Thörn and Fransson (2013). Step 3 is of main importance for BRIE since the original relationship between surfaces is not maintained when drilling and handling the cores.*

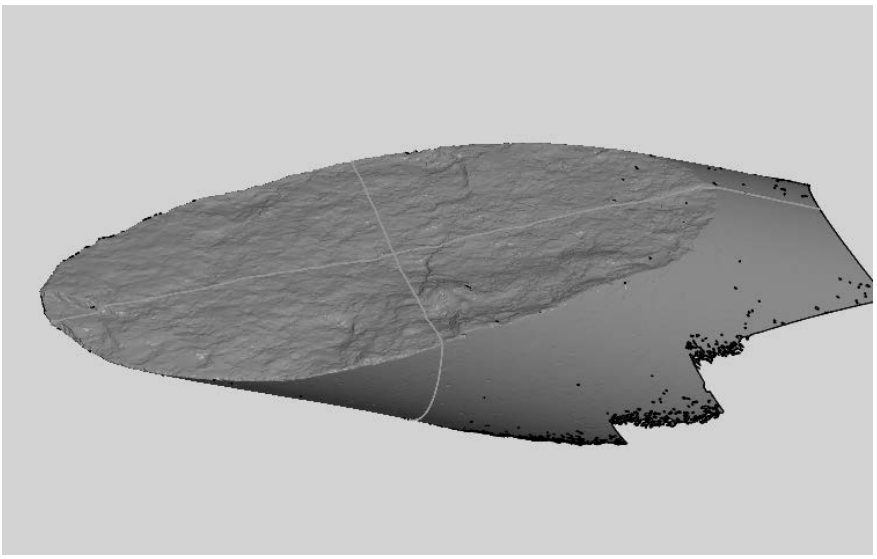

Figure 3-53. *Scanning of one of the fracture surfaces for the fracture of main interest in KO0017G01, see Table 5-5, (from 76 mm core).*

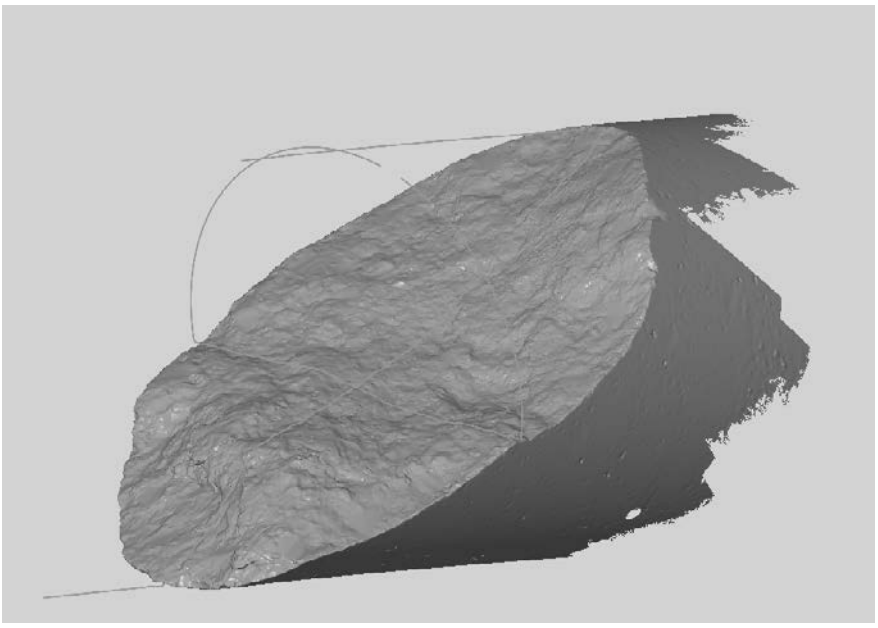

Figure 3-54. *Scanning of one of the fracture surfaces for the fracture of main interest in KO0018G01, see Table 5-5, (from 76 mm core).*

3.6 Characterisation of rock matrix: laboratory investigations

This section reports the results from rock matrix investigations that were performed. To obtain a relative humidity profile (RH), work was carried out in collaboration with the Division of Building technology, Chalmers. The investigations included measurements of:

- Hydraulic conductivity.
- Porosity.
- Water content in relation to relative humidity (as a basis for a water retention curve).
- RH-profiles in borehole walls (from rock blocks adjacent to 300 mm boreholes).

3.6.1 Hydraulic conductivity (vertical), porosity and water content to relative humidity

Investigation of rock matrix hydraulic conductivity was performed in the laboratory and equipment used for these tests was developed, see Fransson and Thörn (2017). In principle, the equipment consists of a cylinder that is pressurized at the top and with an outflow at the bottom. A sample (diameter approximately 60 mm and thickness about 10 mm) is installed and based on flow and gradient, the hydraulic conductivity can be estimated. The equipment does not allow testing of pressurized samples so rock stresses differ from those in the field.

Flow was estimated using the change in water level as a function of time, see b) measurement stand with scale, in Figure 3-55 Pressure was read and documented using the manometer found on the top of the permeameter, see a).

The equipment presented in Figure 3-55 was used for hydraulic testing. The procedure included the following steps, see Fransson and Thörn (2017):

a) Saturation of the rock specimen by water immersion (with periodic agitation to remove trapped air). To facilitate saturation the material was subjected to reduced pressure (vacuum saturation) before saturation.

b) Installation of specimen in the permeameter.

c) Preparation of water levels and measurement of water temperature.

d) Introduction of a pressure of 20 or 25 bars (during an initial test, 5, 10, 20 and 25 bars were used to investigate the validity of Darcy's law, see results in Figure 3-62, gradient approximately 250 m over 0.01 m).

e) Measurement of water temperature and change in level as a function of time.

The hydraulic conductivity, K, was determined based on Darcy's law:

$$Q = K \cdot A_{core} \cdot \frac{p_w}{\rho_w g \cdot L} \tag{3-3}$$

where, Q, is the flow, A_{core}, is the area of the rock specimen subjected to flow (somewhat smaller than the diameter of the sample due to a rubber gasket). Further, p_w, is the pressure (equal to pressure difference since there is atmospheric pressure at the outlet), ρ_w, the density of water, g, acceleration due to gravity and L, the thickness of the sample.

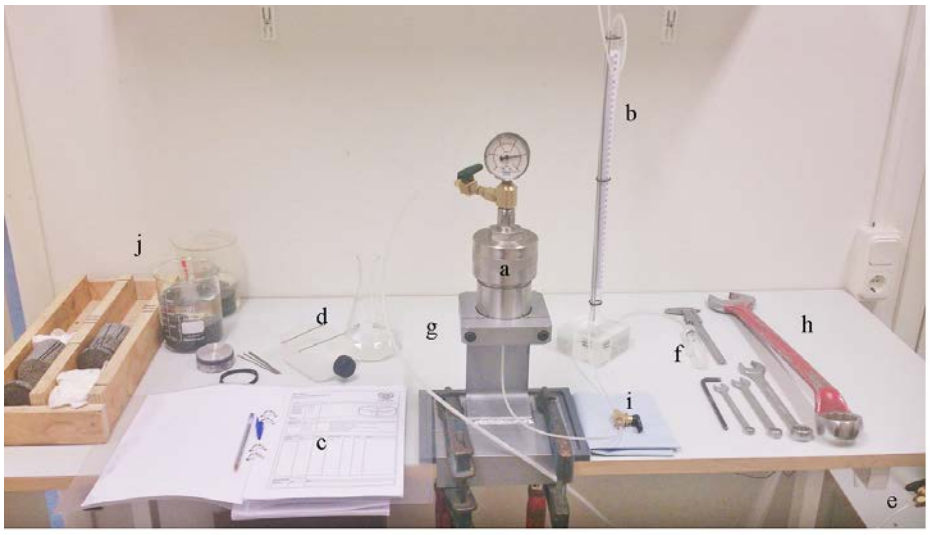

Figure 3-55. *Equipment for hydraulic testing of rock matrix: a) Permeameter including manometer in the mounting stand; b) Measurement stand with scale; c) Note form; d) Wetting container and Erlenmeyer flask: e) Compressed air; f) Syringe; g) Thermometer (not visible); h) Spanners, 11, 14, 22 och 45 mm; i) Lower valve; j) Samples. See Fransson and Thörn (2017).*

Porosity

Porosity was determined using a procedure recommended for regularly shaped specimens (ISRM 1979). The procedure included the following steps:

a) Specimens machined to the geometry of a cylinder (mass at least 50 g).

b) Specimen's bulk volume, V is calculated from an average of several readings for each dimension. Each reading should be accurate to 0.1 mm.

c) Saturation of the specimen by water immersion (with periodic agitation to remove trapped air).

d) Removal of specimen and drying of surface using a moist cloth (only remove surface water, no fragments lost). Determine saturated-surface-dry mass, M_{sat}.

e) Drying of specimen to constant mass at a temperature of 105 °C, allowed to cool for 30 min in a desiccator. Mass is determined to give grain mass, M_s.

The following equipment was used for estimate of porosity:

- Oven, using a temperature of 105 °C (within 3 °C) for at least 24 h.
- A dessicator (keeps the sample dry) to hold specimens during cooling.
- A measuring instrument, here a caliper, capable of measuring specimen dimensions to an accuracy of 0.1 mm.
- Vacuum saturation equipment (sample immersed in water under a vacuum of less than 800 Pa for a period of at least one hour).
- A balance determining the mass to an accuracy of 0.01 %.
- Jar, filled with water (large water surface) RH: 100 %, allow placement of specimens.

The pore volume including saturated-surface-dry mass, M_{sat}, grain mass, M_s, and density of water, ρ_w, was estimated:

$$V_v = (M_{sat} - M_s)/\rho_w \tag{3-4}$$

Further, the porosity [%] was obtained using the pore volume, V_v, and the bulk volume, V, of the specimen:

$$n = 100 V_v/V \tag{3-5}$$

Water content to relative humidity

Water retention curves are used when describing unsaturated flow in rock matrix. In this section, determination of water content as a function of relative humidity is described. Saturated salt solutions in an exicator, Figure 3-56, result in different relative humidity (RH). Equipment and chemicals used to get data for the water retention curves were:

- Exicator (with saturated salt solutions), see Figure 3-56.
- Salt: RH: 32, 59, 85 and 93 % saturated salt solutions of $MgCl_2$, NaBr , KCl and an aqueous unsaturated NaCl solution for 93 % RH. Two molal solution of NaCl (vapor pressure over solution p 2 179 Pa, vapor pressure over pure water, psat 2 339 Pa at 20 °C, RH = p/psat = 93 % (change and weigh, evaporation, leakage).
- Balance.

To determine a water retention curve, a series of exicator- or jar tests were performed, see Wadsö et al. (2004). In these tests, rock samples were equilibrated in a climate with given relative humidity, RH, and then the water content was measured. Equilibration was obtained for different saturated salt solutions. The test procedure is described below:

a) The samples were placed in an exicator (glass jar) with a saturated salt solution (constant relative humidity conditions).

b) The sample was weighed.

c) Equilibrium was obtained (when change in mass of the sample was small).

d) Sample was dried after the measurement (moisture content of a sample usually based on the dry mass of the sample). 105 °C for 24 hours.

To obtain additional values of water content, drying (D1) with the different relative humidities, *RH*, of 100 – 85 – 59 – 32 – "0", see results in Figure 3-60, was followed by wetting (W) with *RH*: "0" – 32 – 93 – "100". Finally the hysteresis loop included a second drying (D2) with *RH*: "100" – 93. This final step included:

e) Saturation of the specimen by water immersion. Before immersion the sample was kept in vacuum for one hour.

f) Remove specimen and dry surface using a moist cloth (only remove surface water, no fragments lost). Determine saturated-surface-dry mass, M_{sat}.

g) Return to a) above.

The volume of water at the specific relative humidity including saturated mass, M_{satRH}, grain mass, M_s, and density of water, ρ_w (998.2 kg/m^3 at 20 °C) was estimated:

$$V_{vRH} = (M_{satRH} - M_s)/\rho_w \quad (3\text{-}6)$$

Further, the water-filled porosity or the volumetric water content, w [%] was obtained using the volume of water, V_{vRH}, and the bulk volume, V, of the specimen:

$$w = 100 V_{vRH}/V \quad (3\text{-}7)$$

This results in water content at different relative humidities.

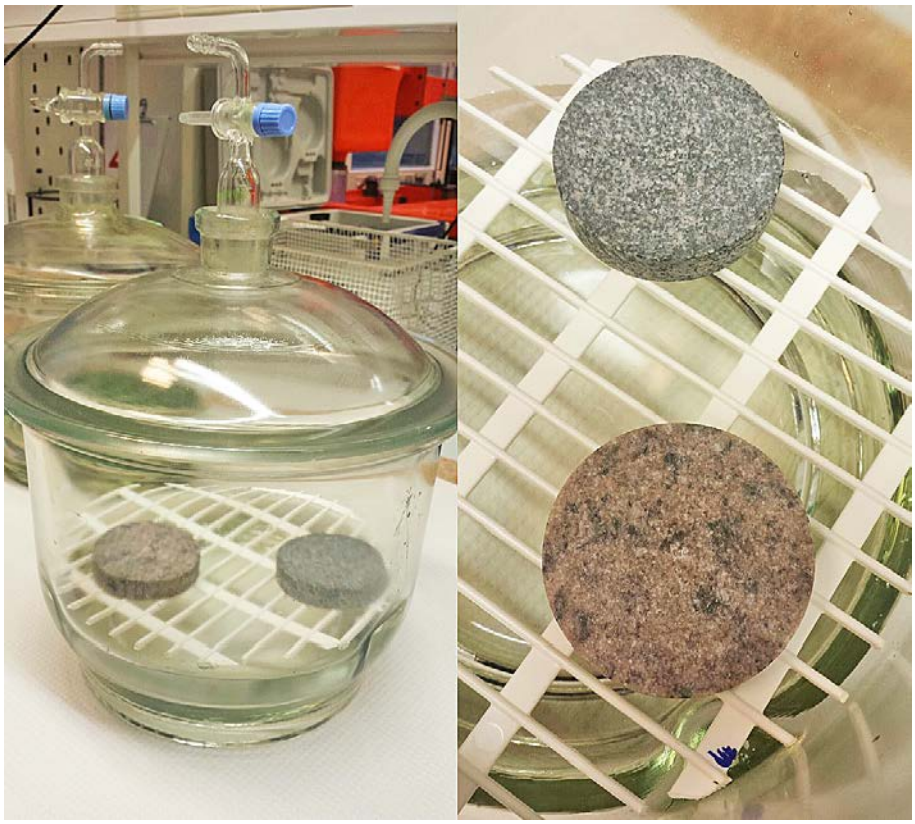

Figure 3-56. *Exicator (with saturated salt solution) and two rock samples, B1 and A1.*

Water retention curve

The saturation degree, see calculations in Appendix D, was estimated by dividing the volumetric water content for the given relative humidity by the volumetric water content when fully saturated (equal to porosity n). Further, relative humidity, RH, was related to suction, s, using Kelvin's law:

$$s(RH,T) = \frac{-ln(RH)\cdot\rho_w\cdot R\cdot(273.15+T)}{M_w} \quad (3\text{-}8)$$

where, T, is the temperature (in °C), R, the general gas constant and M_w, the molar weight of water. Appendix D presents volumetric water content and relative humidity and shows how these data were used to obtain suction and saturation degree for a water retention curve and Van Genuchten curve parameters.

The measurement for each salt solution and the related relative humidity was stopped when the equilibrium criterion below was approximately 5×10^{-9} s^{-1}, see Wadsö et al. (2004):

$$\Omega = \frac{dm/m_i}{dt} \times \frac{\varphi_f - \varphi_i}{(m_f - m_i)/m_i} \quad (3\text{-}9)$$

When major part of sorption step has taken place $m(t) \approx m_f$

$$\Omega = \frac{dm}{dt} \times \frac{\varphi_f - \varphi_i}{(m_f - m_i)} \quad (3\text{-}10)$$

including, m_i, that is the mass for the initial state of a sorption step, m_f, the mass for the final state of a sorption step and φ, the moisture capacity of the sample in the relative humidity.

Rock samples

Samples were taken from KO0017G01, KO0018G01 and KO0020G01 and included diorite, diorite with a pegmatite-vein and fine-grained granite. From Phase 1 and Phase 2 samples were taken from the vertical cores, whereas for Phase 3 samples originate from boreholes drilled in rock blocks and were oriented radially from the borehole wall (horizontal).

Figure 3-57 shows a section of the core from KO0020G01 including diorite and fine-grained granite. The samples were taken between 1.78 m and 2.48 m below the tunnel floor.

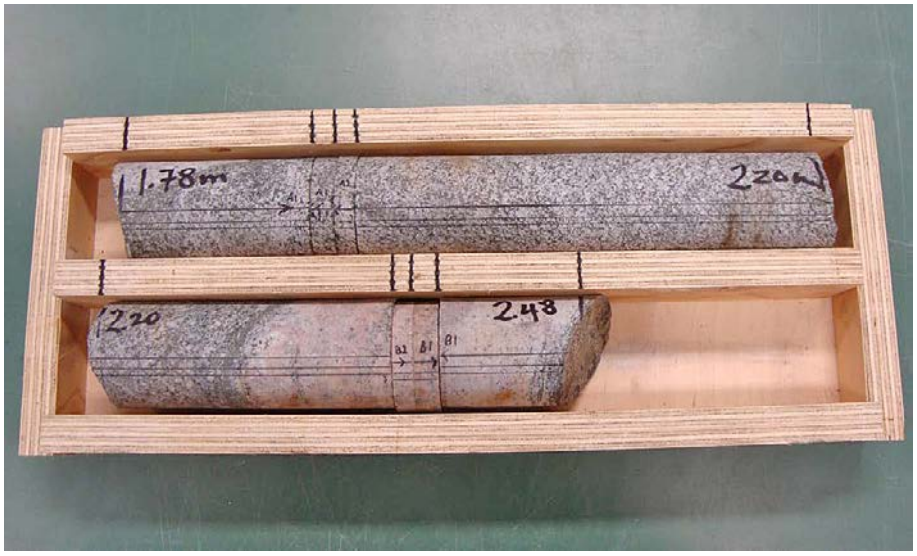

Figure 3-57. *Borehole KO0020G01, depth 1.78–2.48 m, samples from diorite and fine grained granite.*

Figure 3-58. *Samples B2 (fine-grained granite) and A2 (diorite), KO0020G01, diameter and thickness approximately 60 mm and 10 mm respectively.*

Figure 3-59 shows two sections of cores originating from KO0017G01 and KO0018G01 and include diorite and a pegmatite-vein. The samples from KO0017G01 were taken at a depth of approximately 2.3 m and for KO0018G01 the depth was between 2.7 m and 2.8 m below the tunnel floor.

Hydraulic conductivity was estimated to about 10^{-13} m/s, for the samples from KO0020G01, see Table 3-19. An additional test on an aluminium sample was carried out to show that the permeameter itself was tight enough. The impression from testing the aluminium sample was that "no" or very little flow could be measured compared to the other two tests. The conclusion was that the equipment itself was tight enough to allow measurement of sufficiently low hydraulic conductivities. The aluminium sample is here given a hydraulic conductivity that is "still lower" since determination of a value for the sample was difficult.

Table 3-19. Phase 1: Hydraulic conductivity, samples from KO0020G01, see Figure 3-57.

Sample	Pressure [bar]	K [m/s]
Diorite, A1	25	6.5×10^{-13}
Granite, B1	25	2.6×10^{-13}
Aluminium sample	–	Still lower*

* A test on an aluminium sample was carried out to show that the permeameter itself was tight enough.

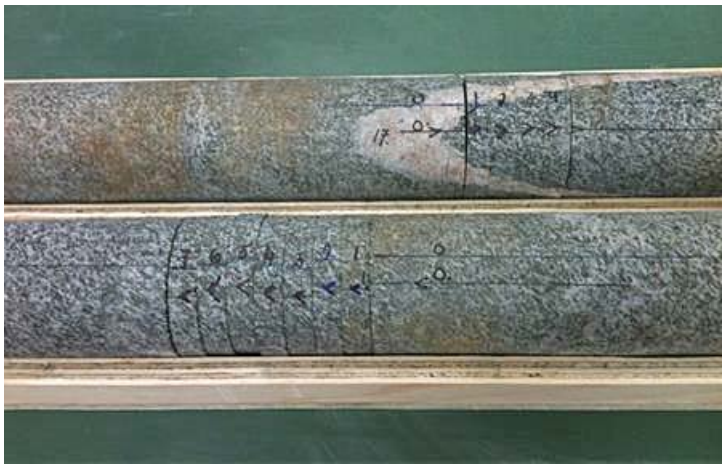

Figure 3-59. *Boreholes KO0017G01 (upper, at approximately 2.3 m) and KO0018G01 (lower, at approximately 2.7–2.8 m), samples from diorite (and a minor occurrence of pegmatite) and diorite.*

Porosity and water retention curve

Table 3-20 and Figure 3-60 present porosity investigated during Phase 1 (Diorite: A1 and A2, and Granite: B1 and B2, filled symbols) and water content for samples Diorite A1 and Granite B1, see samples in Figure 3-57 and Figure 3-58. For the initial fully saturated samples, the saturated-surface-dry mass, M_{sat}, was determined by removing the specimen from water and drying the surface using a moist cloth (only to remove surface water, no fragments lost).

Table 3-20. Phase 1: Porosity, samples from KO0020G01, see Figure 3-57.

Sample	Porosity [–]
Diorite, A1 and A2	Approximately 0.009
Granite, B1 and B2	Approximately 0.005

In Figure 3-60, water content for drying (D1: RH 100 – 85 – 59 – 32 – "0"); wetting (W: RH "0" – 32 – 93 – "100") and a second drying (D2: RH "100" – 93) are shown. To obtain zero relative humidity the samples were dried in an oven (105 °C for 24 hours) and as can be seen the sample was not completely dried since the water content does not reach 0 %, here referred to as "0". To obtain a relative humidity of 100 % as the last step in the "wetting" phase, "100", samples were kept in vacuum for about one hour followed by saturation by water immersion.

Of interest in Figure 3-60 is that the two samples A1, blue, and B1, green, follow similar paths. At an RH of 100 %, the two samples of Diorite (A1 and A2, upper two values) has a porosity of 0.8 and 1.0 % (fully saturated). For the granitic samples (B1 and B2, green and orange triangles) the porosity is close to 0.5 %. When decreasing the relative humidity from 100 to 85 %, the water content for A1 goes from 1.0 % to about 0.3 %. The water content continues to decrease until the final step where the sample was put in the oven. Following the first period of drying (D1), the relative humidity was increased, referred to as wetting (W). Finally a second short period of drying was performed (D2). For both samples (A1 and B1) the water content for a relative humidity of 100 % might be lower following drying and wetting. This could be explained by e.g. trapped air in the rock matrix.

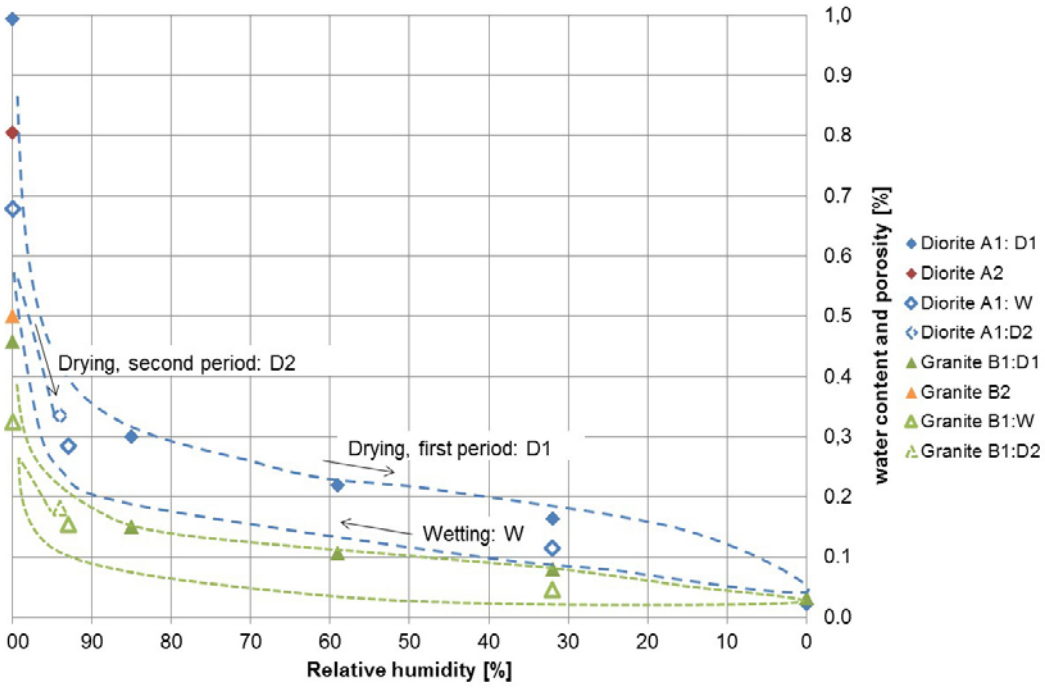

Figure 3-60. *Porosity (Diorite and Granite, filled symbols) and water content (D1: first period of Drying, W: Wetting, D2: second period of Drying). Data and retention curves estimated based on the data for Diorite A1 and Granite B1 are presented in Appendix D.*

Porosity and water content were estimated according to the methods outlined in the previous sections. One important issue was to identify when the water content for a specific relative humidity had reached equilibrium. When changing relative humidity, going from e.g. 85 % relative humidity to 59 %, see Figure 3-60, the sample slowly got dryer with time (the weight decreased), until very small changes was seen. An example of an equilibrium criterion estimate is presented below (approximately 5×10^{-9} s^{-1}, same as in Wadsö et al. 2004):

$$\Omega = \frac{dm}{dt} \times \frac{\varphi_f - \varphi_i}{(m_f - m_i)/m_i}$$

m_i [kg or g] mass (initial state of sorption step)

m_f [kg or g] mass (final state of sorption step)

φ[–] moisture capacity of the sample in the relative humidity

Table 3-21. Example of an equilibrium criterion estimate to determine when to stop the measurements of water content (j from 85.5 % to 59 %)

	Mass [g] Diorite A1	Granite B1
Initial	108,6563 (φi 85,5 %)	103,2904 (φi 85,5 %)
2011-11-29	108,6249 (58,8 %)	103,2731 (58,8 %)
2012-12-02	108,6248 (φf 58.9 %)	103,2730 (φf 58.9 %)

$$\frac{108.6249 - 108.6248}{3 \times 86400} \times \frac{0.59 - 0.85}{(108.6248 - 108.6563)} = 3 \cdot 10^{-9} \text{ s}^{-1}$$

$$\frac{103.2731 - 103.2730}{3 \times 86400} \times \frac{0.59 - 0.85}{103.2730 - 103.2904} = 6 \cdot 10^{-9} \text{ s}^{-1}$$

Hydraulic conductivity measurements were also performed for samples from KO0017G01 and KO0018G01, see Figure 3-59. Table 3-22 and Figure 3-61 presents the result and hydraulic conductivities between 10^{-14} to 10^{-11} m/s were estimated. Initially hydraulic tests were performed for sample 1 (KO0018G01) at four different pressures to investigate the validity of Darcy's law expecting flow being proportional to head (or head gradient, see relationship in Figure 3-61). Using a pressure of 5 bars resulted in a flow that was difficult to measure (too low) and tests were therefore performed at a pressure of 20 bars.

Table 3-22. Phase 2: Hydraulic conductivity, samples from KO0018G01 and KO0017G01, see Figure 3-59.

Sample	Pressure [bar]	K [m/s]
KO0018G01 (Diorite)		
1	25, **20**, 10, 5	6×10^{-14}
3	20	1.5×10^{-13}
4	20	1.5×10^{-13}
5	20	2.5×10^{-13}
7	20	3.3×10^{-13}
KO0017G01 (Diorite, Pegmatite)		
1	20	5.5×10^{-12}
3	20	7.5×10^{-13}
4	20	9.0×10^{-13}

Figure 3-61 shows distributions of hydraulic conductivity for the diorite and the diorite-pegmatite samples. Data are few but could possibly be two different groups with a difference of about one order of magnitude. One explanation could be the presence of the pegmatite vein.

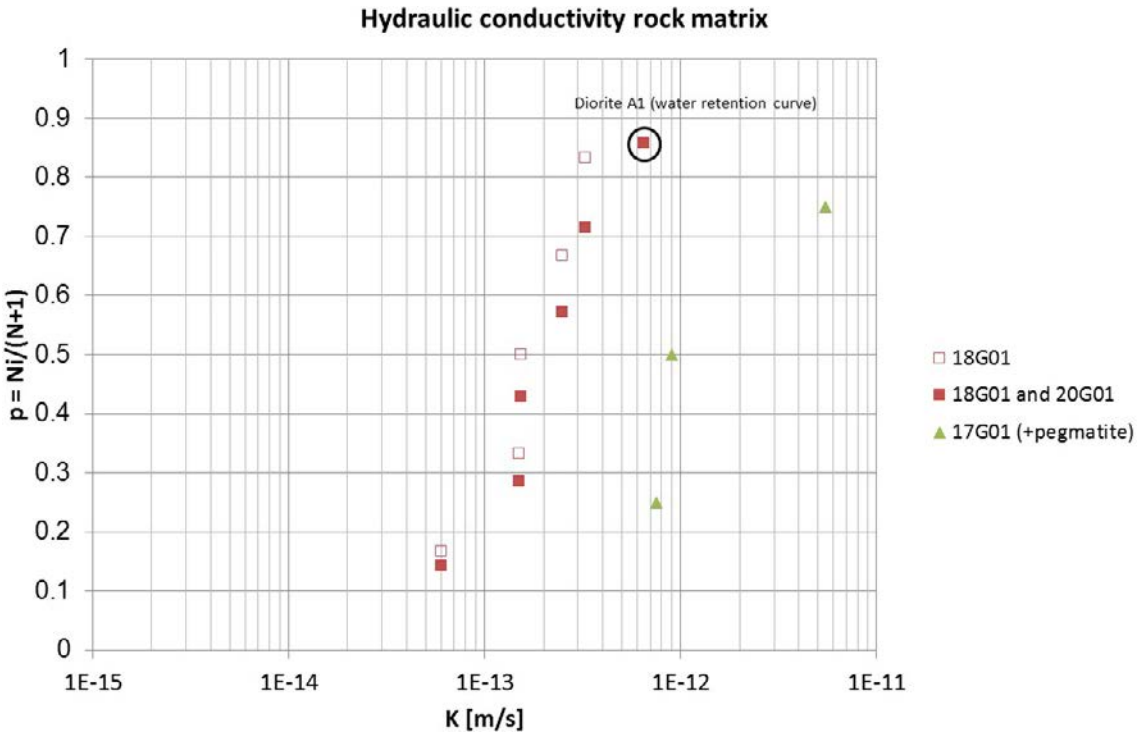

Figure 3-61. *Hydraulic conductivity Phase 2 (KO0020G01 from Phase 1).*

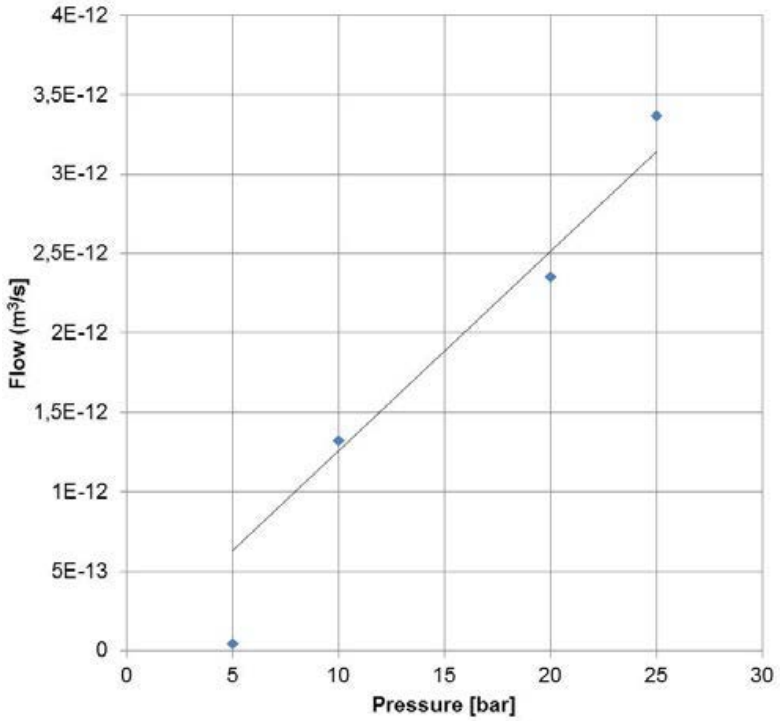

Figure 3-62. *Flow [m^3/s] and pressure [bars] for sample 1, KO0018G01, to investigate the validity of Darcy's law expecting flow being proportional to head (or head gradient). At 5 bars, the flow was too low to allow for a good measurement with the equipment used.*

3.6.2 Hydraulic conductivity (radial) and relative humidity profiles at central borehole walls

Following dismantling of the rock/bentonite parcels, rock blocks were transported to Chalmers and boreholes were carefully and slowly drilled to enable monitoring of relative humidity at 6 different depths (three locations in KO0017G01, Figure 3-63 and Figure 3-64, and one location in KO0018G01, Figure 3-65).

Boreholes for relative humidity measurements were drilled using hammer drilling without using water (to reduce the risk of influencing the humidity of the rock blocks). Following drilling, the boreholes were cleaned using air and plastic tubes were installed, see Figure 3-63. The plastic tubes had the same length to facilitate the identification of borehole depth. The contact between the plastic tubes and the rock was sealed using a plastic material (blue in figure). Measurements were performed using a measurement probe that could be installed in the plastic tubes.

Figure 3-63. *Rock block and monitoring of relative humidity (RH), KO0017G01 (upper part of rock block to the left, right hand of photo shows the upper part of main fracture). The figure also shows the location of the rock core for hydraulic tests. Location referred to as DSU (dry section upper). Samples 2:1 to 2:4 (hydraulic conductivity) originate from the core. Figure 5-24 shows location of measurements in rock in relation to the bentonite parcels.*

Figure 3-64. *Rock blocks and monitoring of relative humidity (RH), KO0017G01 (upper part of rock block to the right). Locations referred to as DSL (Dry Section Lower) and F (closest to the Fracture). The figure also shows the location of the rock core for hydraulic tests. Samples 1:1 to 1:4 (hydraulic conductivity) originate from the core. Figure 5-25 shows location of measurements in rock in relation to the bentonite parcels.*

The location of the RH-profile measurement is seen in Figure 3-63, Figure 3-64 and Figure 3-65. Following these measurements, cores were drilled for hydraulic tests. Figure 5-24**,** Figure 5-25 and Figure 5-26 show location of measurements in rock in relation to the bentonite parcels (e.g. H17_0°_B14:15, borehole KO0017G01, orientation 0° and blocks number 14 and 15).

The locations of the rock cores perpendicular to KO0017G01 used for hydraulic testing are seen in Figure 3-63 and Figure 3-64. Samples are seen in Figure 3-66. Samples 1:1 and 2:1 are found closest to the borehole wall. The figure shows approximate distance due to material lost during preparation (sawing and polishing) of samples (about 3 centimeters per core, 18 and 15 cm thickness of rock blocks).

Figure 3-65. *Rock block and monitoring of relative humidity (RH), KO0018G01, upper part of rock block to the right.*

Figure 3-66. *Boreholes perpendicular to KO0017G01, in rock blocks by the 300 mm borehole wall. Left (three lines) includes samples 2:1 to 2:4 (Dry Section Upper, 26.5 cm above fracture). Right (two lines) includes samples 1:1 to 1:4 (between Dry Section Lower, DSL and F). Samples 1:1 and 2:1 are found closest to the borehole wall. Approximate distance due to material lost during preparation of samples.*

Hydraulic conductivity for Phase 3 samples (perpendicular to KO0017G01) was investigated using the same equipment and method as for the previous, vertical samples, see Figure 3-55. Hydraulic conductivity was estimated to 10^{-15} to 10^{-12} m/s, see Table 3-23 and Figure 3-67. Samples were taken in a horizontal (radial) direction from the borehole wall. Samples 1:1 and 2:1 were closest to the borehole wall.

Table 3-23. Phase 3: Hydraulic conductivity, samples from KO0017G01, see Figure 3-66.

Sample	Pressure [bar]	K [m/s]
2:1 (below DSU)	20	2.2E–14
2:2	20	2.6E–14
2:3	20	1.5E–15
1:1 (between DSL and F)	20	3.5E–14
1:2	20	4.8E–13
1:3	20	4.1E–14
1:4	20	5.1E–14

Relative humidity profiles were compiled based on measurements at six different depths: 0.01; 0.02; 0.03; 0.04; 0.06 and; 0.1 m for three locations in KO0017G01 and one location KO0018G01. Profiles and date are presented in Figure 3-68 and Figure 3-69 showing depth and measured RH. Initially, there was a stabilization of the relative humidity following installation of the measurement probes (see Appendix E). Dashed lines represent measurements performed about one month later. Lifting of bentonite parcels was performed in KO0017G01, 2013-11-21 and first measurement started 2013-11-28. Lifting of bentonite parcels in KO0018G01 was carried out, 2014-03-04 and first measurement started 2014-03-13. The curves in Figure 3-68 are broken since the long boreholes were drilled first to identify desaturation depth. The second round was drilled and measured starting a week later to get additional detail close to the borehole wall.

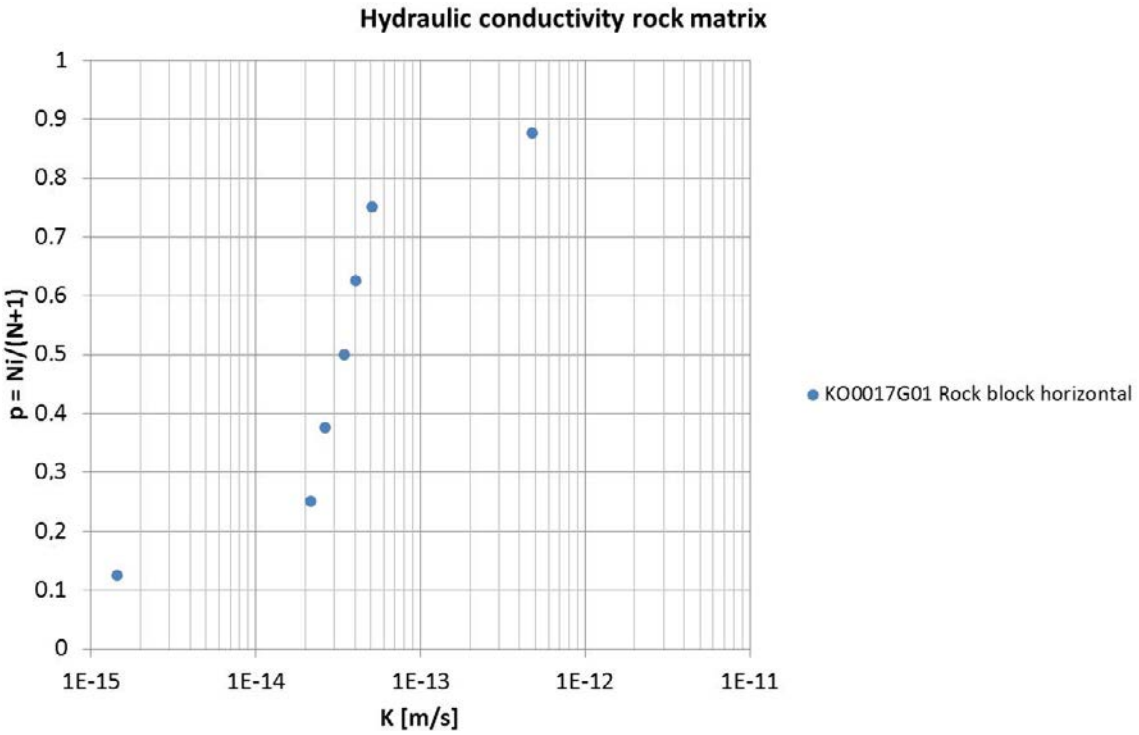

Figure 3-67. *Hydraulic conductivity Phase 3 (KO0017G01 horizontal).*

Table 3-24. Depth and measured RH for KO0017G01, long boreholes, 2013-12-02 (lifting of parcels 2013-11-21, first measurement 2013-11-28).

	Closest to fracture F			"Dry" section lower DSL			"Dry" section upper DSU		
Depth [m]	0.1	0.06	0.04	0.06	0.04	0.1	0.06	0.04	0.1
RH [%]	97.9	97	97.9	95.5	96.2	96.8	96.5	94.7	97.9

Table 3-25. Depth and measured RH for KO0017G01, short boreholes, 2013-12-11 (lifting of parcels 2013-11-21, first measurement 2013-12-06).

	Closest to fracture F			"Dry" section lower DSL			"Dry" section upper DSU		
Depth [m]	0.03	0.02	0.01	0.03	0.02	0.01	0.03	0.02	0.01
RH [%]	95	86.8	88.1	92.1	92	91.8	86.6	89.6	90.6

Table 3-26. Depth and measured RH for KO0018G01, short boreholes, 2014-03-20 (20-mar), lifting of parcels 2014-03-04, first measurement 2014-03-13.

Depth [m]	0.01	0.02	0.03	0.04	0.065	0.105
RH [%]	90.1	94.3	96	96.9	98.4	98.6

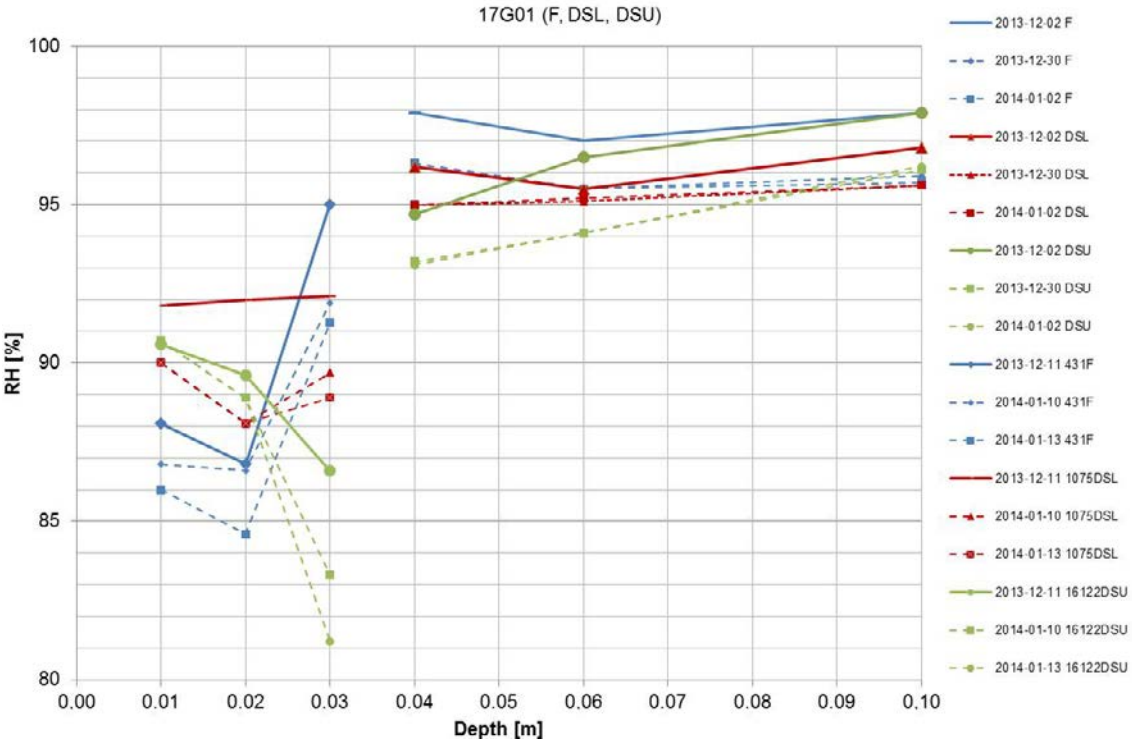

Figure 3-68. *Relative humidity profile for KO0017G01. 2013-12-02 (long boreholes) and 2013-12-11 (short boreholes) are used for the RH-profile, see also Appendix E. F (blue) was located close to the fracture, DSL (red) and DSU (green) were the lower and upper dry sections respectively. Dashed lines represent measurements performed about one month later. The curves are broken since the long boreholes were drilled first to identify desaturation depth. The second round was drilled and measured starting a week later to get additional detail close to the borehole wall.*

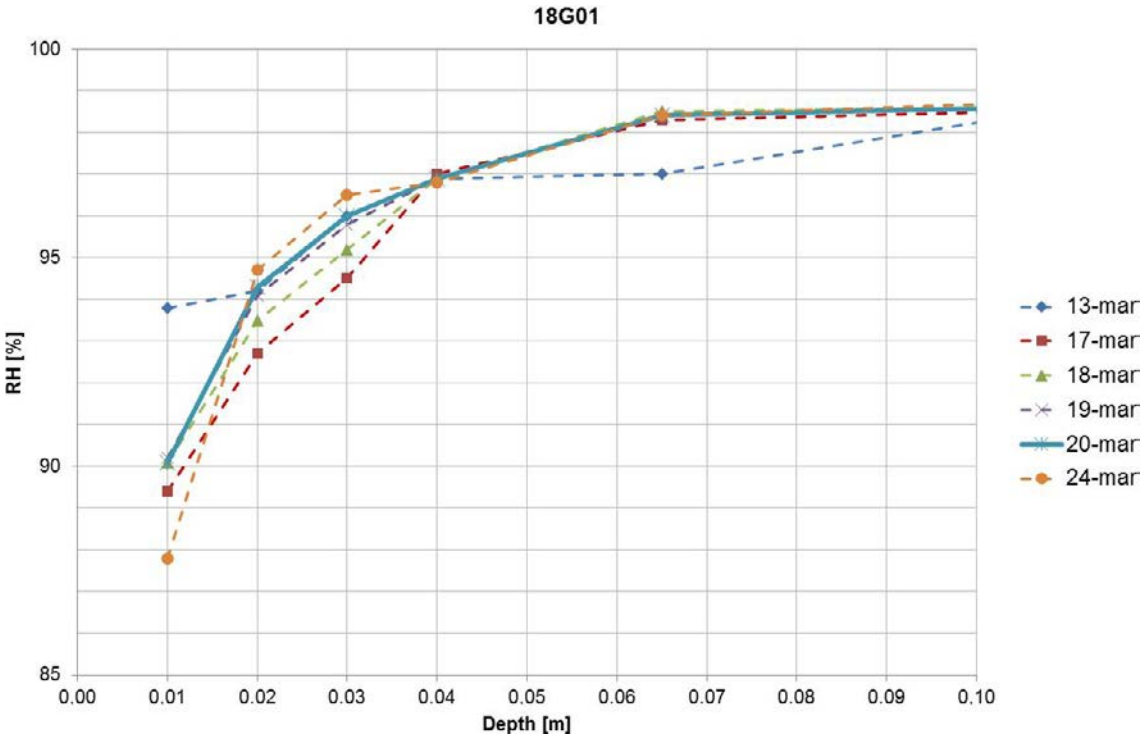

Figure 3-69. *Relative humidity profile for KO0018G01. The profiles change, initially as an effect of an assumed stabilization following installation of measurement probes. The data from 20-mar was used for the RH-profile (13-mar highest, 17-mar low, 19-mar and 20-mar similar and 24-mar lowest).*

4 Bentonite parcels

This chapter presents the work performed with the bentonite parcels investigated in the field experiment. This test was preceded by a number of water uptake tests performed in the laboratory, and these are presented briefly in Section 4.1 and in detail in Appendix F. The design and the installation of the bentonite parcels are described together with information about the manufacturing of the bentonite blocks and the instrumentation in Section 4.2. The monitoring of the sensors and the evolution of relative humidity and pressures are presented in Section 4.3. Finally, the dismantling of the parcels and the subsequent sampling and analysis is presented in Section 4.4 together with results, in particular regarding water content distributions.

Dates for the main events during the course of work with the bentonite parcels are compiled in Table 4-1.

Table 4-1. Summary of main events for installation and dismantling.

Time (date)	Event
2012-09-13	Installation of parcel in Hole 18
2012-09-14	Installation of parcel in Hole 17
2012-09-17	Emptying of 2.2 l in Hole 17
2012-10-20	Flooding of central tube of Hole 18
2012-10-29	Emptying of 1.64 l in Hole 18
2012-10-30	Emptying of 0.96 l in Hole 18
2013-11-07	Disconnection of sensors in Hole 17
2013-11-07	Start dismantling (hammer drilling) of Hole 17
2013-11-21	Lifting of parcel in Hole 17
2014-02-10	Disconnection of sensors in Hole 18
2014-02-13	Start dismantling (hammer drilling) of Hole 18
2014-03-04	Lifting of parcel in Hole 18

4.1 Water-uptake tests

The BRIE water-uptake test was a laboratory test which was performed on bentonite blocks with the same MX-80 bentonite and the same radial dimensions, density and water content as in the field experiment. The objective of the test was to provide data from an experiment with radial water-uptake, which would give a clear-cut description of the hydraulic processes in the bentonite in the BRIE experiment. The hydraulic evaluation of this test resulted in a set of parameter values, which can be used for modeling of the field experiment. A detailed description of these tests is given in Appendix F.

The bentonite blocks were installed in steel cylinders, with steel lids mounted on the top and the bottom (Figure 4-1). A plastic filter was mounted on the inside of the cylinder which facilitated a free access of water along the circumference of the block. The cylinder and the top lid were equipped with sensors for measurement of total pressure and relative humidity. Three tests were performed: i) with free access of water during ~ 200 days; ii) with free access of water during ~ 100 days; and iii) with the access of water limited to an initial filling of the outer slot and left to equilibrate during ~ 100 days.

The tests have resulted in three major sets of experimental data: i) evolutions of the cumulative water uptake; ii) evolutions of the relative humidity and stresses; and iii) profiles of degree of saturation and void ratio (Figure 4-2). The tests results were evaluated through: i) the optimization of two saturation dependent moisture diffusivity functions, which either were based on the water-uptake data (i.e. inflows) or on the water saturation data (measured after dismantling); ii) the adoption of two in-situ retention curves (van Genuchten and square law type), which were based on initial and final data from RH sensors and measured degrees of saturation; and iii) the evaluation of saturation dependent permeability functions from the diffusivity functions and retention curves.

The water-uptake test was finally modelled with Code_Bright as a purely hydraulic problem with a 1D axisymmetric geometry, see Figure 4-1. The block was described as homogenized with a single constant porosity (44 %). The initial water filling of the outer slot was taken into account by applying water saturated conditions from the start in the outer 5 mm of the bentonite. The liquid pressure at the outer boundary was kept constant at an atmospheric level throughout the calculations (203 days). Four different model cases were analyzed.

The main experimental and model results regarding cumulative water-uptake, saturation profiles and RH evolution at sensor positions are shown in Figure 4-2. These tests have independently resulted in a parameter set which is consistent with current material model for MX-80 bentonite (Åkesson et al. 2010) and the data sets provided in the Task 8 definitions.

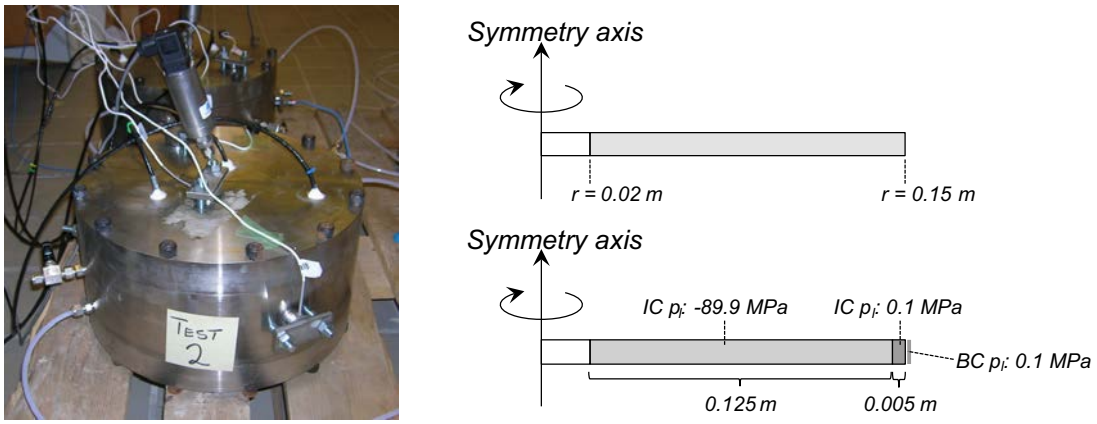

Figure 4-1. *Test cylinder (left), model geometry (top right) and model initial and boundary conditions (bottom right).*

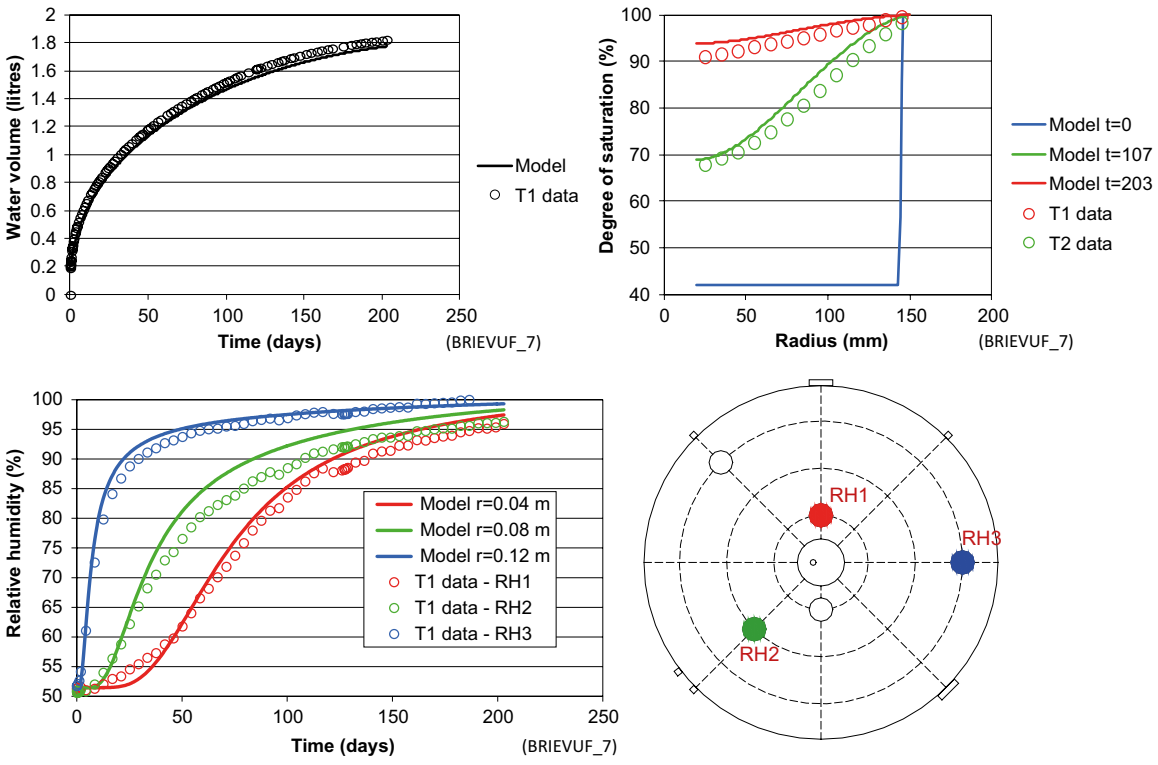

Figure 4-2. *Experimental (symbols) and model results (lines) of cumulative water uptake (upper left), radial distribution of degree of saturation (upper right), and evolution of relative humidity (lower left). Sensor position indicated (lower right).*

4.2 Installation of bentonite parcels

4.2.1 Design of bentonite parcels

The initial proposal of a joint modeling task (see Section 1.1) outlined a design of the bentonite parcel with a number of specified features: i) bentonite blocks with typical buffer density (ρ_{sat} = 2 000 kg/m^3) and a fairly low initial water content (w ~ 10 %); ii) "LOT-sized" bentonite parcels (∅33 cm and 5 m length); iii) a slot between blocks and borehole of ~ 1 mm; iv) instrumentation for measurements of total stress, pore water pressure and RH; v) the parcel should be installed with a central wire or bar in order to keep it together but without any heater; vi) and the bore hole should be sealed with a water tight plug (see also Figure 4-3).

Additional considerations later added three specifications: i) the slot should be filled with water artificially immediately after installation in order to obtain a controlled swelling/closing of the slot; ii) anchors in the floor should be avoided; and iii) the length of the parcels should be limited to 3 m.

The final design of the parcel generally addressed all these specifications but with some minor modifications (Figure 4-4): i) the diameters of the blocks and boreholes were decided to be 298 and 300 mm, respectively, thereby implying a slot width of 1 mm; ii) cables from instruments were to be installed through a central tube (∅40 mm); iii) the bentonite blocks were to be threaded along this central tube; iv) the bottom block would rest on a bottom plate, which was welded to the central tube; v) the bottom plate, in turn, would be placed on top of a sand filling (macadam 2–4 mm) in the bottom of the bore hole; vi) a top plate would be placed on top of the blocks; and vii) a retaining pillar would be placed between the top plate and a bolted plate in the roof.

The sand-filling was motivated by: i) to provide a means to fill the outer slot with water; ii) to level the uneven bottom of the bore holes; and iii) to adjust the level of the bentonite parcel above. The first motive would be facilitated with a thin tube (inner diameter 4 mm), located within the central tube, which would be attached to a hole through the centre of the bottom plate.

Three quite novel features were thus used in the design: the 1 mm slot, the central tube for installing cables, and a retaining pillar.

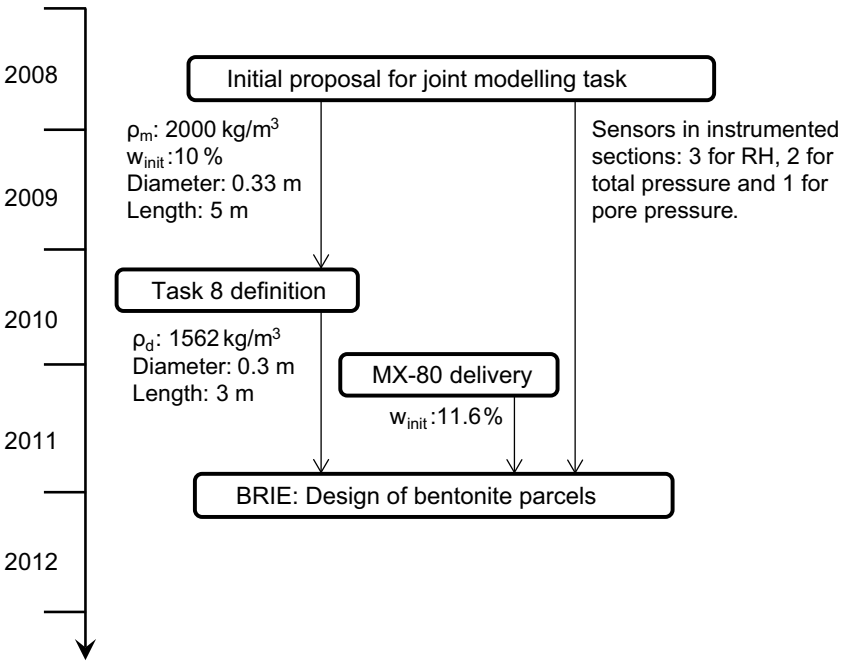

Figure 4-3. *Schematic illustration of the input to the design of the bentonite parcels regarding initial conditions, dimensions and instrumentation.*

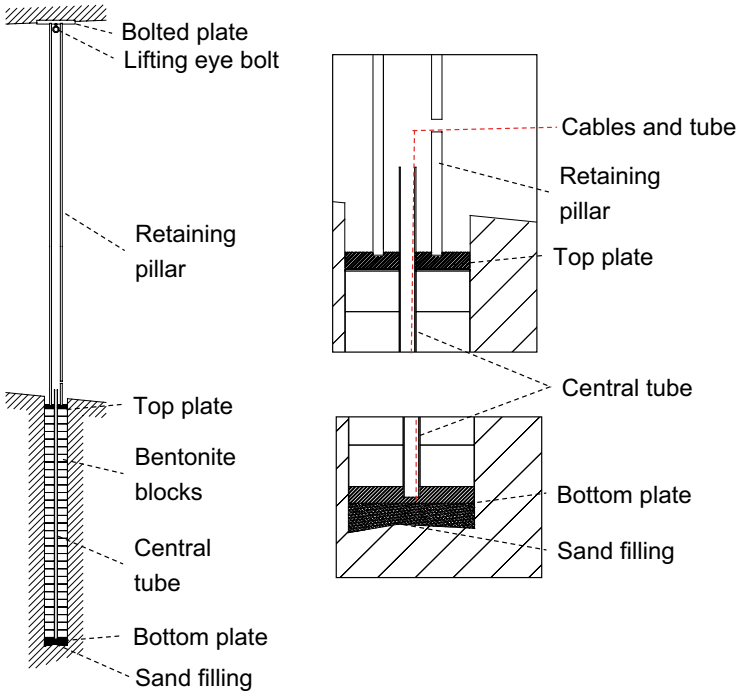

Figure 4-4. *Principal design of bentonite parcels.*

4.2.2 Test of boreholes

For testing the ∅300 mm boreholes, and to ensure that the bentonite parcels could be installed, a dummy was designed and manufactured (Figure 4-5). This consisted of a 3 m long central tube with four attached discs (∅298 mm). The bore holes were tested (with a positive outcome) at two different occasions, on the 7th of May 2012, i.e. four months before the installation, and also 2–3 days before the installation.

Figure 4-5. *Test of bore holes with dummy.*

4.2.3 Bentonite blocks

Within the Task 8 description, a bentonite filling was prescribed with the following definitions: a diameter of 300 mm; a dry density of 1 562 kg/m^3, and an initial water content of 10 % (Figure 4-3). A 1 mm slot was strived for in order to facilitate the installation of pre-compacted blocks in the boreholes. The block would therefore have an initial diameter of 298 mm, and an initial dry density slightly higher than the prescribed one. Knowledge about the required block compaction was acquired during the manufacturing of the bentonite blocks for the water-uptake tests (Section 4.1). At that stage it was also noticed that the assigned bentonite had a water content of slightly below 12 %. The target dry density and block height could be obtained through filling the specially designed form (Figure 4-6) with 13.08 kg of bentonite, after which this was compacted to a piston position corresponding to a block height of 100 mm. This procedure led to a bulk density of approximately 1 775 kg/m^3.

Manufacturing of blocks

The bentonite blocks used for the parcels were made of MX-80, and were taken from the same big bag as the material used for the water uptake tests. Representative samples (eight) were taken at the same time as the material was weighed for the block compactions, and were thereafter analyzed for water content. These showed that the water content was 11.6 ± 0.2 % (mean ± SD).

A central hole was drilled though each block in order to be able to thread these along the central tube. This was performed in a drill press with an adjustable drill bit. A template was prepared in order to achieve high precision. The diameter of the holes was 40.0–40.5 mm.

The blocks had a slightly conical shape after the compaction and had an average diameter of approximately 307 mm. The blocks were machined with a lathe to a cylindrical shape with a diameter of 298 mm.

4.2.4 Instrumentation

Each bentonite parcel was instrumented at two sections: one “wet” section dominated by fracture flow, and one “dry” section potentially dominated by matrix flow. These sections denote specified levels, each with two instrumented blocks – one upper block immediately above these levels, and one lower block beneath.

A general scheme with sensor positions internally specified for each section was adopted. The upper blocks contained three RH-sensors, whereas the lower blocks contained two total pressure sensors and one pore pressure sensor (see Figure 4-7, Figure 4-8 and Table 4-2). The pore pressure sensor was located in such a way that the measuring point was positioned at the interface towards the borehole wall. Following types of instruments were used in the instrumented blocks: RH-sensors (Aitemin SHT75 V3); total pressure sensors (Geokon 4800 – max 10 MPa); and pore pressure sensors (Geokon 4500Ti – max 2 MPa).

Figure 4-6. *Form for compaction of bentonite blocks.*

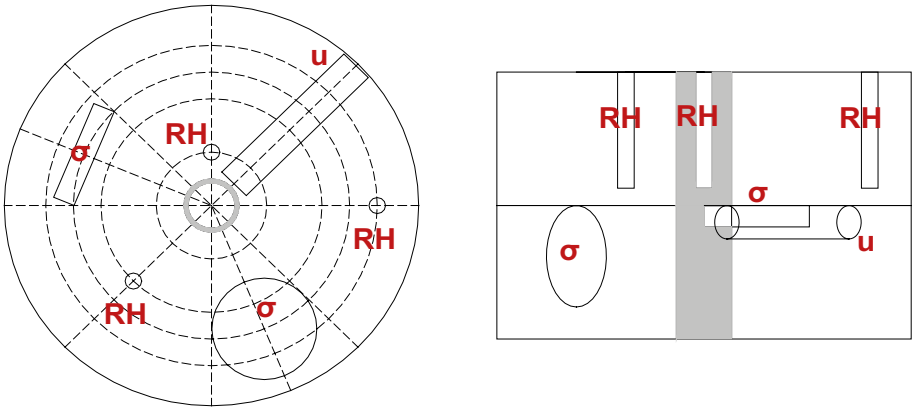

Figure 4-7. *Outline of sensor positions in instrumented blocks. RH: relative humidity, σ: total pressure, and u: pore pressure.*

Figure 4-8. *Instrumentation of blocks; left: block with pressures sensors; right: block with RH sensors.*

These sections were oriented in the plane so that the pore pressure sensor came as close as possible to the fracture of interest in each borehole. For Hole 17, the level at 2.6 m depth was defined as the wet section (considering that the main inflow from the fracture at 2.9 m was found at the uppermost part of this), whereas the level at 2.3 m was defined as the dry section (Figure 4-9). Both instrumented blocks were oriented with their pore pressure sensors opposite the dip direction in order to minimize the distance between the fracture and theses sensors. For Hole 18, the level at 2.3 m depth was defined as the wet section (basically the mid section of the main fraction in this hole) whereas the level at 2.7 m was defined as the dry section. The pore pressure sensor in the dry section was oriented in line with the dip direction, whereas the sensor in the wet section was oriented perpendicular (right hand) to the dip direction.

All cabling from the sensors was made through the central tubes. After the installation, the tubes leading to the sand fillings at the bottom of the bore holes were connected to pore pressure sensors (Druck) located in the TASO tunnel.

Table 4-2. Sensor positions in instrumented blocks.

Sensor	Radius (mm)	Orientation (°)*	Level (mm)**
RH (inner)	40	315	13
RH (mid)	80	180	13
RH (outer)	120	45	13
Total pressure (axial)	80	112.5	−8
Total pressure (radial)	100	247.5	−38
Pore pressure	150	0	−12

* Orientation relative pore pressure sensor.

** Level relative joint between blocks.

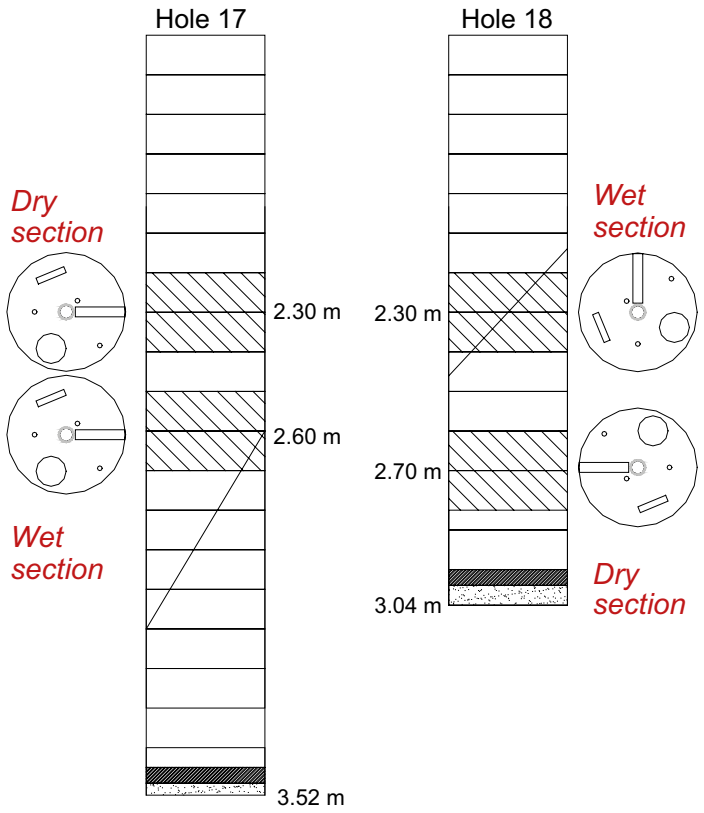

Figure 4-9. *Orientation of instruments in relation to major fractures. Marked fractures illustrate the dip and the depth with the information available prior to the installation. See Section 5.3.1 for a final evaluation of fracture positions.*

4.2.5 Installation of parcels

The blocks which were devoted for instruments were machined in order to make holes and slots for the different sensors. During this process it was found necessary to modify the radial position of the axially oriented total pressure sensors from a radius of 100 to 80 mm (center of sensor).

Each block was thereafter checked through weighing before they were threaded on the parcels. Those blocks which were not instrumented should have a mass of 12.16 kg. The mass of most blocks were found to be 12.15 or 12.10 kg according to these measurements (a few cases showed 12.20 or 12.25 kg). These measurements showed that the blocks which were located close to the instrumented sections could be considered to have the sought after density.

The central tube was welded to the bottom plate and was thereafter mounted in upright vertical position. The bentonite blocks were threaded, one by one, on the central tube. Instruments could be installed in the holes and slots of the machined bentonite blocks after the cables had been inserted through drilled holes in the central tube and through the central tube itself.

The total lengths of the two parcels were also measured. A total number of 28.5 blocks (one of the blocks was cut in half) were used for the parcel in Hole 18 and length of the blocks was measured to 2 870 mm. For the 33.5 blocks used for Hole 17 the corresponding length was 3 378 mm. The average effective block height was thus 100.7 and 100.8 mm, respectively. The heights of the different components are summarized in Table 4-3.

Two modifications of the design were made prior to the installation:

- The rubber mats just below the top-plates were omitted, since they were regarded as unnecessary and that they could potentially complicate the installation.
- The top-plates were welded to the central tubes, which meant that the packages could be lifted in the top plates.

The orientation of the main fracture of interest of each test hole (the dip direction) was marked with a yellow spot close to each test hole by the geo-hydrologists prior to the installation. The aligned direction of each parcel was marked with a red line along the entire height of the parcel. The sinking of the parcels into the test holes could thus be guided with these lines and spots (see Figure 4-10). The installation of the two parcels took place at the following times: for Hole 18: 2012-09-13 17:12; and for Hole 17: 2012-09-14 10:19. The retaining pillars were put in place immediately after these two events.

The installation operation went generally quite well:

- The bentonite-packages were lowered into the holes with gravity alone, and with no additional force.
- The instruments were located as planned.
- The insertion of cables through the central tube could be performed as planned.
- The installation of the retaining pillars (Figure 4-11) went very smooth and rapidly.
- The final lengths of the parcels were well adapted to the lengths of the holes.

Table 4-3. Heights of different component in bentonite parcels

Component	Height (mm)		Comment
	Hole 18	Hole 17	
Top plate	50	50	∅298 mm, welded to central tube (∅40 mm)
Bentonite	2870	3378	Initial outer diameter: 298 mm; inner diameter: 40 mm
Bottom plate	40	40	∅298 mm, welded to central tube (∅40 mm)
Sand filling	50	30	Macadam 2–4 mm

It was nevertheless noted after the installation that the holes through the central tube, through which the sensor cables were inserted, could have been sealed, e.g. with silicon. This may have lead to an avoidance of the "flooding event" observed in both parcels (see below).

Another drawback was that the upper end of the tube connected to the sand-filling in Hole 18 could have been protected during the threading of the bentonite blocks along the central tube. This appears to have lead to the sealing of the tube connected to the sand-filling, which it turn made it impossible to water-fill the slot through the sand-filling (see below).

Figure 4-10. *Installation of bentonite parcel in Hole 17.*

Figure 4-11. Pillars between bentonite parcels and roof.

Water filling of outer slot

3.1 liter of formation water was poured into the outer slot of Hole 18 from above (i.e. at the slot between the bore hole and the top-plate) at 17:45 (2012-09-13). The outer slot appeared to be water-filled since water started to accumulate at the top-plate. The outer slot was used for this operation since the tube to the sand filling was found to be sealed.

6.85 liter of formation water was poured through the sand filling of Hole 17 during 10:21 to 10:30 (2012-09-14). 1.05 liter was poured into the outer slot of from above immediately afterwards. Later on, it was noticed that water has entered the central tube of Hole 17, and this tube was therefore emptied of 2.2 liters on 2012-09-17 at approximately 10 am.

The total volumes that have been poured into the systems, can be compared with different estimated (easily accessible) pore volumes, i.e. the outer slot, the sand filling and the central tube (found in hole 17 only), see Table 4-4. For Hole 17 there is a minor excess of water which could be accounted for by slots and cavities between the bentonite blocks. For Hole 18, the difference between the added volume and the estimated pore volume can be explained by the inflowing water from upper parts of the hole during the time period when the hole was open.

Table 4-4. Simple water balance for the filling of the outer-slot.

	Hole 17	Hole 18
Total added water volume	7.9 liter	3.1 liter
Outer slot	3.5 m á 0.1 liter/dm	3.1 m á 0.1 liter/dm
	3.5 liter	3.1 liter
Sand-filling with estimated porosity of 40 %	40 % of 4 liter	40 % of 5 liter
	1.6 liter	2 liter
Water in central tube	2.2 liter	–
Total	7.3 liter	5.1 liter
Excess	0.6 liter	−2 liter
	Possibly due to slots and cavities between blocks.	Due to inflowing water from the upper parts while the hole was open.

Installed dry density and coordinates

The average value of the measured water contents (11.6 %) is regarded to be a representative value which should be used within Task 8. A homogenized dry density was calculated from the bulk density value of 1 775 kg/m^3, a water content of 11.6 %, and a radial swelling from 149 to 150 mm in radius. This implies a dry density of 1 569 kg/m^3 and a void ratio of 0.772. An additional axial swelling from 100.0 to 100.8 mm in height would imply a dry density of 1 557 kg/m^3 and a void ratio of 0.785. These values are close to those that were previously used in Task 8 (dry density of 1 562 kg/m^3 and a void ratio of 0.78). It was therefore judged to be relevant to continue to use these values for the task.

The z-coordinate of the top plates were measured by the Äspö surveyor. From these values, a detailed drawing, with specified z-coordinates, could be prepared (Figure 4-12).

The dip directions of the main fractures of interest were quantified from photographs depicting the test hole in question and the geo-hydrologists markings, as well as one nearby investigation borehole (Figure 4-13). The angle between the marking and the investigation borehole were evaluated graphically for each test hole. These angles were subsequently used together with the coordinates for the test holes and the investigation borehole in order to evaluate the dip directions.

The coordinate of all sensors are shown in Table 4-5. The positions of the RH-sensors and the pore pressure sensors are illustrated in Figure 4-14.

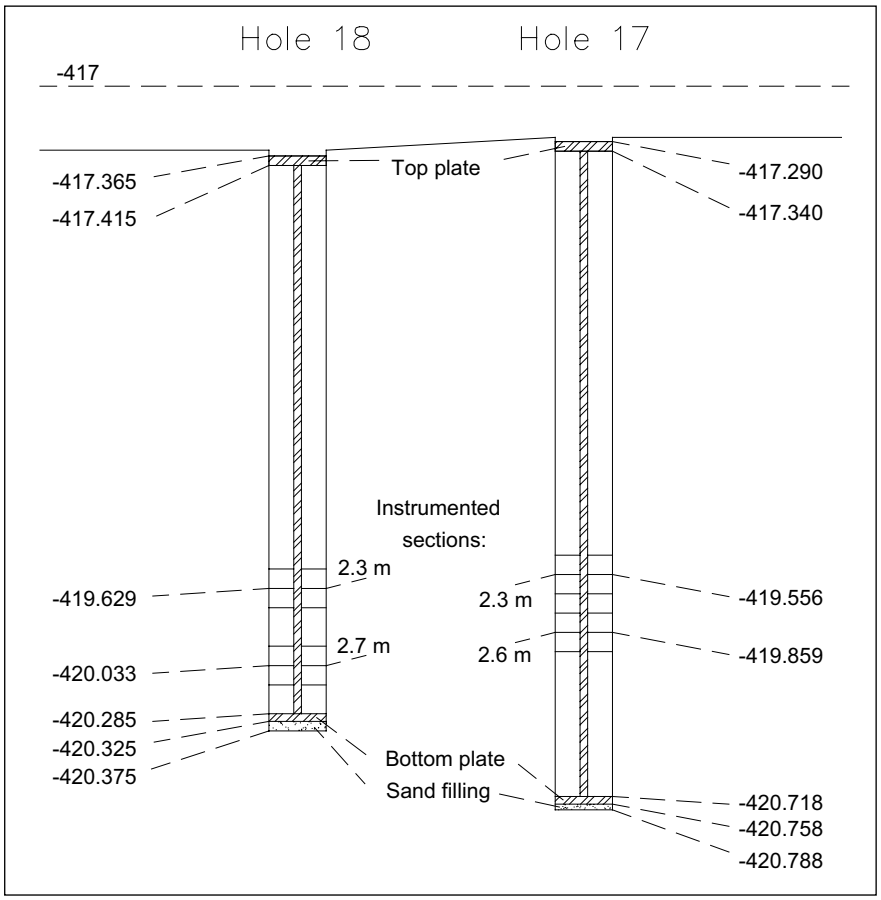

Figure 4-12. *Outline and final dimensions of bentonite parcels.*

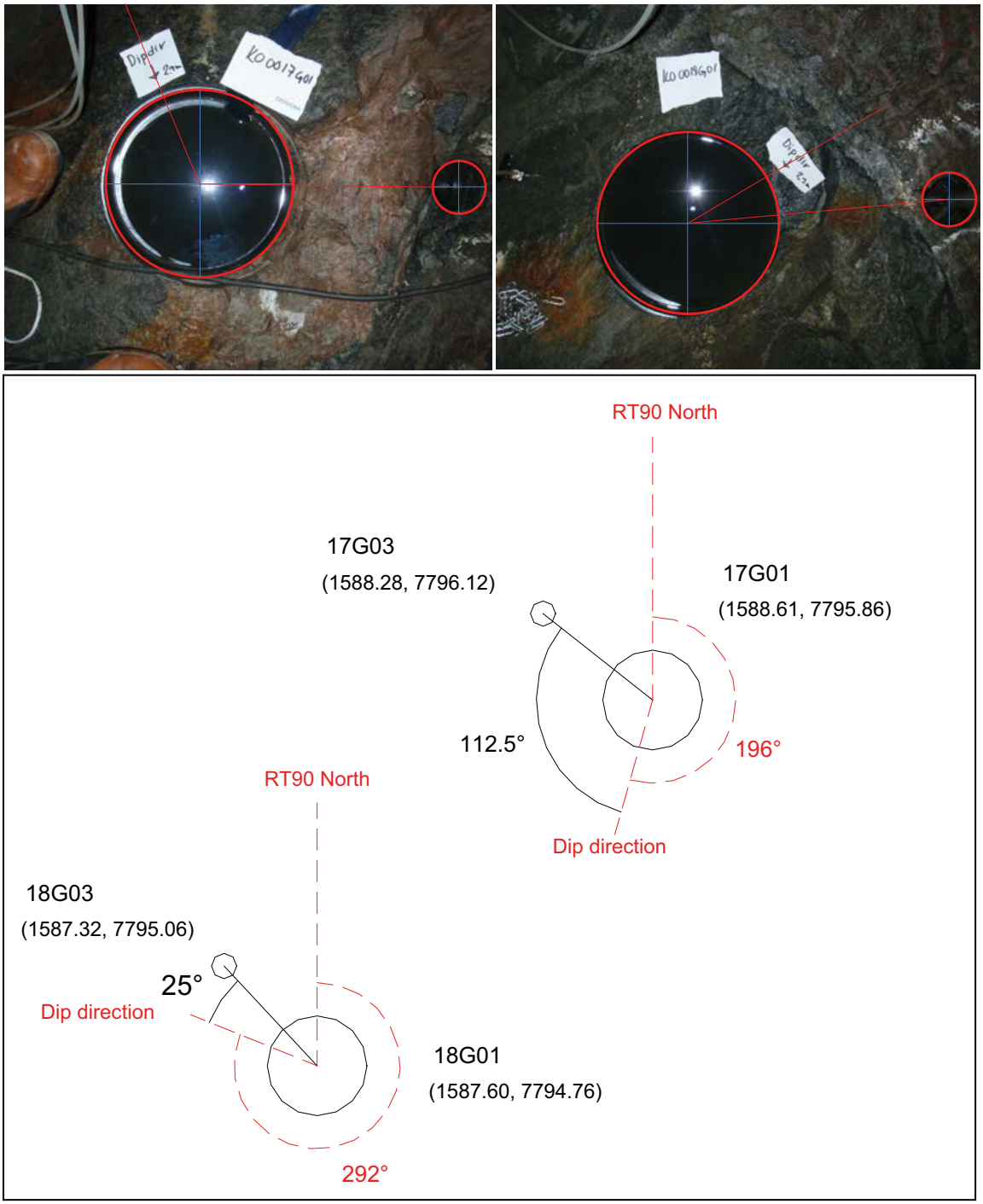

Figure 4-13. *Quantification of dip directions for main fractures of interest in Hole 17 and 18. Coordinates correspond to RT90 with the first three figures omitted.*

Table 4-5. Sensor location of installed instruments (RT90).

Sensor type	Sensor	x	Y	z	Hole	Section	Comment
Total pressure	PBR0001	1551588.67	6367795.81	−419.867	17	2.6	Axial
	PBR0002	1551588.51	6367795.85	−419.897	17	2.6	Radial
	PBR0003	1551588.67	6367795.81	−419.564	17	2.3	Axial
	PBR0004	1551588.51	6367795.85	−419.594	17	2.3	Radial
	PBR0005	1551587.66	6367794.70	−419.637	18	2.3	Axial
	PBR0006	1551587.50	6367794.76	−419.667	18	2.3	Radial
	PBR0007	1551587.66	6367794.82	−420.041	18	2.7	Axial
	PBR0008	1551587.60	6367794.66	−420.071	18	2.7	Radial
Pore pressure	UBR0001	1551588.65	6367796.00	−419.871	17	2.6	
	UBR0002	1551588.65	6367796.00	−419.568	17	2.3	
	UBR0003	1551587.66	6367794.90	−419.641	18	2.3	
	UBR0004	1551587.46	6367794.82	−420.045	18	2.7	
	UBR0005	1551588.61	6367795.86	−420.758	17	3.5	In sand
	UBR0006	1551587.60	6367794.76	−420.325	18	3.1	In sand
Relative humidity	WBR0001	1551588.59	6367795.89	−419.846	17	2.6	
	WBR0002	1551588.59	6367795.78	−419.846	17	2.6	
	WBR0003	1551588.71	6367795.92	−419.846	17	2.6	
	WBR0004	1551588.59	6367795.89	−419.543	17	2.3	
	WBR0005	1551588.59	6367795.78	−419.543	17	2.3	
	WBR0006	1551588.71	6367795.92	−419.543	17	2.3	
	WBR0007	1551587.58	6367794.80	−419.616	18	2.3	
	WBR0008	1551587.57	6367794.69	−419.616	18	2.3	
	WBR0009	1551587.71	6367794.81	−419.616	18	2.3	
	WBR0010	1551587.56	6367794.74	−420.020	18	2.7	
	WBR0011	1551587.67	6367794.73	−420.020	18	2.7	
	WBR0012	1551587.55	6367794.87	−420.020	18	2.7	

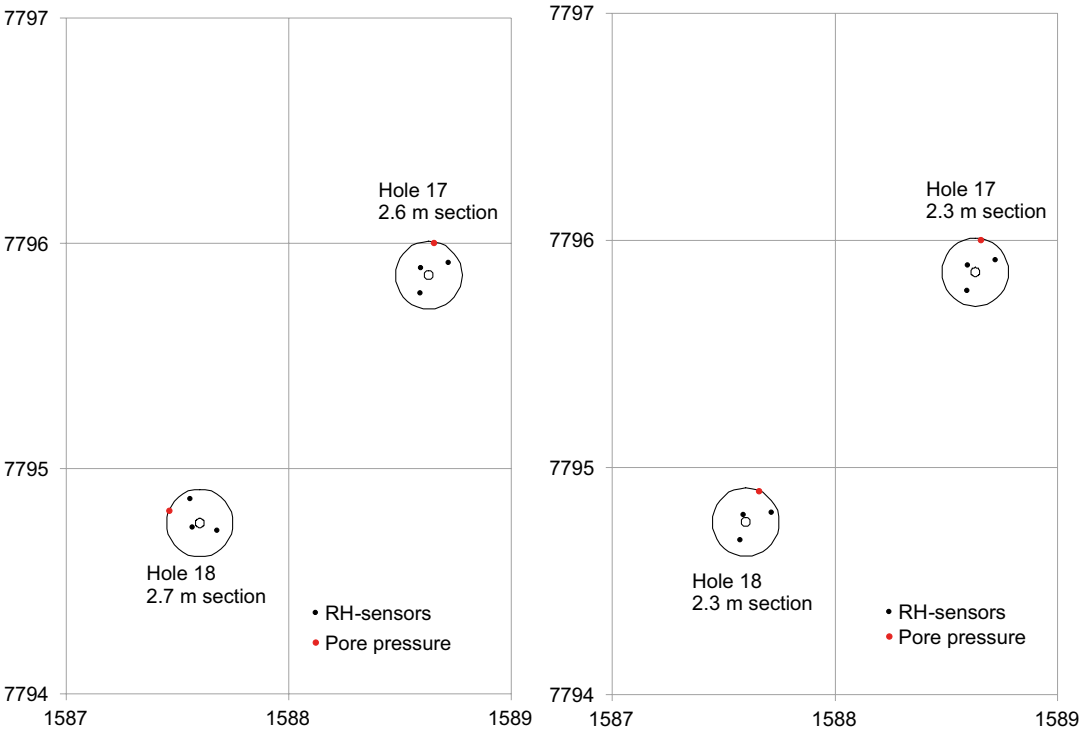

Figure 4-14. *Illustration of sensor positions in borehole KO0017G01 and KO0018G01. Coordinates correspond to RT90 with the first three figures omitted.*

4.3 Monitoring of sensors in parcels

The evolution of RH at the sensor positions is shown in Figure 4-15. Data from Hole 17 (upper graph) showed a clear response from sensors in the wet section (W1–W3), whereas the corresponding response in the dry section (W4–W6) was very slow. Data from Hole 18 (lower graph) indicated less differences between the wet (W7–W9) and dry (W10–W12) sections, although the hydration of the wet section appeared to be slightly more rapid than the dry one.

The evolution of the RH in Hole 17 as well as in Hole 18 has displayed disturbances caused by flooding of the central tubes. In Hole 17, this occurred immediately after the installation and the filling of the outer slot (see Section 4.2.5). In Hole 18, this occurred around day 50: the RH levels displayed very small changes before day 37, although a slight increase could be noted at sensors W9 and W12, which both were located in the outermost position. After day 37, however several sensors displayed rapidly increasing trends. This was probably caused by a high water level on the "floor" in the tunnel, which led to the water filling the central tube. The problem was noticed on day 46, after which the floor, as well as the central tube, was cleared from water. From the central tube 1.64 l was emptied, and on the subsequent day another 0.96 l was emptied. The major increasing trends of W10 and W8 were reversed after this.

All sensors showed approximately 59 % immediately after the installation. After the filling of the outer slots, and after the flooding events, no sensor showed values below a level of 64 %. This is illustrated by the sensors of the dry section of Hole 17 (W4–W6), and to some extent also by the sensors in the driest locations in Hole 18.

The temperature at the location of the RH-sensors was found to be 14–16 °C during the test period.

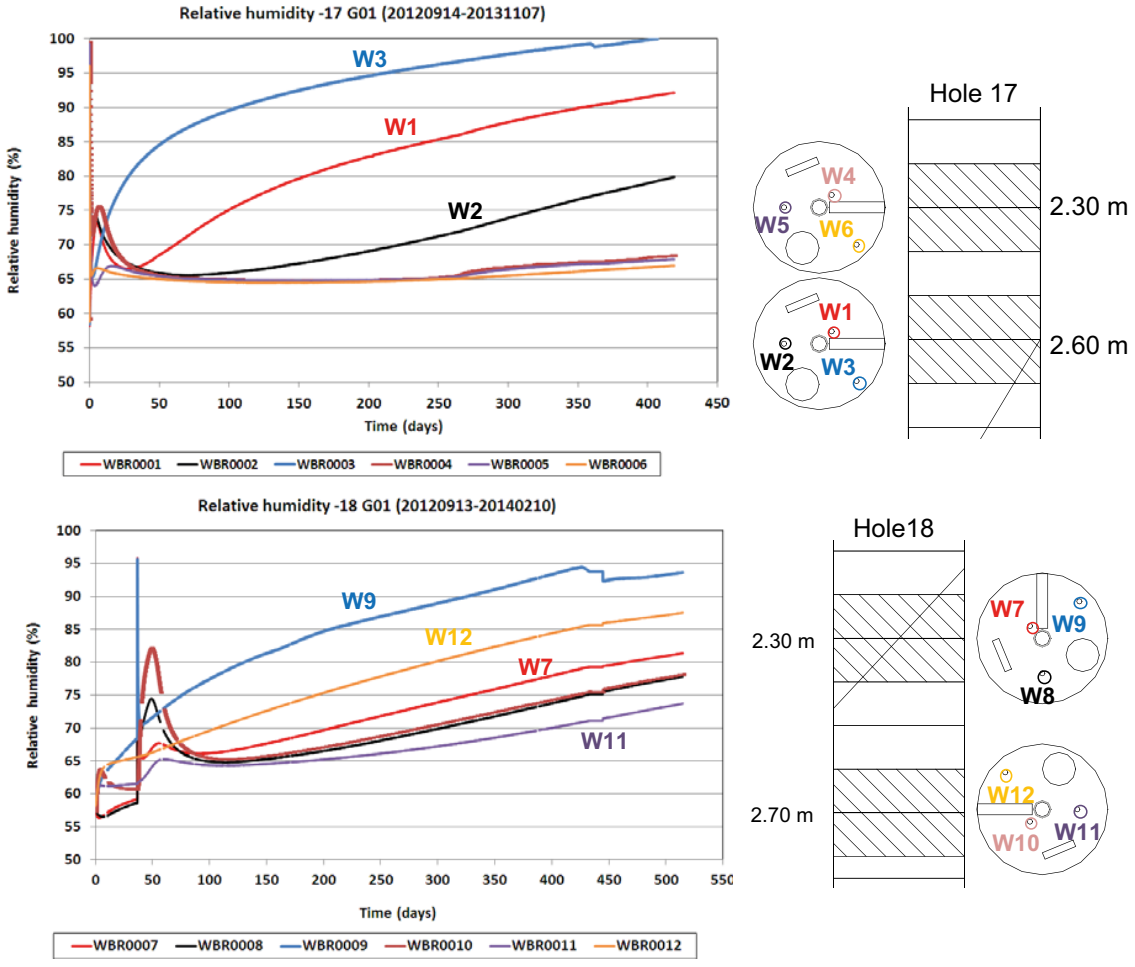

Figure 4-15. *Evolution of RH at sensor positions. The rapid increase immediately after the installation in Hole 17, and after day 37 in Hole 18, was caused by flooding of the central tubes.*

The evolution of total pressures and pore pressures at the sensor positions in the bentonite is shown in Figure 4-16. (Total pressure is the total stress in the direction of the sensor, whereas the pore pressure is exerted by the fluid in the soil. Both quantities are defined as relative to atmospheric pressure.) All axially oriented total pressure sensors have shown significant pressure levels, at least 2 MPa before the end of the test. The highest value was exhibited by the sensor in the wet section of Hole 17 (P1), from which the signal tended to level out at 4.5 MPa at the end.

Only one radially oriented total pressure sensor, in the wet section of Hole 17 (P2) have shown significant levels: slightly more than 2 MPa at the end of the test. This signal also tended to level out at the end. All other radially oriented sensors have only displayed a minor increase with a few bars pressure.

All pore pressure sensors in the bentonite have shown zero pressure levels. Pore pressures in sand fillings were measured through the hydration tubes for filling the slot, with Druck sensors up in the tunnel. The pore pressure in Hole 17 increased rapidly and has shown approximately 13 bar during the test period, whereas the sensor for Hole 18 displayed zero pressure. This may have been an effect of the sealing of the hydration tube with bentonite. An additional explanation could be that the inflow into the sand filling from the rock was lower than the water uptake capacity of the bentonite. This appears to be supported by the dismantling data (see Section 4.4.4).

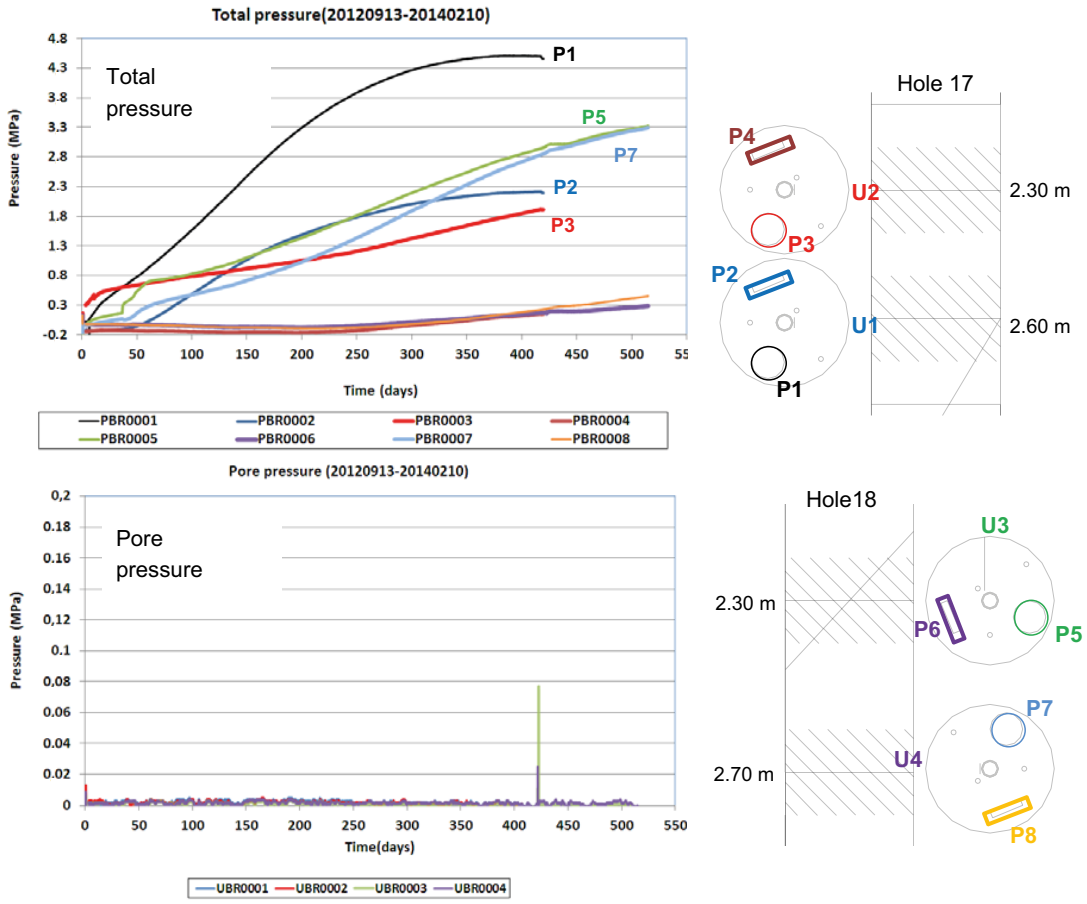

Figure 4-16. *Evolution of total pressure (upper graph) and pore pressure (lower graph) at sensor positions.*

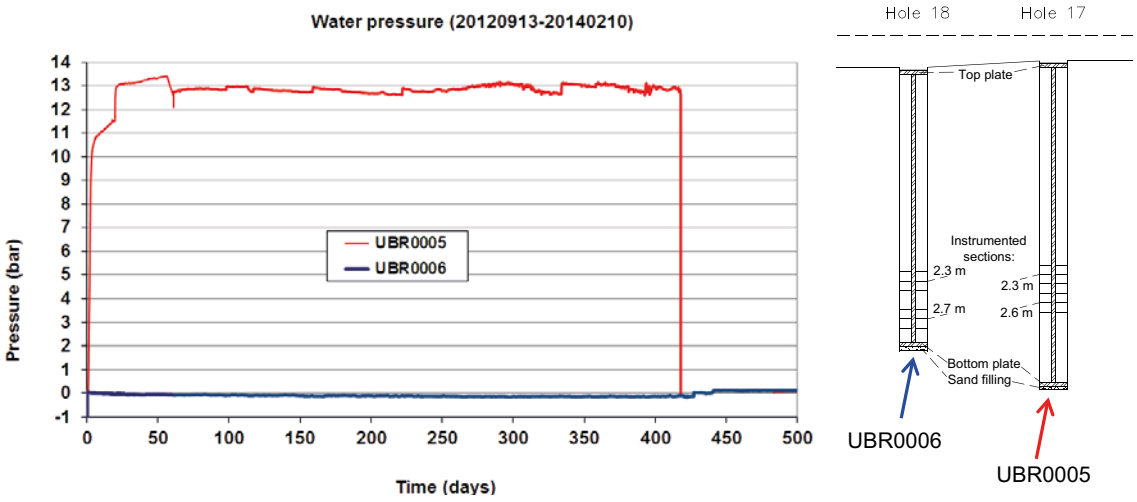

Figure 4-17. *Evolution of pore pressure in sand fillings.*

4.4 Dismantling and analyses of bentonite parcels

4.4.1 Dismantling of parcels

The intended general method for dismantling of the bentonite parcel is schematically illustrated in Figure 4-18. The first step would be to make a circular rock pillar through stitch drilling with hammer-drilling (89 mm). The planned diameter of the pillar was approximately 0.7 m, and the pillar would thus "contain" the bentonite parcel. Two ∅250 mm holes would subsequently be drilled through core drilling. These holes would enable the cutting of the rock pillar through wire sawing. Under the condition that the rock pillar was fairly intact, then it would be possible to lift it through enclosing it with wires. The final step of the plan would then be to remove the rock cover from the bentonite, before the partitioning and the sampling of the bentonite could begin.

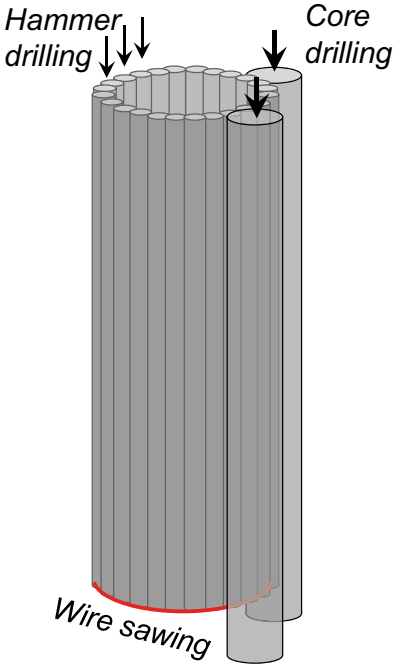

Figure 4-18. *Schematic principle of dismantling.*

The actual realization of the dismantling of Hole 17 was quite different than the planned procedure (see photos in Figure 4-19). The hammer drilling could be performed as intended. Still, after the completion it was noticed that the upper part (approximately 1 m) of the rock pillar was shredded (including the bentonite), and all these pieces had to be removed before the work could proceed. Moreover, the drifting tendency associated with this drilling technique at large depth was also noticed, and this mean that quite a lot of effort had to be spend on removing remaining contact points between the pillar and the surrounding rock, either through core drilling or through manual force. At this stage, the upper part of the central tube was cut from the lower part of the parcel (without damage to the sensor wires). This piece also contained approximately three bentonite blocks and the top-plate.

Figure 4-19. *Pictures for dismanling of parcel in Hole 17. On-going stich-drilling (upper left), stich-drilling compleated (upper center), core-drilling of ∅250 mm holes (upper right), wire-sawing completed (middle left), lifting of rock piece (middle centre), remaining bentonite parcel and rock blocks (middle right), pulling of parcel (bottom left), remaining rock blocks (bottom right).*

Figure 4-20. *Pictures for dismanling of parcel in Hole 18. Wire-sawing completed (upper left), pulling of parcel (right), remaining rock blocks (bottom left)*

After these drawbacks, the core drilling of the ∅250 mm holes could begin, and was performed as planned. The wire sawing was subsequently performed and this also proceeded as planned until only a minor part of the cutting area remained. At this point some significant movement occurred, among which the most noticeable was the fallout of protruding rock pieces in the slot at a depth of approximately 2 meters. Another implication was that the sawing wire was stuck.

After this an attempt was made to lift the rock pillar, but due to the protruding pieces it was not possible to enclose it with wires beneath that depth. This meant that a rock piece from a depth of approximately 1–2 m could be lifted. This rock piece contained several bentonite blocks, and since the remaining part of the parcel was left in the hole this meant that the central tube had to be slid out through the bentonite blocks in the rock piece, when this was lifted. This could be made quite easily, probably due to the apparently dry state of these blocks.

When this major rock piece was gone it was noticed that the rock pillar beneath it was fragmented by several fractures, and several rock pieces were therefore lifted out of the hole (among which two were sent immediately to Chalmers). It was also noticed that the rock piece directly below the

top part of the main fracture of interest in Hole 17 was easily accessible (the piece above was sent to Chalmers). Three fragmented bentonite blocks were also lifted out, among which the two lower blocks could be safely documented and packaged in plastic bags.

At this stage it was considered safe to lift the bentonite parcel directly by pulling the central tube. The main part of interest of the parcel, including 15 bentonite blocks, could in this way be safely recovered by packaging the entire parcel in a plastic bag and by covering it with wooden planks.

The dismantling of Hole 18 was also quite different than the planned procedure. As with Hole 17, the hammer drilling could be performed as intended, but with the resulting splitting of the upper part of the rock pillar (approximately 0.6 m in Hole 18). The bentonite was intact in this case though. In addition, a significant amount of finely shredded rock was accumulated in the slot, but this could be removed after the core drilling of the ∅250 mm holes. The wire sawing of the rock pillar could be performed as planned.

After the completion of the wire sawing it was noted that the entire pillar was tilted with a few centimeters at the top level. It was also found that large rock pieces had loosened from the pillar, and that some of these were extended down to a depth of 2 m below the floor level. It was therefore concluded that it would be difficult and possibly hazardous to try to lift the rock pillar as planned. Instead, an alternative procedure was implemented by which the bentonite parcel was pulled directly from the test hole.

Two safety measures were made before the lifting: i) a new welding was made between the top plate and the central tube; and ii) a scale was attached to the top plate in order to measure the load on the parcel during the lifting. The maximum load was found to be approximately 700 kg after which the parcel was successfully pulled from the test hole. The entire parcel was finally packaged in a plastic bag and covered with wooden planks.

4.4.2 Documentation and partitioning of parcels

After the bentonite parcel from Hole 17 was uncovered from the plastic bag and wooden planks it was documented through photography (together with a carpenter's ruler) and marked with filter pen: a red line was drawn along the 0°-line indicated by the position of two pore pressure sensors, a green line marking the opposite direction (180°), and also the block number (counting from below). The bentonite blocks were then removed, photographed and packaged one by one. The upper blocks could easily be lifted off since many of them were not completely intact, whereas the remaining blocks had to be "threaded off" the central tube. The lowermost blocks, actually had to be partitioned from each other by use of a sabre saw (probably due to a high water content). Block 1 and 2 were left as one piece in the packaging. Unfortunately, the parcel was uncovered in a horizontal position which implied that the dry blocks at the top (Block 10–15) began to fracture and therefore had to be removed before the parcel could be raised in a vertical position.

The parcel from Hole 18 was uncovered after it has been mounted in an upright vertical position. The bentonite blocks were then marked with: i) a black line, intersecting the pore pressure sensor in Block 7 indicating the 0°-direction; ii) a red line, indicating the dip direction corresponding to the 270°-direction; iii) a black line, indicating the 180°-direction; and iv) the block numbers. The parcel was subsequently documented through photography (see Figure 4-21). The total length of the bentonite blocks was found to be 2913 mm, i.e. 43 mm longer than at the installation. It was subsequently concluded that the welding made during the installation was broken. The top plate was finally separated from the central tube. Each bentonite block was subsequently removed from the central tube, photographed, weighed and packaged one by one. Block 1 and 2 were left as one piece in the packaging. The measured masses of the blocks were used together with the initial block masses to estimate the total water content of each block (see Figure 4-22)

The final objective of the partitioning was to salvage the sensors and to verify their locations. This could be performed in very much the same way (but in the opposite direction) as during the installation. All sensors (from Hole 17 and 18) could be safely removed and verified for location.

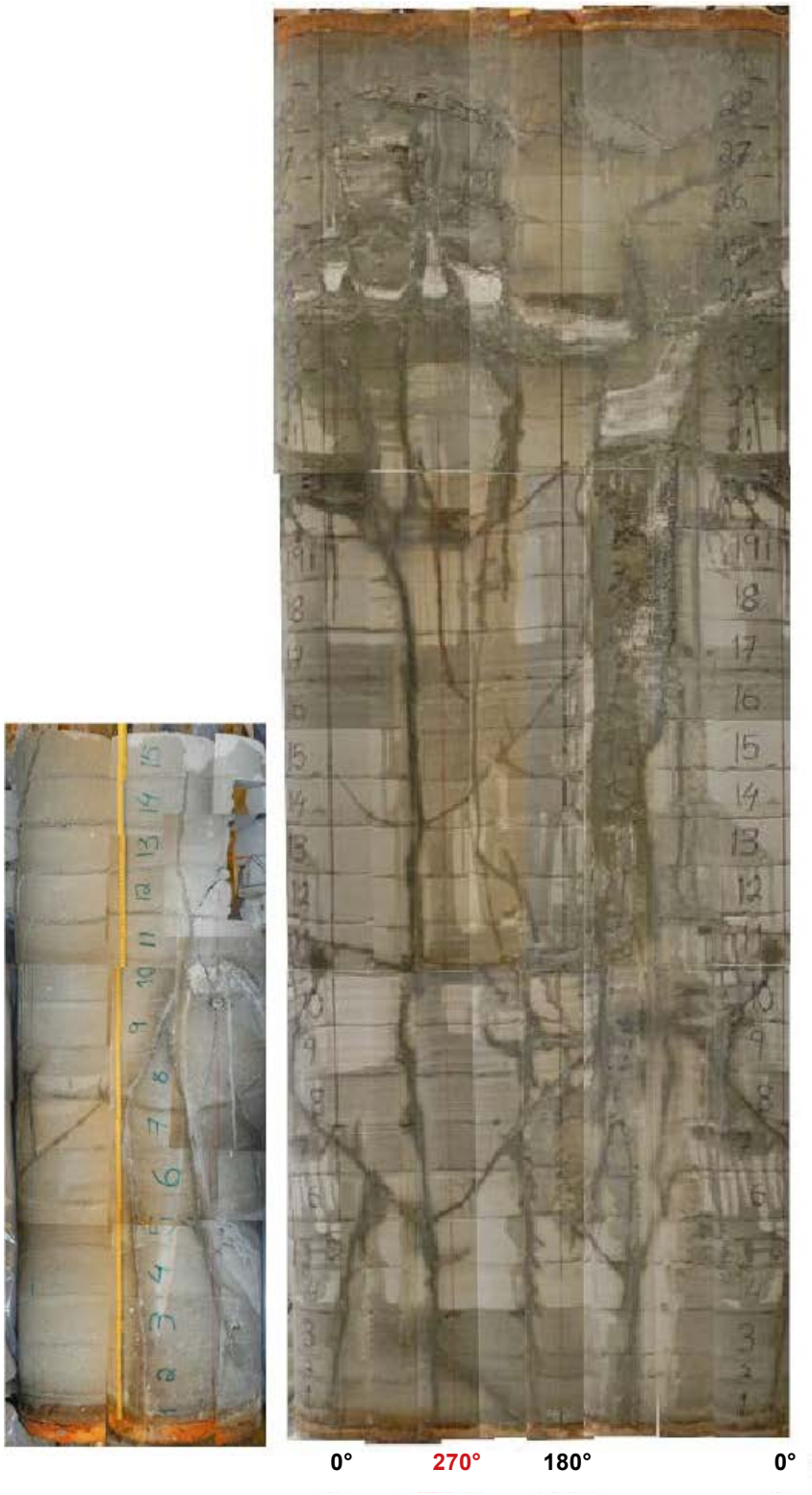

Figure 4-21. *Documentation of 15 lower blocks from parcel in Hole 17, and all blocks from parcel in Hole 18. The latter image covers the complete circumference of the parcel (in contrast to the former image) and the marked angles correspond to the marked lines on the bentonite surface.*

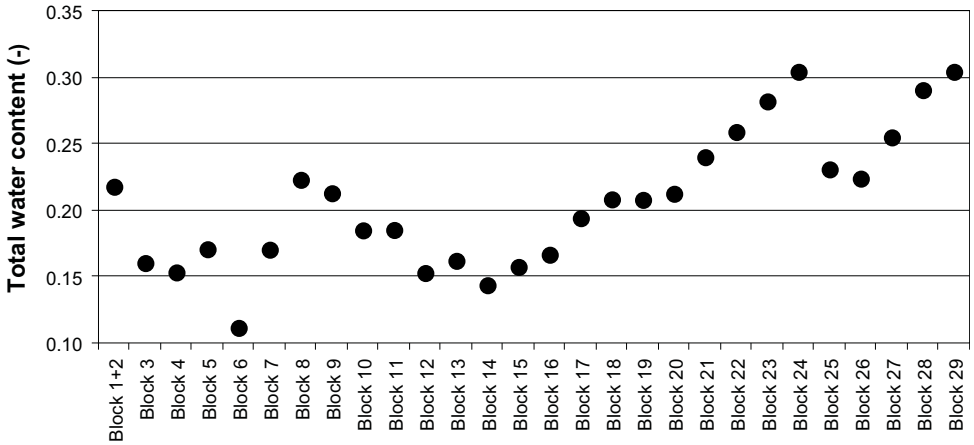

Figure 4-22. *Total water contents estimated from block masses for blocks in Hole 18. It should be noted that some blocks were broken in several pieces and thus constitute an uncertainty. Especially the water content value for Block 6 is considered to be non-relevant.*

4.4.3 Sampling and analyses of bentonite

A general sample scheme was defined in which samples (30 mm wide) were taken in five azimuthal directions, at six radial positions and at three levels in each block (Figure 4-23). The plan was thus to take 90 samples from each investigated bentonite block. Two of the blocks, Block 1 in Hole 17 and Block 2 in Hole 18, were 50 mm high and were therefore sampled at two levels. 13 blocks were analyzed in line with this scheme in Hole 17 with the intention to obtain detailed information around the instrumented blocks and also above the bottom plate. In the parcel from Hole 18, the 12 blocks in the lower end were analyzed in the same way.

A second sampling scheme was subsequently defined with the intention to obtain even more detailed information in the vicinity of the top part of the main fracture of interest in Hole 17. According to this scheme samples were taken from the "leftovers" from the first sampling in 20 azimuthal directions,

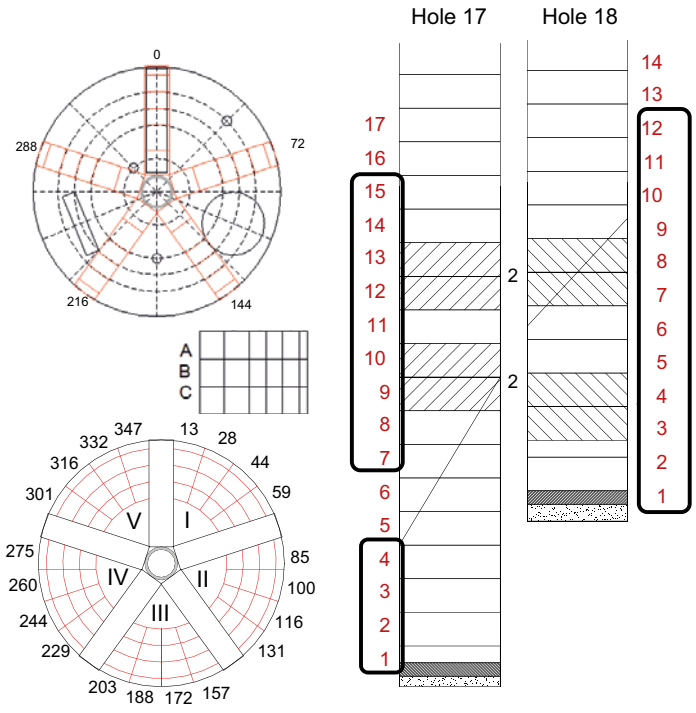

Figure 4-23. *Sampling scheme for Hole 17 and 18.*

at four radial positions and at one level (the mid-level) in each analyzed block. Three blocks from Hole 17 (Blocks 8, 9 and 10) and two blocks from Hole 18 (Blocks 5 and 9) were analyzed according to this scheme.

All sampling was made with a band saw. Each sample was divided in two parts: one devoted for analysis of water content, the other one devoted for a density measurement. In total, 2 590 samples were to be taken according to the implemented sampling plan. 34 of these samples could not be taken due broken blocks or interfering sensors. Some sample orientations were slightly shifted tangentially (not more than 3 cm) in order to obtain the intended samples as far as possible.

The denomination of samples was made according to the following example:

H17_B8_O144_HB_R130 where:
H17: Hole 17;
B8: Block 8;
O144: Orientation 144° (0°, 72°, 144°, 218° or 288°);
HB: Vertical level B (A at the top, B at the centre or C at the bottom);
R130: Radius of sample centre 130 mm (35, 65, 90, 110, 130 or 145 mm).

The analyses of water content and density followed the procedures:

Water content

The gravimetric water content w_0 is defined as mass water per mass dry substance, Equation (4-1).

$$w_0 = m_w/m_s \quad (4\text{-}1)$$

where m_w = mass water and m_s = mass dry substance

A sample was placed in an aluminum baking-tin. The sample total mass m_{tot} was determined using a laboratory balance. The sample was then placed in an aired oven at 105 °C and after 24 hours the dry substance mass, m_s, was determined by once more weighing the sample. The original mass water m_w could then be calculated according to Equation (4-2) .

$$m_w = m_{tot} - m_s \quad (4\text{-}2)$$

Finally the water content was determined with Equation (4-1).

Bulk density

The bulk density of the sample was determined using the paraffin oil method based on the Archimedes principle. The bulk mass m_b was determined by weighing the sample freely suspended in air. Then the weight of the sample lowered in paraffin oil, $m_{bp,}$ was determined and the volume was calculated with Equation (4-3).

$$V = \frac{m_b - m_{bp}}{\rho_p} \quad (4\text{-}3)$$

where V is the sample volume and ρ_p is the paraffin oil density. Finally the bulk density of the sample was determined using Equation (4-4).

$$\rho_b = \frac{m_b}{V} \quad (4\text{-}4)$$

Dry Density

Having both the sample bulk density and the water content the dry density ρ_d was determined using Equation (4-5).

$$\rho_d = \frac{\rho_b}{(1 + w_0)} \quad (4\text{-}5)$$

4.4.4 Results from analyses

Results from measurements of water content of the parcel from Hole 17 are presented as contour plots in Figure 4-24: both vertical plots for the five sampling directions and horizontal plots for blocks of special interest. Instrumented blocks are marked as the Dry section and the Wet section.

The following observations can be made from the water contents in Hole 17:

- The water content was almost unaffected in the two blocks in the *Dry section* (Block 12 and 13), and the two blocks above this (Block 14 and 15). The minimum water content was 12 %.
- The main fracture of interest had affected the water content in three directions (0, 72 and 288°) in the Wet section (Block 9 and 10) and the two blocks below this (Block 7 and 8).
- The water content in the lower blocks (Block 1–4) has been affected. This was most pronounced in directions 72 and 288° which probably coincided with the pegmatite veins close to these directions.
- The very slow increase of RH in the *Dry section* (see data for W4 –W6 in Figure 4-15) appeared to be caused by moisture transfer from the main fracture of interest in the Wet section. This was indicated by the major gradient in water content in the 0° direction, in which there was a difference in water content of 32–14 = 18 % over a distance less than 0.3 m. See also Figure G-1 in Appendix G.

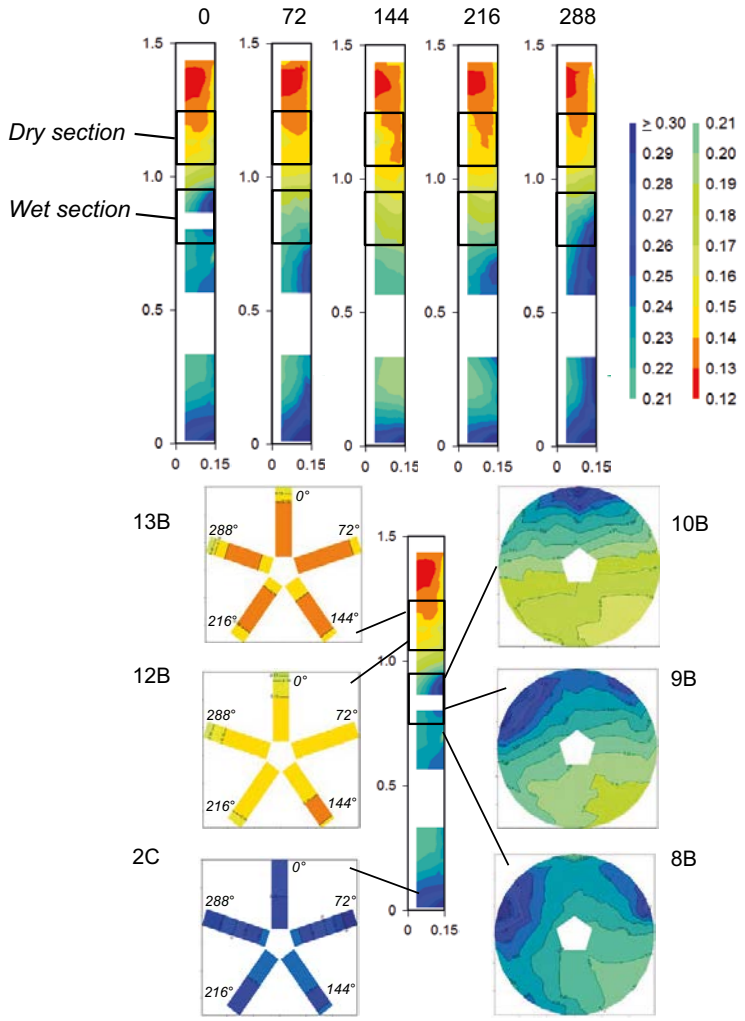

Figure 4-24. *Contourplots of water content in Hole 17. Upper graphs show vertical plots for five sampling directions (height: 0 to 1.5 m; radius: 0 to 0.15 m). Lower graphs show horizontal plots for blocks and levels of special interest (see marking): Circular plots show results from general and second sampling scheme. Star shaped plots show results from general scheme only. Color coding of legend is common for both upper and lower graphs.*

Corresponding plots for the parcel from Hole 18 are presented in Figure 4-25. The following observations can be made:

- The minimum water content of Block 1 was 20 %. The corresponding limit for Block 1 in Hole 17 was 25 %. This suggests that there was no free access of water in the bottom section of Hole 18.
- The driest section of the parcel in Hole 18 was found in Block 5 in which the minimum water content was 14 %. The corresponding limit for Block 14 and 15 in Hole 17 was 12 %. This indicates that there was a small but significant water uptake in this section.
- ”Inward directed” gradients in water content in Block 5 (see the horizontal plot in Figure 4-25) indicates inflow from rock wall. The highest water contents coincide however with dark traces in the photographs (Figure 4-21) and may therefore be caused by fracture flow from non-registered fractures rather than matrix flow.

The water-filling of the slot and the flooding events appear to only have left remaining traces in a few cases of the water content data, i.e. the upper blocks (no 12–15) of Hole 17. The outermost samples in these blocks showed approximately 15–16 %. This is quite consistent with the results from the water-uptake test Test 3, in which the water supply was limited to the filling of the slot (Appendix F). The minor increase in water content in the inner parts of block 12 and 13 was probably caused by the flooding event in this hole.

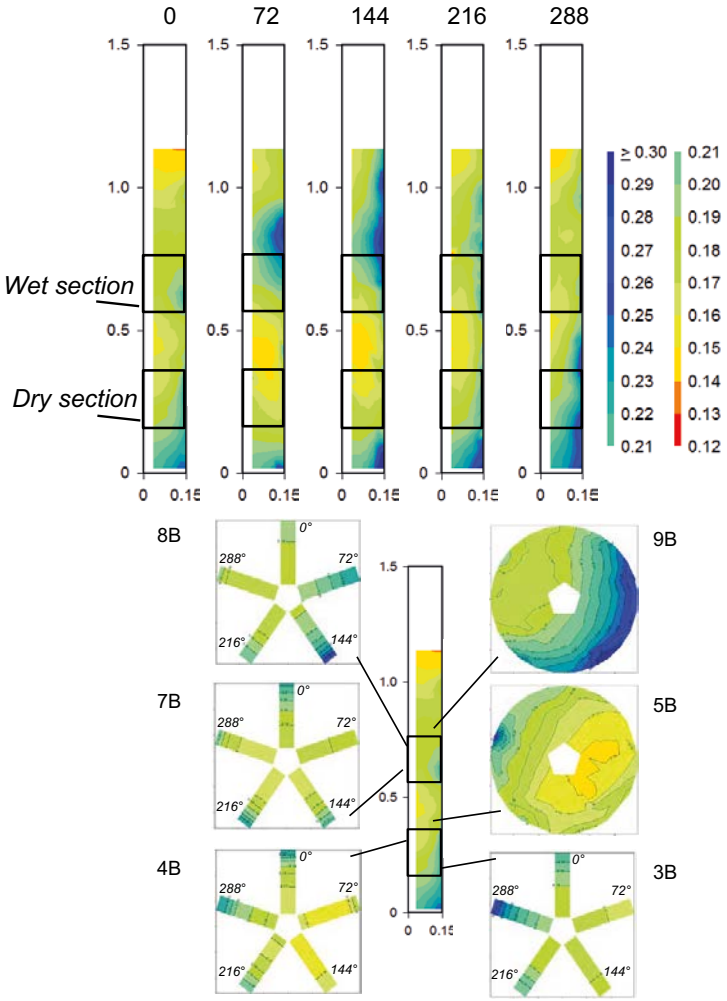

Figure 4-25. *Contourplots of water content in Hole 18. Upper graphs show vertical plots for five sampling directions (height: 0 to 1.5 m; radius: 0 to 0.15 m). Lower graphs show horizontal plots for blocks and levels of special interest (see marking): Circular plots show results from general and second sampling scheme. Star shaped plots show results from general scheme only. Color coding of legend is common for both upper and lower graphs.*

Measured and evaluated water content, dry density and degree of saturation are presented as axial distributions along different planes (representing different directions) and for different radii (Figure 4-26). A complete set of graphs is given in Appendix G.

The water contents are directly based on measured result and correspond to the vertical plot in Figure 4-24.

The dry densities are based in measured results of (bulk) densities as well as water contents. The general level in the lower part of the parcel (~ 1 520 kg/m^3) is significantly lower than target dry density level (1 562 kg/m^3). This different is probably caused by swelling. The dry material in the upper part of the analyzed blocks displayed dry density values which were higher than initial block value (~ 1 590 kg/m^3). This difference reflects a limitation in the used method of density measurements.

The degree of saturation values are based on measured results of densities and water contents, as well as a value of the particle density (2 780 kg/m^3). The high dry density values in the dry section would however imply that the degree of saturation would be unrealistically high. The following procedure was followed in order to obtain saturation profiles (to be used for model comparison) with as few assumptions as possible: these are based on measured density values for samples with $\rho_d \leq$ 1 562 kg/m^3, otherwise the dry density value of 1 562 kg/m^3 was used (corresponding to e = 0.78).

The dry densities are generally fairly homogenous which means that the overall observation of the relative changes and distributions regarding the degree of saturation was essentially the same as for the water content.

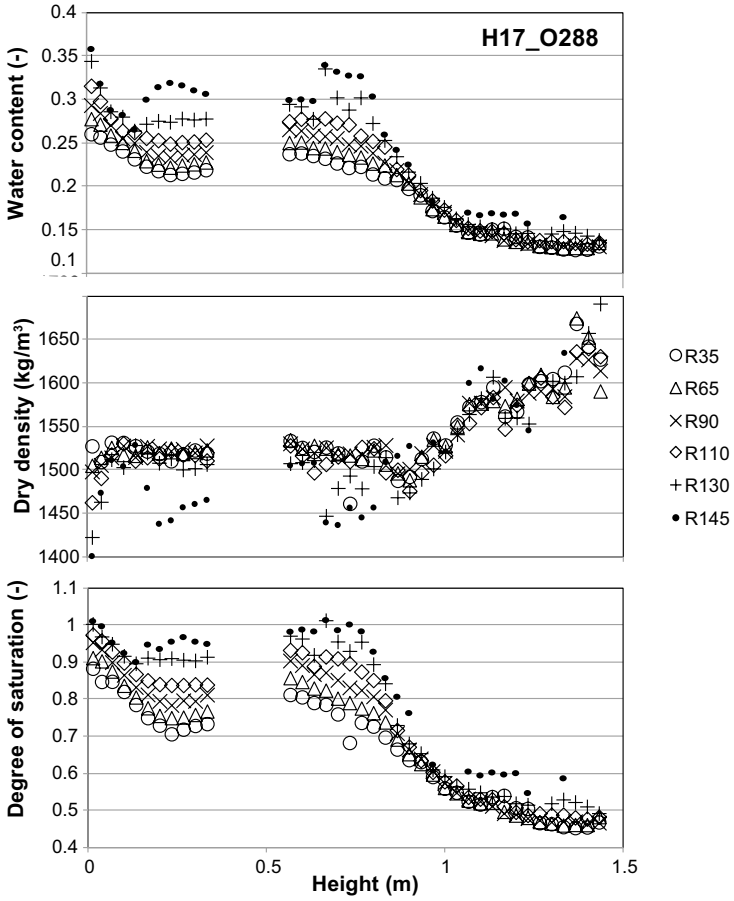

Figure 4-26. *Axial distributions of water content, dry density and saturation degree in Hole 17 orientation 288°. The initial values for these quantities were 11.6 %, 1 562 kg/m^3 (target) and 41 %, respectively. The symbols denote the radial position of the sample (in mm, see legend). The height was defined from the upper surface of the bottom plate.*

4.4.5 Function control of RH sensors

The function of the RH sensors was investigated in order to verify the relevance of the recorded RH data (as presented in Section 4.3).

One of the sensors (W2) did not display any output signal and was therefore immediately disregarded.

The function of the other used RH sensors were analysed in a climate chamber (type LabRumKlimat, model TH-ME-065). The method was chosen in order to minimize the time required for the function control. All sensors were analysed jointly and placed together in the chamber. In addition, an independent Vaisala sensor was used as a reference and was also put in the same chamber.

The sensors were tested in three different climates RH 60, 75 and 92 % and a temperature of 25 °C. The results are presented in Figure 4-27. In general, the Aitemin data were in fair agreement with the reference data, although slightly higher. Still, the scatter of data from the different Aitemin sensors was within a range of approx. 4 % units. It is therefore possible that the results would be even more positive if a conventional test procedure with salt solutions would have been employed.

In general, these sensors appear to be very reliable and convenient.

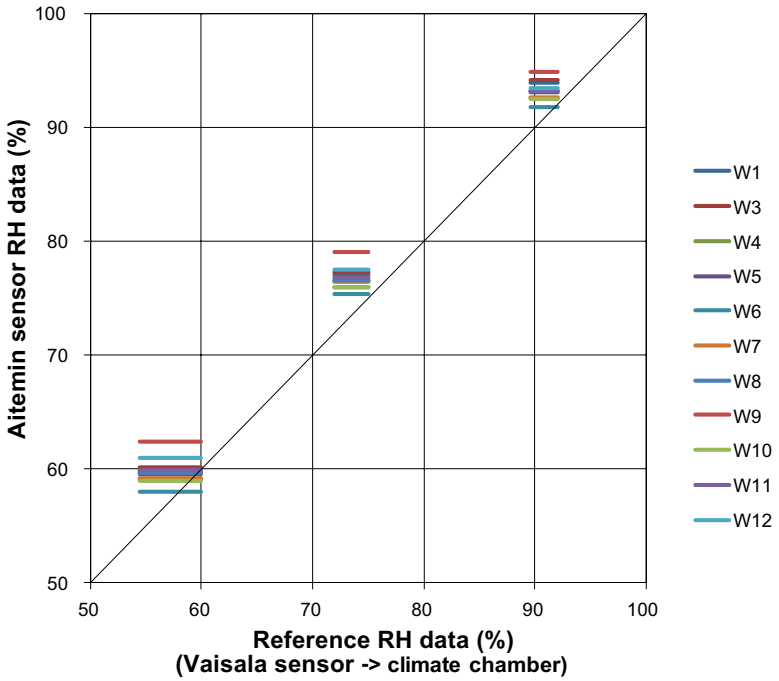

Figure 4-27. *Results from function control of RH sensors. Data from the investigated Aitemin sensors are plotted versus ranges of reference data as provided by a Vaisala sensor (lower end) and the climate chamber itself (upper end).*

5 A conceptual model of the BRIE site

5.1 Rock: Geology and hydrogeology

This section suggests a conceptual model and a site description for the test site. Focus is on fluid flow. To some extent mechanics and hydromechanical coupling is also discussed. The conceptual model and the site description is an important basis for handling the objectives: Increased scientific understanding of the exchange of water across the bentonite-rock interface; and better predictions of the wetting of the bentonite buffer.

5.1.1 Conceptual model: scheme

A conceptual model can be described as a set of assumptions that is used to describe a system for a given purpose. The scheme presented in Table 5-1, see Olsson et al. (1994), includes a number of headings and was used to identify: model scope or purpose; processes; geometric framework and parameters; material properties; spatial assignment method; boundary conditions and output parameters. The scheme was useful when designing the field experiment and facilitates going from reality to numerical models.

Focus in BRIE was on bentonite rock interaction, i.e. exchange of water across the bentonite-rock interface and wetting of the bentonite buffer. Describing the near-field of the central boreholes, the main water-bearing fractures and matrix in direct contact with borehole wall/bentonite, was assumed being of main importance. Further, deformation zones expected to provide water (pressure and flow) to these water-bearing fractures, matrix and the TASO-tunnel were of interest. The limited flows expected to the central boreholes were assumed to have no or very little influence on the pressure in the more conductive deformation zone intersecting the tunnel.

5.1.2 Site description: Overview

The site description below gives an overview of the BRIE-site including geometric framework and corresponding properties for key features i.e. main water-bearing fractures and rock matrix for boreholes KO0017G01 and KO0018G01, see Figure 5-2 and Table 5-2. These are essential for the exchange of water across the bentonite-rock interface and the wetting of the bentonite. Further, Table 5-3 presents important features identified in the tunnel (deformation zone and excavation damaged zone). Flow to tunnel and pressure in boreholes in tunnel wall are looked upon as boundary conditions. Figure 5-2 shows the five primary boreholes, the main rock types and the two sections of main interest for the wetting of bentonite.

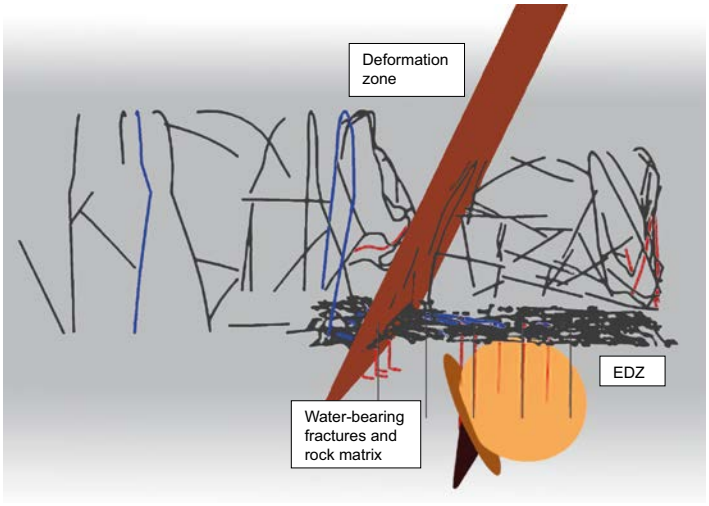

Figure 5-1. *Principal sketch of the BRIE site including main water-bearing fractures and matrix in the central boreholes KO0017G01 and KO0018G01, the deformation zone identified in the middle of the tunnel and an excavation damaged zone (EDZ).*

Table 5-1. Conceptual model of geology and hydrogeology for BRIE: scheme (Olsson et al. 1994).

Model Name/Definition **Conceptual model for BRIE (geology-hydrogeology)**	
Model scope or purpose *Specify the intended use of the model* Bentonite Rock Interaction (exchange of water across the bentonite-rock interface and wetting of the bentonite buffer) with focus on fluid flow (saturated and unsaturated) in rock, pressure (head), and to some extent hydromechanical coupling.	
Process description *Specification of the processes accounted for in the model, definition of constitutive equations* Fluid flow (saturated-unsaturated): Darcy's law, Water retention curve for unsaturated flow (bentonite and rock matrix) Suction and Wetting (bentonite) – (Geomechanics-Hydromechanical coupling)	
CONCEPTS	**DATA**
Geometric framework and parameters	
Dimensionality and/or symmetry of model *Specification of what the geometric (structural) units of the model are and the geometric parameters (the ones fixed implicitly in the model and the variable parameters)*	*Specify size of modelled volume* *Specify source of data for geometric parameters (or geometric structure)* *Specify size of units or resolution*
2D (cylindrical flow) to tunnel **2D (-3D) to tunnel front** **Fractures**	TASO and adjacent tunnels (TASD, TASK): Focus on TASO. Geological mapping of tunnel (wall, roof and floor), cored boreholes (and cores) and central boreholes (and cores). Flow and pressure response during drilling; hydraulic testing
Conductive fractures/deformation zones **2D or 1D flow in fractures** Fractures (deterministic) strike/dip/location 2D/1D/no flow (open, partly sealed, sealed) "Large" distance/Large (conductive) zones – intermediate distance/ intermediate zones or fractures (e.g. FPIs) – fracture mapping of tunnel floor volume – detailed description of fractures/matrix in direct contact with central borehole wall/bentonite.	Larger ÄSPÖ zones near TASO if needed for numerical modelling. Large zones/fractures e.g. FPIs identified in TASO (and adjacent tunnels/deposition holes). Other zones/fractures in TASO to limited extent. Detailed description of TASO tunnel floor volume (deterministic water-bearing fractures and matrix in direct contact with central boreholes KO0017G01 and KO0018G01).
Material properties	
Specification of the material parameters contained in the model (should be possible to derive from the process and structural descriptions)	*Specify source of data for material parameters (should normally be derived from output of some other model)*
Fracture transmissivity, *T* [m^2/s] **Specific capacity, *Q/dh* [m^2/s]** Aperture, *b(T* or *Q/dh)*-variation [m], 2D or 1D	Hydraulic tests in TASO
Hydraulic conductivity (bentonite/matrix), *K* [m/s] **Water content to relative humidity (water retention curves**) (bentonite/matrix), RH profiles, rock	Laboratory experiments Laboratory experiments
Water chemistry	Water sampling
Spatial assignment method	
Specification of the principles for how material (and if applicable geometric) parameters are assigned throughout the modelled volume	*Specify source of data for model, material and geometric parameters as well as stochastic parameters*
Deterministic ***T*** and ***K***	See above
Boundary conditions	
Specification of (type of) boundary conditions for the modelled volume	*Specify source of data on boundary and initial conditions*
Flow to tunnel, *Q* **Hydraulic head, *h*,** boreholes in tunnel wall intersecting deformation zones (if possible).	Sorbing mats Pressure measurements in boreholes. Pressure from Äspö HRL model.

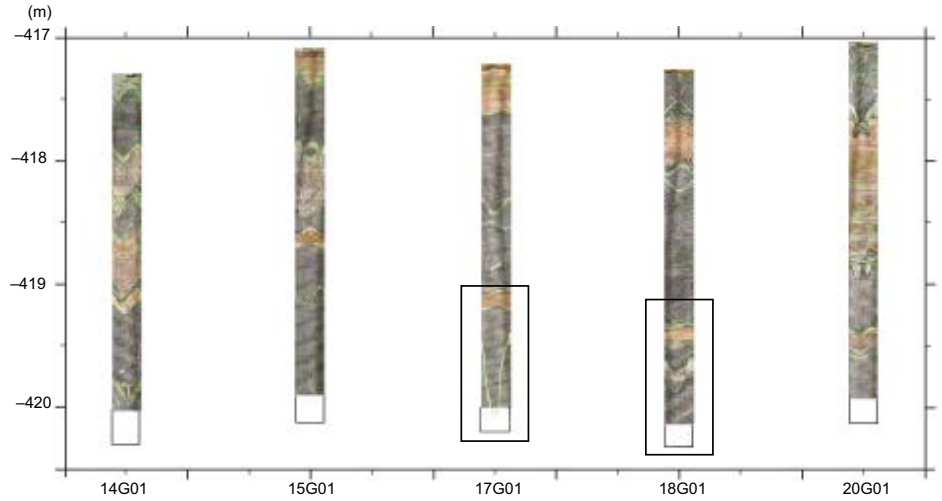

Figure 5-2. *The five primary boreholes, rock types and the two sections of main interest for investigation of wetting. Compilation of BIPS-images (orientation is not adjusted in this picture). Main rock types are diorite, fine-grained granite and pegmatite.*

Table 5-2. Key features (water-bearing fractures and rock matrix) and investigated properties included in conceptual model. In addition RH-profiles from rock blocks are also presented.

Feature	Data	Comment	Reference
Fractures			
Transmissivity 17G01	4.5×10^{-11} m^2/s	0.5–2.97 m	Appendix B
Orientation 17G01 (strike/dip)	118/66	Dip from BIPS and bentonite 300 mm	Table 5-5
Flow (nappy test) 17G01	~ 0.15 ml/min	2.25–3.25 m	Appendix C
Orientation 18G01 (strike/dip)	224/53	Dip from BIPS and bentonite 300 mm	Table 5-5
Rock matrix			
Hydraulic conductivity	2.6 and 6.5×10^{-13} m/s 6×10^{-14} to 5.5×10^{-12} m/s 2×10^{-15} to 5×10^{-13} m/s	Phase 1 (vertical) Phase 2 (vertical) Phase 3 (horizontal, borehole wall)	Table 3-19 Table 3-22 Table 3-23
Porosity and water content	0.5 to 1 % (RH 100 %)	Based on water content and RH (focus on two samples, Phase 1)	Table 3-20 Figure 3-60 Appendix D
RH-profiles KO0017G01	RH: 86 to 98 (0.01 to 0.1 m)	Measurements performed within an area and with time delay. Indicative.	Table 3-24 Table 3-25 Figure 3-68
RH-profile KO0018G01	RH:90 to 99 (0.01 to 0.105 m)	See above	Table 3-26 Figure 3-69

Table 5-3. Features (deformation zone and EDZ) and investigated properties included in conceptual model. Flow to tunnel and pressure in boreholes in tunnel wall are looked upon as boundary conditions.

Feature	Data	Comment	Reference
Deformation zone			
Transmissivity	3.5×10^{-9} m^2/s	One transient test	Appendix B
Orientation (strike/dip)	315/75	Estimated from mapping (structure 10 and 12)	Table 3-8
Excavation Damage Zone			
Specific capacity	4.5×10^{-7} m^2/s	Example from KO0018G01	Table 3-7
Depth	0.5–1 m	Based on core mapping	Figure 3-9
Flow tunnel		Sorbing mats, new method, Indicative. Humidity in ventilation not included.	Figure 3-50 Table 3-18
Pressure boreholes	0–27 bars	Influenced by packer location, number of drilled boreholes etc.	Figure 3-5 Figure 3-12 Figure 3-28

5.1.3 Important water-bearing fractures in KO0017G01 and KO0018G01

Figure 5-3, Figure 5-5 and Figure 5-6 present the most important sections of boreholes KO0017G01 and KO0018G01. Main flows in KO0017G01 were found at approximately 2.45–2.65 m in a north-easterly direction. Similar locations were identified both in the photo, Figure 5-4, and for the nappy test in KO0017G01, Figure 3-47. Flow based on nappy test was presented for borehole KO0017G01 only since flow in KO0018G01 was too low (in combination with a large flow in the upper section of the borehole).

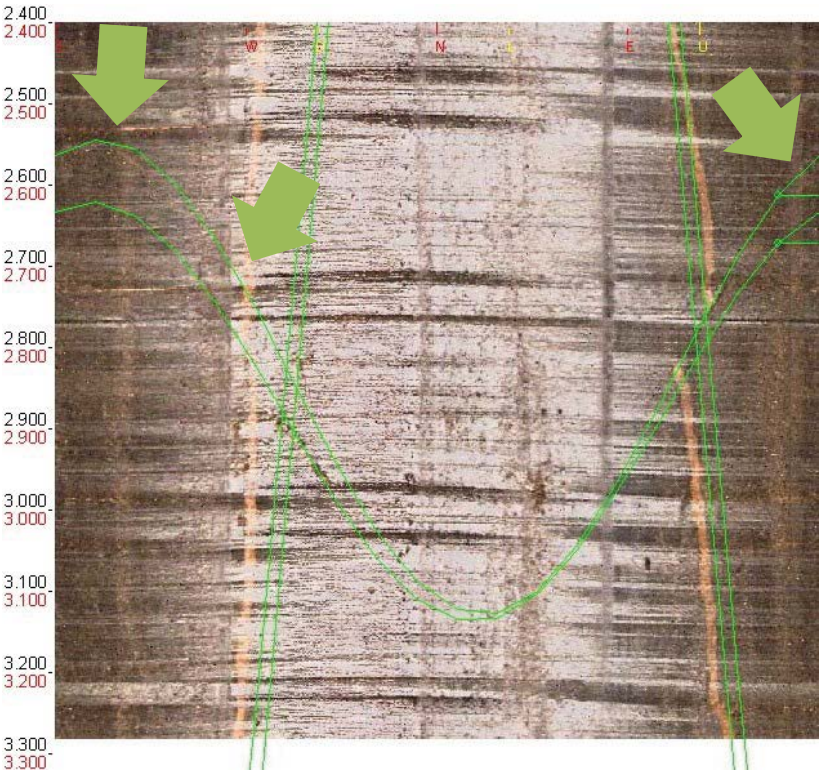

Figure 5-3. *BIPS-image from KO0017G01 (300 mm). Main flows indicated by green arrows at approximately 2.45–2.65 m, (orientation in BIPS-image not adjusted).*

Figure 5-4. *Location of main flows (green arrows) in main water-bearing fracture, KO0017G01. The arrows indicate the upper part of the fracture (opposite the dip-direction).*

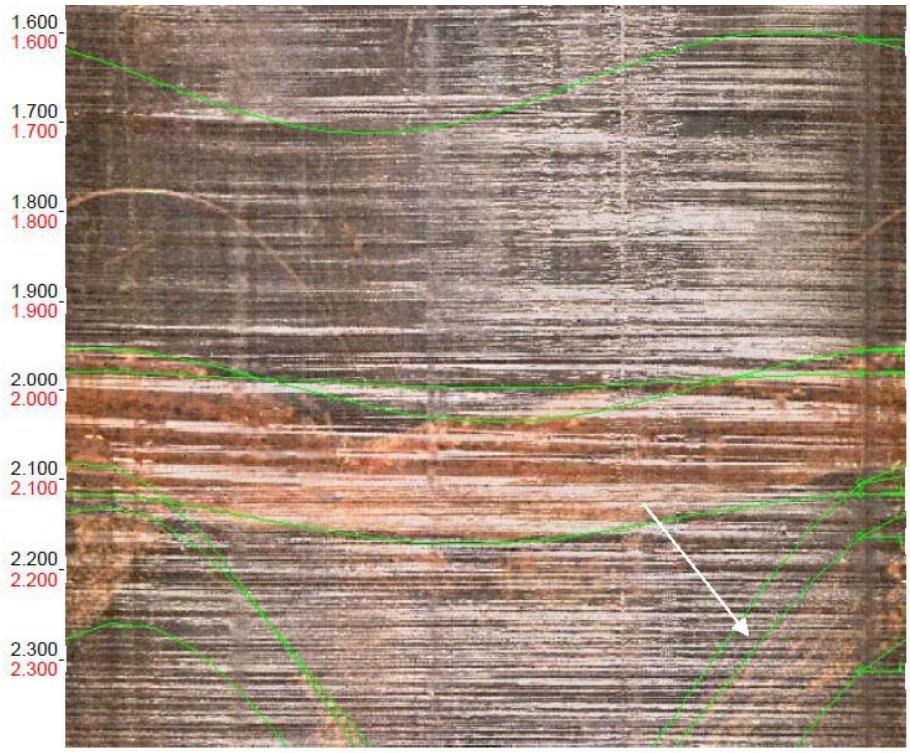

Figure 5-5. *BIPS-image from KO0018G01, 1.6–2.4 m, 300 mm (orientation not adjusted). Fracture of interest indicated by a white arrow.*

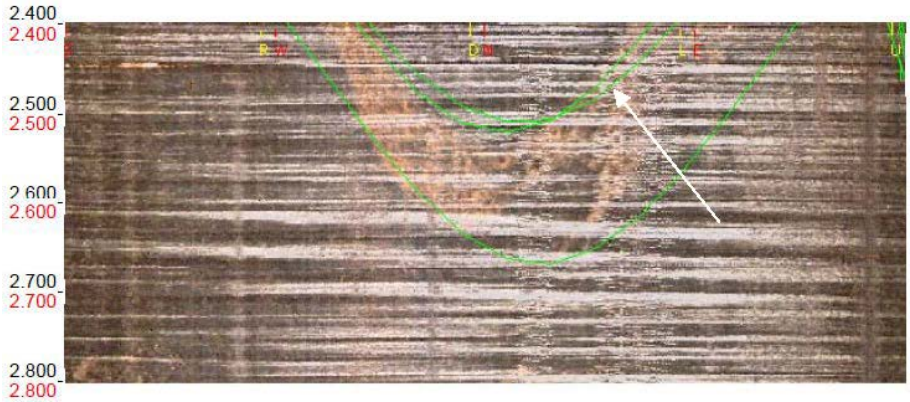

Figure 5-6 . *BIPS-image from KO0018G01, 2.4–2.8 m, 300 mm (orientation not adjusted). Fracture of interest (lower part) indicated by a white arrow.*

5.1.4 Rock matrix

Hydraulic conductivity was investigated on the cores originating from the 76 mm boreholes (cores approximately 60 mm) meaning that any (micro) fractures in the rock matrix are expected to be smaller than this size. Hydraulic conductivity of the rock matrix was found in an interval from 10^{-15} to 10^{-11} m/s, see Figure 5-7. Samples had an approximate diameter of 60 mm and a thickness of 10 mm. A high hydraulic head and gradient was used in the laboratory to enable flow measurements. Porosity was estimated for a few samples and was about 0.5 to 1 %.

The volumetric water content estimated for different relative humidity follow a drying-wetting-drying curve that is reasonable indicating that a lower saturation is reached when wetting. This could be due to e.g. trapped air. The volumetric water content and the relative humidity were used to obtain a water retention curve and van Genuchten parameters, see Table 5-2 and Appendix D.

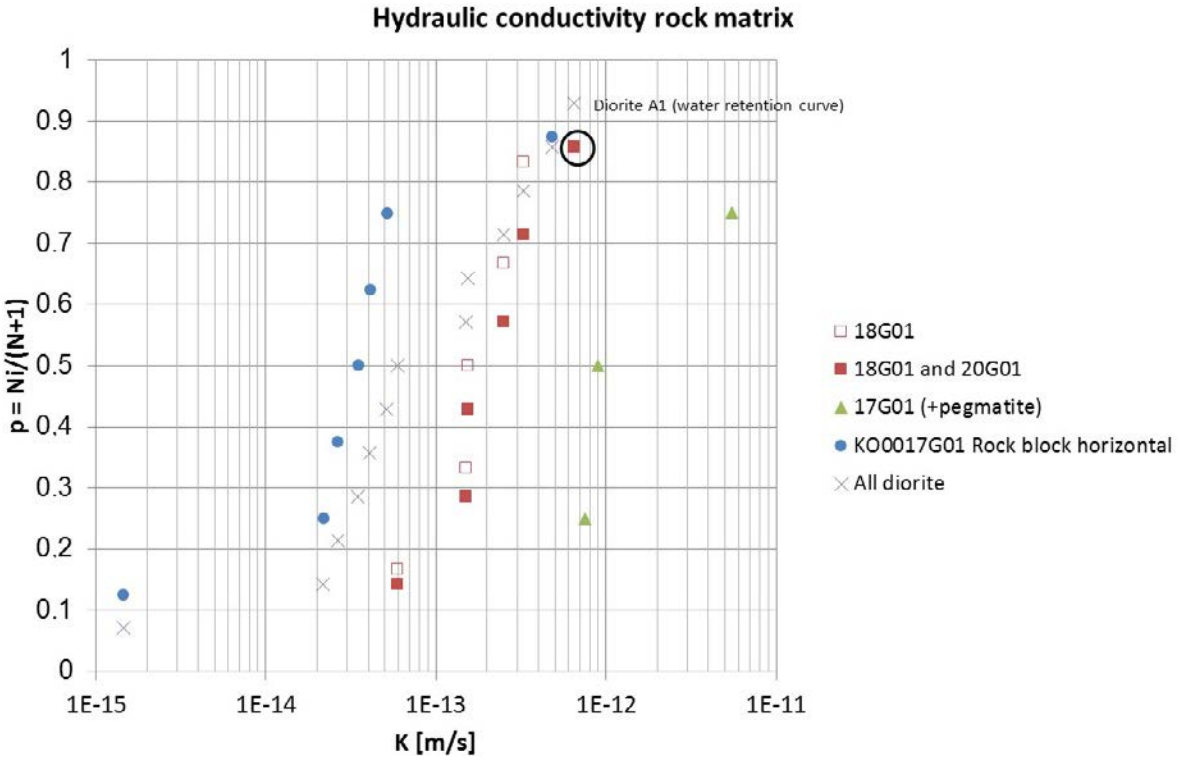

Figure 5-7. *Hydraulic conductivity Phases 1–3. Hydraulic conductivity was investigated on the cores originating from the 76 mm boreholes (cores approximately 60 mm) meaning that any (micro) fractures in the rock matrix are expected to be smaller than this size. All diorite (X in legend) include all diorite samples (18G01, 20G01 and 17G01).*

Relative humidity profiles were obtained at four different locations investigating relative humidity as a function of depth. A more pronounced de-saturated zone extending about five centimeters was identified (influence is seen also at the deepest measurement of 0.1 m but the influence is small). For two of the RH-profiles the relative humidity had its lowest value a few centimeters into the rock. Since measurements were performed within an area, see Figure 3-63 to Figure 3-65, and with time delay due to transport of rock blocks and preparations before measuring, these data should be looked upon as indicative.

5.1.5 Deformation zone

The main deformation zone identified in the TASO-tunnel, see Figure 5-8, had an estimated transmissivity of 3.5×10^{-9} m^2/s. The zone is assumed to be a boundary condition providing flow and influencing pressure. The value originates from one transient hydraulic test. The deformation zone is complex and strike and dip was here estimated based on structure 10 and 12 seen in Figure 3-25.

5.1.6 Excavation damaged zone (EDZ)

The frequency of open and partly open fractures is highest between the rock surface and a depth of one meter (4–9 fractures/m) and lowest at a depth of 2–3 meters. The higher number of fractures in the uppermost meter is probably due to an excavation damaged zone, since 21 out of the 28 open or partly open fractures mapped as “no detectable fracture mineral” are situated in the first 0.5 meters. The higher fracture frequency and the absent fracture minerals was assumed to reflect new fractures being part of an EDZ. The highest fracture frequencies among the boreholes are found in boreholes KO0014G01 and KO0015G01. This is also the location of a conductive deformation zone intersecting the tunnel.

Specific capacity estimated from an injection test in borehole KO0018G01 was 4.5×10^{-7} m^2/s, Table 3-7. In this borehole fractures in the upper 1 to 1.5 m were the main water-bearing features. The other boreholes had however lower values.

Figure 5-8. *Photos of deformation zone in left and right wall. The deformation zone is complex and strike and dip was estimated based on structure 10 and 12 seen in Figure 3-25.*

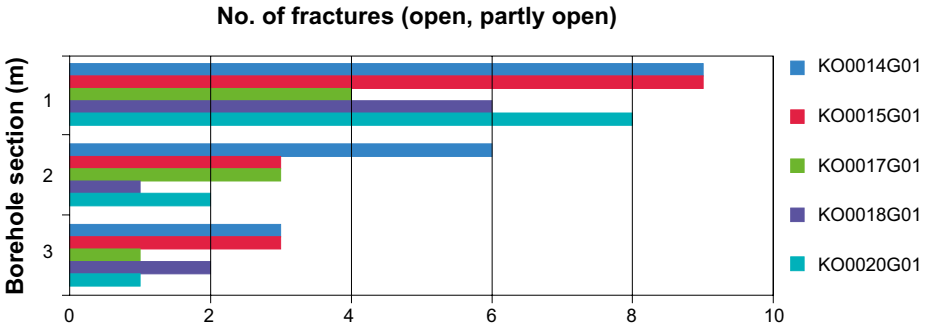

Figure 5-9. *Fracture frequencies of the five primary boreholes. The higher number of fractures in the uppermost meter is probably due to an excavation damaged zone, since 21 out of the 28 open or partly open fractures mapped as "no detectable fracture mineral" are situated in the first 0.5 meters.*

5.1.7 Tunnel flow: Sorbing mats

Main flows were found in the vicinity of the deformation zone. Sorbing mats have not been used for this purpose before and a comparative study using both a weir and sorbing mats would be interesting to further evaluate the method. Locations of the sorbing mats are shown in Figure 3-50 and the results from the measurements are presented in Table 3-18. When flows are low it should be kept in mind that water (that might be of importance) will also be transported from the tunnel due to ventilation (total flow to tunnel is higher than measured).

5.1.8 Comments on mechanics and hydromechanics main water-bearing fractures

Figure 5-10 presents stereo-plots with the approximate orientations of the deformation zone (indicated by a star) and main fractures in KO0017G01 and KO0018G01 (indicated by a circle and a square respectively). The dashed line shows the orientation of the TASO-tunnel. Both the deformation zone and the fracture found in KO0017G01 are found in an orientation where shearing could be possible since Coulomb Failure Stress, CFS, is close to zero meaning that the fractures may slip. The in situ stress used for Figure 5-10 originates from Andersson (2007), see Table 5-4 and does

not take account of the tunnel. Estimate of effective normal stress (pore pressure assumed to be 4.1 MPa, similar as tunnel depth) and CFS for this particular case was further described in Fransson et al. (2012). Results presented in Fransson et al. (2012) should be considered as examples of deformational behavior for different orientations since the orientations for specific fractures were not correct. Given a strike-slip stress field as presented below, the deformation zone and the fracture in KO0017G01 have a strike where shearing is most likely to occur (north-west as for the deformation zone or east-west).

Table 5-4 In situ stress (Andersson 2007).

	σ_1	σ_2	σ_3
Magnitude (MPa)	30	15	10
Trend (RT 90)	298	–	208
Plunge (from horizontal)	0	90	0

Figure 5-11 shows fracture topography based on the intersected fractures of the cores from the 76 mm boreholes. The methodology was described in the section including Figure 3-52. This type of data can be used to estimate mechanical input data. This was however not further developed in this report.

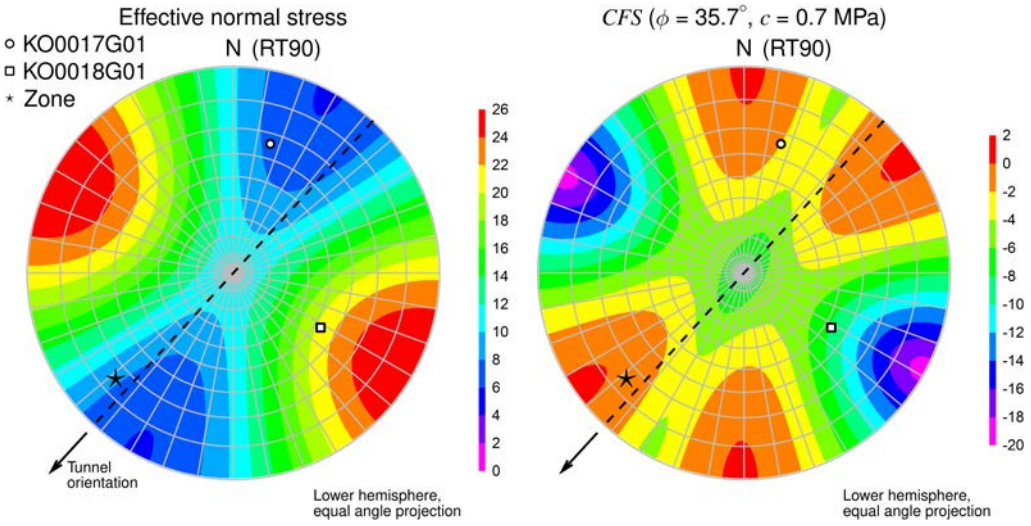

Figure 5-10. *Approximate orientations of deformation zone and main fractures in KO0017G01 and KO0018G01.*

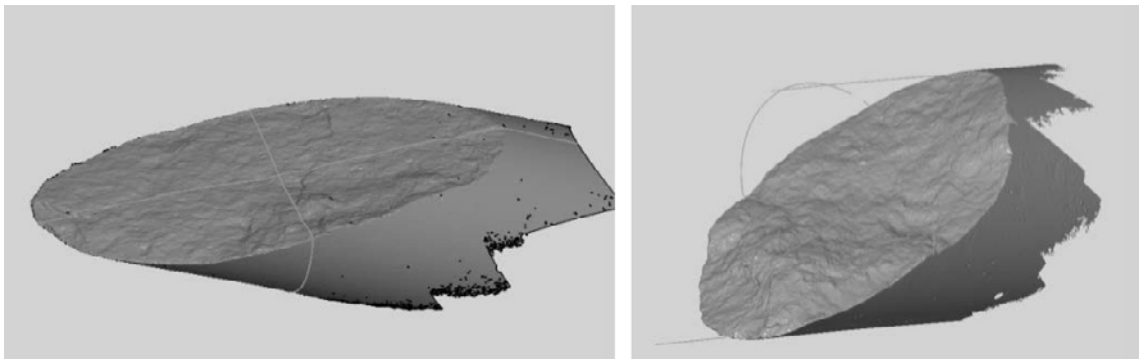

Figure 5-11. *Fracture surface scanning (76 mm) for main fractures of interest in KO0017G01 and KO0018G01.*

5.1.9 Characterisation methods for deposition holes

This section aims at discussing the objective: Better characterisation methods of the deposition holes. The intention is to give some general suggestions/comments considering characterisation methods for deposition holes based on experiences from the experiment.

Based on the experiences from the experiment the following steps and characterisation methods are suggested:

- Subdivide the rock mass into domains.
  - Host rock (fractured rock mass).
  - Deformation zones to identify boundary condition.
- Drilling.
  - Documentation of depth as a function of time (e.g. start, 0.5 m, 1.0 m etc.).
  - Indicate on the upper end of the rock/core a predetermined direction (e.g. direction of tunnel). to facilitate orientation of core (and fractures). Fracture orientation is very important.
  - Observe/Measure changes in inflow (link to depth).
  - Installation of a packer and saturation of borehole (preferably below the expected EDZ) to monitor pressure during drilling.
- BIPS.
  - Include a photo of the rock surface with the indication of orientation.
- Core mapping.
- Posiva Flow Log.
- Short duration hydraulic tests (flow and injection).
- Transient hydraulic tests (Injection and Recovery and/or Flow and Pressure Build Up).
- Nappy test if interested in flow distribution around the central (or deposition) borehole wall.

For all hydraulic tests it is of importance to consider measurement limit. PFL was useful only for the most water-bearing boreholes and the equipment used for hydraulic testing (long and short duration) had a low measurement limit (flow organ, Figure 3-10).

5.2 Bentonite parcels

Evaluated dry density values were generally lower than the target dry density level at 1 562 kg/m^3. For the lower part of the parcel in Hole 17 the overall level was found to be approximately 1 520 kg/m^3 (Figure G-2).The corresponding overall level for the parcel in Hole 18 was slightly lower at approximately 1 500 kg/m^3, although the data displayed a larger scatter (Figure G-5). This reduction in dry density suggested that the bentonite had expanded with approximately 2.8 % (Hole 17) and 4.1 % (Hole 18). Such volumetric expansions can to some extent be explained by axial swelling. For Hole 18 it was noted the length had increased with 43 mm (Section 4.4.2) and this would imply an axial swelling of 1.5 %. A corresponding value could be estimated for Hole 17 (from the yardstick reading in Figure 4-21) to 1.9 %. The difference between the volumetric expansions and the axial swelling strains appears to be caused by radial swelling. For Hole 17 this would suffice with an increase of the outer radius of 0.7 mm, whereas for Hole 18 the increase would have to be 1.9 mm. The relatively larger strain value for the parcel in Hole 18 is consistent with the longer time period required for dismantling of this parcel (3 weeks as compared with 2 weeks for Hole 17). This swelling probably occurred during the dismantling operation: from the removal of the pillars and the completion of the stitch drilling, to the lifting of the parcels.

The density analyses tended to overestimate the density for samples with low water content. The reason for this seems to be that paraffin oil enters the sample which thereby leads to an underestimation of the sample volume.

An in-situ water retention data set was evaluated by relating the last reading from each RH sensor with the analysed water contents in bentonite samples most closely located to the sensors. The identification of adjacent samples is illustrated in Figure 5-12. The compilation of the data sets of water contents and RH is shown in Figure 5-13. The line marking for the initial conditions represents the first RH readings (59 %) and the minimum level subsequently observed (64 %), see Section 4.3.

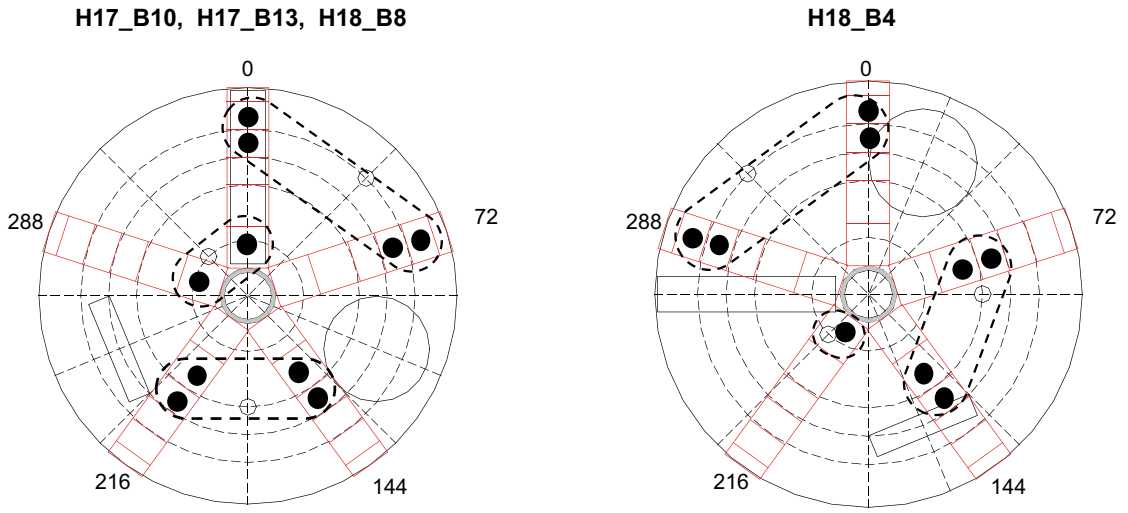

Figure 5-12. *Positions for samples (filled circles) close to RH sensors (open small circles) for which water contents were related to final RH readings. Dashed rounded rectangles indicate the assemblages of samples and sensors.*

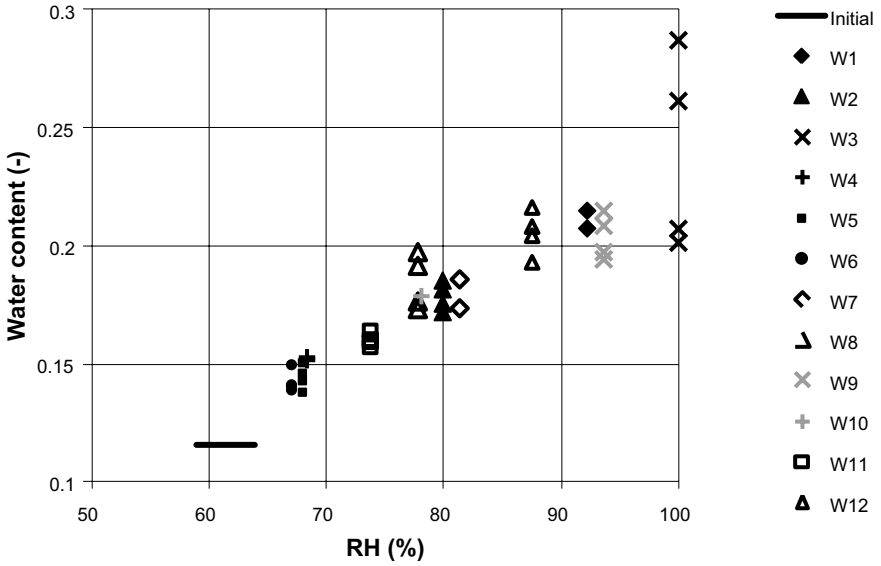

Figure 5-13. *In-situ water retention data set.*

The shift in RH from 59 to 64 % appears to be caused by the filling of the outer slot. This notion is supported by the results from Test 3 of the water-uptake test. A similar increase of RH was recorded by the innermost sensor in this test although the water content in the corresponding position apparently did not change during the test period.

5.3 Bentonite-Rock interaction

5.3.1 Bentonite, bentonite water content and fractured rock: wetting

The positions of the main fractures of interest were evaluated from the photos of the parcel surfaces and the markings of the fractures (Figure 5-14). In general, these marking demonstrated that the used dip direction (or strike) for the fracture in Hole 17 was satisfactory, whereas the depth of the fracture was overestimated with approximately 7–8 cm. For the fracture in Hole 18 the dip direction was underestimated with approx. 10°, whereas the depth was satisfactory.

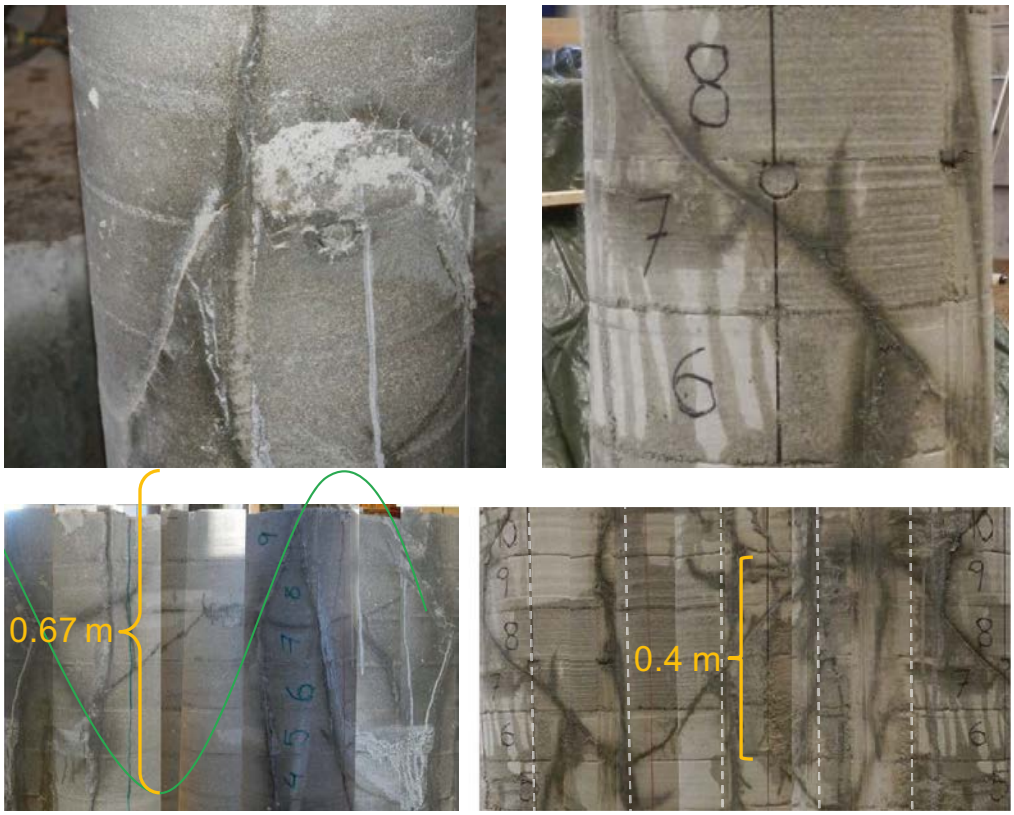

Figure 5-14. *Markings of main fracture of interest in Hole 17 (left) and Hole 18 (right). Estimations of the height between the upper and lower point of each fracture is shown in the lower pictures.*

A more detailed evaluation of the strike, dip and z coordinates for the main fractures of interest are presented in Table 5-5. The strike values were based on the evaluated dip directions, see Figure 4-13, adjusted to the Äspö 96 system, and for the fracture in Hole 18 an angle of 10° was added due to the observed underestimation. The dip values were based on the height between the upper and lower end points of the markings from the fractures (see Figure 5-14) and the diameter of the holes. The z-coordinates were based on levels for instrumented sections (joints between blocks, see Figure 4-12) and the observed distanced between the joints and the dark markings on the bentonite surface.

Table 5-5. Evaluation of position for the main fractures of interest. The translation from dip direction to strike, and from RT90 to Äspö96 was calculated as −90° and +12°, respectively.

Test hole	Strike	dip	z-coordinate
KO0017G01	196 (dip dir; RT90) + 0 → 118 (Äspö 96)	arctan(6.7/3) = 66°	−419.86 + 0.07 – 0.33 = −420.12
KO0018G01	292 (dip dir; RT90) + 10 → 224 (Äspö 96)	arctan(4/3) = 53°	−419.63

The water content distribution was in many cases correlated with the dark traces found on the surface of the bentonite parcels. For the parcel in KO0017G01, traces of the upper part of the main fracture of interest were found on the surface of Block 8–10, and this was reflected by the high water contents in directions 72°, 0° and 288° (Figure 5-15). Traces of the pegmatite veins, see rock core in Figure 5-16, were similarly found on the surface of the Block 1–7, and this was reflected by the water contents in directions 72° and 288°. A trace of an uncharted fracture was found on the surface on Block 8 which also was reflected by the water contents in the 216° direction. For the parcel in Hole 18, traces of the uppermost part of the main fracture of interest, see Figure 5-18, were found on the surface of Block 9–10, and this was reflected by the high water contents in directions 144° and 72° (Figure 5-17). Finally, traces of several uncharted fractures were found on the surface on Block 1–6 (and above in some cases) and this corresponded to increased water contents in the 0°, 288° and 216° directions.

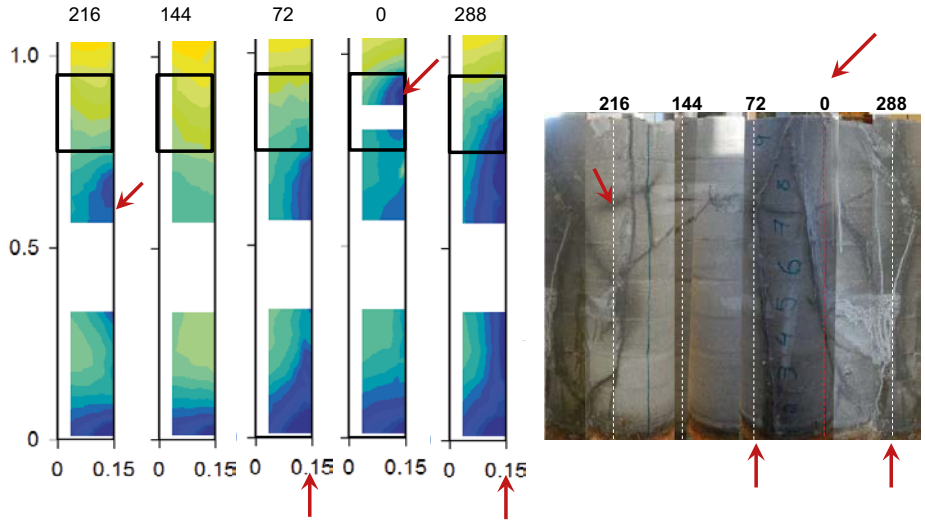

Figure 5-15. *Comparison of water content plots with markings on parcel surface for KO0017G01.*

Figure 5-16. *Comparison of some fractures in rock core and traces on bentonite for KO0017G01. Black dashed line approximate location of main fracture and white dashed line approximate location of pegmatite vein.*

Some dark traces did not correspond to any significant increase in water content, for instance on the surface of block 10–15 in KO0017G01. This trace corresponds however to a fracture between different rock blocks (Figure 5-19). So if this fracture existed throughout the test period (which the dark trace suggests) then this would indicate that the surrounding rock in this section had a low access of water and/or was affected by a major drawdown.

The measured water contents were also correlated with the results from the RH sensors. This was clearly demonstrated by the evaluated in-situ retention curve (Figure 5-13). Of special interest was the RH sensor W12 in Block 4 in the parcel of KO0018G01. This was located in the 315° direction only 30 mm from the borehole wall, and thus quite close to the dark trace in the 288° direction. Since the W12 exhibited a quite rapid RH increase, this supports the notion that there actually was

a water bearing fracture in this direction throughout the test period. Other sensors of significant interest were the W4–W6 sensors which exhibited a very slow RH increase. This increase appears to be caused by moisture transfer from the main fracture of interest in KO0017G01 and this is supported by the major gradient in water content in the 0° direction. This does not necessarily imply that the surrounding rock in this section was virtually impermeable, but rather that the surrounding rock had low access of water and/or was affected by a major drawdown.

Finally, the measured water contents also displayed some relation with results from pore pressure sensors. All Geokon pore pressure sensors have displayed zero pressures and this appears to correspond to the fact that none of the sensors were located close to a water bearing fracture. The Druck sensor connected to the sand filling in the bottom of Hole 17 displayed however a pressure of 13 bar throughout the test period and this was reflected by the high water content in Block 1 which was higher than or equal to 25 %. The corresponding water content in Block 1 in KO0018G01 was significantly lower (higher than or equal to 20 %) and this therefore appears to support the notion that the access of water was limited in the bottom of this hole. This in turn, appears to support the recorded zero water pressure in this part.

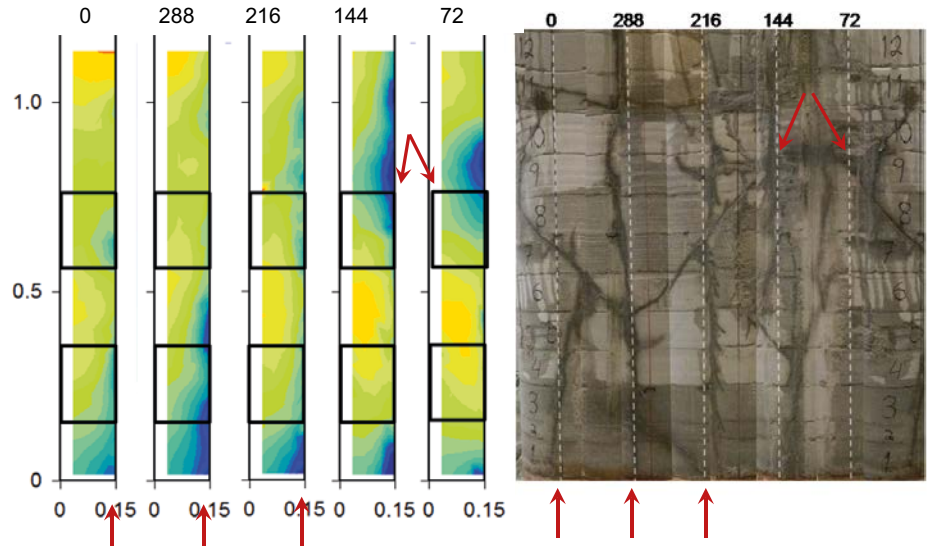

Figure 5-17. *Comparison of water content plots with markings on parcel surface for KO0018G01.*

Figure 5-18. *Comparison of some fractures in rock core and traces on bentonite for KO0018G01. The core is broken by the main water-bearing fracture.*

Figure 5-19. *Dark trace on surface of Blocks 10–15 in KO0017G01 and corresponding fracture between rock blocks (image reversed). Note the main fracture of interest, and the trace from this, at the lower end of the photos.*

The two major fractures that were identified during investigations of boreholes KO0017G01 and KO0018G01 were as described above also main providers of water to the bentonite (deepest wetting). In addition to these, other previously not identified fractures were seen. Some of them could be explained by smaller fractures with a low transmissivity (below measurement limit for the hydraulic investigations). This issue could possibly be further investigated by a detailed mapping (including dyeing) of the 300 mm-cores and by comparing photos from these cores to the photos of the bentonite. Hydraulic testing of the rock matrix in the laboratory indicated a difference between samples with diorite only compared to the hydraulic conductivity of diorite including a pegmatite vein, see Figure 5-7. Likely is therefore that both minor fractures as well as differences in rock type results in different ability to transmit water.

In addition to smaller fractures, a number of vertical, not previously identified, fractures with pronounced wetting were seen on and inside the bentonite (see lower part of bentonite in direction 0°, 288° and 216° Figure 5-17). These fractures are more or less perpendicular or parallel to the tunnel and also close to in line with adjacent boreholes (secondary boreholes, see Figure 3-1, Figure 5-20 and Figure 5-21). One possibility could be drilling-induced tensile fractures due to the minimum circumferential stress becoming negative (circumferential stress less than tensile strength). These fractures would occur as pairs of mutually opposed, vertically dipping conductive fractures (e.g. Bailey et al. 2014). Breakout formation would be expected parallel or close to the minimum horizontal stress (circumferential stress exceeds compressive rock strength). Numerical modelling would be interesting to investigate if rock stresses and tunnel/borehole geometry at TASO could further explain the observed fracture behaviour at the site.

The overall water content of the bentonite at the time of the dismantling can be used to estimate the water inflow into the borehole, as long as bentonite doesn't come close to water saturation. This is thus a type of evaluation analogous to the nappy tests. An inflow per unit length (Q/L) can be calculated as a function of the final water content (w):

$$Q/L(w) = \frac{(w - w_i) \cdot m_s}{t \cdot \rho_w \cdot h_b} \qquad (5\text{-}1)$$

were w_i is the initial content (11.6 %), m_s is the solid mass for each block (10.9 kg), t is the time of duration of the test (518 days for Hole 18), ρ_w is the density of water, and h_b is the height of each block (0.1 m). This line is shown in Figure 5-22. It can be noted that the range of final water contents in Hole 18 (with a rough average level of 20 %) corresponds to an inflow per unit length of ~ 0.01 ml/min/m, which is consistent with the measured inflows from the characterisation program.

Figure 5-20. *Borehole KO0017G01 following stitch drilling and dismantling. New (not previously identified) fractures being more or less parallel or perpendicular to tunnel and close to in line with adjacent boreholes.*

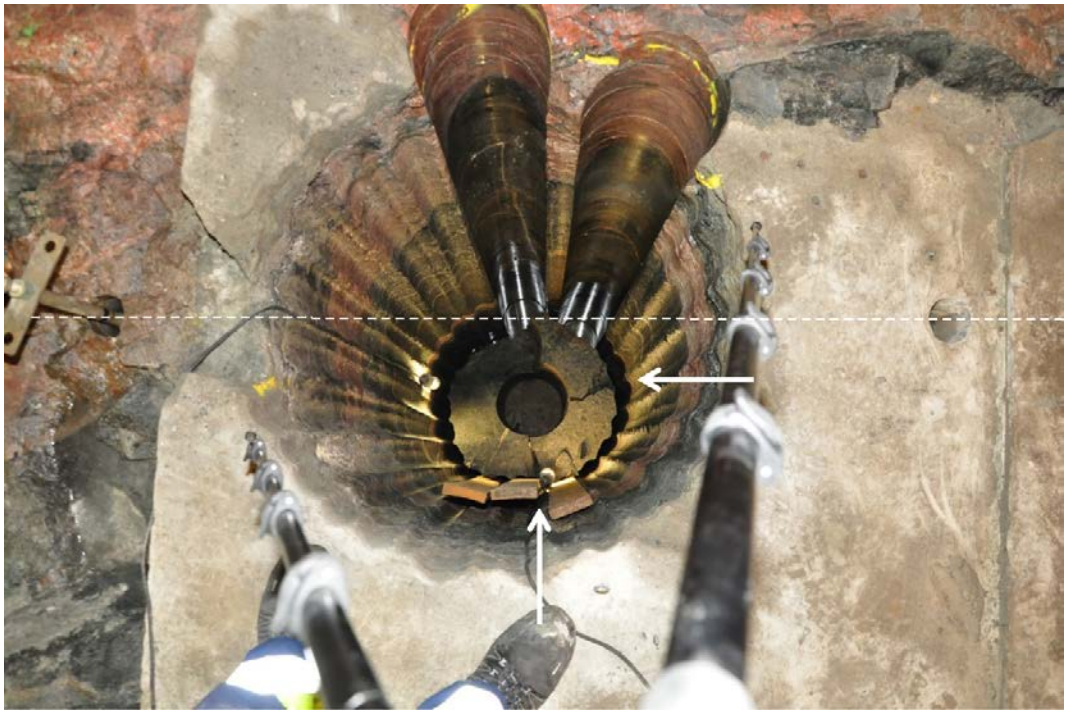

Figure 5-21. *Borehole KO0018G01 following stitch drilling and dismantling. New (not previously identified) fractures being more or less parallel or perpendicular to tunnel (indicated by dashed, white line) and close to in line with adjacent boreholes.*

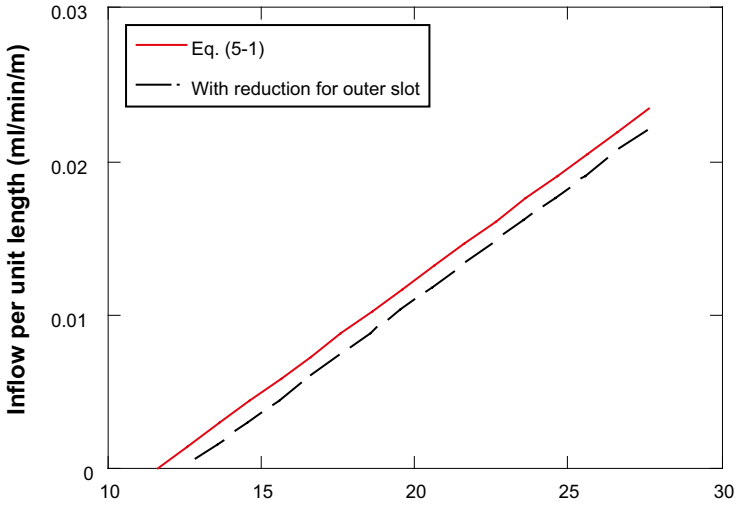

Figure 5-22. *Estimated relation between inflow per unit length and the final water content. Adopted for the time of duration of Hole 18. The dashed black line illustrates the effect of taking the filling of the outer slot into account.*

5.3.2 Relative humidity-profiles bentonite-rock interface

Figure 5-24, Figure 5-25 and Figure 5-26 present snap-shots of RH-profile in bentonite and rock for KO0017G01 and KO0018G01. In addition, contour plots of water content, see Figure 4-24 and Figure 4-25, are added. Relative humidity for bentonite was estimated from measured water contents, and with a tentative relation adopted from the in-situ retention data (Figure 5-23). The following function was used:

$$RH(w) = \begin{cases} 59 + 367 \cdot (w - 0.12) & w < 0.21 \\ 92 + 114 \cdot (w - 0.21) & w \geq 0.21 \end{cases} \qquad (5\text{-}2)$$

For measurement of relative humidity in rock there was a delay caused by transport of rock blocks and preparation. The rock blocks were covered by plastic during transportation and preparation to limit the risk of drying or wetting. For KO0017G01 boreholes of 0.04 to 0.1 m depth were initially drilled to investigate the extent of a de-saturated zone, see rock block and boreholes in Figure 3-63. To get a picture of the close vicinity to the 300 mm borehole wall, boreholes of 0.01–0.03 m were subsequently drilled. Table 5-6 and Table 5-7 present compilations of dates for the procedure.

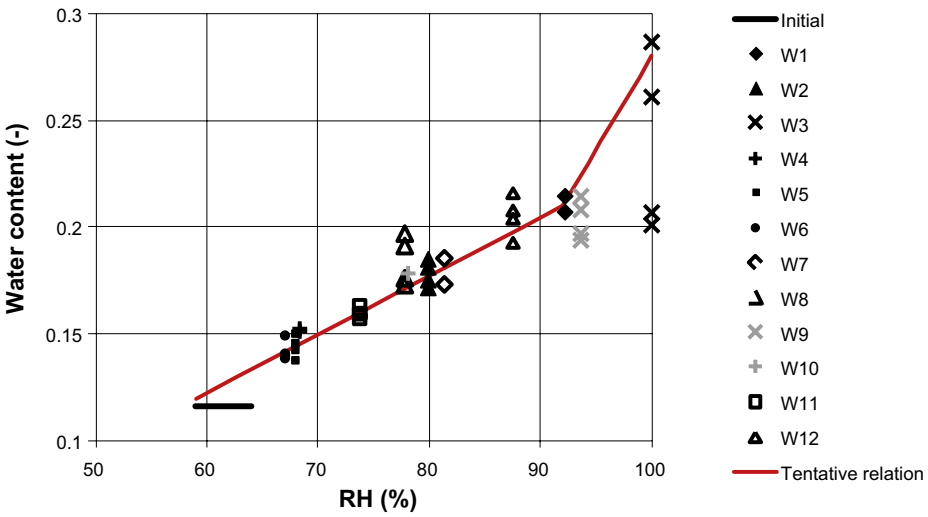

Figure 5-23. *Adoption of a tentative retention relation used for translation of water content data into RH data.*

Table 5-6 Lifting of parcels, preparation and measurements of RH for KO0017G01.

	17G01
Lifting of parcels	2013-11-21
Drilling of boreholes (0.04–0.1 m)	2013-11-25
Measurement	2013-12-02
Drilling of boreholes (0.01–0.03 m)	2013-12-05
Measurement	2013-12-11

Figure 5-24 shows relative humidity in bentonite (radius 0 to 0.15 m) and rock (0.15 to 0.25 m) and indicates a de-saturated zone in rock by the borehole wall. A dip in relative humidity is seen a few centimetres into the rock and the more pronounced de-saturated zone reaches about five centimetres. The sampling profile is found above section 13B seen in Figure 7-23 and it seems to be the driest of the investigated sections. Limited (if any) influence from the main fracture.

Both sections in Figure 5-25 indicate a de-saturated zone in rock and the more pronounced de-saturated zone reaches about five centimetres into the rock (influence is seen also at the deepest measurement of 0.1 m but the influence is small). For the dry sections (Dry Section Upper, DSU, and Dry Section Lower, DSL) profiles are similar (except for the dip in relative humidity seen in DSU). For the section in Figure 5-25 found closer to the fracture (F), the profile in rock is similar to the previous (with a dip at a few centimetres). However, if looking at the dashed lines in the water content contour plots for sections 8B and 9B, the higher water content or relative humidity in the bentonite might be due to transport of water in bentonite from the main fracture in KO0017G01. Any effect of flow from the rock matrix into the bentonite would be masked by the flow through the bentonite from the fracture.

Finally, Figure 5-26, as the previous figures, indicates a de-saturated zone in rock and the more pronounced de-saturated zone reaches about five centimetres into the rock. The dashed triangle in the water content contour plots for section 9B shows the location of the evaluated relative humidity data. The higher water content or relative humidity in the bentonite might be due to transport of water in bentonite from the main fracture in 18G01. For the 288°-profile, limited influence is seen.

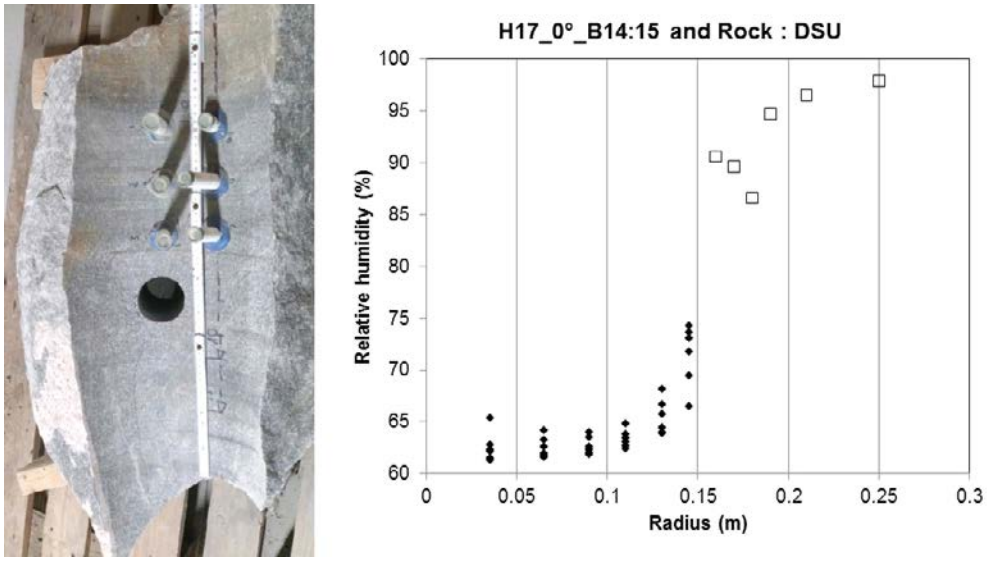

Figure 5-24. *Snap-shot of RH-profile in bentonite and rock (squares), KO0017G01 Dry Section Upper (DSU) found just above the main water-bearing fracture. Lifting of parcels 2013-11-21. Drilling of boreholes in rock (0.04–0.1 m, 2013-11-25) and measurement 2013-12-02. Drilling of shallow boreholes (0.01–0.03 m, 2013-12-05) and measurement 2013-12-11. Upper part of fracture identified in lower part of photo. Sampling profile found above section 13B seen in Figure 5-25.*

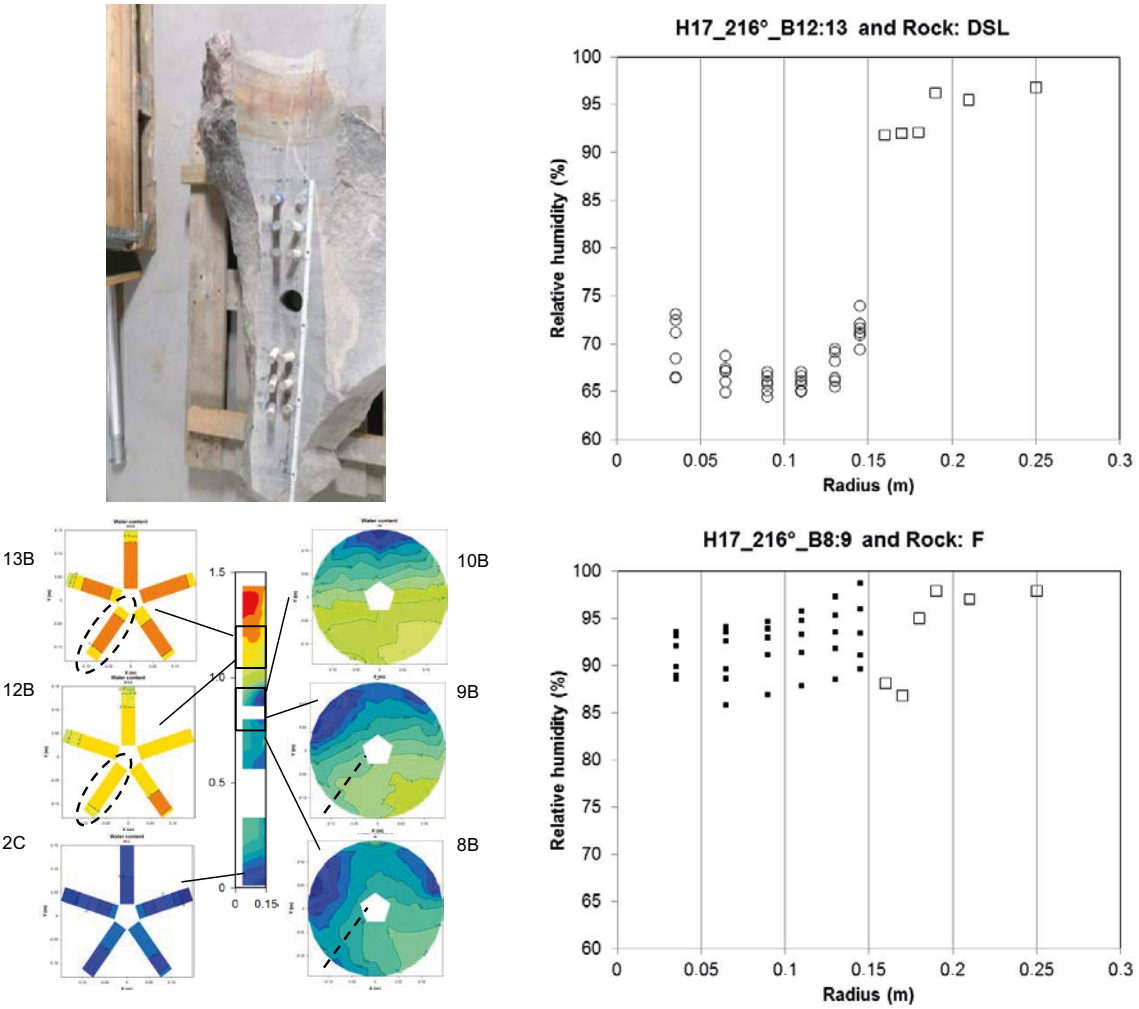

Figure 5-25. *Snap-shot of RH-profile in bentonite and rock, 17G01. Dry Section Lower (DSL) and close to fracture (F). Lifting of parcels 2013-11-21. Drilling of boreholes in rock (0.04–0.1 m, 2013-11-25) and measurement 2013-12-02. Drilling of shallow boreholes (0.01–0.03 m, 2013-12-05) and measurement 2013-12-11.Dashed ellipses (B12:13) and lines (B8:9) on the contour plots of water content give the approximate orientation of sampling profiles.*

Table 5-7 Lifting of parcel, preparation and measurements of RH for KO0018G01.

	KO0018G01
Lifting of parcel	2014-03-04
Drilling of all boreholes (0.01–0.105 m)	2014-03-12
Measurement	2014-03-20

Based on the four RH-profiles for rock blocks above, a de-saturated zone within the rock matrix was indicated. The more pronounced de-saturated zone reaches about five centimetres into the rock. A dip in relative humidity was seen a few centimetres into the rock for two of the profiles. Flow from fractures that is transported in the bentonite (axial transport) may influence relative humidity in bentonite and mask effects of matrix wetting.

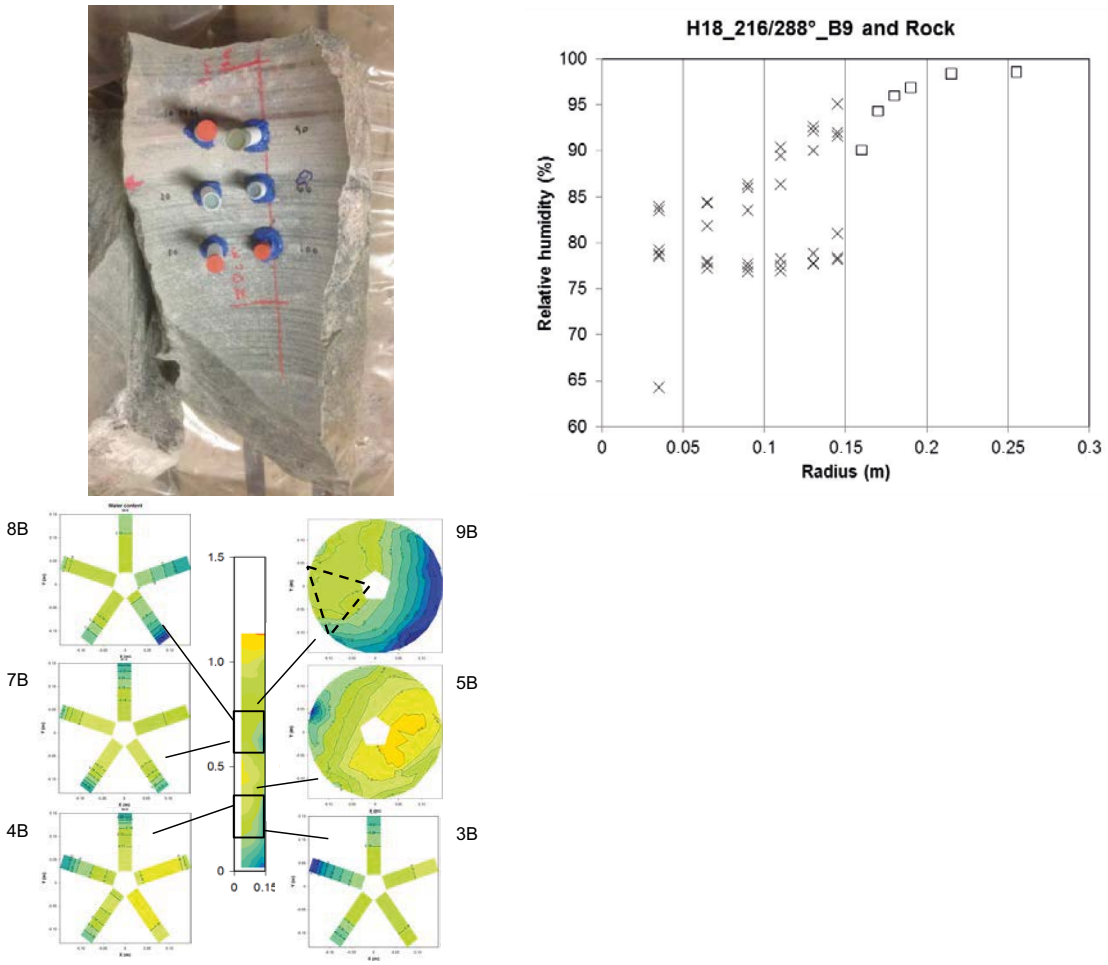

Figure 5-26. *Snap-shot of RH-profile in bentonite and rock, KO0018G01, Lifting of parcel 2014-03-04. Drilling of boreholes in rock (0.01–0.1 05 m, 2014-03-12) and measurement 2014-03-20. Dashed triangle on the contour plots of water content compilation give the approximate orientations of sampling profiles.*

6 Concluding remarks

The concluding remarks are presented using the sub-headings: Methods; Results and Potential improvements of methods.

Methods

Characterisation of rock included development of both equipment and investigation methods:

- The Nappy test equipment was developed at Chalmers University of Technology and consists of a cylinder of approximately 1 m length and 0.3 m diameter covered by rubber that can be inflated using gas pressure to fit the borehole. Nappies are attached to its surface before inflating.
- Tunnel flow measurements were performed on the tunnel floor using sorbing mats. Sorbing mats have not been used for this purpose before and a comparative study using both a weir and sorbing mats would be interesting to further evaluate the method.
- A permeameter was developed for investigation of hydraulic conductivity of rock samples (diameter 60 mm and thickness 10 mm).
- Scanning of the fracture surfaces for the two fractures of main interest in 17G01and 18G01 were made through photogrammetry.
- The method used for measurement of relative humidity in rock blocks is commonly used for measurements of humidity in e.g. concrete floors. Measurements and calibration were performed by staff at the Division of Building Technology, Chalmers.

Three novel features were included in the design of the bentonite parcels:

- Parcels were designed for a 1 mm slot width between block and borehole wall.
- Parcels were designed so that the wires from the instrumentation were led through a central tube instead of on the outer surface.
- Parcels were retained with pillars against the tunnel roof instead of through anchor cables in the floor.

Instrumentation of the parcels has provided data on evolution of RH and stresses, and the dismantling operation has provided data on distributions of water content and density. In addition, photography has been used for documentation of traces of fractures.

Results

The conceptual model and the site description was an important basis for handling the objectives: An increased scientific understanding of the exchange of water across the bentonite-rock interface; and Better predictions of the wetting of the bentonite buffer.

- The conceptual scheme (Olsson et al. 1994), Table 5-1, was found useful to identify important processes, geometric features and material properties.
- Four key features were identified: One deformation zone, an EDZ, main water-bearing fractures and the rock “matrix”.
- Main fractures in the lower part of 17G01 and 18G01 provided the main wetting. Other features contributed to a smaller extent, with the exception of vertical fractures that could potentially be man-made.
- Hydraulic conductivity was found to be low and heterogeneous (10^{-15} to 10^{-11} m/s). Hydraulic conductivity was investigated on cores originating from the 76 mm boreholes (cores approximately 60 mm) meaning that any (micro) fractures in the rock matrix are expected to be smaller than this size. Likely is that both minor fractures as well as differences in rock type results in different ability to transmit water.

- Based on four RH-profiles for rock blocks from the low conductivity sections of the boreholes (rock “matrix”) a de-saturated zone was indicated. The more pronounced de-saturated zone reaches about five centimetres into the rock. A dip in relative humidity was seen a few centimetres into the rock for two of the profiles. Since measurements were performed within an area, see Figure 3-63 to Figure 3-65, and with time delay due to transport of rock blocks and preparations before measuring, these data should be looked upon as indicative.

The final objective was better characterisation methods of the deposition holes. Since investigations were chosen to investigate fluid flow in the rock mass, transport at the interface and wetting of bentonite, the different steps presented in this report (selection of site, characterisation of site and characterisation of central boreholes) give examples of a possible way to perform investigations. Increasing the knowledge from phase to phase.

Based on the experiences from the experiment a subdivision of the rock mass into domains is suggested: host rock; deformation zones and; Excavation Damaged Zone (EDZ). This is a good basis for better understanding of the system (e.g. boundary conditions or flow from deformation zone through an EDZ to adjacent boreholes).

Based on the experiences from the experiment the following steps and characterisation methods are suggested:

- Drilling
  - Documentation of depth as a function of time (e.g. start, 0.5 m, 1.0 m etc.).
  - Indicate on the upper end of the rock/core a predetermined direction (e.g. direction of tunnel) to facilitate orientation of core (and fractures). Fracture orientation is very important.
  - Observe/Measure changes in inflow (link to depth).
  - Installation of a packer and saturation of borehole (preferably below the expected EDZ) to monitor pressure during drilling.
- BIPS
  - Include a photo of the rock surface with the indication of orientation.
- Core mapping.
- Posiva Flow Log
- Short duration hydraulic tests (flow and injection).
- Transient hydraulic tests (Injection and Recovery and/or Flow and Pressure Build Up).
- Nappy test if interested in flow distribution around the central (or deposition) borehole wall.

For all hydraulic tests it is of importance to consider measurement limit. PFL was useful only for the most water-bearing boreholes (detection limit approximately 30 ml/h) and the equipment used for hydraulic testing (long and short duration) had a low measurement limit (flow organ, Figure 3-10).

Features having hydraulic properties between what were identified in the field (using boreholes) and the laboratory (hydraulic properties of rock samples, diameter 60 mm and thickness 10 mm) were not described sufficiently well to provide detailed data for wetting. Since the experiment was focusing on wet and dry sections it did not provide data for all features.

Considering mechanics and hydromechanics, numerical modelling would be interesting to investigate if rock stresses and tunnel/borehole geometry at TASO could further explain the observed fracture behaviour at the site (e.g. fractures identified in bentonite but not in rock).

Considering the bentonite and the bentonite-rock interaction:

Water-uptake tests have resulted in a complete set of independently determined hydraulic parameter values, and have also contributed to a validation of the material model for MX-80.

The bentonite parcels have resulted in consistent data sets with major increases of RH and water content close to the main fractures of interest, especially in the lower parts of KO0017G01 and KO0018G01. Similarly, they have resulted in consistent data sets with minor increases of RH and water content in a borehole section with low water inflow, especially in section at 2.3 m depth in KO0017G01.

The average water content increase in the lower part of Hole 18 was consistent with the measured water inflow during the last phase of the characterisation program.

A pronounced gradient in water content in KO0017G01 between the main fracture of interest and the dry section indicates that the slow increase of RH observed in this section was caused by water from the fracture in question.

Inward directed gradients in water content in the lower part of KO0018G01 (Block 5) suggest that the inflow is *distributed* along the entire circumference, rather than at *localized* to discrete fractures only. A definite clarification of this question will probably require some form of modeling.

Wetting seems to be governed by fractures providing water from the geosphere, water that is further transported (axially) within the bentonite. This is expected to be particularly pronounced for fractured rock with low conductivity rock "matrix".

Potential improvement of methods

Since some of the methods related to the characterisation of rock are new (e.g. Nappy test) or used for a new purpose (sorbing mats for tunnel flow measurements), further investigation and development would be valuable. For Nappy tests it is of importance to limit the amount of water reaching the nappies from water-bearing fractures in the upper part of the borehole. Further, comparison of weir measurement to measurements using sorbing mats would be one interesting step.

Although the work with the bentonite parcels largely was made according to plan, some potential improvements of the methodology can be envisioned for future similar tests. A few minor such adjustments can be identified:

- Holes in the central tube (for cables) should be sealed, for instance with silicon.
- Pore-pressure sensors with smaller dimensions than the ones used should be more practical, since this would imply that the risk of creating a flow path from the borehole wall to the central tube would decrease.

The technique for dismantling the parcels appears to be a major task for method development.

7 Acknowledgement

Thanks to: Aaro Pirhonen for collaboration in the development and manufacturing of nappy test- and permeameter equipment; Johan Thörn for work performed in relation to hydraulic testing of rock samples in the laboratory; Christian Butron for assisting during Nappy test measurements at Äspö HRL; and Mona Pålsson performing measurements related to porosity and water content. Appreciation is also expressed for the help provided by Marek Machowski at the Division of Building Technology, Chalmers university of technology, who carried out the relative humidity measurements in rock blocks.

Several co-workers made contributions to the work with the bentonite parcels: Stefan Grandin Svärdh, Skanska, basically performed all field work in this subproject; Mats Lundqvist, SKB, was the coordinator; Terese Bladström, Lernia, performed the analyses of water content and density; Reza Goudarzi, Clay Technology, was responsible for the collection and the management of the sensors data; and Ulf Nilsson, Clay Technology, performed the function control of the RH sensors. The work and help provided by the staff at Äspö HRL and external consultants (e.g. Geosigma) is highly appreciated.

The initiation of the project and the support and participation of Anders Sjöland, Lennart Börgesson, Gunnar Gustafson, Patrik Vidstrand, Björn Gylling, Bill Lanyon, Stefan Finsterle and participants in Task 8 is also acknowledged.

References

SKB's (Svensk Kärnbränslehantering AB) publications can be found at www.skb.com/publications.

Andersson J C, 2007. Äspö Hard Rock Laboratory. Äspö Pillar Stability Experiment, Final report. Rock mass response to coupled mechanical thermal loading. SKB TR-07-01, Svensk Kärnbränslehantering AB.

Andersson J C, Martin D, 2009. The Äspö pillar stability experiment: Part I – Experiment design. International Journal of Rock Mechanics and Mining Sciences 46, 865–878.

Andersson J C, Martin D, Stille H, 2009. The Äspö pillar stability experiment: Part II – Rock mass response to coupled excavation-induced and thermal-induced stresses. International Journal of Rock Mechanics and Mining Sciences 46, 879–895.

Autio J, 1997. Characterisation of the excavation disturbance caused by boring of the experimental full scale deposition holes in the Research Tunnel at Olkiluoto. SKB TR 97-24, Svensk Kärnbränslehantering AB.

Bailey A, King R, Holford S, Sage J, Backe G, Hand M, 2014. Remote sensing of subsurface fractures in the Otway basin, South Australia. Journal of Geophysical Research: Solid Earth 119, 6591–6612.

Bäckblom G, 2008. Excavation damage and disturbance in crystalline rock – results from experiments and analyses. SKB TR-08-08, Svensk Kärnbränslehantering AB.

Börgesson L, 2001. Äspö Hard Rock Laboratory. Compilation of laboratory data for buffer and backfill materials in the Prototype Repository. SKB IPR-01-34, Svensk Kärnbränslehantering AB.

Börgesson L, Hernelind J, 2006. Earthquake induced rock shear through a deposition hole. Influence of shear plane inclination and location as well as buffer properties on the damage caused to the canister. SKB TR-06-43, Svensk Kärnbränslehantering AB.

Carlsten S, Stråhle A, Ludvigson J-E, 2001. Conductive fracture mapping. A study on the correlation between borehole TV- and radar images and difference flow logging results in borehole KLX02. SKB R-01-48, Svensk Kärnbränslehantering AB.

Chijimatsu M, Fujita T, Sugita Y, Amemiya K, Kobayashi A, 2001. Field experiment, results and THM behavior in the Kamaishi mine experiment. International Journal of Rock Mechanics and Mining Sciences 38, 67–78.

Cooper H H, Jacob C E, 1946. A generalized graphical method for evaluating formation constants and summarizing well-field history. Eos, Transactions American Geophysical Union 27, 526–534.

de Marsily G, 1986. Quantitative hydrogeology: groundwater hydrology for engineers. Orlando: Academic Press.

Dershowitz W S, Herda H H, 1992. Interpretation of fracture spacing and intensity. In Proceedings of the 33th U.S. Symposium on Rock Mechanics (USRMS), Santa Fe, New Mexico, 3–5 June 1992. Rotterdam: Balkema, 757–766.

Dershowitz W, Winberg A, Hermanson J, Byegård J, Tullborg E-L, Anderssson P, Mazurek M, 2003. Äspö Hard Rock Laboratory. Äspö Task Force on modeling of groundwater flow and transport of solutes. Task 6c. A semi-synthetic model of block scale conductive structures at the Äspö HRL. SKB IPR-03-13, Svensk Kärnbränslehantering AB.

Dixon D A, Chandler N A, Stroes-Gascoyne S, Kozak E, 2001. The isothermal buffer-rock-concrete plug interaction test: final report. Report 06819-REP-01200-10056-R00, Ontario Power Generation, Nuclear Waste Management Division, Canada.

Dougherty D E, Babu D K, 1984. Flow to a partially penetrating well in a double-porosity reservoir. Water Resources Research 20, 1116–1122.

Dueck A, 2004. Hydro-mechanical properties of a water unsaturated sodium bentonite: laboratory study and theoretical interpretation. PhD thesis. Lund university.

Eng A, Nilsson U, Svensson D, 2007. Äspö Hard Rock Laboratory. Alternative Buffer Material. Installation report. SKB IPR-07-15, Svensk Kärnbränslehantering AB.

Enresa, 2006. FEBEX: Full-scale Engineered Barriers Experiment. Updated final report 1994–2004. Enresa Report 05-0/2006, Enresa, Madrid.

Fransson Å, Thörn, J, 2017. Rock matrix permeability Development of a permeameter and hydraulic characterisation of crystalline rock cores. Report 2016:2, Chalmers University of Technology, Sweden.

Fransson Å, Thörn J, Ericsson L O, Lönnqvist M, Stigsson M, 2012. Hydromechanical characterisation of fractures close to a tunnel opening: a case study. In Proceedings of Eurock2012, Stockholm, 28–30 May 2012.

Graham J, Chandler N A, Dixon D A, Roach P J, To T, Wan A W L, 1997. The buffer/container experiment: results, synthesis, issues. AECL-11746, COG-97-46-I, Atomic Energy of Canada Limited.

Gustafsson C, 2013. Äspö Hard Rock Laboratory. BIPS, radar and Flexit in KA2051A01, KA3007A01, KJ0044F01 and KJ0050F01. SKB P-13-17, Svensk Kärnbränslehantering AB.

Hurmerinta E, 2015. Site investigation Äspö Hard Rock Laboratory. Difference flow logging in boreholes KO0011A01, KO0014G01, KO0015G01, KO0016G01, KO0017G01, KO0017G02, KO0017G03 and KO0017G04. SKB P-12-11, Svensk Kärnbränslehantering AB.

Hökmark H, Fälth B, Wallroth T, 2006. T-H-M couplings in rock. Overview of results of importance to the SR-Can safety assessment. SKB R-06-88, Svensk Kärnbränslehantering AB.

Hökmark H, Lönnqvist M, Kristensson O, Sundberg J, Hellström G, 2009. Strategy for thermal dimensioning of the final repository for spent nuclear fuel. SKB R-09-04, Svensk Kärnbränslehantering AB.

ISRM, 1979. Suggested methods for determining water content, porosity, density, absorption and related properties and swelling and slake-durability index properties: Part 1: Suggested methods for determining water content, porosity, density, absorption and related properties. International Journal of Rock Mechanics and Mining Sciences & Geomechanics Abstracts 16, 143–151.

Jarsjö J, Destouni G, Gale J, 2001. Groundwater degassing and two-phase flow in fractured rock. Summary of results and conclusions achieved during the period 1994–2000. SKB TR-01-13, Svensk Kärnbränslehantering AB.

Karnland O, Sandén T, Johannesson L-E, Eriksen T E, Jansson M, Wold S, Pedersen K, Motamedi M, Rosborg B, 2000. Long term test of buffer material. Final report on the pilot parcels. SKB TR-00-22, Svensk Kärnbränslehantering AB.

Karnland O, Olsson S, Nilsson U, 2006. Mineralogy and sealing properties of various bentonites and smectite-rich clay materials. SKB TR-06-30, Svensk Kärnbränslehantering AB.

Karnland O, Olsson S, Dueck A, Birgersson M, Nilsson U, Hernan-Håkansson T, Pedersen K, Nilsson S, Eriksen T E, Rosborg B, 2009. Long term test of buffer material at the Äspö Hard Rock Laboratory, LOT project. Final report on the A2 test parcel. SKB TR-09-29, Svensk Kärnbränslehantering AB.

Kristensson O, Börgesson L, 2015. Canister Retrieval Test. Final report. SKB TR-14-19, Svensk Kärnbränslehantering AB.

Munier R, 2006. Using observations in deposition tunnels to avoid intersections with critical fractures in deposition holes. SKB R-06-54, Svensk Kärnbränslehantering AB.

Olsson O, Bäckblom G, Gustafson G, Rhén I, Stanfors R, Wikberg P, 1994. The structure of conceptual models with application to the Äspö HRL Project. SKB TR 94-08, Svensk Kärnbränslehantering AB.

Rhén I, Follin S, Hermanson J, 2003. Hydrogeological Site Descriptive Model – a strategy for its development during site investigations. SKB R-03-08, Svensk Kärnbränslehantering AB.

Rutqvist J, Stephansson O, 2003. The role of hydromechanical coupling in fractured rock engineering. Hydrogeology Journal 11, 7–40.

Rutqvist J, Tsang C-F, 2008. Review of SKB's work on coupled THM processes within SR-Can. External review contribution in support of SKI's and SSI's review of SR-Can. SKI Report 2008:08, Statens kärnkraftinspektion (Swedish Nuclear Power Inspectorate).

Rutqvist J, Noorishad J, Tsang C-F, Stephansson O, 1998. Determination of fracture storativity in hard rocks using high-pressure injection testing. Water Resources Research 34, 2551–2560.

Sigurdsson O, 2013. Äspö Hard Rock Laboratory. Boremap mapping of core drilled boreholes KA2051A01 and KA3007A01. SKB P-13-32, Svensk Kärnbränslehantering AB.

SKB, 2009. Design premises for a KBS-3V repository based on results from the safety assessment SR-Can and some subsequent analyses. SKB TR-09-22, Svensk Kärnbränslehantering AB.

SKB, 2010a. Design, construction and initial state of the underground openings. SKB TR-10-18, Svensk Kärnbränslehantering AB.

SKB, 2010b. Design, production and initial state of the buffer. SKB TR-10-15, Svensk Kärnbränslehantering AB.

SKB, 2011. Long-term safety for the final repository for spent nuclear fuel at Forsmark. Main report of the SR-Site project. SKB TR-11-01, Svensk Kärnbränslehantering AB.

Snow D T, 1968. Rock fracture spacings, openings and porosities. Journal of the Soil Mechanics and Foundation Division 94, 73–91.

Svemar C, Johannesson L-E, Grahm P, Svensson D, Kristensson O, Lönnqvist M, Nilsson U, 2016. Prototype Repository. Opening and retrieval of outer section of Prototype Repository at Äspö Hard Rock Laboratory. Summary report. SKB TR-13-22, Svensk Kärnbränslehantering AB.

Svensson U (ed), Vidstrand P, Neretnieks I, Wallin B, 2008. Towards a new generation of flow and transport models for the Äspö Hard Rock Laboratory. Main results from the project Äspömodels 2005. SKB R-08-74, Svensk Kärnbränslehantering AB.

Svensson D, Dueck A, Nilsson U, Olsson S, Sandén T, Lydmark S, Jägerwall S, Pedersen K, Hansen S, 2011. Alternative buffer material. Status of the ongoing laboratory investigation of reference materials and test package 1. SKB TR-11-06, Svensk Kärnbränslehantering AB.

Terzaghi R D, 1965. Sources of error in joint surveys. Geotechnique 15, 287–304.

Thörn J, Fransson Å, 2013. Fracture aperture measurement and consequences for grouting. 7th Nordic grouting symposium, Göteborg, Sweden, 13 November 2013.

Thörn J, Fransson Å, 2014. Assigning fracture stiffness from in-situ deformation measurements. In Proceedings of DFNE 2014, 1st International Conference on Discrete Fracture Network Engineering, Vancouver, Canada, 19–22 October 2014.

Wadsö L, Svennberg K, Dueck A, 2004. An experimentally simple method for measuring sorption isotherms. Drying Technology 22, 2427–2440.

Zimmerman R W, Bodvarsson G S, 1996. Hydraulic conductivity of rock fractures. Transport in Porous Media 23, 1–30.

Åkesson M, 2012. Temperature Buffer Test. Final report. SKB TR-12-04, Svensk Kärnbränslehantering AB.

Åkesson M, Börgesson L, Kristensson O, 2010. SR-Site Data report. THM modeling of buffer, backfill and other system components. SKB TR-10-44, Svensk Kärnbränslehantering AB.

Åkesson M, Olsson S, Dueck A, Nilsson U, Karnland O, Kiviranta L, Kumpulainen S, Lindén J, 2012. Temperature Buffer Test. Hydro-mechanical and chemical/mineralogical characterisations. SKB P-12-06, Svensk Kärnbränslehantering AB.

Appendix A

Core mapping 300 mm KO0017G01 and KO0018G01

Examples from Phase 3: Characterisation of central boreholes – 300 mm boreholes.

Table A-1. Rock types KO0017G01 and KO0018G01.

Idcode	Adjusted Secup (m)	Adjusted Seclow (m)	Recorded_ Secup (m)	Recorded_ Seclow (m)	Feature	Name
KO0017G01	0.341	3.500	0.341	3.500	Rock Type	Gabbroid-dioritoid
KO0017G01	0.001	0.341	0.001	0.341	Rock Type	Fine grained granite
KO0018G01	0.009	3.100	0.009	3.100	Rock Type	Gabbroid-dioritoid

Table A-2. Rock occurrence KO0017G01 and KO0018G01.

Idcode	Varname	Adjusted Secup (m)	Adjusted Seclow (m)	Type	Name
KO0017G01	Rock Occurrence	0.072	0.127	Vein	Pegmatite
KO0017G01	Rock Occurrence	1.030	1.069	Vein	Pegmatite
KO0017G01	Rock Occurrence	1.235	1.271	Vein	Pegmatite
KO0017G01	Rock Occurrence	1.764	1.816	Dyke	Pegmatite
KO0017G01	Rock Occurrence	1.825	1.896	Vein	Fine grained granite
KO0017G01	Rock Occurrence	2.551	2.697	Vein	Fine grained granite
KO0018G01	Rock Occurrence	0.224	0.252	Vein	Fine grained granite
KO0018G01	Rock Occurrence	0.359	0.423	Dyke	Pegmatite
KO0018G01	Rock Occurrence	0.426	0.700	Dyke	Fine grained granite
KO0018G01	Rock Occurrence	0.735	0.777	Vein	Fine grained granite
KO0018G01	Rock Occurrence	0.885	0.915	Vein	Fine grained granite
KO0018G01	Rock Occurrence	1.168	1.183	Vein	Fine grained granite
KO0018G01	Rock Occurrence	1.213	1.240	Vein	Fine grained granite
KO0018G01	Rock Occurrence	1.987	2.145	Vein	Fine grained granite
KO0018G01	Rock Occurrence	2.322	2.466	Vein	Fine grained granite

Figure A-1. *KO0017G01, 0.0–0.3 m, 300 mm.*

Figure A-2. *KO0017G01, 0.3–1.0 m, 300 mm.*

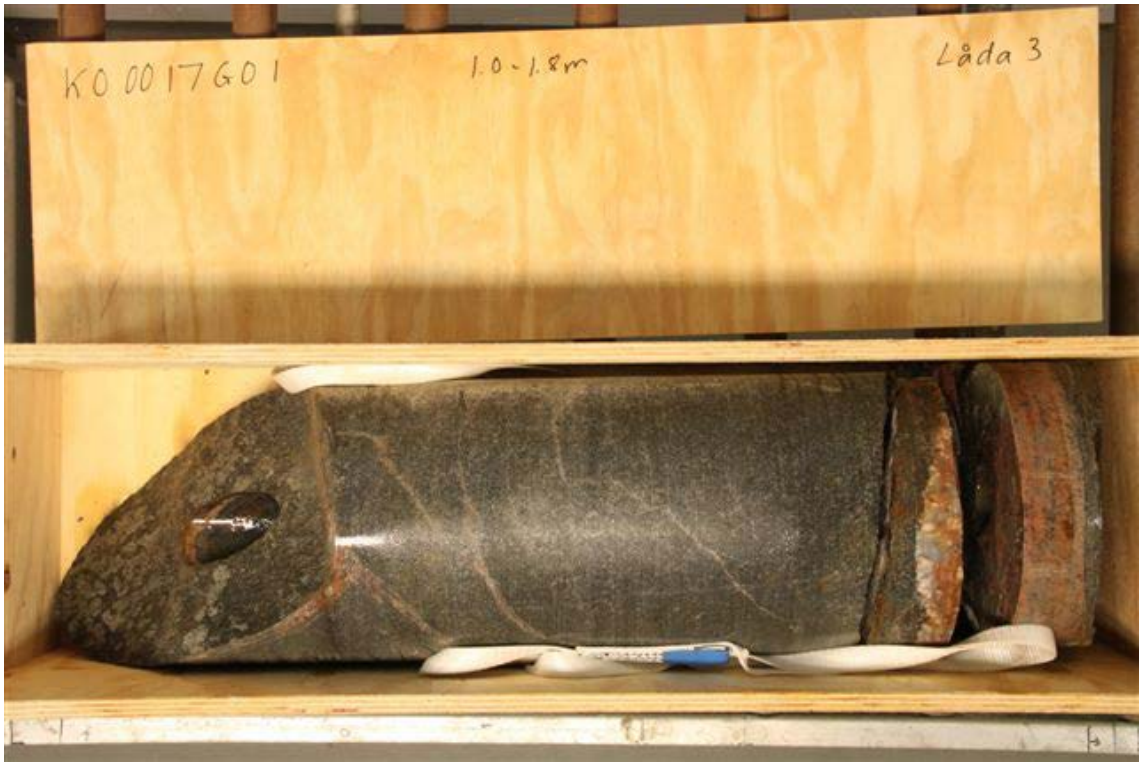

Figure A-3. *KO0017G01, 1.0–1.8 m, 300 mm.*

Figure A-4. *KO0017G01, section 1.8–2.6 m, 300 mm.*

Figure A-5. *KO0017G01, section 2.6–3.5 m, 300 mm.*

Figure A-6. *KO0018G01, 0.0–0.7 m, 300 mm.*

Figure A-7. *KO0018G01, 0.7–1.6 m, 300 mm.*

Figure A-8. *KO0018G01, 1.6–2.3 m, 300 mm. Main fracture of interest is indicated.*

Figure A-9. *KO0018G01, 2.3–3.1 m, 300 mm. Main fracture of interest is indicated (deepest part of the core).*

Table A-3. Fracture mapping KO0017G01, 300 mm.

Idcode	Adjusted Secup (m)	Recorded Secup (m)	Fract Mapped	Fract Interpret	Strike Reference	Strike (degrees)	Dip (degrees)
KO0017G01	0.346	0.35	Broken	Open	ÄSPÖ96	119.5	24.9
KO0017G01	0.997	1.00	Broken	Open	ÄSPÖ96	274.1	53.7
KO0017G01	1.692	1.69	Broken	Open	ÄSPÖ96	318.9	8.5
KO0017G01	1.842	1.84	Broken	Sealed	ÄSPÖ96	172.4	0.5
KO0017G01	1.863	1.86	Broken	Sealed	ÄSPÖ96	136.9	0.7
KO0017G01	1.940	1.94	Unbroken	Sealed	ÄSPÖ96	156.8	23.8
KO0017G01	1.978	1.98	Broken	Sealed	ÄSPÖ96	328.0	4.2
KO0017G01	**2.837**	**2.84**	**Broken**	**Sealed**	**ÄSPÖ96**	**151.3**	**62.8**
KO0017G01	2.880	2.88	Unbroken	Partly open	ÄSPÖ96	156.6	60.7

Table A-4. Evaluation of position for the main fractures of interest. The translation from dip direction to strike, and from RT90 to Äspö96 was calculated as −90° and +12°, respectively.

Test hole	Strike	Dip
KO0017G01	196 (dip dir; RT90) + 0 → **118** (Äspö 96)	arctan(6.7/3) = **66°**
KO0017G01	**151.3** (+33.3)	**62.8** (−3.2)

→ for KO0017G01 fractures strike should be reduced by 33.3 degrees.
Dip is approximately the same (−3.2 degrees).

Figure A-10. KO0017G01, Strike/dip (bold style in Table A-3) relate to (one of the two) fracture(s) found from 2.6 m to 3.1 m.

Figure A-11. BIPS KO0017G01, section 1.6–2.4 m, 300 mm (orientation not adjusted).

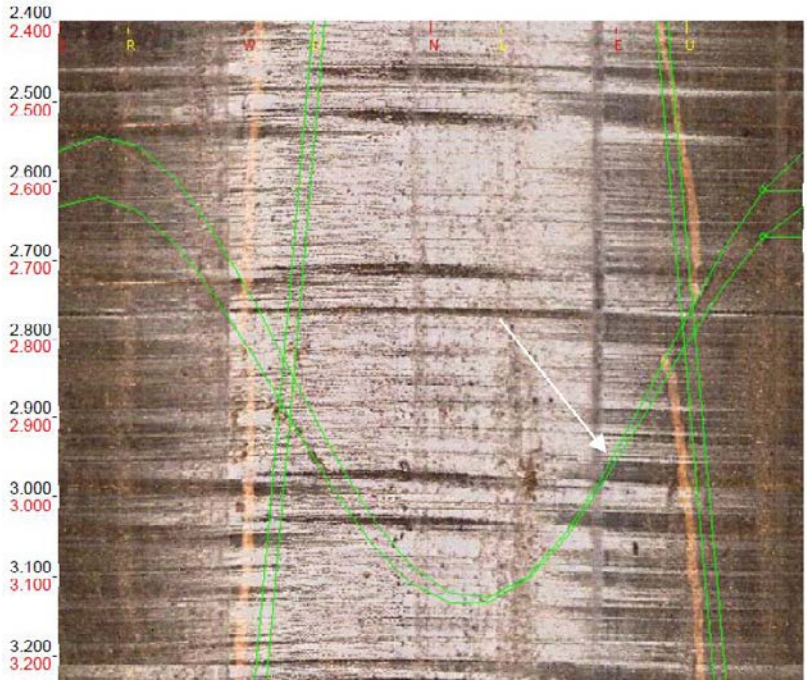

Figure A-12. *BIPS KO0017G01, section 2.4–3.3 m, 300 mm (orientation not adjusted). Main fracture, indicated by an arrow in the image, see Table A-4).*

Table A-5. Fracture mapping KO0018G01, 300 mm.

Idcode	Adjusted Secup (m)	Recorded Secup (m)	Fract Mapped	Fract Interpret	Strike Reference	Strike (degrees)	Dip (degrees)
KO0018G01	0.294	0.29	Broken	Sealed	ÄSPÖ96	41.5	23.7
KO0018G01	0.733	0.73	Broken	Sealed	ÄSPÖ96	106.2	28.8
KO0018G01	1.615	1.61	Broken	Sealed	ÄSPÖ96	234.4	42.6
KO0018G01	1.990	1.99	Broken	Sealed	ÄSPÖ96	233.8	3.8
KO0018G01	**2.302**	**2.30**	**Broken**	**Sealed**	**ÄSPÖ96**	**226.5**	**54.1**

Table A-6. Evaluation of position for the main fractures of interest. The translation from dip direction to strike, and from RT90 to Äspö96 was calculated as −90° and +12°, respectively.

Test hole	Strike	Dip
KO0018G01	292 (dip dir; RT90) + 10 → **224** (Äspö 96)	arctan(4/3) = **53°**
KO0018G01	**226.5** (+2.5)	**54.1** (−1.1)

→ for KO0018G01 strike is approximately the same (+2.5 degrees).
Dip is approximately the same (−1.1 degrees).

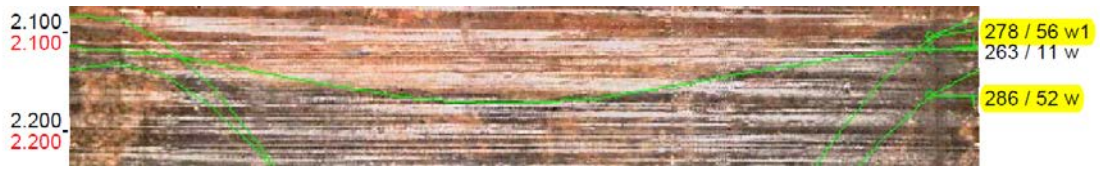

Figure A-13. *KO0018G01, Strike/dip (bold style in Table A-5) relate to (one of the two) fracture(s) fracture found from 2.1 m to 2.5 m.*

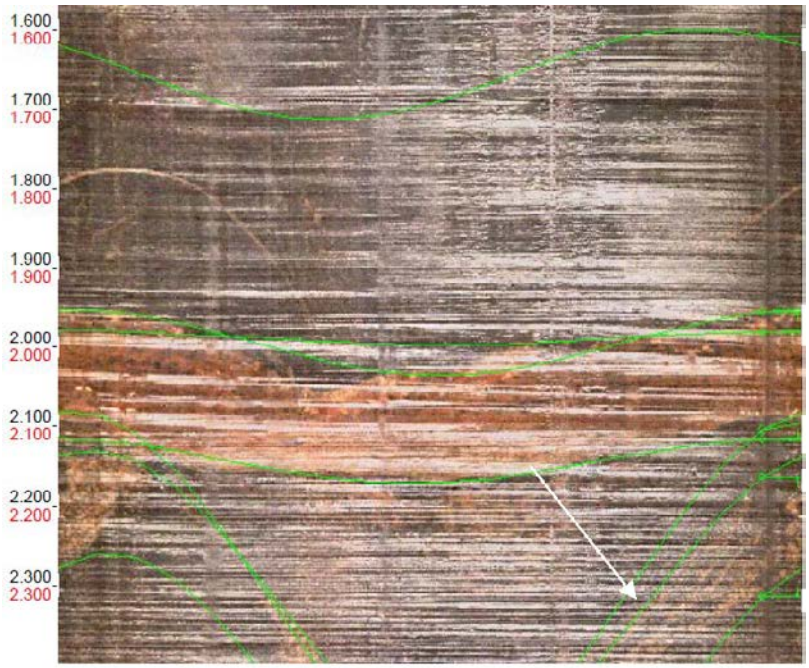

Figure A-14. *BIPS KO0018G01, section 1.6–2.4 m, 300 mm (orientation not adjusted). Main fracture, indicated by an arrow in the image, is presented in Table A-6.*

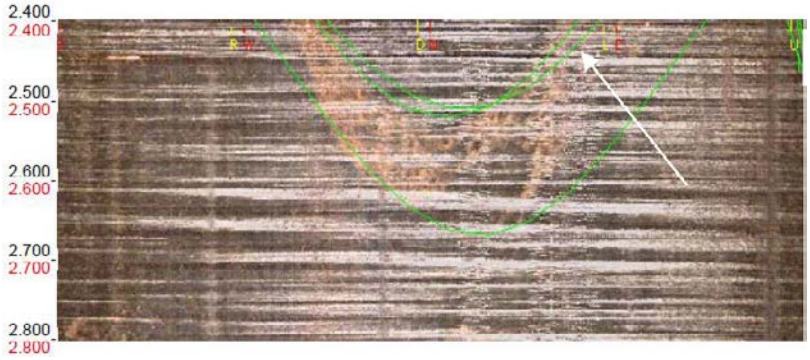

Figure A-15. *BIPS KO0018G01, 2.4–2.8 m, 300 mm (orientation not adjusted). Main fracture, indicated by an arrow in the image, is presented in Table A-6.*

Appendix B

Hydraulic tests

B1 Date, time (start, stop), activity (type of hydraulic test), object (borehole) and position along object, Phases 1–3

Table B-1. Hydraulic tests Phase 1.

Date	Time		Flag	Activity	Sub-activty ID	Object	Position along object	
	Start	Stop					From (m)	To (m)
2010-11-30	16:19	16:19	E	Injection test	2	KO0018G01	0.55	3.06
2010-12-01	15:56	18:57	EF	Injection test	2	KO0018G01	0.55	3.06
2010-12-02	09:32	10:33	EF	Injection test	3	KO0015G01	0.75	3.03
2010-12-02	11:01	18:01	CF	Injection test	3	KO0015G01	0.75	3.03
2010-12-03	09:20	09:46	E	Injection test	4	KO0020G01	0.82	3.1
2010-12-03	10:05	12:36	CF	Injection test	4	KO0020G01	0.82	3.1
2010-12-03	14:35	17:04	CF	Injection test	2	KO0018G01	0.55	3.06
2010-12-06	13:23	20:24	CF	Injection test	5	KO0017G01	0.5	2.97
2010-12-07	10:10	10:15	EF	Injection test	6	KO0014G01	0.5	3
2010-12-07	10:30	16:55	CF	Injection test	6	KO0014G01	0.5	3
2010-12-08	10:08	12:38	CF	Injection step test	7	KO0017G01	0.5	2.97
2010-12-08	14:36	17:08	CF	Injection step test	8	KO0017G01	0.5	2.97
2010-12-08	17:53	18:23	CF	Injection step test	8x	KO0015G01	0.75	3.03
2010-12-09	11:39	18:39	CF	Injection test	9	KO0014G01	0.5	3
2010-12-10	08:35	11:05	CF	Injection step test	10	KO0014G01	0.5	3
2010-12-13	13:46	20:46	CF	Constant Pressure Test	11	KO0017G01	0.5	2.97
2010-12-14	12:56	17:27	CF	Constant Pressure Step Test	13	KO0017G01	0.5	2.97
2010-12-14	18:07	18:17	F	Injection test	10x	KO0020G01	0.82	3.1
2010-12-14	19:10	19:22	F	Injection test	10x	KO0020G01	1	3.1
2010-12-14	19:52	20:02	F	Injection test	10x	KO0020G01	1.5	3.1
2010-12-14	20:14	20:24	F	Injection test	10x	KO0020G01	2	3.1
2010-12-15	08:24	08:34	F	Injection test	10x	KO0017G01	0.5	2.97
2010-12-15	09:00	09:12	F	Injection test	10x	KO0017G01	1	2.97
2010-12-15	09:28	09:38	F	Injection test	10x	KO0017G01	1.5	2.97
2010-12-15	09:54	10:04	EF	Injection test	10x	KO0017G01	2.02	2.97
2010-12-15	10:37	10:47	CF	Injection test	10x	KO0017G01	2	2.97
2010-12-15	11:56	12:06	CF	Injection test	10x	KO0018G01	0.55	3.06
2010-12-15	13:45	13:55	F	Injection test	10x	KO0018G01	1	3.06
2010-12-15	14:24	14:34	F	Injection test	10x	KO0018G01	1.5	3.06
2010-12-15	14:41	15:01	CF	Injection test	10x	KO0018G01	1.95	3.06
2010-12-15	15:54	16:54	F	Constant Pressure Test	12	KO0017G01	2	2.97
2010-12-16	07:53	14:53	F	Constant Pressure Test	14	KO0014G01	0.5	3
2010-12-17	08:52	09:11	EF	Constant Pressure Step Test	15	KO0014G01	0.5	3
2010-12-17	09:56	13:15	CF	Constant Pressure Step Test	15	KO0014G01	0.5	3

E = Error, C = Activity comment, F = File in File Storage (Sicada).

Table B-2. Hydraulic tests Phase 2.

Date	Time		Flag	Activity	Sub-activty ID	Object	Position along object	
	Start	Stop					From (m)	To (m)
2011-09-08	09:10		E	Injection test	ID02	KO0017G01	1.32	2.57
2011-09-08	10:00		E	Injection test	ID02	KO0017G01	1.32	2.57
2011-09-08	12:30	13:22		Injection test	ID02	KO0017G01	1.32	2.57
2011-09-08	14:25	16:26		Constant Pressure Test	ID03	KO0017G01	1.32	2.57
2011-09-09	09:45	11:45		Constant Pressure Test	ID05	KO0011A01	1.01	10
2011-09-09	13:40	16:10		Constant Pressure Test	ID06	KO0018A01	1.11	10
2011-09-12	10:50	17:51		Constant Pressure Test	ID07	KO0017G01	2.11	2.97
2011-09-13	09:32		E	Injection test	ID08	KO0017G01	2.11	2.97
2011-09-13	09:57	10:17		Injection test	ID08	KO0017G01	2.11	2.97
2011-09-14	08:14	08:29		Constant Pressure Test	ID09	KO0020G04	2.0	3.5
2011-09-14	08:26	08:41		Constant Pressure Test	ID09	KO0020G03	2.0	3.5
2011-09-14	08:58	09:13		Constant Pressure Test	ID09	KO0020G02	1.42	3.5
2011-09-14	09:16	09:31		Constant Pressure Test	ID09	KO0020G01	1.0	3.10
2011-09-14	09:34	09:49		Constant Pressure Test	ID09	KO0019G01	1.42	3.5
2011-09-14	09:55	10:10		Constant Pressure Test	ID09	KO0018G03	1.42	3.5
2011-09-14	10:11	10:26		Constant Pressure Test	ID09	KO0018G02	1.42	3.5
2011-09-14	10:36	10:44		Constant Pressure Test	ID09	KO0018G01	1.42	3.06
2011-09-14	10:52	11:07		Constant Pressure Test	ID09	KO0015G01	2.1	3.03
2011-09-14	11:16	11:17		Constant Pressure Test	ID09	KO0017G04	2.21	3.5
2011-09-14	11:28	11:43		Constant Pressure Test	ID09	KO0017G03	2.1	3.5
2011-09-14	13:12	4 13:18		Constant Pressure Test	ID09	KO0017G02	1.42	3.5
2011-09-14	13:23	13:38		Constant Pressure Test	ID09	KO0017G01	2.11	2.97
2011-09-14	13:45	14:00		Constant Pressure Test	ID09	KO0016G01	2.11	3.5
2011-09-15	09:25	11:55		Constant Pressure Test	ID12	KO0011B01	1.24	10
2011-09-15	14:10	16:40		Constant Pressure Test	ID13	KO0018B01	1.28	10
2011-09-16	06:45	13:45		Injection test	ID14	KO0014G01	1.33	1.66
2011-09-19	12:53	13:13		Constant Pressure Test	ID15	KO0014G01	1.33	1.66
2011-09-19	14:09	14:29		Injection test	ID17	KO0020G04	1.42	3.5
2011-09-19	15:40	16:00		Injection test	ID17	KO0020G02	1.42	3.5
2011-09-19	16:25	16:45		Injection test	ID17	KO0020G01	1.0	3.1
2011-09-19	17:09	17:29		Injection test	ID17	KO0019G01	1.42	3.5
2011-09-19	17:47	18:07		Injection test	ID17	KO0018G03	1.42	3.5
2011-09-19	18:27	18:47		Injection test	ID17	KO0018G02	1.42	3.5
2011-09-19	19:23	19:43		Injection test	ID17	KO0018G01	2.0	3.06
2011-09-19	20:05	20:25		Injection test	ID17	KO0018G01	1.5	3.06
2011-09-19	20:45	21:05		Injection test	ID17	KO0020G03	1.40	3.5
2011-09-20	07:32		E	Injection test	ID18	KO0014G01	1.33	3.00
2011-09-20	07:41	14:41		Injection test	ID18	KO0014G01	1.33	3.00
2011-09-21	08:15	08:35		Constant Pressure Test	ID19	KO0014G01	1.33	3.00
2011-09-21	09:49	10:09		Constant Pressure Test	ID20	KO0014G04	0.525	1.5
2011-09-21	10:23	10:43		Constant Pressure Test	ID20	KO0014G02	0.575	1.5
2011-09-21	10:52	11:12		Constant Pressure Test	ID20	KO0014G03	0.57	1.5
2011-09-21	11:27	11:47		Constant Pressure Test	ID20	KO0013G01	0.535	1.5
2011-09-21	14:08	14:28		Constant Pressure Test	ID20	KO0014G01	0.52	3.00
2011-09-21	15:29	15:39		Injection test	ID21	KO0015G01	2.1	3.03
2011-09-21	16:17	16:37		Injection test	ID21	KO0017G04	2.21	3.5
2011-09-21	16:54	17:16		Injection test	ID21	KO0017G03	2.1	3.5
2011-09-21	17:50	18:10		Injection test	ID21	KO0017G02	1.42	3.5
2011-09-21	18:59	19:19		Injection test	ID21	KO0017G01	2.0	2.97
2011-09-21	19:43	19:58		Injection test	ID21	KO0016G01	2.21	3.5
2011-09-22	07:43	08:03		Injection test	ID21	KO0014G04	0.525	1.5
2011-09-22	08:15	08:35		Injection test	ID21	KO0014G03	0.57	1.5
2011-09-22	08:46	09:06		Injection test	ID21	KO0014G02	0.575	1.5
2011-09-22	09:27	09:47		Injection test	ID21	KO0013G01	0.535	1.5
2011-09-22	10:42	11:02		Injection test	ID21	KO0014G01	1.98	3.00
2011-09-26	15:37		E	Injection step test	ID22A	KO0017G01	2.7	2.97
2011-09-27	07:22	10:02		Injection step test	ID22A	KO0017G01	2.7	2.97
2011-09-27	11:11		E	Injection step test	ID22B	KO0017G01	1.0	2.97
2011-09-27	12:30	15:00		Injection step test	ID22B	KO0017G01	1.0	2.97
2011-09-28	08:52	11:52		Injection step test	ID22C	KO0015G01	1.0	3.03
2011-09-28	14:23	16:53		Injection step test	ID22D	KO0014G01	1.0	3.00
2011-09-28	17:25	19:55		Injection step test	ID22E	KO0014G01	1.0	3.00
2011-09-29	08:02	10:34		Injection step test	ID22F	KO0014G01	1.0	3.00

E = Error.

Table B-3. Hydraulic tests Phase 3.

Date	Time		Flag	Activity	Sub-activty ID	Object	Position along object	
	Start	Stop					From (m)	To (m)
2012-02-23	05:57	12:57		Constant Pressure Test	ID02	KO0018G01	2.1	3.1
2012-02-24	05:26	12:26		Constant Pressure Test	ID03	KO0017G01	2.1	3.5
2012-02-27	05:32	12:46		Constant Pressure Test	ID04	KO0015G01	2.1	3.03
2012-02-28	06:13	13:13		Constant Pressure Test	ID05	KO0014G04	0.535	1.5
2012-02-29	05:33	12:33		Constant Pressure Test	ID06	KO0018G03	1.42	3.62
2012-03-12	06:22	13:22		Constant Pressure Test	ID07	KO0017G03	2.1	3.5
2012-03-05	11:00	13:30		Deformation/Injection step test	ID08A	KO0014G04	0.53	1.5
2012-03-05	15:25	17:55		Deformation/Injection step test	ID08B	KO0014G04	0.53	1.5
2012-03-05	19:15	21:45		Deformation/ Injection step test	ID08C	KO0014G01	1	3
2012-03-06	08:48	11:48		Deformation/Injection step test	ID08D	KO0015G01	2.1	3.03
2012-03-06	14:02	16:32		Deformation/Injection step test	ID08E	KO0016G01	2.0	3.50
2012-03-06	17:52	20:22		Deformation/Injection step test	ID08F	KO0017G03	3.1	3.5
2012-03-07	07:09		E	Injection test	ID10	KO0017G01	2.1	3.5
2012-03-07	07:27	07:36	E	Injection test	ID10	KO0017G01	2.1	3.5
2012-03-07	08:08	08:38		Injection test	ID10	KO0017G01	2.1	3.5
2012-03-12	09:05	16:05		Constant Pressure Test	ID12	KO0017G01	3	3.5
2012-03-13	09:11	09:36		Injection test	ID13	KO0017G01	3	3.5
2012-03-13	11:27	11:47		Injection test	ID13x	KO0017G01	3.4	3.5
2012-03-13	12:47	13:52		Constant Pressure Test	ID13xx	KO0017G01	3.45	3.5

E = Error.

B2 Evaluation of two hydraulic tests

20101213 1346 2046 2051 ID11 KO0017G01 0.5 2.97 m, see Table 3-5.

2010-12-13 13:46 Pressure decreases

According to compilation test ends at 20:46, however pressure recovery starts at 20:51:01 and flow is measured for 425 min (13:46 + 425 min = 20:51). End time 20:51.

Time adjusted to Agarwal time.
Flow set to 4.17×10^{-9} m^3/s (constant).

For pseudoradial flow: horizontal derivative.
Transmissivity evaluated to 4.5×10^{-11} m^2/s.

Pumping test evaluated using Dougherty-Babu (Theis and Cooper Jacob see e.g. Cooper and Jacob (1946) and de Marsily (1986)).

20110909 0945 1145 Constant Pressure Test ID5 KO0011A01 1.01–10 m, see Table 3-11.

Time adjusted to Agarwal time.
Flow set to 1.75×10^{-6} m^3/s (constant).

Transmissivity evaluated to 3.5×10^{-9} m^2/s.

Pumping test evaluated using Dougherty-Babu (Theis and Cooper Jacob)

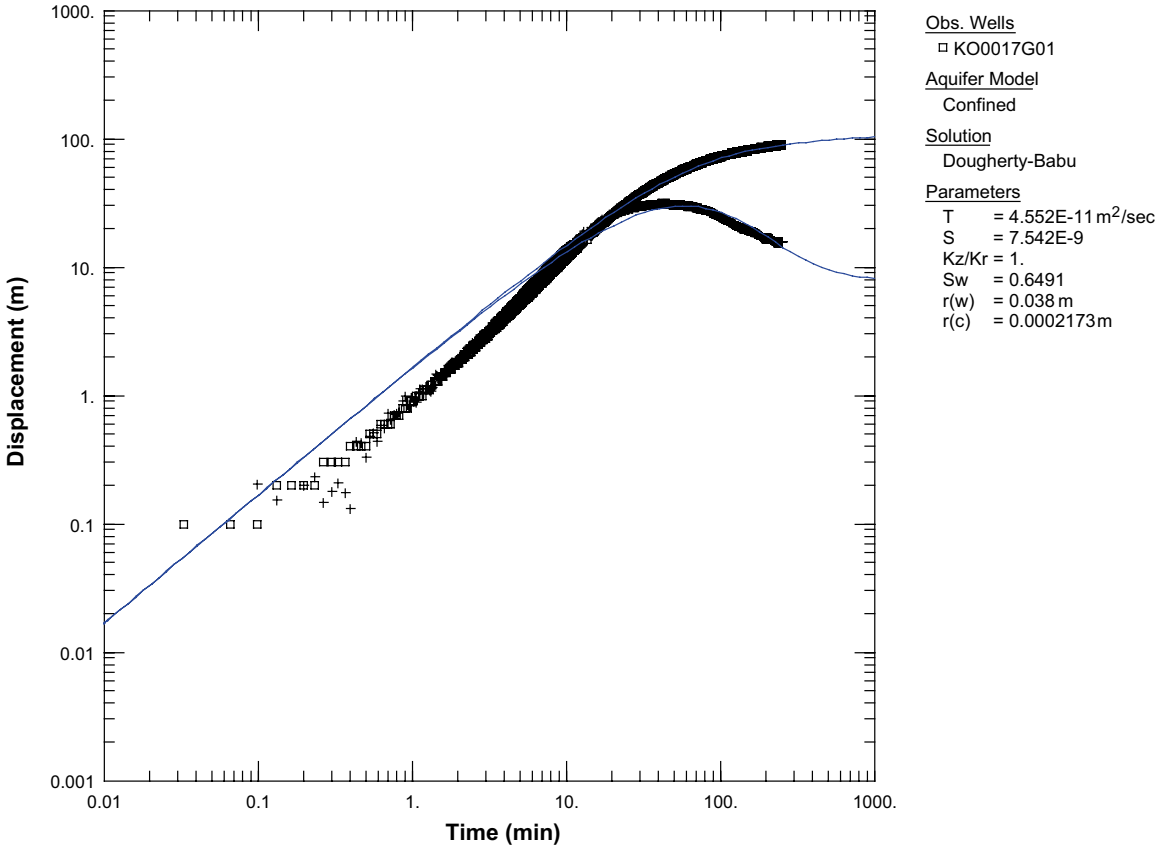

Figure B-1. *Hydraulic test KO0017G01 0.5 2.97 m.*

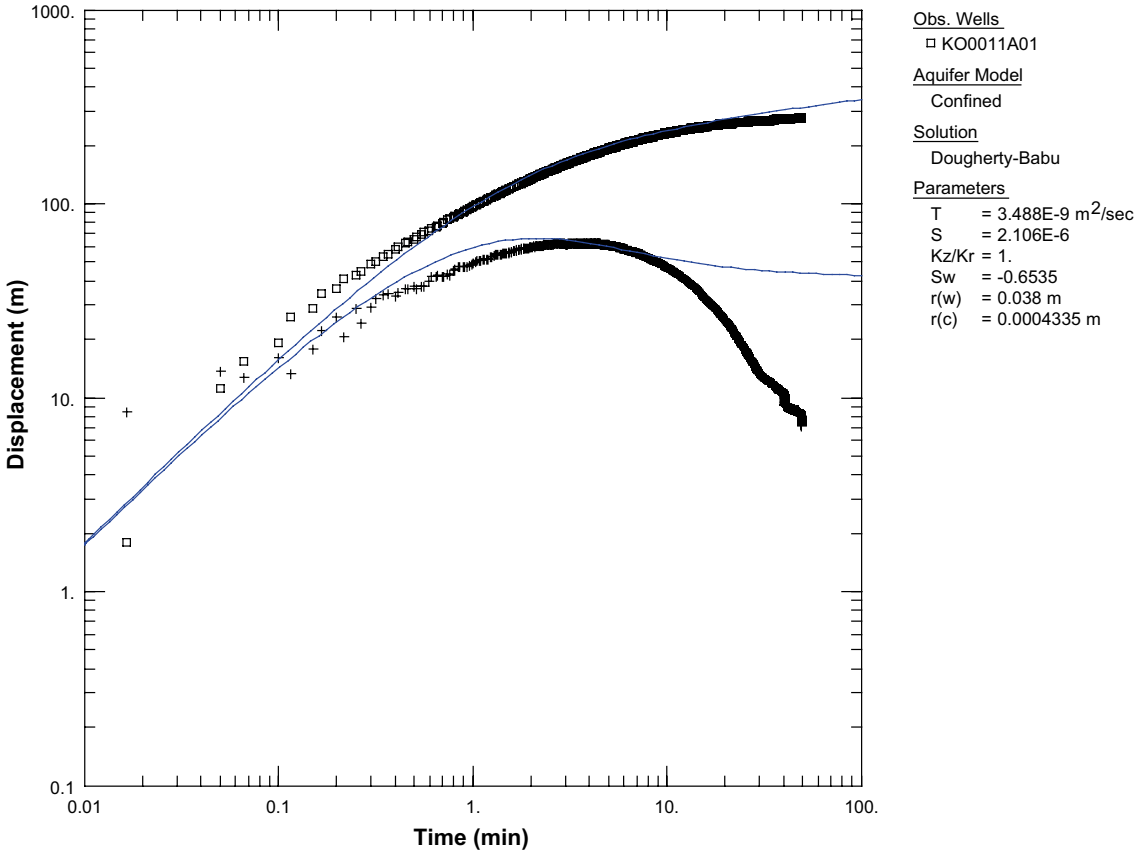

Figure B-2. *Hydraulic test KO0011A01 1.01–10 m.*

B3 Results gas sampling Phase 3

Flow Test KO0018G01 2.1–3.1 m

The interval gave a very low flow 0.011–0.033 mL/min, apart from the greater initial flow.

The total volume that flowed during the test was calculated to about 21 ml. The low flow can be a reason no gas evolution was observed during the test.

The pressure in the borehole section was read to 0.65 bar the day before and 0.56 bar just before the test. During the test the pressure in the section varied between −0.02 and −0.10 bar.

Flow Test KO0017G01 2.1–3.5 m

This test has a higher flow rate (in the range of 0.1–0.25 ml/min when excluding higher initial flow). The total volume that flowed during the test was calculated to about 116 ml. An unexpectedly high gas volume was captured by the trap: 31.25 ml. It is so great that one cannot ignore the fact that air bubbles, although thorough venting, was stuck in the borehole and then followed with the flow during the test.

The pressure in the borehole section was read to 0.23 bar the day before and to 0.19 bar just before the test. During the test the pressure in the section varied between 0.03 and −0.10 bar.

Flow Test KO0015G01 2.1–3.03 m

The test shows a declining flow from approximately 0.2–0.3 mL/min to about 0.18 ml/min. The total flow volume was estimated to about 97 ml. This is of the same magnitude as the previous test, but the gas volume is considerably lower, 0.3 ml.

The pressure in the borehole section was read to 5.71 bar the day before and even immediately before the test. During the test the pressure in the section varied between 0.08 and –0.15 bar.

Flow Test KO0014G04 0.535–1.5 m

This test gave by far the highest flow of the four. Final flow was 2.75 ml/min and the total flowed volume was about 790 ml. Despite the high flow the gas volume was relatively low, 0.7 mL/min

The pressure in the borehole section was read to the 0.21 bar the day before and 0.08 bar just before the test. During the test the pressure in the section varied, in the beginning it was up to 0.06 bar, but during the second half of the flow period it was −0.1 bar.

Appendix C

Nappy tests

	South							North								
2.25	A	B	C	D	E	F	G	H	I	J	K	L	M	N	O	
2.45	0.005	0.007	0.006	0.006	0.005	0.006	0.006	0.005	0.006	0.005	0.004	0.004	0.004	0.005	0.007	0.08
2.65	0.006	0.006	0.006	0.006	0.005	0.006	0.006	0.009	0.024	0.009	0.023	0.005	0.005	0.006	0.006	0.13
2.85	0.016	0.008	0.005	0.007	0.006	0.007	0.007	0.007	0.006	0.006	0.004	0.010	0.014	0.007	0.010	0.12
3.05	0.010	0.009	0.008	0.005	0.007	0.006	0.007	0.007	0.006	0.006	0.007	0.005	0.015	0.007	0.008	0.11
3.25	0.009	0.013	0.007	0.007	0.008	0.006	0.011	0.007	0.007	0.007	0.007	0.008	0.012	0.008	0.008	0.13
																0.57 ml/min
																0.087 ml/min
																0.127 ml/min

Figure C-1. *Columns A to O represented by numbers 1–15 in report (direction South-West-North-East). Consequently data above (from left to right) represents what would be seen if looking at the borehole wall from inside the borehole. 2.25 to 3.25 (row) represent the approximate depth [m].*

All nappies: 0.57 ml/min
Green: 0.087 ml/min
Green + yellow: 0.127 ml/min

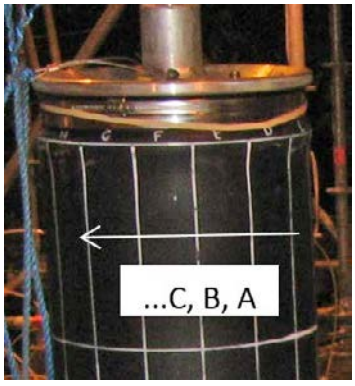

Figure C-2. *A, B, C etc for nappy test.*

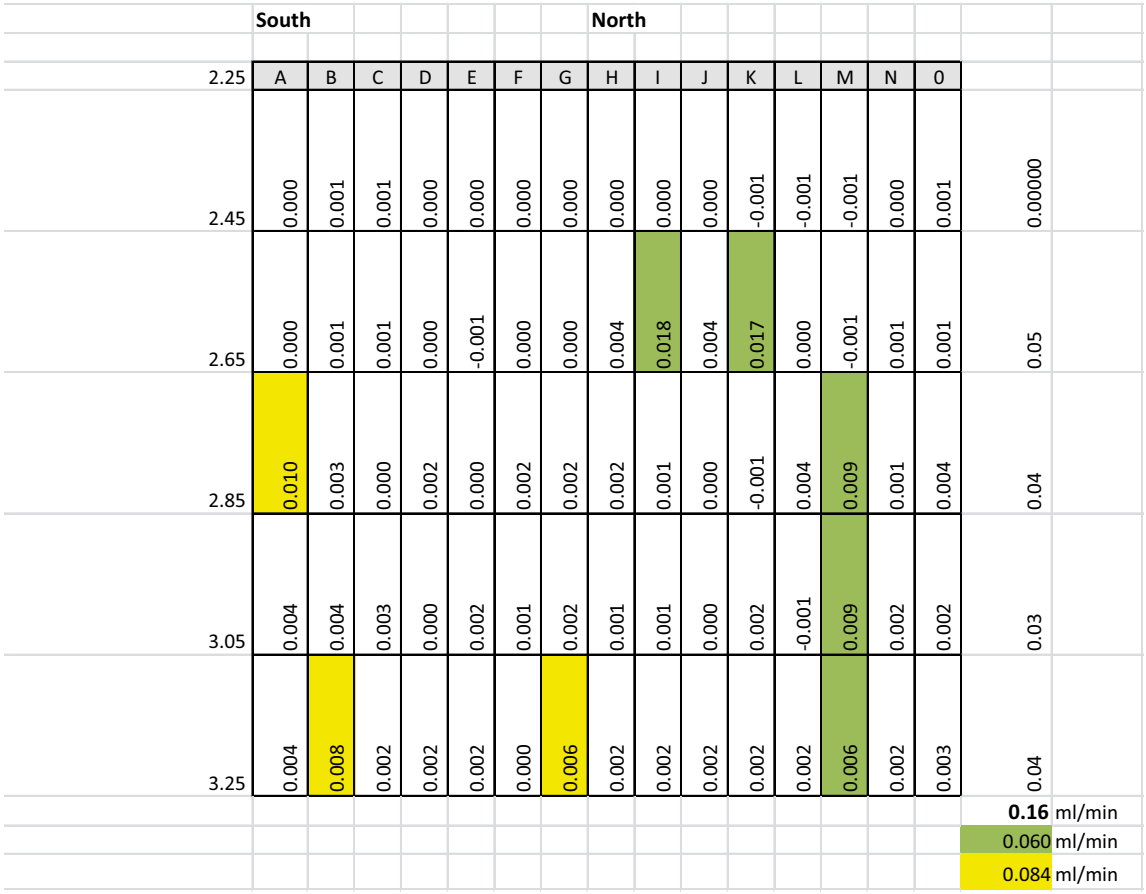

Figure C-3. *Columns A to O represented by numbers 1–15 in report (direction South-West-North-East). Consequently data above represents what would be seen if looking at the borehole wall from inside the borehole. 2.25 to 3.25 (row) represent the approximate depth [m].*

All nappies: 0.16 ml/min

Green: 0.06 ml/min

Green + yellow: 0.084 ml/min
(if subtracting background value based on upper row)

Depth [m]	Nappy [ml/min]			Inflow sections [ml/min]		
2.1						
2.15			0	**0.12**		
2.2			0.05	**0.25**		
2.25						
2.3						
2.35						
2.4						
2.45						
2.5						
2.55	0.018	0.017				
2.6	*0.024*	*0.023*				
2.65						
2.7						
2.75	0.009	0.01				
2.8	*0.014*	*0.016*				
2.85						
2.9						
2.95	0.009					
3	*0.015*		0.05		**0.13**	
3.05			0.13		**0.2**	
3.1						
3.15	0.006	0.014				
3.2	*0.012*	*0.024*				
3.25						
3.3						
3.35						
3.4						
3.45						
3.5			0.07			**0.06-0.08**

Figure C-4. *Compilation of results from nappy test (left) and hydraulic section flow (right in relation to depth). Middle column represents a possible distribution based on the two investigation methods.*

Relative humidity, water content and water retention curves

$$RH\theta := \begin{pmatrix} & \text{Diorite} & \text{Granite} \\ 100 & 0.994446 & 0.458413 \\ 85 & 0.299689 & 0.15095 \\ 59 & 0.21914 & 0.10695 \\ 32 & 0.1634 & 0.0799 \\ 10^{-1} & 0.022502 & 0.032364 \end{pmatrix}$$

RH and volumetric water contents

(Measurements at RH=0 are omitted)

$$\psi(rh) := \frac{-\ln\left(\frac{rh}{100}\right)\cdot 10^3 \cdot 8.314 \cdot (19 + 273.15)}{0.018 \cdot 10^6}$$

$i := 0..4$

$$Ret_{i,0} := \psi\left(RH\theta_{i,0}\right) \qquad Ret_{i,1} := \frac{RH\theta_{i,1}}{RH\theta_{0,1}} \qquad Ret_{i,2} := \frac{RH\theta_{i,2}}{RH\theta_{0,2}}$$

$$Ret = \begin{pmatrix} 0 & 1 & 1 \\ 21.93 & 0.301 & 0.329 \\ 71.199 & 0.22 & 0.233 \\ 153.756 & 0.164 & 0.174 \\ 932.138 & 0.023 & 0.071 \end{pmatrix}$$

Suction and saturation degrees

$P_0 := 0.6 \qquad \lambda := 0.24$

$$S_l(\psi) := \left[1 + \left(\frac{\psi}{P_0}\right)^{\frac{1}{1-\lambda}}\right]^{-\lambda}$$

van Genuchten curve

$i := 1..3$

$s1 := 0.1, 0.2.. 1000$

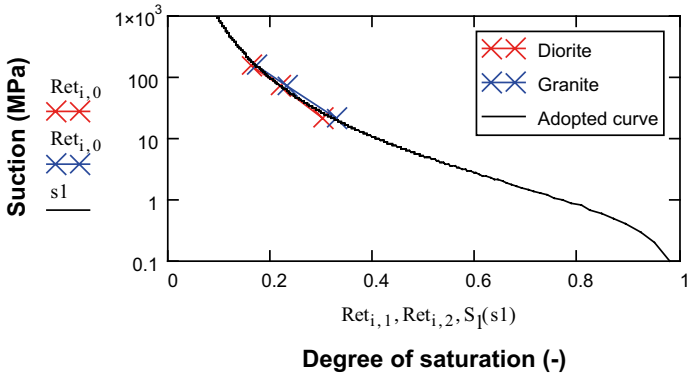

Appendix E

RH profiles Rock blocks

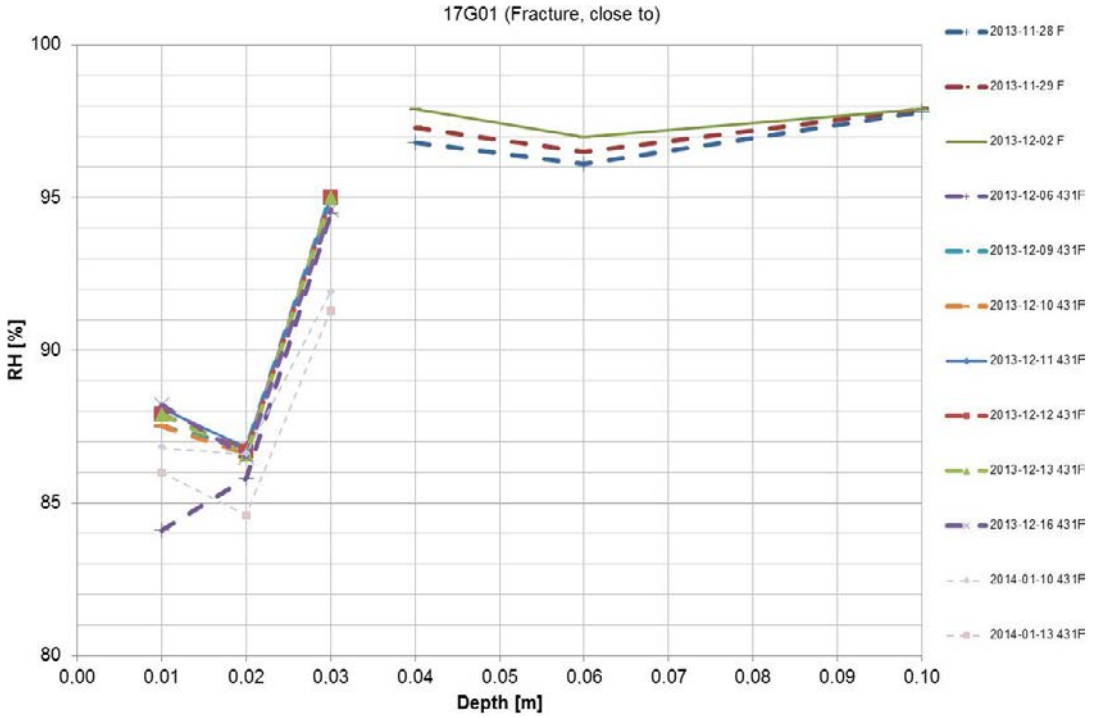

Figure E-1. *Relative humidity measurements, 17G01, close to (above) fracture,* ***F****. 2013-12-02 F (long boreholes) and 2013-12-11 431F used for RH-profile. 431F refers to gauges and location.*

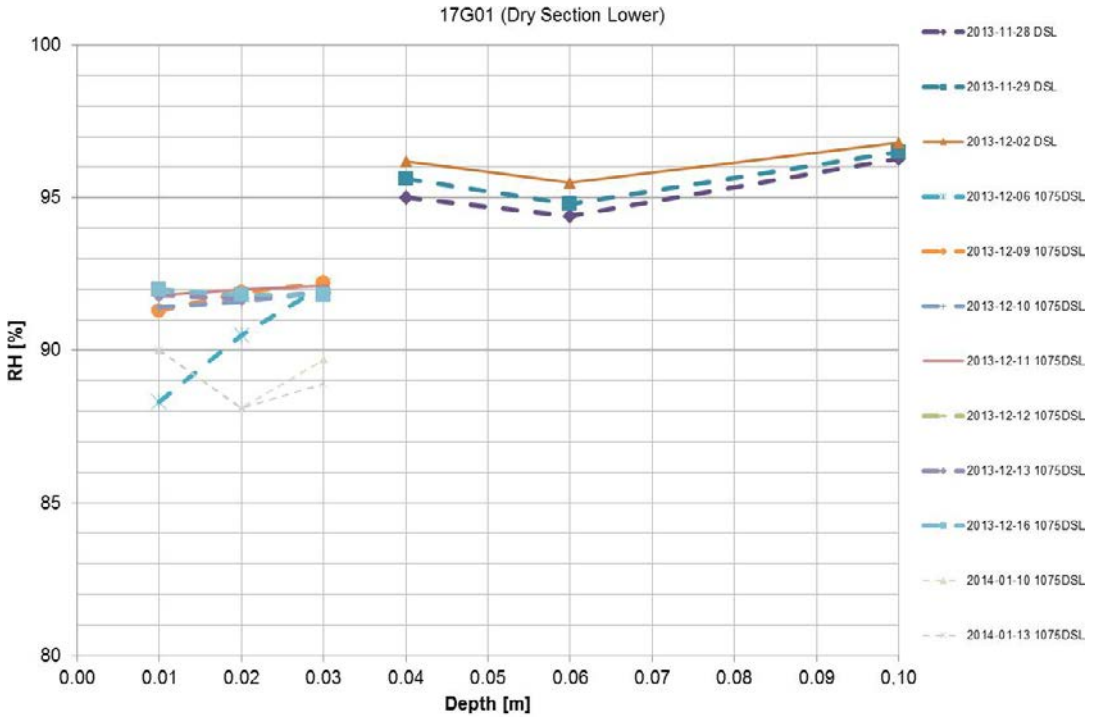

Figure E-2. *Relative humidity measurements, 17G01, lower dry section,* ***DSL****. 2013-12-02 DSL (long boreholes) and 2013-12-11 1075DSL used for RH-profile. 1075DSL refers to gauges and location.*

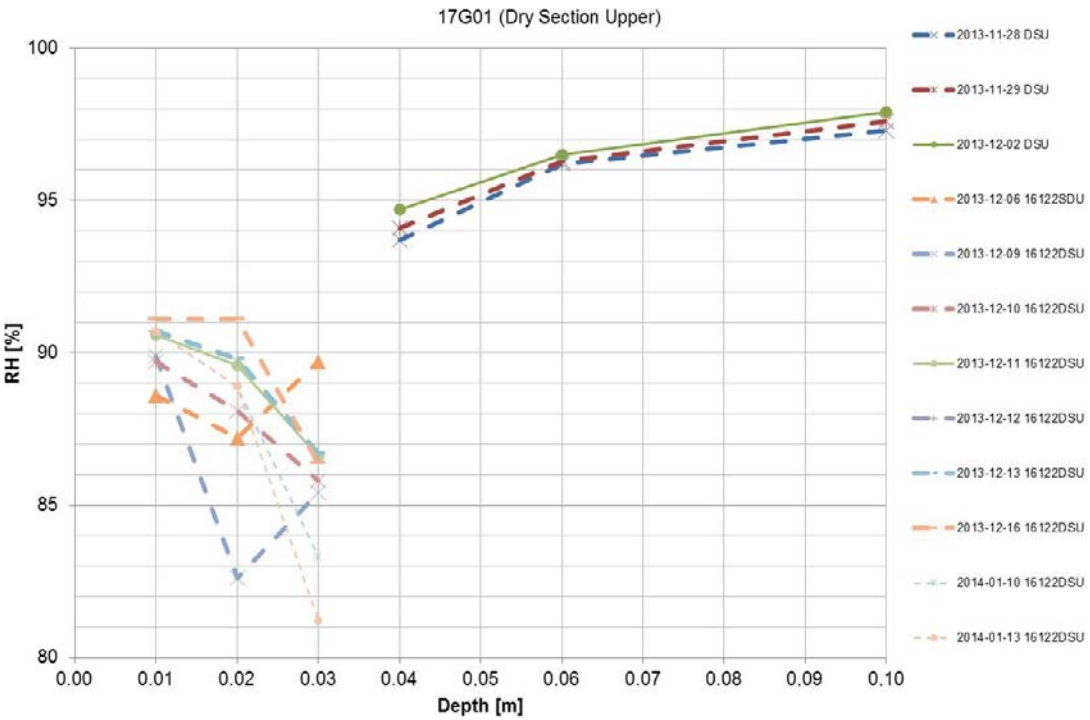

Figure E-3. *Relative humidity measurements, 17G01, upper dry section,* ***DSU****. 2013-12-02 DSU (long boreholes) and 2013-12-11 16122DSU used for RH-profile. 16122DSU refers to gauges and location.*

Appendix F

Water up-take test

F.1 Introduction

During the planning of the BRIE experiment it was noted that it would be valuable to perform parallel water-uptake tests in laboratory, and the idea was to use the same MX-80 bentonite and the same radial dimensions, density and water content as in the field test. The objective would thereby be to provide data from experiments with the two extreme conditions with completely wet and completely dry rock, which would give a clear-cut description of the hydraulic processes in the bentonite in the BRIE experiment. Apart from this it would be a significant step in the attempts to validate the material model. This report presents a description of the water-uptake tests, the results from the tests and, finally, a hydraulic evaluation.

F.2 Test program

Each test consisted of a steel cylinder with steel lids on the top and the bottom, and with a bentonite block on the inside (see Figure F-1). A dummy representing a central tube in the field experiment was inserted in the centre of the block. Water was supplied through a filter surrounding the block on the inside of the cylinder. This filter was connected to an external water reservoir. Finally, sensors for measurement of relative humidity (RH) and pressure were installed on the side and on the top lid.

Two cylinders were used in parallel for three different tests (Table F-1). One of the cylinders was hydrated with free access of water with the same approximate duration as the planned field experiment (Test 1). The other cylinder was hydrated in the same way with free access of water, but only during half the duration (Test 2). During the remaining time period another test was performed (Test 3), but this test only had access of water through the initial water filling of the slot between the block and the cylinder.

Table F-1. Analyzed test cases.

Test 1	Test 2
Free access of water ~ 200 days	Free access of water ~ 100 days
	Test 3
	Limited access of water ~ 100 days

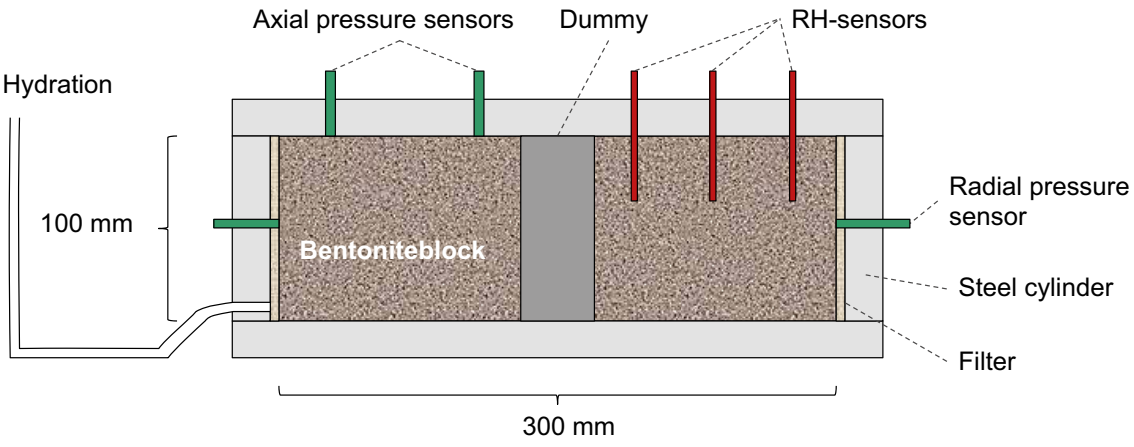

Figure F-1. *Schematic design of test cylinders.*

F.3 Manufacturing of bentonite blocks

Compaction of blocks

The blocks were compacted in a form designed for the BRIE project (see Figure F-2). The blocks had cylindrical shape with a slightly conical outer surface with a difference of approximately 5 mm between the upper and the lower diameter.

The first few blocks were used to develop a procedure for the compaction. An initial bentonite mass of 13.08 kg, and a final piston position corresponding to a block height of 100 mm, were found to give the sought dry density. Data for five blocks after compaction is given in Table F-2.

Machining and drilling

The blocks were machined with a lathe in order to obtain the sought diameter. The machining was performed by Akademiska verkstaden. For the blocks of Test 1 and Test 2 the target diameter was 298 mm, whereas the corresponding diameter for Test 3 was 302 mm. Data for five blocks after machining are given in Table F-3.

A hole was drilled in the centre of each block in order to make room for the PVC dummy representing the central tube. This was performed in a drill press with an adjustable drill bit. The diameter of the holes was 40.0–40.5 mm.

Figure F-2. *Form for compaction of bentonite blocks.*

Figure F-3. *Two bentonite blocks ready for installation.*

Two of the used blocks are shown in Figure F-3. Block with label LAB4 was used for Test 1, LAB5 was used for Test 2, and LAB3 was used for Test 3.

Table F-2. Data for bentonite blocks after compaction.

Quantity	Block LAB2	LAB3	LAB4	LAB5	LAB6
Mass (kg)	13.16	13.14	13.08	13.08	13.08
Water content (%)	11.9	11.8	11.8	11.7	11.7
Dry mass (kg)	11.76	11.75	11.70	11.71	11.71
Volume (l)	7.39	7.38	7.37	7.37	7.36
Dry density (kg/m^3)	1 591	1 591	1 586	1 588	1 590

Table F-3. Data for bentonite blocks after machining.

Quantity	Block LAB2	LAB3	LAB4	LAB5	LAB6
Mass (kg)	12.64	12.72	12.34	12.34	12.66
Diameter (mm)	300.60	301.80	297.80	297.85	301.90
Height (mm)	99.9	99.9	99.8	99.7	99.7
Volume (l)	7.09	7.15	6.95	6.95	7.14
Dry density (kg/m^3)	1 592	1 592	1 587	1 589	1 588

F.4 Test cylinders

Description of cylinders

Each bentonite block was installed in a steel cylinder which on the inside was equipped with a plastic filter. The thickness of the filter material was 2 mm, while the inner diameter of the cylinders was 304 mm. The height of the cylinders was 100 mm (see Figure F-4 and Figure F-5). Each cylinder was equipped with two holes (∅4 mm) and valves for hydration. These were located on opposite sides of the cylinders in order to maximize the distance between them. One of them (BH1) was located 10 mm from the lower end of the cylinder, while the other (BH2) was located 10 mm from the upper end. The cylinders were equipped with two additional holes (∅4 mm) and valves with membranes for sampling. These were located at mid-height (50 mm from both ends): the first one in-between the hydration holes (PH1), and the second one (PH2) was located close to hydration hole BH1. Finally, the cylinders were equipped with three holes (∅20 mm) for pressure measurements. This was made with pistons through the cylinder, and with force transducers which were installed at the outside. Two holes were equipped with pressure transducers (RP1 and RP2). The third hole served as a backup, and was sealed with a piston.

Figure F-4. *Lid with holders for RH-sensors, and filter for gas pressure sensor (left). Cylinder with filter, water inlets and force transducers with pistons (right).*

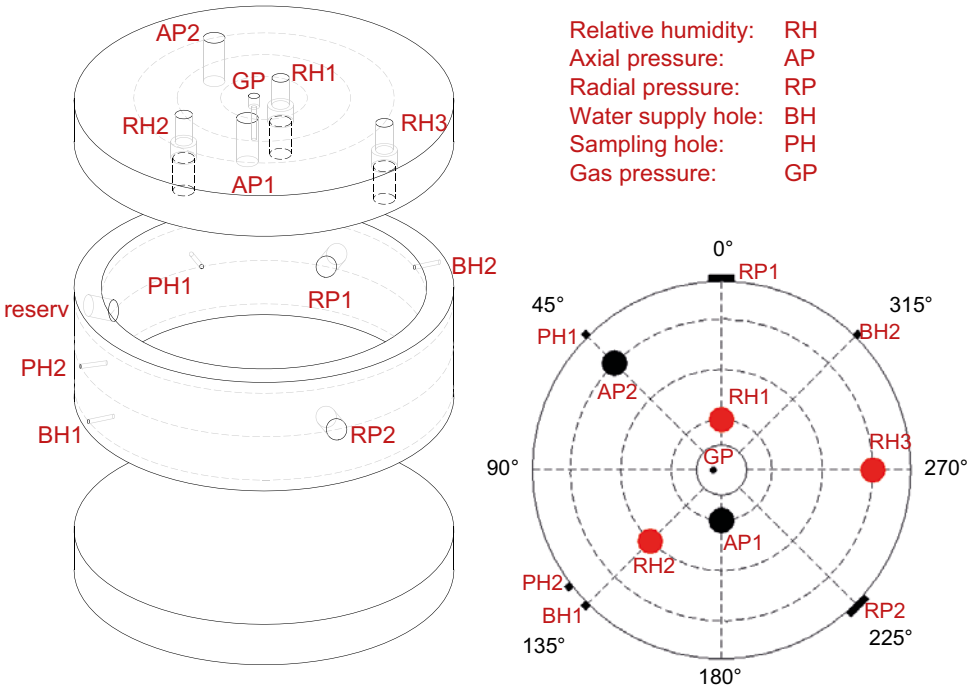

Figure F-5. *Placements of holes for ports and instruments.*

Steel lids with a thickness of 40 mm were mounted on the top and the bottom of the cylinders (see Figure F-4 and Figure F-5). The pressure measurements on the top lid were made in the same way as on the side with pistons (∅20 mm) through the lid and with force transducers. Two sets of pistons and transducers (AP1 and AP2) were located at the radii 40 and 120 mm, respectively. The RH-sensors were mounted in tubes (∅20 mm) equipped with filters which were inserted 30 mm into the bentonite. Three RH-sensors were located at the radii 40, 80 and 120 mm (RH1, RH2 and RH3). Finally, the lids were equipped with centered circular groove (∅50 mm) with a hole through the lid. Plastic filters were placed in the grooves, whereas a pressure sensor (Druck) was attached on the outside for monitoring of the gas pressure (GP). It can be noted that the radial positions of the RH-sensors are identical to the positions of the corresponding sensors in the BRIE field test.

Installation of blocks

The bottom lid was first attached to the cylinder. The block was thereafter put in place from the top of the cylinder, and centered with a feeler gauge (see Figure F-6). After this, the top lid was temporarily mounted on the cylinder without the RH sensor holders. Holes could thereby be drilled through the lid in the bentonite in which the RH sensor holders could be placed (see Figure F-7). Finally, the top lid was attached together with the sensor holders to the cylinders.

Figure F-6. *Installation of block in cylinder (left). Centering of block (right). The PVC dummy representing the central tube is seen to the left of the right picture.*

Figure F-7. Drilling of holes for RH-sensor holders.

F.5 Sensors

Force transducers

The pressure was measured with force transducers (fabricate: Sensotec) and pistons which were placed in holes through the cylinder and the top lid (Figure F-8).

All force transducers were calibrated with a load cell before the start of Test 1 and Test 2. The function of the sensors used in Test 2 was checked after the dismantling of this test, and before the start of Test 3. The function of all sensors was checked again after the dismantling of Test 1 and Test 3. These analyses showed that the original calibrations still were satisfactory.

RH sensors

The relative humidity was measured with capacitive RH sensor (fabricate: Vaisala) which were placed in holders on the top lid. These sensors were sealed off from the ambient air with silicon (Figure F-8).

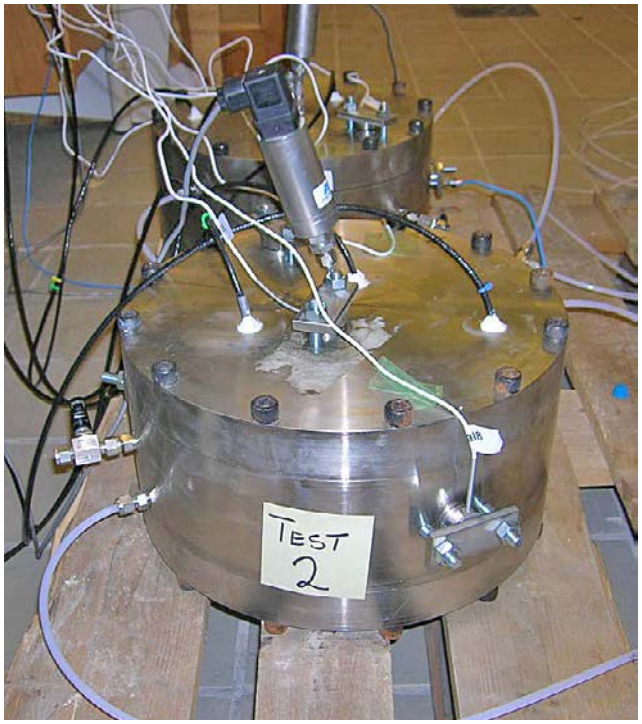

Figure F-8. Fully instrumented test cylinder; one force transducer on the side to the right; three sealed (white silicon) RH sensors on the lid; and a pressure sensor attached at the center.

All RH-sensors were calibrated in three different RH climates (RH 11.3, 75.5 and 97.6 %) before the start of Test 1 and Test 2. One of the sensors was noted to make a distinct step between two different output levels when it was exposed to RH 97.6 %, and this sensor was used for the RH3 positions in Test 2, where it showed values above 100 % (Figure F-16), and subsequently also in Test 3. The function of all RH sensors was checked after the dismantling of Test 1 and Test 3 in different RH climates (RH 33.1, 75.5 and 97.6 %). These analyses showed that the original calibrations still were satisfactory. However, a scatter within ±1.5 % was found for the RH level at 75.5 % (i.e. with output signals between RH 74 and 77). In addition, the RH3 sensor used in Test 2 and Test 3, mentioned above, showed values above 100 % in the climate with the highest RH.

Gas pressure sensors

Each cylinder was equipped with one pressure sensor (fabricate: Druck) in order to monitor the potential build-up of gas pressure in the cylinders.

Data logger

A 24-channel data logger (fabricate: Intab) was used for data collection. This was controlled through the EasyView software installed on a PC laptop.

F.6 Water supply system

Water with a content of 4 g NaCl + 2 g $CaCl_2$ per litre was used for the water uptake. This composition was chosen with the intention to resemble the concentrations at the field test. The water was supplied to each cylinder from a reservoir with constant head. The reservoir consisted of a transparent plastic cylinder with a mm scale for manual volume reading (see Figure F-9).

The first step of all tests was the water-filling of the circumference (i.e. the slot and the filter in Test 1 and 2) without trapping air in the systems.

The original plan was first to evacuate the entire system, and then to let in water from the two ports (BH1 and BH2) simultaneously. The plan was however modified in a way so that no evacuation was required. At first water was let in from one side (BH1) while the other port (BH2) was open to the atmosphere (Figure F-10).

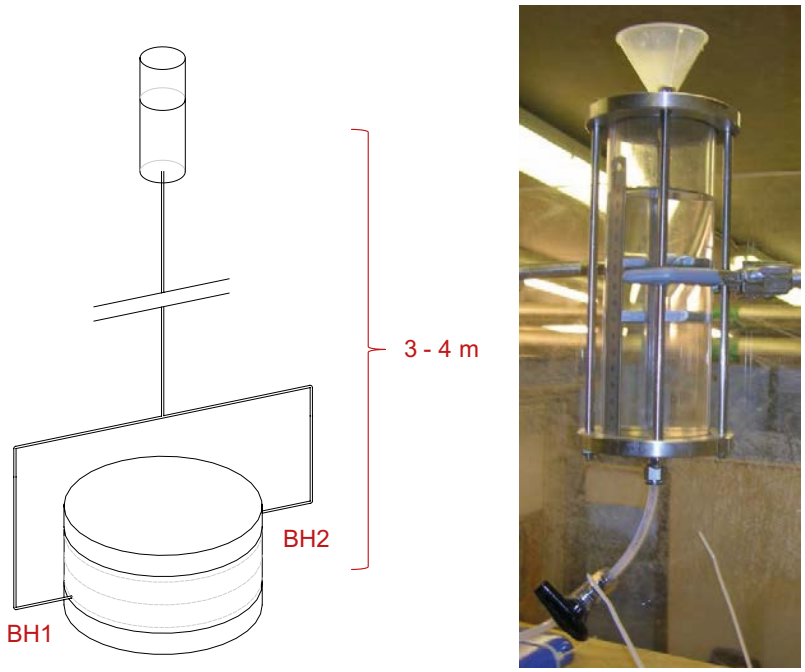

Figure F-9. *Water reservoir for maintaining a constant head (left) and for flow measurements (right).*

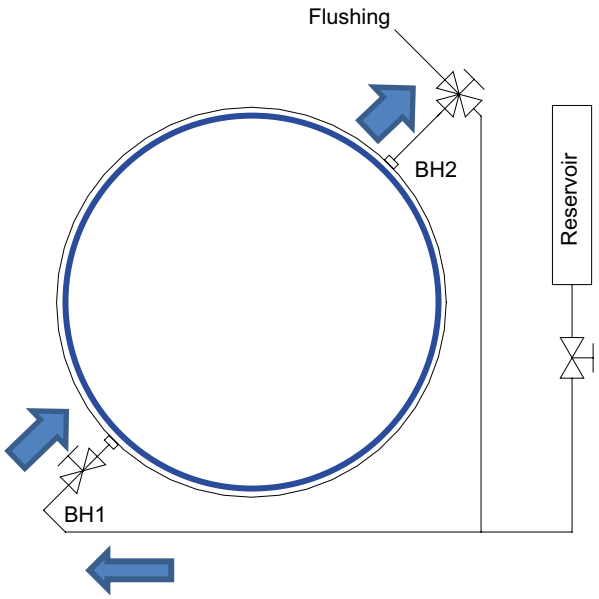

Figure F-10. *Scheme for the water supply during the filling of the filter.*

The water was allowed to flow though the system for a few minutes in order to release air bubbles, while all out-flowing water was collected. After this the water was let in from both ports. The inflow rate in Test 1 was quite different than the rate in Test 2. In Test 1 it took approximately 40 s to fill the first 0.3 l, while the filling of the corresponding volume in Test 2 took approximately 10 min. This difference is discussed in Section F.11. After one day, the system was "flushed" again for a few minutes in order to release air bubbles. All out-flowing water was collected.

The start of Test 3 (which did not include any filter) followed a similar procedure, in which 0.13 l was filled during approximately 30 s. In that case it was not possible to do any additional flushing of the system.

F.7 Operation

A compilation of major activities and events is shown in Table F-4. This consists mainly of start and end dates of the different tests, and also the dates when filter water was sampled. A major event was the moving of Test 1 from one laboratory to another. This was made with continuous water supply, but without electricity which implied that the data sampling was cut. The data collection was restored after one day.

Table F-4. Diary with major activities and events.

Date	Activity
2012-01-30	Start of Test 1 and Test 2
2012-01-31	Flushing of filters in Test 1 and 2 (day 1)
2012-02-09	Filter water sampling Test 1 and 2 (day 10)
2012-03-20	Filter water sampling Test 1 and 2 (day 50)
2012-03-27	Power failure during one hour
2012-05-09	Filter water sampling Test 1 and 2 (day 100)
2012-05-16	End and dismantling of Test 2 (day 107)
2012-05-28	Change of location for Test 1
2012-06-05	Start of Test 3
2012-06-29	Filter water sampling Test 1 (day 151)
2012-08-20	End and dismantling of Test 1 (day 203)
2012-09-20	End and dismantling of Test 3 (day 107)

F.8 Dismantling procedure

The dismantling of the different tests followed a general procedure:

i. The valves to the reservoir and the hydration port BH1were closed. Hydration port BH2 was open to the atmosphere. Hydration port BH1 was connected to a vacuum pump with water trap. The tube from the reservoir was disconnected.

ii. Evacuation was performed through BH1 and with open BH2. Direction was changed with evacuation through BH2 and with open BH1. The valves to sampling ports PH1 and PH2, and also the backup radial piston, was successively removed. After this the evacuation was terminated.

iii. Disconnection of all force transducers, valves, pressure sensors, RH sensors, couplings and grounding.

iv. The bolts of the upper lid were released and removed. The bolts of the lower lid were released and removed. The lids were released and removed.

v. The dummy was removed.

vi. Four directions: 60, 150, 240 and 330° were marked with lines on both sides of the block. The top side lines were marked with an "x" (see Figure F-11).

vii. The block was cut with a tiger saw in the approximate direction of 15, 195 and 285° (see Figure F-12). The latter direction was not needed in Test 3. The different parts of the block were removed from the cylinder and covered with plastic foil.

viii. In Test 1 and 2 the filter material was finally removed. In the case of Test 1, the mass of the filter parts was measured and subsequently dried for determination of water content.

ix. Twelve beam-shaped blocks (approximately 2 x 3 x 13 cm) was sawed from each block. Blocks were taken from four directions denoted 60, 150, 240 and 330°; and from three levels – denoted A, B and C (see Figure F-12 and Figure F-13). These blocks were subsequently sawed in 13 samples – denoted from 1 (at inner position) to 13 (at outer position). These were covered in double plastic bags for storage.

x. Eight of the twelve sample profiles were analyzed for water content and density.

xi. One of the twelve sample profiles (from Test 1 and Test 2) was devoted for analyses of anions and exchangeable cations.

xii. The remaining sample profiles were kept as reserve.

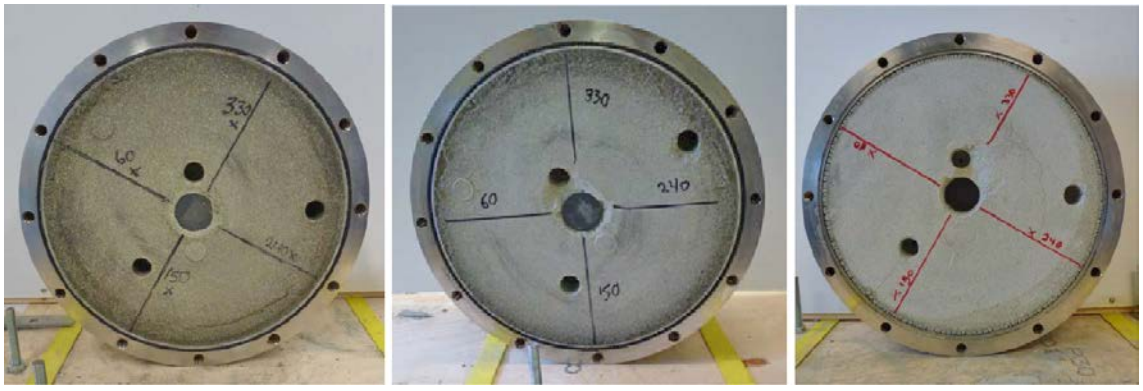

Figure F-11. *Top faces of blocks at dismantling. Test 1 (left), Test 2 (middle), and Test 3 (right).*

Figure F-12. *Sawing of block for removing block from cylinder (left) and for obtaining samples for analyses. Photos from the dismantling of Test 2.*

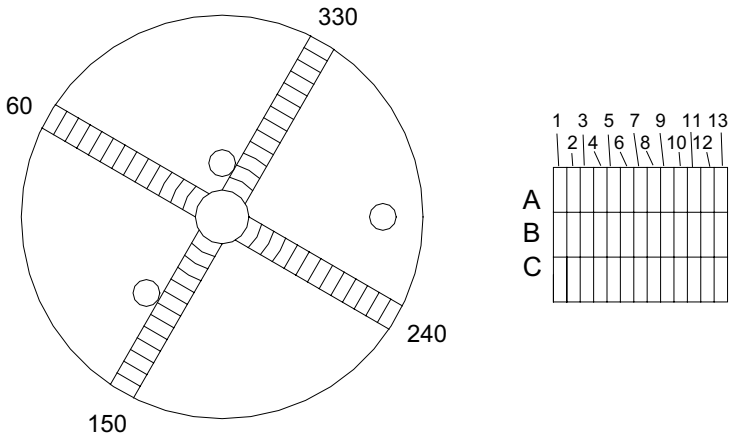

Figure F-13. *Sample profiles and principle for denomination of specific sample positions.*

The analyses of water content and density followed the procedure:

Water content

The gravimetric water content w_0 is defined as mass water per mass dry substance:

$$w_0 = m_w/m_s \quad \text{(F-1)}$$

where m_w = mass water and m_s = mass dry substance

A sample was placed in an aluminum baking-tin. The sample total mass m_{tot} was determined using a laboratory balance. The sample was then placed in an aired oven at 105 °C and after 24 hours the dry substance mass, m_s, was determined by once more weighing the sample. The original mass water m_w could then be calculated according to:

$$m_w = m_{tot} - m_s \quad \text{(F-2)}$$

Finally the water content was determined with Equation (F-1).

Bulk density

The bulk density of the sample was determined using the paraffin oil method based on the Archimedes principle. The bulk mass m_b was determined by weighing the sample freely suspended in air. Then the weight of the sample lowered in paraffin oil, $m_{bp,}$ was determined and the volume was calculated according to:

$$V = \frac{m_b - m_{bp}}{\rho_p} \quad \text{(F-3)}$$

where V is the sample volume and ρ_p is the paraffin oil density

Finally the bulk density of the sample was determined as:

$$\rho_b = \frac{m_b}{V} \quad \text{(F-4)}$$

Dry Density

Having both the sample bulk density and the water content the dry density ρ_d was determined as:

$$\rho_d = \frac{\rho_b}{(1 + w_0)} \quad \text{(F-5)}$$

F.9 Salt analyses

Sampling and analyses of filter water

Filter water samples with an approximate volume of 2 ml were collected with a syringe (see Figure F-14) from the two sampling ports of Test 1 and Test 2 at day 10, 50 and 100, and from Test 1 also at day 151. A number of samples: eight filter samples from Test 1, the two flushed water volumes from the start of Test 1, the evacuated water from the dismantling of Test 1, and a reference water sample were analysed with ion chromatography and ICP-AES equipment at the Department of Ecology, Lund University.

Analyses of bentonite samples

Bentonite samples from the 60_A positions from both Test 1 and Test 2, as well as a reference sample, were analysed for the concentration of major anions and cations.

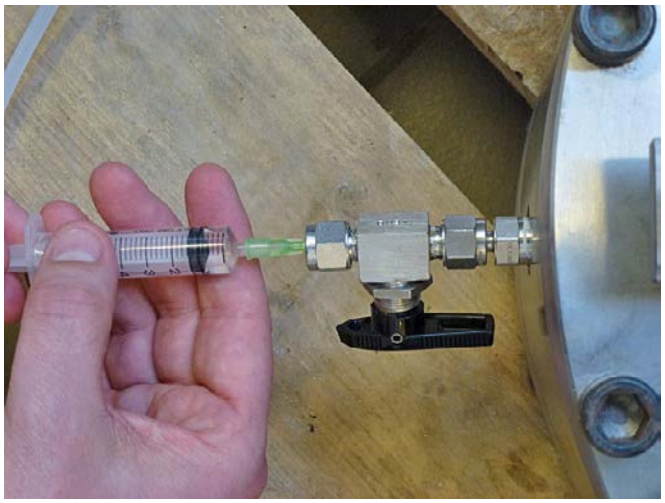

Figure F-14. *Sampling of filter water.*

Aqueous leaching of the bulk bentonite was used to obtain information about the composition of solutes and soluble salts in the bentonite. The dried (105 °C) and ground bentonite was dispersed in deionised water (solid:liquid ratio 1:100) by stirring. The suspension was left for 5 days at room temperature to allow equilibration and sedimentation. After phase separation by centrifugation and stepwise ultra-filtration using filters of decreasing pore size (from 2 to 0.2 µm syringe filters Acrodisc PF), major anions were determined by use of ion chromatography at the Department of Ecology, Lund University. The first anion analyses on bentonite samples from Test 1 gave inconsistent results when the samples were subjected to a second analysis, and these results were therefore disregarded. A new set of samples from Test 1 was subsequently prepared and analyzed.

The exchangeable cations of the bulk bentonite were determined by extraction into alcoholic ammonium chloride solution (0.15 M NH_4Cl in ~ 80 % ethanol) according to a procedure originally recommended for CEC determinations of gypsiferous/calcareous soils. An alcoholic solution was used to minimize dissolution of gypsum and calcite, which are soluble in aqueous solutions. 0.8 g of the ground sample was shaken for 30 minutes in approximately one third of a total volume of 50 ml of the extractant. After centrifugation the supernatant was collected. This treatment was repeated three times. After evaporation of the alcohol and adjustment of the volume with deionised water, the concentration of Ca, Mg, Na and K was determined by use of an ICP-AES equipment at the Department of Ecology, Lund University.

F.10 Results

Water uptake

The cumulative water-uptake in Test 1 and 2 is shown in Figure F-15. This data is based on the difference between every two successive readings of the water levels in the reservoirs. All extracted volumes from the systems (initial flushing and filter water sampling) have been subtracted from the cumulative volumes.

The first value was in both tests 0.2 litres, which represents the volume of the outer slot and the pore volume of the filter. This pore volume is discussed in Section F.11.

The evaporation from the reservoirs has been assessed with a third plastic cylinder with a mm scale. For the test period of Test 1, the evaporation in this cylinder was found to be 0.03 litres.

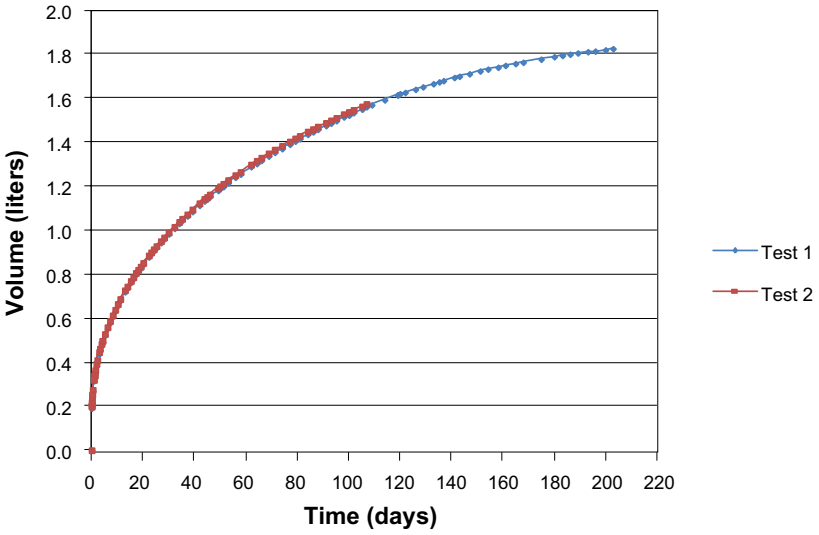

Figure F-15. *Evolution of cumulative water uptake in Test 1 and 2.*

Sensors data

Results from the RH sensors and the force transducers in Test 1 and Test 2 are shown in Figure F-16 and Figure F-17, respectively. The results from the force transducers are presented as pressures which were calculated as the ratio between the force and the piston area (3.1 cm^2). The initial RH levels were 51–52 % in both Test 1 and 2, and these levels increased successively to levels above 85 % in Test 2 and above 95 % in Test 1. The pressures increased from zero to 3–5 MPa in Test 2 and to 4–6 MPa in Test 1. The build-up of stresses at the innermost axial sensor did not start until after 40–60 days. It can be noted that the data from the first 100 days and from the same radial positions in Test 1 and 2 are quite similar. It can also be noted that the outermost RH sensor in Test 2 showed RH 100 % at day 100, and displayed higher values during the subsequent week, which obviously is unphysical.

Corresponding results of RH and pressure from Test 3 are shown in Figure F-18 and Figure F-19 respectively. These evolutions were quite different than in Test 1 and 2. The initial RH levels were 47–49 % and these increased to 56–58 % during the test period, although the outermost sensor showed temporarily slightly higher values. The difference between the final RH levels appears to be caused by the scatter of the RH sensors (see Section F.5). Finally, among the force transducers, only the radial oriented sensor showed significant values between 0.05–0.15 MPa.

Temperatures measured with the RH sensors are presented in Figure F-20 (left) which shows that the temperature varied between 12 and 24 °C. Measured gas pressures are presented in Figure F-20 (right), which shows that the gas pressure displayed a minor increase to 0.03–0.06 bar just after the start-up of Test 1 and 2, but these levels decreased thereafter.

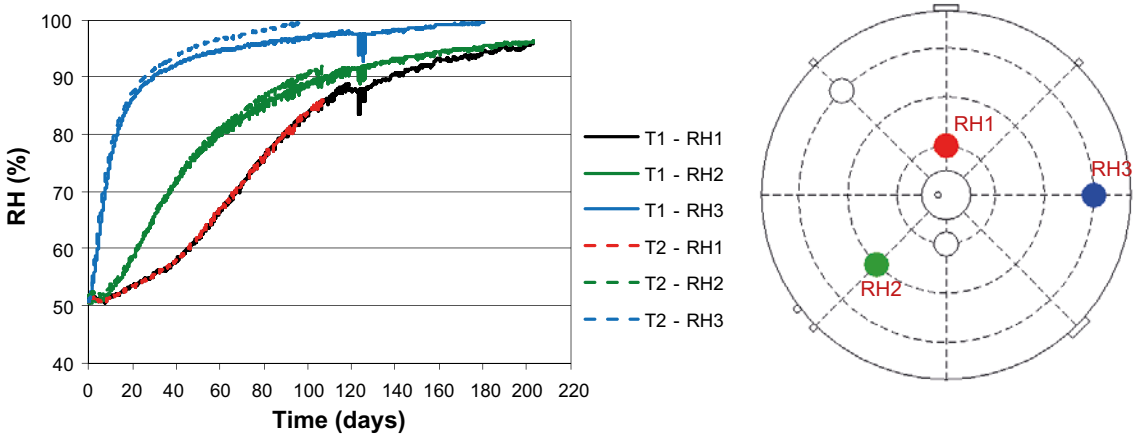

Figure F-16. *Evolution of RH in Test 1 and 2.*

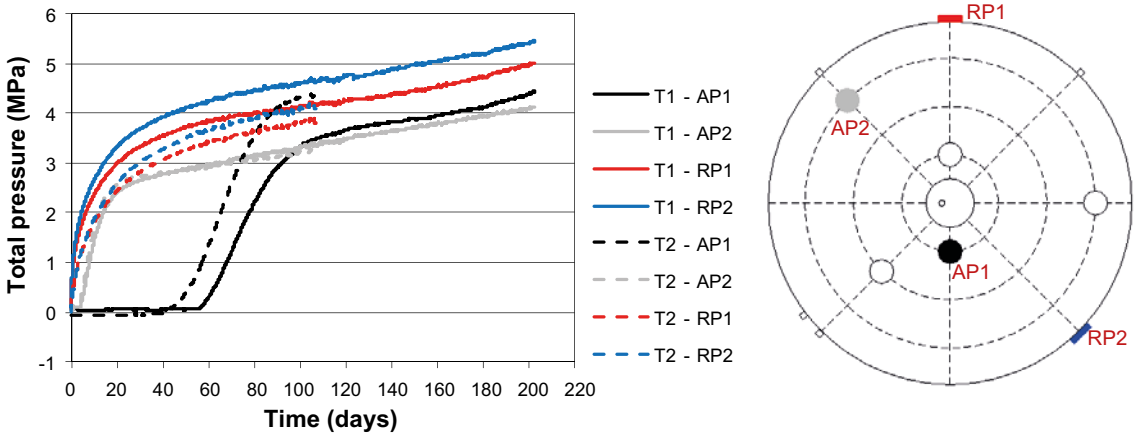

Figure F-17. *Evolution of stresses in Test 1 and 2.*

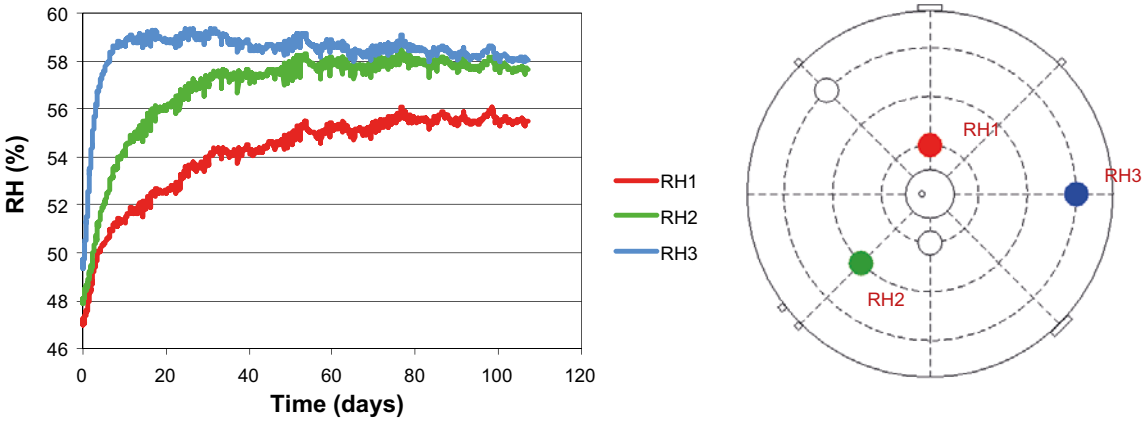

Figure F-18. Evolution of RH in Test 3.

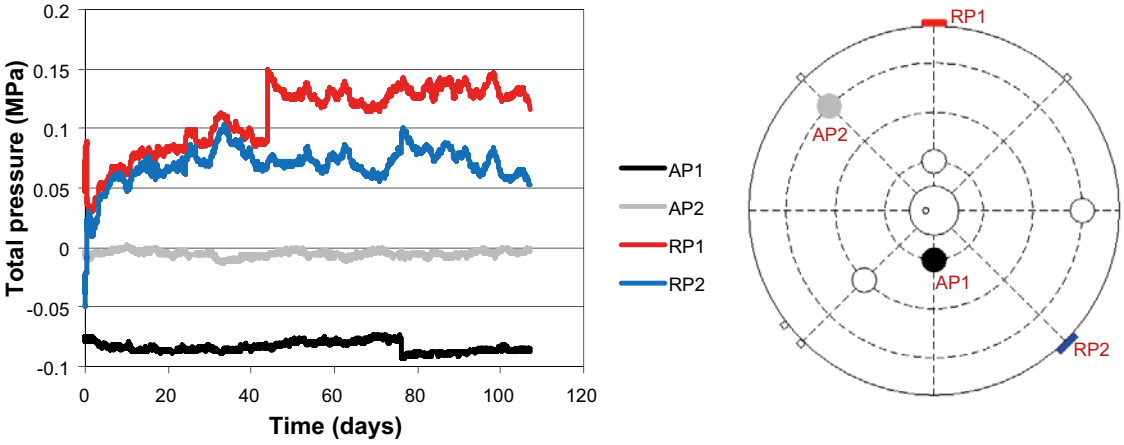

Figure F-19. Evolution of stresses in Test 3.

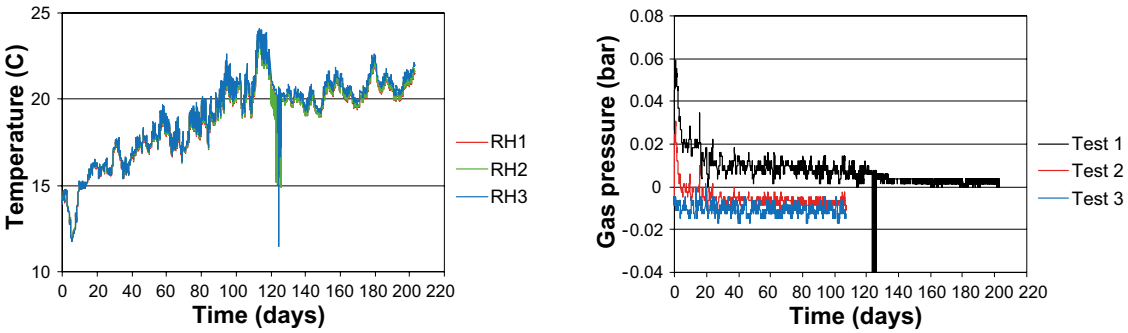

Figure F-20. Evolution of temperature in Test 1 (left) and gas pressure in all tests (right).

Dismantling data

Results from all analyses of the samples from the dismantling of Test 1 and Test 2 regarding water content and density are presented as degree of saturation in Figure F-21 and as void ratio in Figure F-22. The degree of saturation increased from an initial level of 42–44 % to values above 67–68 % in Test 2 and above 89–92 % in Test 1. The void ratio increased from a general initial value of 0.75 to profiles with values between 0.75 and 0.80 in the ten inner sample positions, and between 0.78 and 0.95 in the three outer positions. These high void ratios are commented in Section F.11.

The presentation of results from analyses of samples from Test 3 is limited to profiles of water content (Figure F-23).The density analyses are commented in Section F.11. The water content increased from a general initial value of 11.8 % to a profile with approximately the same value in the nine inner sample positions, and increasing values up to 15.6 % in the outermost position.

The initial and final data regarding degree of saturation and relative humidity from Test 1 and Test 2 can be compiled to form an in-situ retention curve (Table F-5, Figure F-24). The final degree of saturation associated with the final RH values was derived from analyzed samples with radial positions close to the radii of the RH sensors.

For Test 3, it can be noted that the final RH levels appeared to be equilibrated (Figure F-18), whereas the final water content distribution still displayed gradients (Figure F-23).

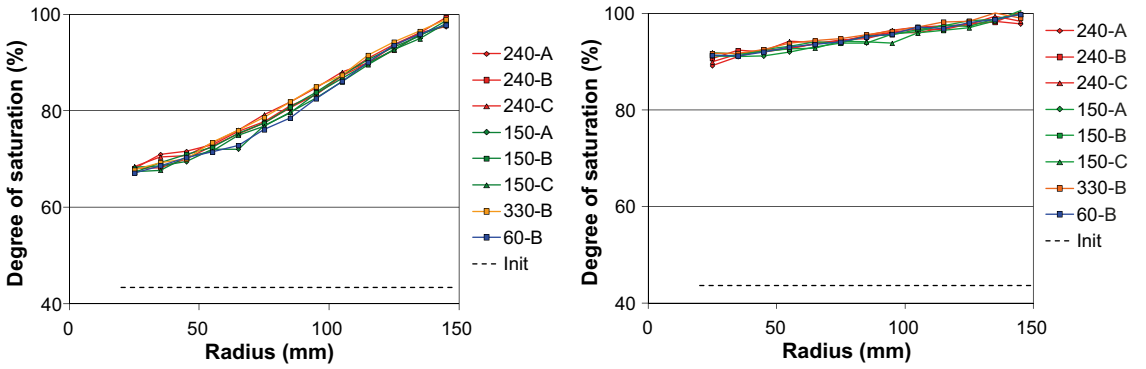

Figure F-21. *Profiles of degree of saturation in Test 2 (day 107, left) and Test 1 (day 203, right).*

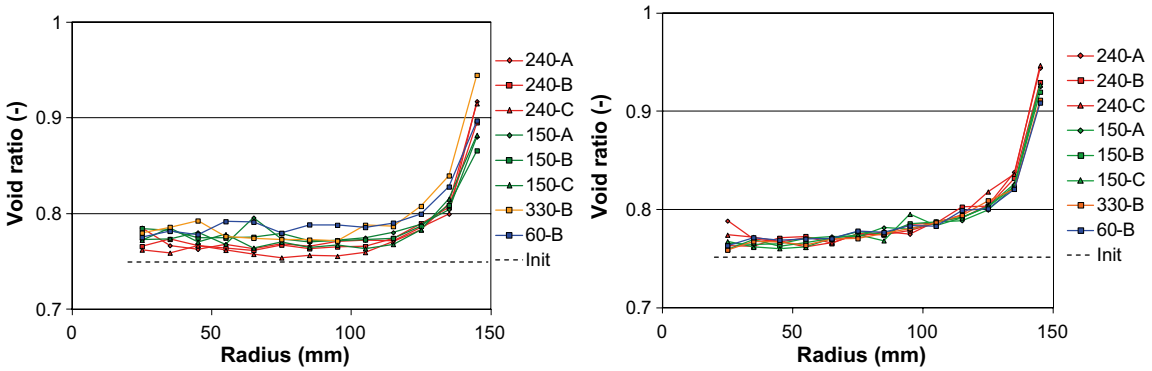

Figure F-22. *Profiles of void ratio in Test 2 (day 107, left) and Test 1 (day 203, right). The samples in the outermost position (radius 145 mm) appear to have taken up water during the dismantling operation (see Section F.11 for a discussion) and should therefore not be used for modeling.*

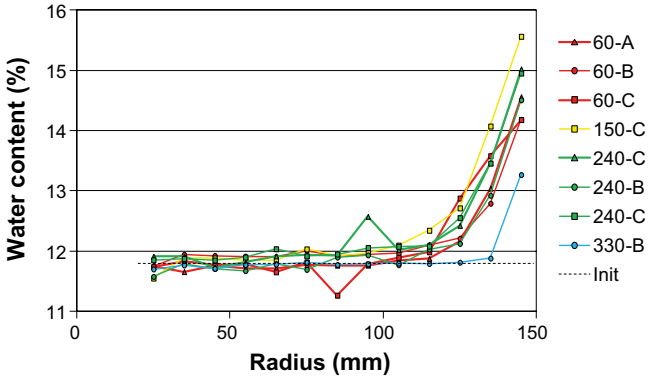

Figure F-23. *Profiles of water content in Test 3 (day 107).*

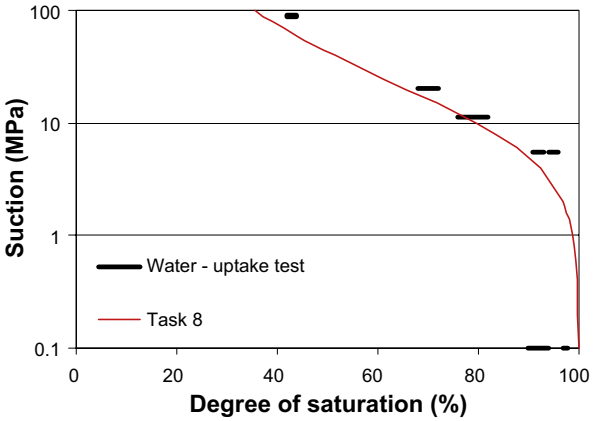

Figure F-24. *In-situ retention curve (black lines) and retention curve used in Task 8 (red line). (RH 100 % plotted at suction 0.1 MPa).*

Table F-5. Compilation of saturation and RH data.

Time, test and position	Degree of saturation (%)	RH (%)
Initial values Test 1 and 2	42–44	51–52
Final value Test 2 at 40 mm	68 –72	86
Final value Test 2 at 80 mm	76– 82	92
Final value Test 2 at 120 mm	90–94	100*
Final value Test 1 at 40 mm	91– 93	96
Final value Test 1 at 80 mm	94–96	96
Final value Test 1 at 120 mm	97–98	100*

* Final readings exceeded 100 %.

Salt analyses

Results from analyses of filter water are shown in Figure F-25. The concentration of Na^+ and Cl^- increased quite rapidly in the PH1 position (i.e. in-between the hydration holes), at least three-fold after ten days, whereas the increase in the PH2 position was slower. In the final sample obtained through evacuation of the filter at the end of the test the Cl^- had increased more than three-fold. Apart from the major increase of Na^+ and Cl^-, a minor increase could also be noted for the SO_4^{2-} and Mg^{2+} ions, whereas the Ca^{2+} ion was relatively constant.

Results from analyses of bentonite samples are shown in Figure F-26 and Figure F-27. The concentration of all major ions, with the exception for Cl^-, was found to be relatively constant on a dry matter basis. This is consistent with the notion of charge balance by the fact that the Cl^- concentration was much lower than the cation concentrations. The Cl^--level of 0.5 mg/g in Figure F-26 (left) corresponds to 1.4 meq/100 g, which is approximately 2 % of the Na^+ concentration shown in Figure F-27. In addition, the SO_4-S concentration was found to decrease in the samples close to the filter, and this is consistent with the increase of SO_4-S in the filter water (Figure F-25, right). It should be noted that the cations and the SO_4-S are not presented as clay water concentrations since this would only reflect the dilution caused by the water uptake. The Cl^- concentrations (dry matter basis), in contrast, were found to increase significantly, as well as the corresponding clay water concentrations, which were calculated by taking the water content into account (Figure F-26). At day 203 the Cl^- in the clay water was found to be in the order of 40–60 mM, which can be compared with the Cl^- in the filter water which at the same time was 340 mM.

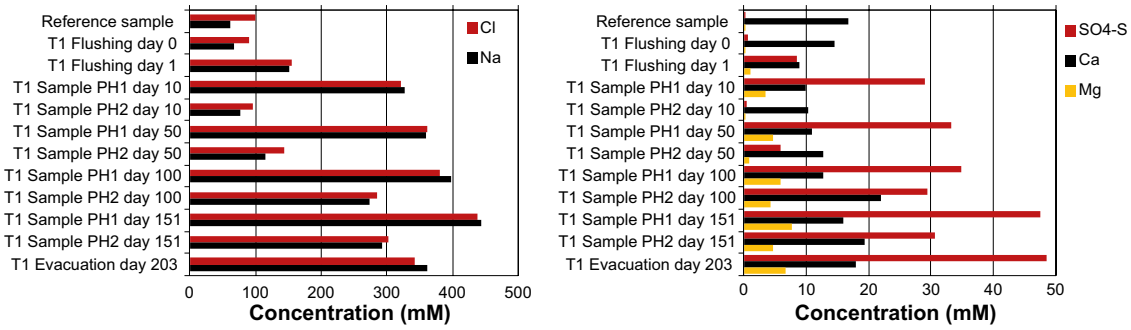

Figure F-25. *Evolution of major ions in filter water in Test 1.*

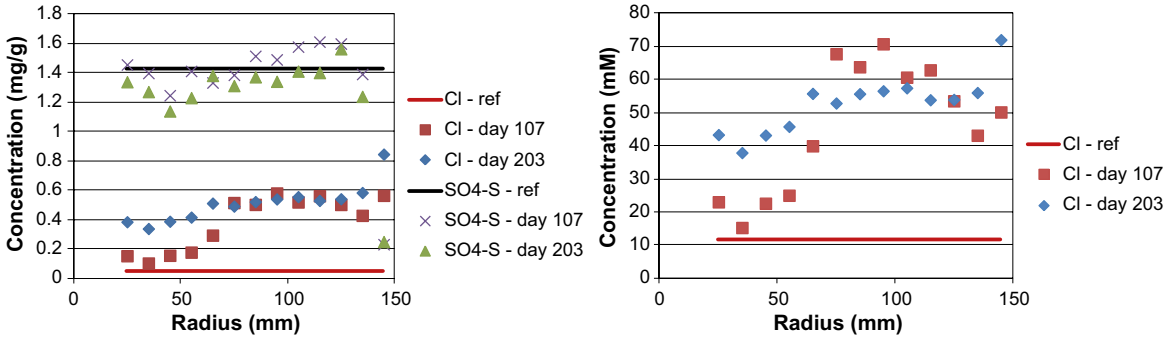

Figure F-26. *Concentration profiles of Cl^- and SO_4-S (on a dry matter basis) in Test 1 and Test2 (left). Corresponding Cl^- clay water concentration shown in right graph.*

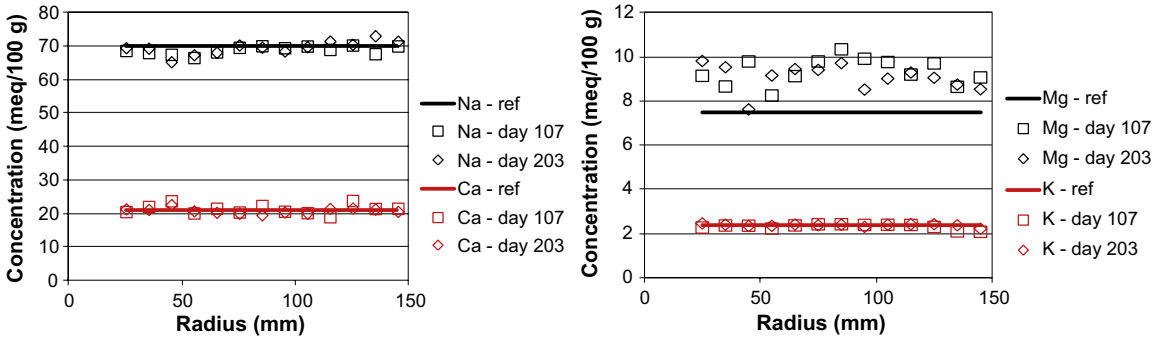

Figure F-27. *Profiles of cation concentrations in Test 1 and Test2. Note that all cations are presented as equivalents on a dry matter basis.*

F.11 Discussion

Similarities and differences between tests

Test 1 and Test 2 displayed very similar results concerning the water uptake, RH and the stresses, and this strengthens the validity of these data sets. Some minor differences could however be noticed concerning: i) the time to fill the filter and the slot with water; and ii) the early build-up of radial stresses (Figure F-28). This could tentatively be caused by differences in the positioning of the blocks in the cylinders (Figure F-29). If the block in Test 2 was located close to the water supply hole BH1 and thereby "far away" from the radial force transducers RP1 and RP2, then this could explain the slow inflow into cylinder and the slow build-up of stresses. The slow inflow would be a consequence of the water had to pass only through the filter, and not through the slot. The slow build-up of stresses would be a consequence of "long distance" the bentonite had to swell before the force transducers were affected.

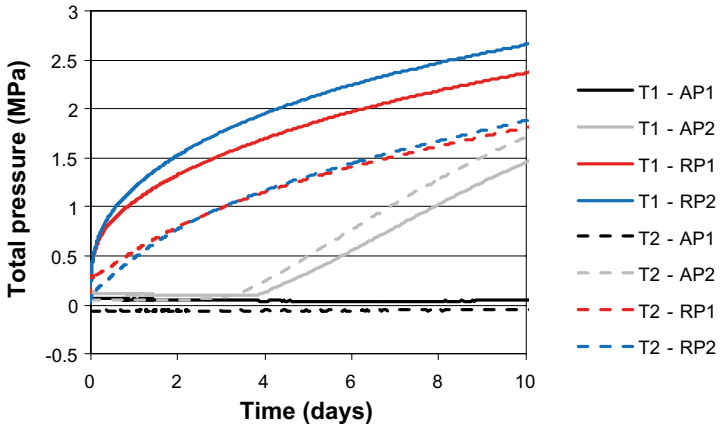

Figure F-28. *Early build-up of stresses.*

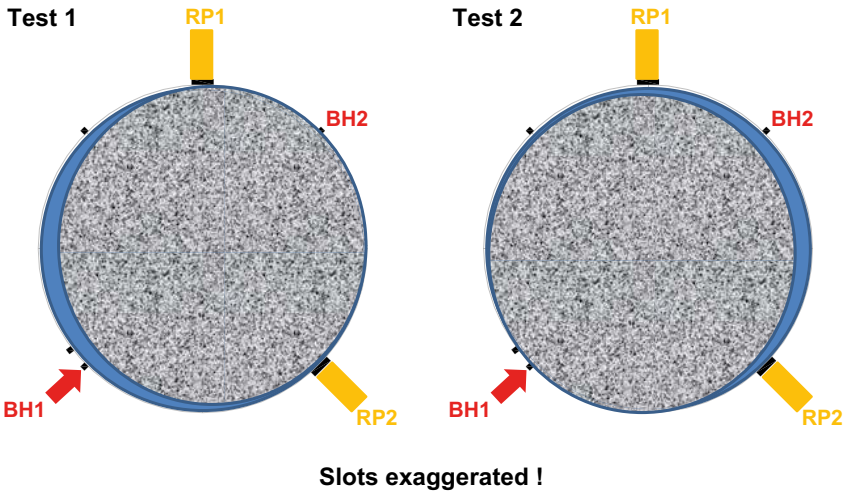

Figure F-29. *Interpretation of test behavior during start-up.*

Pore volumes of slot and filter

The initial slot volume between the block and the filter, and especially the pore volume of the filter constitute two minor uncertainties of the tests. The initial volume should be given as a ring with 1 mm thickness, 100 mm height and 300 mm diameter, i.e. 0.09 litres. The corresponding volume of the filter, with a thickness of 2 mm, would then be 0.2 litres. No information about the porosity of the filter has been found. This has instead been estimated from a measured dry density of the filter material and from tabulated values of solid densities for HDBE to approximately 0.4. In total, the pore volume of the filter would thereby be 0.08 litres. The total available volume at the start of the test would thereby be in the order of 0.2 litres, which corresponds quite well with the first values of the water uptake in Figure F-15. Still, it should be stressed that the estimation above is based on values with only one significant digit, especially due to the uncertainty of the porosity value. With two significant digits the available volume would be 0.16 litres.

Evacuated filter volumes and peripheral void ratios

The filters in Test 1 and Test 2 were purged through evacuation during the dismantling operation, and the extracted water was collected. The extracted volumes were 17 ml in Test 1 and 26 ml in Test 2. In Test 1, the dismantled filter material was also dried in order to quantify the remaining amount of water after the evacuation. The mass loss after drying was found to be approximately 10 gram. These volumes are significantly lower (~ 50 ml) than the estimated pore volume of the filters of 80 ml.

One possible explanation for this difference is that some filter water was lost to the outer part of the bentonite block during the dismantling. This could also explain the high void ratios in the outermost sample positions (Figure F-22). For example: the outermost sample in Figure F-22 represents a volume of 0.91 litres ($\pi \cdot [0.15^2 – 0.14^2] \cdot 0.1$ m^3). Moreover, an increase of the void ratio from 0.83 to 0.93 (which were the mean values for the two outer sample positions in Test 1) represents a strain of 5.5 % ([0.93–0.83]/[1+0.83]). Taken together this implies a volume increase of ~ 50 ml, which is the same value as the "missing" filter water volume.

Gas tightness

The evolution of gas pressure (see Figure F-20) reveals that the cylinders were not gas tight. The gas pressure in Test 1 and Test 2 displayed a minor increase (30–60 mbar) during the first hours, but these trends were subsequently reversed.

Density measurements at low water contents

The analyses of bentonite samples from Test 3 also included density measurements. These analyses tended however to overestimate the density. Later tests revealed that this discrepancy appears to be difficult to avoid at relatively low water contents and densities. The reason for this seems to be that paraffin oil enters the sample which thereby leads to an underestimation of the sample volume. In the case of Test 3, it was therefore decided that these results should not be taken into account. If the final profile of degree of saturation in Test 3 would be of interest, then it is advised that such a profile is based on analysed water contents and the initial dry density.

F.12 Hydraulic evaluation

Water balance

A water balance of the water-uptake tests (Test 1 and Test 2) is illustrated in Figure F-30. The lower bars represent water masses determined from data on water content, density, and volumes; the mean initial mass as well as the final masses for Test 2 and Test 1, respectively. The upper bars represent the total water-uptake in Test 2 and Test 1, respectively. The water-uptake masses are added to the initial mass, except for the filter volume which was subtracted. Some fraction of the filter water may have been absorbed by the bentonite during the dismantling and should therefore not be subtracted. This was however neglected, since the calculated final masses were based on the confining volume of the equipment (cylinder and lids), which implies a minor underestimation of the final masses.

A comparison of the right ends of the bars shows the largest discrepancy for water mass in T2 (0.12 kg). One explanation for this could be an elastic expansion during the dismantling of the tests, which would imply that the measured dry density values, and therefore also the evaluated saturation

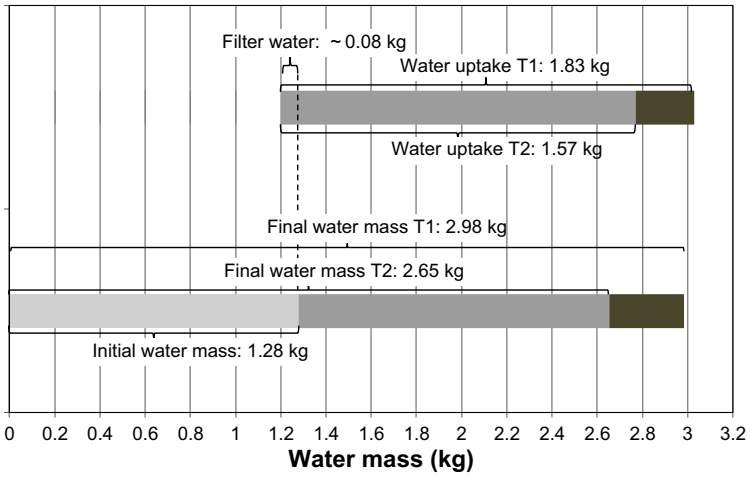

Figure F-30. *Water balance for Test 1 and Test 2. Upper bar based on inflow data. Lower bar based on data on water content, density and volumes.*

degree values were slightly underestimated. Another explanation for the discrepancy may be that water was lost from the water supply reservoirs during the test period. The evaporated mass was however measured with a reference reservoir, and was found to be ~ 0.03 kg and therefore neglected from the water balance. Still, the observed discrepancy illustrates that different experimental data sets can imply different values of the water transport coefficients.

Tool for water-uptake calculations in terms of moisture diffusivity

In order to have an efficient and transparent tool for evaluating the water-uptake a MathCad algorithm has been prepared, in which the water transport is described by a saturation dependent moisture diffusivity function $D(S)$, and in which the diffusion equation is solved with an explicit finite-difference method.

The 1D radial geometry of the water-uptake tests are discretized in n elements according to Figure F-31 (left). The index i, with values between 0 and n-1, denote the element. The radial width of each element is $\Delta r = (R_{out} - R_{in})/(\text{n-1})$, except for the inner and outer elements which have half this width. The numerical scheme used to calculate the saturation profile for a point in time, with index j, is illustrated in Figure F-31 (right). The time step between two successive point in time is denoted Δt.

The diffusion equation for radial diffusion can be developed in the following four terms:

$$\frac{\partial S}{\partial t} = \frac{1}{r}\cdot\frac{\partial}{\partial r}\left(rD\frac{\partial S}{\partial r}\right) = D\frac{\partial^2 S}{\partial r^2} + \frac{D}{r}\cdot\frac{\partial S}{\partial r} + \frac{\partial D}{\partial r}\cdot\frac{\partial S}{\partial r} \tag{F-6}$$

These terms with partial derivatives are estimated with the following corresponding finite differences:

$$\begin{cases} \dfrac{\partial S}{\partial t} & \approx & \dfrac{S_{j,i} - S_{j-1,i}}{\Delta t} \\ D\dfrac{\partial^2 S}{\partial r^2} & \approx & D(S_{j-1,i})\cdot\dfrac{S_{j-1,i+1} - 2S_{j-1,i} + S_{j-1,i-1}}{\Delta r^2} \\ \dfrac{D}{r}\cdot\dfrac{\partial S}{\partial r} & \approx & \dfrac{D(S_{j-1,i})}{R_{in} + i\cdot\Delta r}\cdot\dfrac{S_{j-1,i+1} - S_{j-1,i-1}}{2\cdot\Delta r} \\ \dfrac{\partial D}{\partial r}\cdot\dfrac{\partial S}{\partial r} & \approx & \dfrac{D(S_{j-1,i+1}) - D(S_{j-1,i-1})}{2\cdot\Delta r}\cdot\dfrac{S_{j-1,i+1} - S_{j-1,i-1}}{2\cdot\Delta r} \end{cases} \tag{F-7}$$

Note that the radius of element i is expressed as $R_{in} + i\cdot\Delta$r. For convenience, the following constant is defined:

$$R = \frac{\Delta t}{\Delta r^2} \tag{F-8}$$

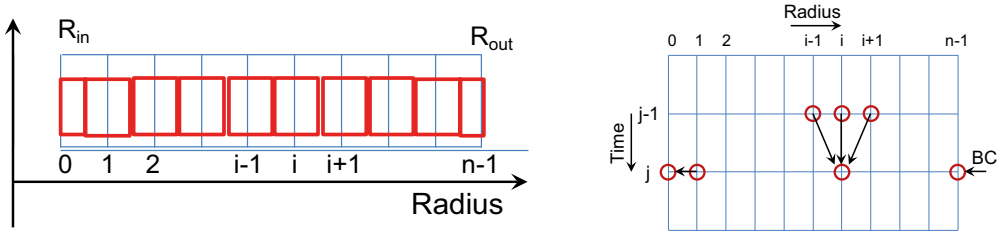

Figure F-31. *Discretization of geometry in n elements with index i, shown as red boxes (left). Numerical scheme used to update the saturation profile (right). Points in time are denoted with index j.*

Based on Equations (F-6) to (F-8), the following expressions can be derived for the saturation degree in all elements, except for the inner and outer elements:

$$S_{j,i} = S_{j-1,i} + R \cdot D(S_{j-1,i}) \cdot \left[S_{j-1,i+1} - 2S_{j-1,i} + S_{j-1,i-1}\right] + \frac{\Delta t}{2\Delta r} \frac{D(S_{j-1,i})}{R_{in} + i \cdot \Delta r} \cdot \left[S_{j-1,i+1} - S_{j-1,i-1}\right] + \frac{R}{4}\left[D(S_{j-1,i+1}) - D(S_{j-1,i-1})\right] \cdot \left[S_{j-1,i+1} - S_{j-1,i-1}\right] \quad \text{(F-9)}$$

The saturation degree of the inner element is the same as for the adjacent element ($S_{j,0} = S_{j,1}$), and for the outer element this is given as a boundary condition, which is full saturation ($S_{j,n-1} = 1$).

A function describing the moisture diffusivity was defined with two parameters: D_0, which describes the level of the diffusivity half way between initial and final saturation value (S_{mid}), and k, which describes the influence of the saturation (Figure F-32):

$$D(S) = D_0 \cdot \left(\frac{S}{S_{mid}}\right)^k \quad \text{(F-10)}$$

These two parameters are defined as input to the algorithm for the water-uptake calculations. The output from the same algorithm is the saturation profiles and the water-uptake.

The following parameters and geometries have been defined for the water-uptake tests:

- Inner radius: 0.02 m.
- Outer radius 0.15 m; i.e. a homogenized description of the bentonite.
- Height: 0.1 m.
- Porosity: 0.44; based on a block dry density of 1 587 kg/m3 and a radial swelling from 0.149 to 0.15 m.
- Initial saturation: 0.42; based on a water content of 11.75 %.
- Number of element: 14; If the outer element is kept saturated from the start, this implies that the initially added volume of water in the model corresponds to the volume of the slot immediately filled at the start, i.e. 0.20–0.08 (in filter) = 0.12 liter.
- Number of time steps: 10 000.

A complete file of the tool is provided in the Figure F-33 and Figure F-34.

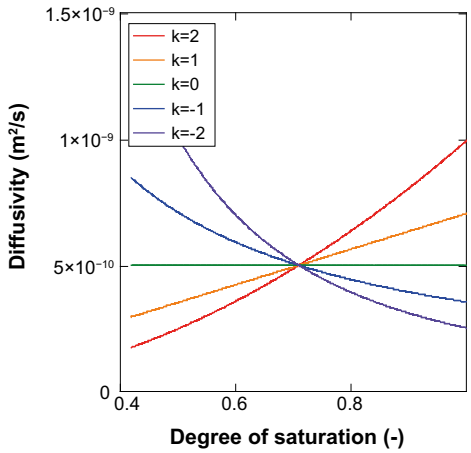

Figure F-32. *Moisture diffusivity function. Influence of the parameter k.*

Radii: $R_{in} \equiv 0.02 \quad R_{out} \equiv 0.15$

Duration: $T \equiv 203 \cdot days$

Number of elements: $n \equiv 14$

Number of time steps: $m \equiv 10000$

Radial element width: $\Delta r := \left(R_{out} - R_{in}\right) \cdot (n-1)^{-1}$

Time step: $\Delta t := T \cdot (m-1)^{-1}$

Constant: $R := \Delta t \cdot \Delta r^{-2}$

Seconds per day: $days \equiv 3600 \cdot 24$

Initial saturation: $S_{in} \equiv 0.42$

Porosity: $\phi \equiv 0.44$

Initial water volume: $V0 := \pi \cdot 0.1 \cdot \phi \cdot S_{in} \cdot \left(R_{out}^{\,2} - R_{in}^{\,2}\right)$

Moisture diffusivity function:

$$D\left(D_0, k, S\right) := D_0 \cdot 10^{-10} \cdot \left[\frac{S}{\left(S_{in} + 1\right) \cdot 0.5}\right]^k$$

Pore volumes in element array:

$$\text{PoreVolume} := \left| \begin{array}{l} PV_0 \leftarrow 0.1 \cdot \pi \cdot \phi \cdot \left[\left(R_{in} + 0.5 \cdot \Delta r\right)^2 - \left(R_{in}\right)^2\right] \\ \text{for } i \in 1..n-2 \\ \quad PV_i \leftarrow 0.1\pi \cdot \left[\left[R_{in} + \Delta r \cdot (i + 0.5)\right]^2 - \left[R_{in} + \Delta r \cdot (i - 0.5)\right]^2\right] \cdot \phi \\ PV_{n-1} \leftarrow 0.1\pi \cdot \left[\left[R_{in} + \Delta r \cdot (n-1)\right]^2 - \left[R_{in} + \Delta r \cdot (n-1.5)\right]^2\right] \cdot \phi \\ PV \end{array} \right.$$

$$V_P := \text{PoreVolume}$$

$$M\left(D_0, k1\right) := \left| \begin{array}{l} \text{for } i \in 0..n-2 \\ \quad S_{0,i} \leftarrow S_{in} \\ S_{0,n-1} \leftarrow 1 \\ WU_0 \leftarrow \sum_{i=0}^{n-1} \left(S_{0,i} \cdot V_{P_i}\right) - V0 \\ \text{for } j \in 1..m-1 \\ \quad S_{j,n-1} \leftarrow 1 \\ \quad \text{for } i \in 1..n-2 \\ \quad\quad S_{j,i} \leftarrow S_{j-1,i} + R \cdot D\left(D_0, k1, S_{j-1,i}\right) \cdot \left(S_{j-1,i+1} - 2 \cdot S_{j-1,i} + S_{j-1,i-1}\right) \\ \quad\quad S_{j,i} \leftarrow S_{j,i} + \frac{\Delta t}{2 \cdot \Delta r} \cdot \frac{D\left(D_0, k1, S_{j-1,i}\right)}{R_{in} + i \cdot \Delta r} \cdot \left(S_{j-1,i+1} - S_{j-1,i-1}\right) \\ \quad\quad S_{j,i} \leftarrow S_{j,i} + \frac{R}{4} \cdot \left(D\left(D_0, k1, S_{j-1,i+1}\right) - D\left(D_0, k1, S_{j-1,i-1}\right)\right) \cdot \left[\left(S_{j-1,i+1}\right) - \left(S_{j-1,i-1}\right)\right] \\ \quad S_{j,0} \leftarrow S_{j,1} \\ \quad WU_j \leftarrow \sum_{i=0}^{n-1} \left(S_{j,i} \cdot V_{P_i}\right) - V0 \\ \left(S \;\; WU\right)^T \end{array} \right.$$

Figure F-33. *MathCad algorithm for water uptake calculation.*

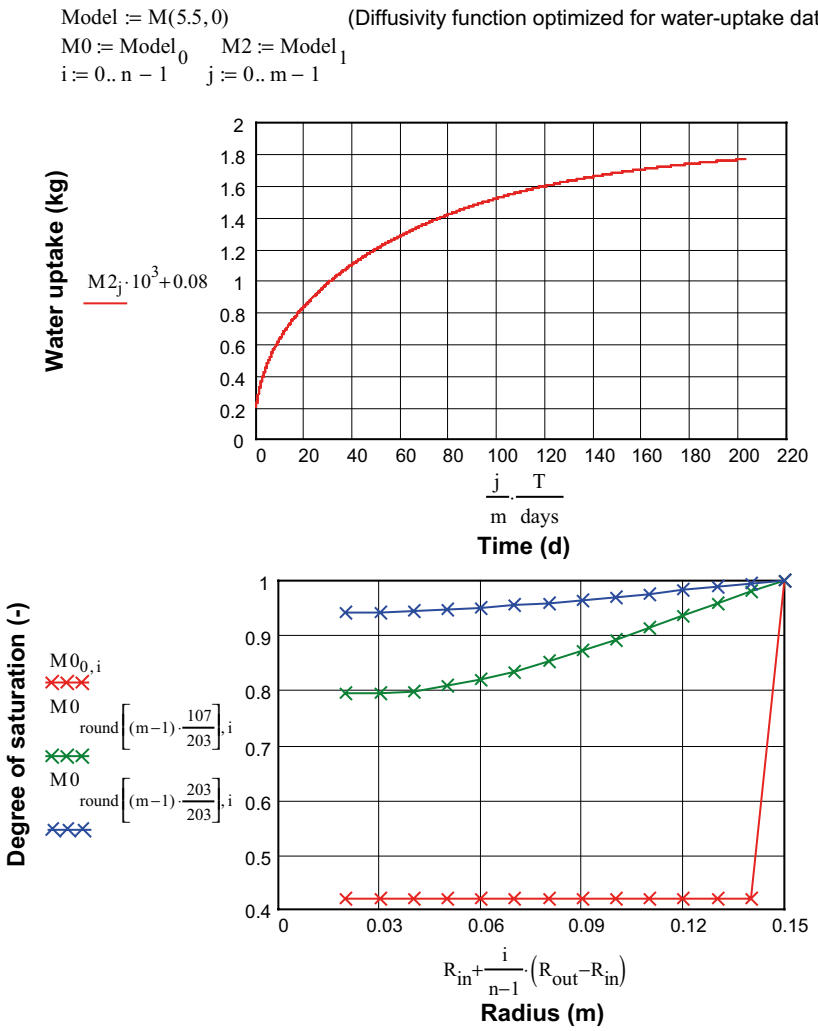

Figure F-34. *MathCad algorithm for water uptake calculation (cont).*

Optimization of moisture diffusivity functions

The moisture diffusivity function was optimized through: i) calculating the error between the model results and the experimental data for a specific set of parameters D_0 and k; and ii) by performing a parameter analysis of the influence of parameters D_0 and k. A parameter set which yields a minimum error was considered to be optimized. Due to the discrepancy of the water balance as noted in Figure F-30, this analysis was performed in two different ways.

In the first analysis, the model was compared with water-uptake data. Cumulative volumes from Test 1 (V_{T1}) for 17 points in time (t_i) were compared with corresponding volumes from the model (V_{model}). The points in time when the test volume reached the values of 0.2, 0.3 … up to 1.8 liters were selected. The error was calculated with the following expression:

$$\log\left(\sum_{i=0}^{16}\left[V_{\mathrm{T1}}(t_i)-V_{\mathrm{model}}(t_i)\right]^2\right) \qquad \text{(F-11)}$$

Note that the filter volume of 0.08 liters was added to the V_{model} values. The result from the parameter analysis of the error is shown in Figure F-35 (left), and a minimum can be identified for the parameter set: $D_0 = 5.5 \times 10^{-10}$ m^2/s and $k = 0$.

In the second analysis, the model was compared with water saturation data. Measured saturation degree values from innermost sample positions in Test 2 and Test 1 (i.e. 68 and 91 % respectively), were compared with the corresponding saturation values in the inner element of the model (S_{model}) after 107 and 203 days, respectively. The error was calculated with the following expression:

$$\log\left(\left[S^{i=0}_{\text{model}}(t=107d)-0.68\right]^2+\left[S^{i=0}_{\text{model}}(t=203d)-0.91\right]^2\right) \qquad \text{(F-12)}$$

The result from the parameter analysis of the error is shown in Figure F-35 (right), and a minimum can be identified for the parameter set: $D_0 = 3.7\times10^{-10}$ m^2/s and $k = 1.2$.

Model results for the optimized parameter sets regarding: i) water-uptake and, ii) saturation profiles for day 107 and 203, are shown together with experimental results in Figure F-36. As expected, the agreement with the water-uptake curve is best for the first parameters set, whereas for the saturation profiles the agreement is best for the second parameters set.

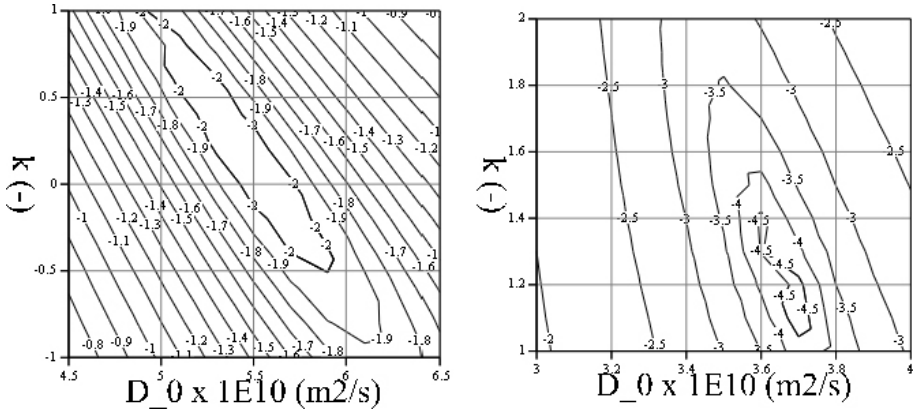

Figure F-35. *Log sum of squared error as a function of the parameter D_0 and k. Left graph shows results for comparison with water-uptake curve. Right graph shows results for comparison with degree of saturation at inner points at day 107 and 203.*

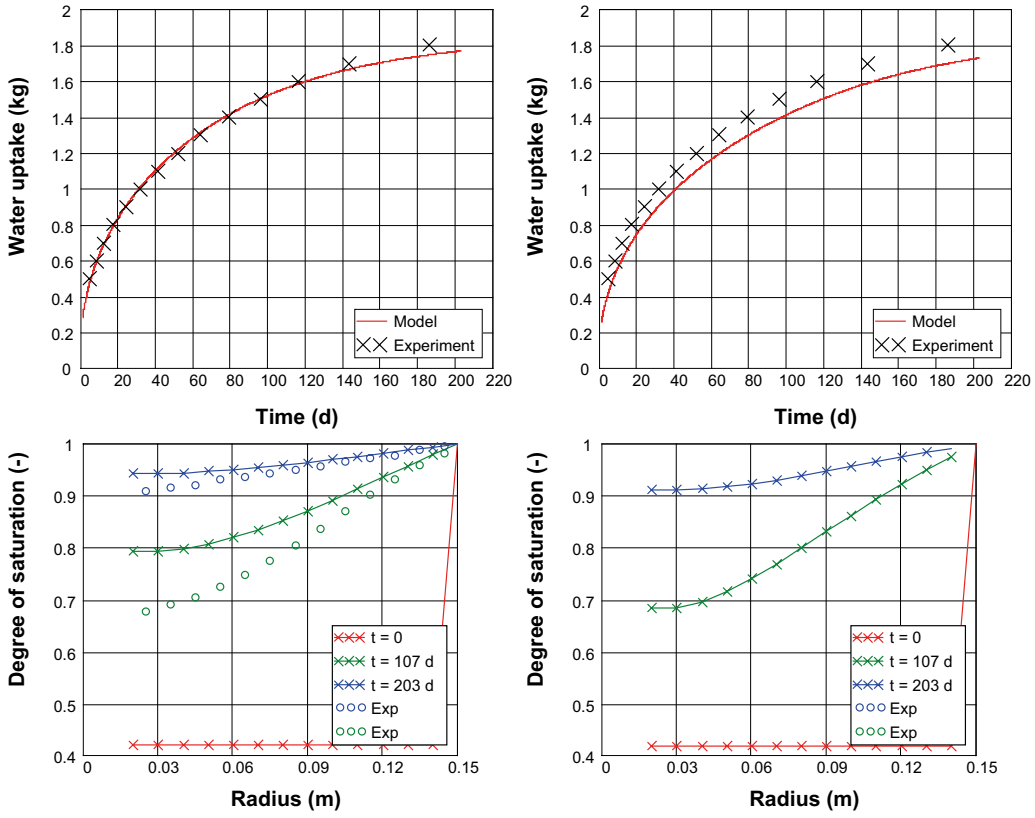

Figure F-36. *Model results for optimized diffusivity function: $D_0 = 5.5\times10^{-10}$; k = 0 (left graphs); $D_0 = 3.7\times10^{-10}$; k = 1.2 (right graphs).*

Parameter value adoption

An optimized moisture diffusivity function can, together with an in-situ retention curve, be used to adopt parameter values for the standard hydraulic model, i.e. the intrinsic permeability, the relative permeability relation and the retention curve.

The experimental data points, i.e. initial and final points for Test 1 and Test 2, are presented together with two adopted retention curves in Figure F-37. Both curves were adopted so that the initial saturation degree of 42 % corresponds to a suction value of 90 MPa.

The first curve follows the van Genuchten expression with the parameter values P_0 = 10 MPa and λ = 0.28:

$$S_l(P_l) = \left(1 + \left(\frac{P_g - P_l}{P_0}\right)^{\frac{1}{1-\lambda}}\right)^{-\lambda} \qquad \text{(F-13)}$$

The second curve follows the so-called square law (implemented in Code_Bright) with the parameter value P_0 = 19.3 MPa:

$$S_l(P_l) = \frac{1}{\sqrt{1 + \frac{P_g - P_l}{P_0}}} \qquad \text{(F-14)}$$

The moisture diffusivity function $D(S_l)$ is related to the permeability function $k \cdot k_r(S_l)$, the derivative of the inverse retention curve dP_l/dS_l, the porosity n, and the water viscosity μ according to the following equation:

$$D(S_l) = \frac{k \cdot k_r(S_l)}{n \cdot \mu} \cdot \frac{dP_l}{dS_l} \qquad (m^2/s) \qquad \text{(F-15)}$$

The permeability function can be evaluated by rearranging this to:

$$k \cdot k_r(S_l) = \frac{n \cdot \mu \cdot D(S_l)}{\frac{dP_l}{dS_l}} \qquad (m^2) \qquad \text{(F-16)}$$

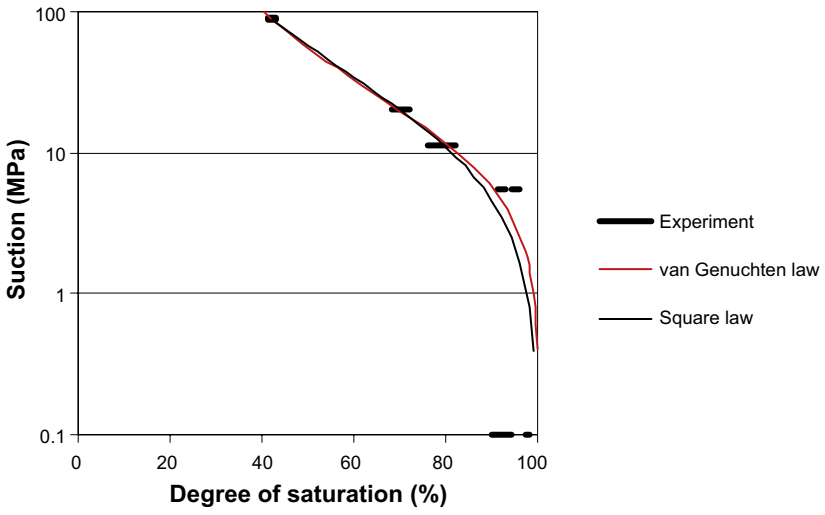

Figure F-37. *In-situ retention curve. Experimental data points and adopted functions.*

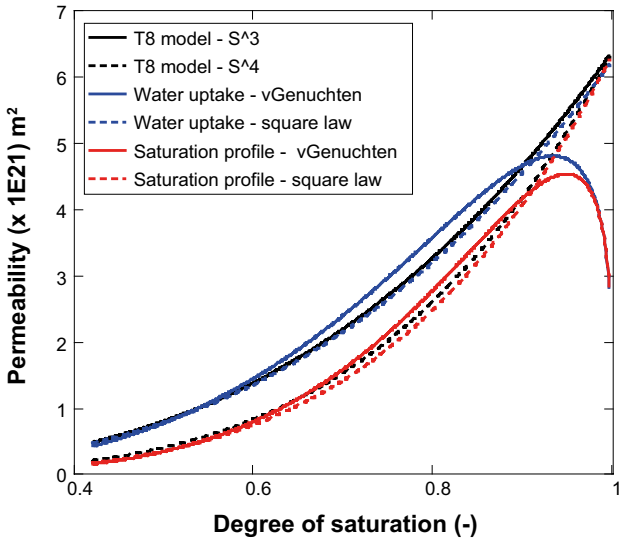

Figure F-38. *Evaluated permeability functions.*

This function has been evaluated for four different parameter combinations which are shown in Figure F-38. Relations based on a moisture diffusivity function optimized from water-uptake data are marked with blue lines, whereas corresponding relation based on a diffusivity function optimized from saturation data are marked with red lines. Relations based on the van Genuchten type of retention curve are marked with solid coloured lines, whereas corresponding relations based on the square law type of retention curve are marked with dotted coloured lines. A standard permeability function, previously used in Task 8, i.e. $S_l^3 \times 6.4 \times 10^{-21}$ m^2, is shown for comparison with a solid black line. A modified relation in which the exponent in the relative permeability law is changed to 4 is shown with a dotted black line.

It can be noted that blue lines (optimized from water-uptake data) are very close to the standard Task 8 relation, whereas the red lines (optimized from saturation data) are very close to the relation with a fourth order power law. It can also be noted that van Genuchten based relations display a strong decreasing trend close to saturation, and therefore diverges from the standard permeability relations, whereas the square law based relations are very similar to the standard permeability relations.

Code_Bright models of water-uptake tests

The water-uptake test was modelled with Code_Bright (v4) as a purely hydraulic problem with a 1D axisymmetric geometry, see Figure F-39. The block was described as homogenized with a single constant porosity (44 %). The initial degree of saturation (42 %) was applied with an initial suction value of 90 MPa and the adopted retention curves. The initial water filling of the outer slot was taken into account by applying water saturated conditions from the start in the outer 5 mm of the bentonite (corresponding to an additional water volume of 0.12 liters for a height of 0.1 m). The liquid pressure at the outer boundary was kept constant at an atmospheric level (0.1 MPa) throughout the calculations. The used parameter values are shown in Table F-6. The models were run for 203 days, at a constant gas pressure of 0.1 MPa, at a constant temperature of 20 °C (which implies a constant viscosity), and with no gravity. The geometry was discretized as an array of 130 elements. Four different model cases were analyzed according to Table F-7.

The model results are shown in Figure F-40 to Figure F-42. The modelled evolution of RH at the radii 0.04, 0.08 and 0.12 m are shown together with data from the RH sensors in Test 1 in Figure F-40. Modelled saturation profiles for day 0, 107 and 203 are shown in Figure F-41 together with measured saturation profiles at the dismantling of Test 1 and 2. The modelled water-uptake is shown in Figure F-42 together with the measured cumulative water-uptake in Test 1. The water-uptake was evaluated as the flow rate for the entire circumference, and adjusted for a block height of 0.1 m. Moreover, an initial inflow 0.2 litres was added to the water-uptake (0.08 litres representing the filter volume, and 0.12 litres volume of the outer slot, see above).

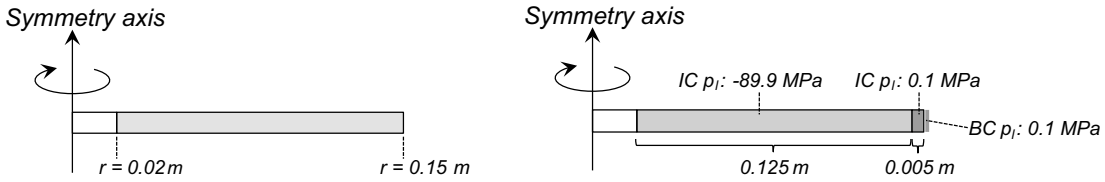

Figure F-39. *Model geometry (left) and model initial and boundary conditions (right).*

Table F-6. Parameter values.

Parameter		Value		
Porosity	n (–)	0.44		
Intrinsic permeability	k (m^2)	6.4×10^{-21}		
Relative permeability	k_r (–)	S_l^3	or	S_l^4
Water retention curve		van Genuchten law:	or	Square law:
		P_0: 10 MPa; λ: 0.28		P_0: 19.3 MPa
Water density	ρ_l (kg/m^3)	1 000		
Water viscosity	μ_l (Pa·s)	0.001		

Table F-7. Model cases.

Model	Relative permeability	Water retention curve
BRIEVUF_6	S_l^3	van Genuchten law: P_0: 10 MPa; λ: 0.28
BRIEVUF_7	S_l^4	van Genuchten law: P_0: 10 MPa; λ: 0.28
BRIEVUF_8	S_l^3	Square law: P_0: 19.3 MPa
BRIEVUF_9	S_l^4	Square law: P_0: 19.3 MPa

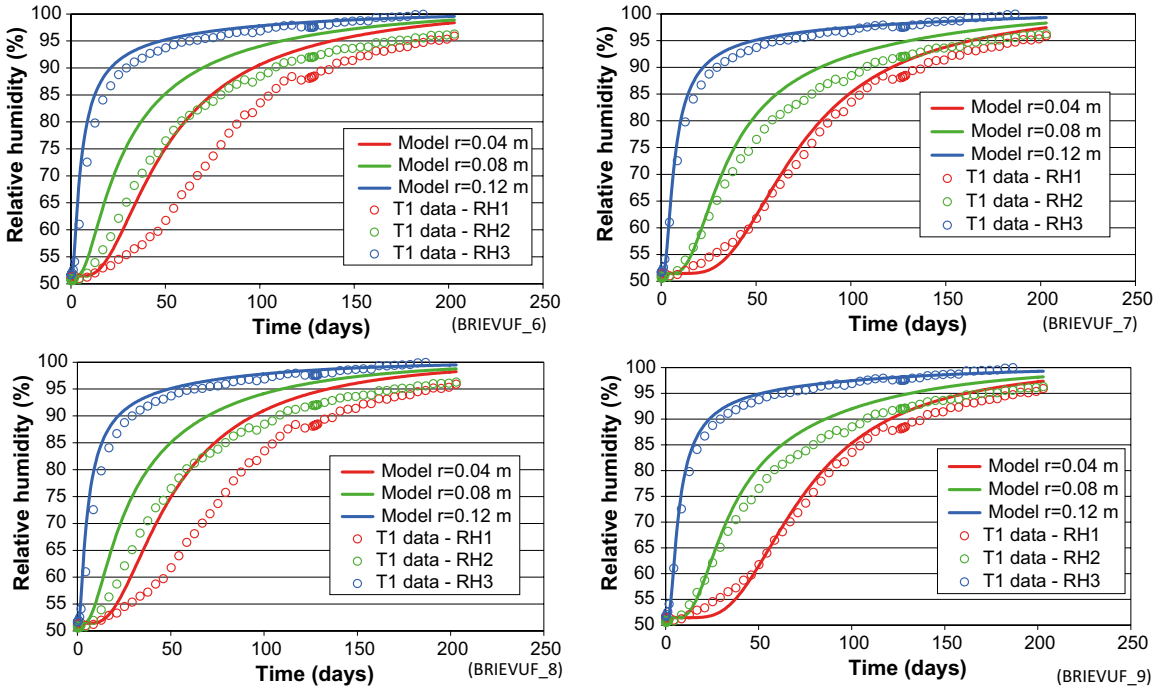

Figure F-40. *Modelled evolution of RH at three radii and data from RH sensors in Test 1; van Genuchten retention curve (upper graphs); square law retention curve (lower graphs). $k_r(S_l) = S_l^3$ (left graphs); and $k_r(S_l) = S_l^4$ (right graphs).*

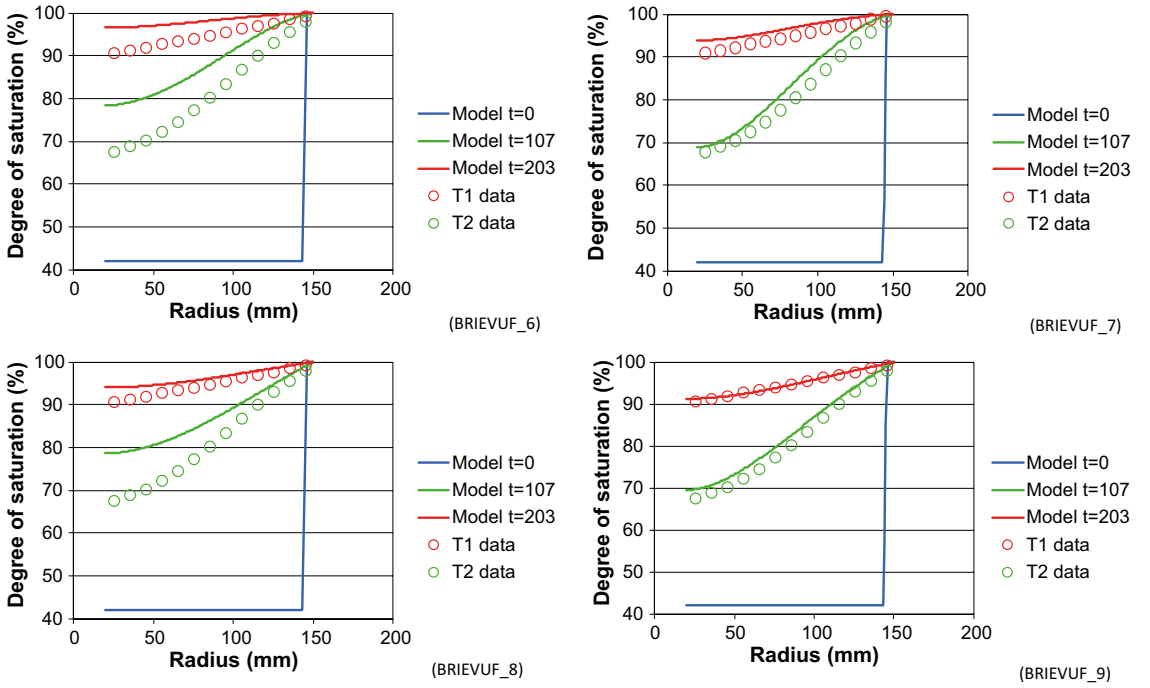

Figure F-41. *Modelled saturation profiles at day 0, 107 and 203 and measured data from Test 1 and Test 2; van Genuchten retention curve (upper graphs); square law retention curve (lower graphs). $k_r(S_l) = S_l^3$ (left graphs); and $k_r(S_l) = S_l^4$ (right graphs).*

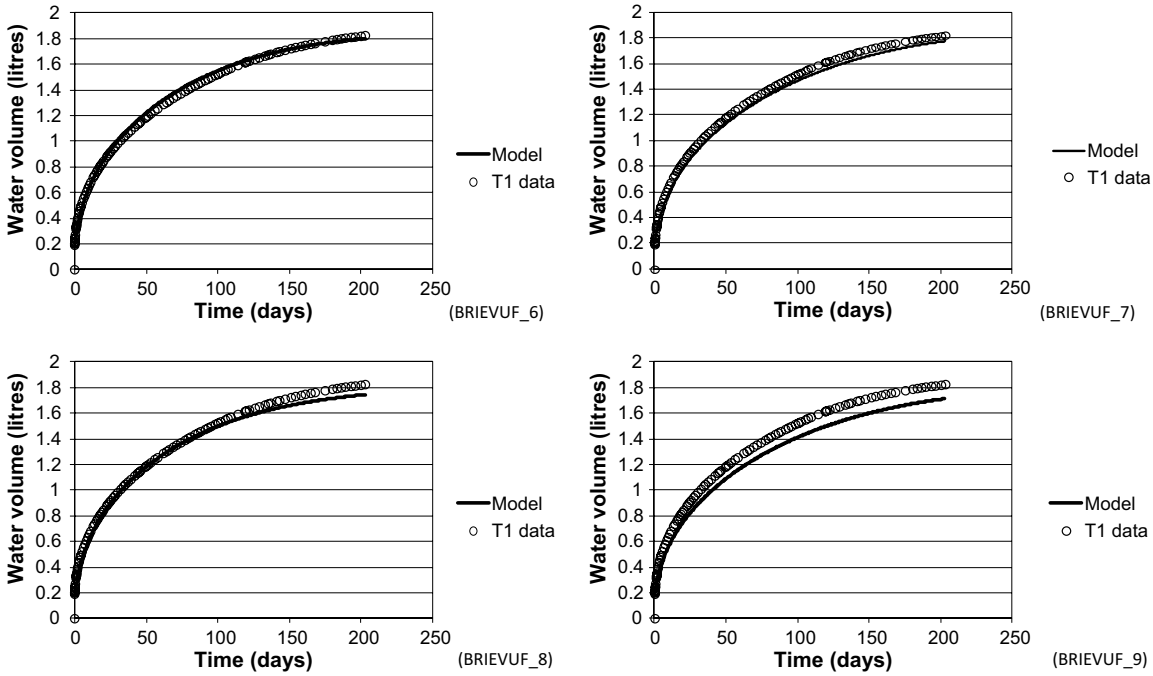

Figure F-42. *Modelled cumulative water upt and measured data from Test 1; van Genuchten retention curve (upper graphs); square law retention curve (lower graphs). $k_r(S_l) = S_l^3$ (left graphs); and $k_r(S_l) = S_l^4$ (right graphs).*

It can be noted that the models with a cubic power law generally display a better agreement than the models with the fourth order power law concerning the experimental water-uptake data (Figure F-42). In contrast, the models with the fourth order power law generally display a better agreement with the measured RH-evolution (Figure F-40) and the measured saturation profiles (Figure F-41). In addition, it can be noted that the models with the van Genuchten retention curve generally display a faster hydration than the models with the square law retention curve (e.g. see the red curves in Figure F-41), and also faster than the diffusivity based model (c.f. lower graphs in Figure F-36).

Final remarks on hydraulic evaluation

The presented evaluation demonstrates how all hydraulic parameters can be quantified from one single experiment. The chosen approach to do this was to first evaluate a moisture diffusivity function, and secondly to evaluate a permeability function from the diffusivity and an in-situ retention curve. An alternative approach could be to adopt the retention curve to begin with, and then to make a parameter analysis of the intrinsic permeability and the exponent in the relative permeability law and make the parameter value adoption in this way.

One advantage of the chosen approach is however that the moisture diffusivity can be evaluated independently of any retention curve. And if the tests weren't equipped with RH sensors, then it would still be possible to evaluate the moisture diffusivity without making any assumptions about the retention properties, which would be case if the permeability parameters were evaluated.

It is also quite interesting to notice that one of the data sets (the water-uptake data) implies that the water-uptake can be described by one single parameter value (i.e. the D_0 value, see Figure F-36, left). A constant diffusivity value implies that the cubic power law for the relative permeability is precisely associated with a square law for the retention curve, according to Equation (F-16).

Finally, it has been decided that the water-uptake tests should be included as a specific task in Task 8, and that this task should follow a highly specified description, thereby enabling a comparison of codes. In addition to this, the modelers are free to use alternative parameter values and constitutive laws if they wish. Among the four cases presented above, the case with a fourth order power law for the relative permeability and a van Genuchten retention curve was selected as a task to be included in Task 8. The former relation was chosen due to the better agreement concerning the RH-evolution and the saturation profiles, whereas the latter curve was chosen for its widespread use and implementation.

A comparison of the parameter values defined in this task and in previous Task 8 definitions yields the following remarks:

- Hydraulic conductivity: 6.4×10^{-14} m/s (or intrinsic permeability 6.4×10^{-21} m^2) is exactly the same as previously.
- Relative permeability law: a fourth order power law (S_l^4) is defined instead of a cubic power law (S_l^3).
- van Genuchten retention curve parameters: $P_0 = 10$ MPa and $\lambda = 0.28$ are defined instead of $P_0 = 9.23$ MPa and $\lambda = 0.3$.

It can thus be noted that the differences between the two data sets are small.

F.13 Acknowledgements

Several co-workers at Clay Technology have made contributions to this work during the course of the BRIE water-uptake tests: Torbjörn Sandén constructed and made the drawings of the cylinders; Ulf Nilsson prepared the different sensors and the logger system; and Emelie Hansen prepared the bentonite samples for the analyses of anions and exchangeable cations.

Appendix G

Graphs water content Bentonite

This section presents the results from all performed analyses.

Results from the general sampling scheme of the parcel in Hole 17 are presented as axial distributions of water content (Figure G-1), dry density (Figure G-2), and degree of saturation (Figure G-3). Corresponding graphs for the parcel in Hole 18 are shown Figure G-5, Figure G-3 and Figure G-6, respectively. Results from the second sampling scheme of the selected blocks from Hole 17 as well as Hole 18 are presented as tangential distributions of water content (Figure G-7), dry density (Figure G-8), and degree of saturation (Figure G-9).

It should be noted that the saturation degree values were based on measured density values for samples with $\rho_d \leq 1\,562$ kg/m^3, otherwise the dry density value of 1 562 kg/m^3 was used (corresponding to $e = 0.78$), see Section 4.4.4.

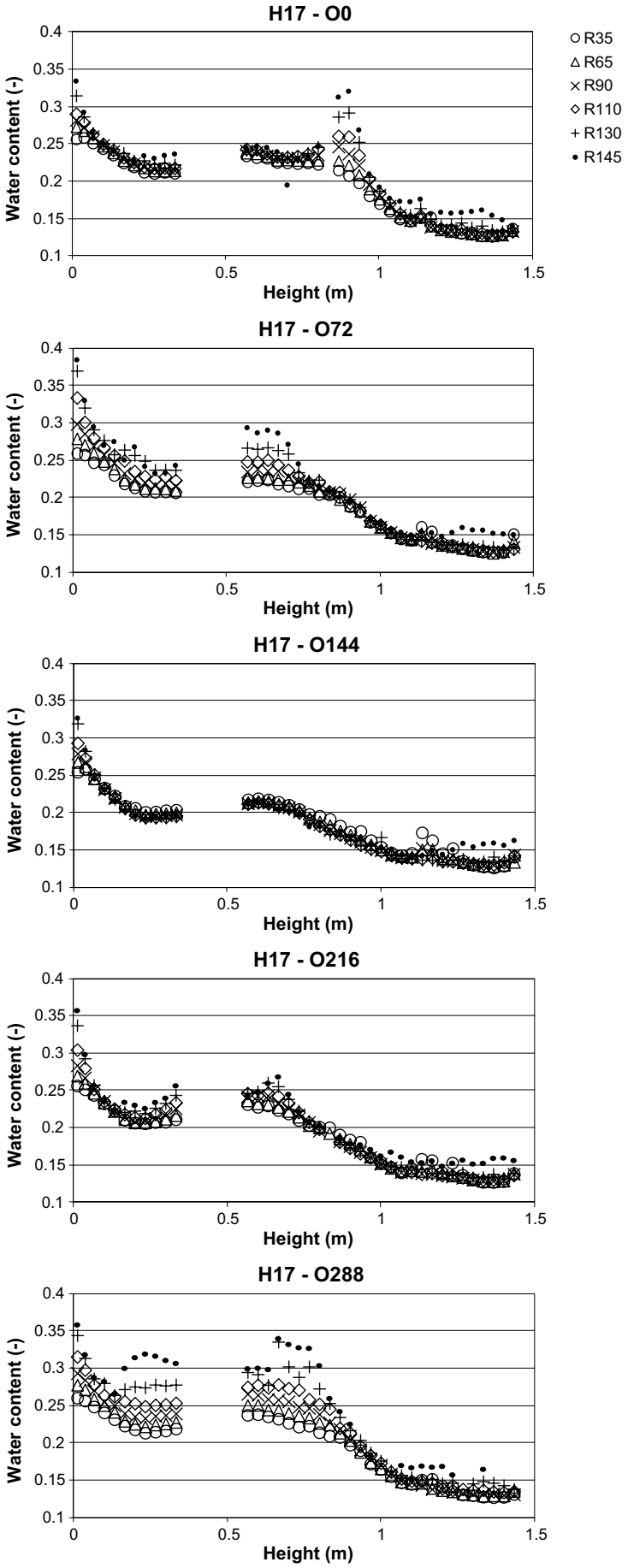

Figure G-1. *Axial distributions of water content in different directions in Hole 17.*

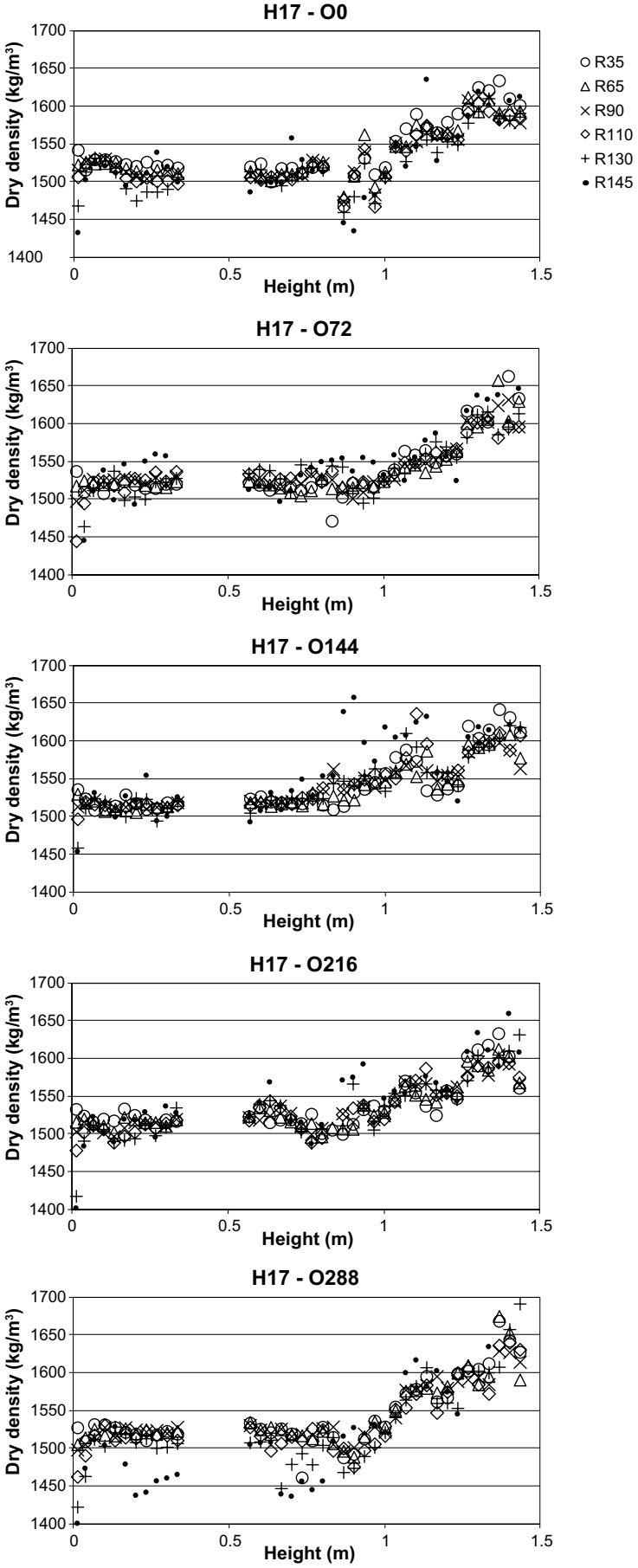

Figure G-2. *Axial distributions of dry density in different directions in Hole 17.*

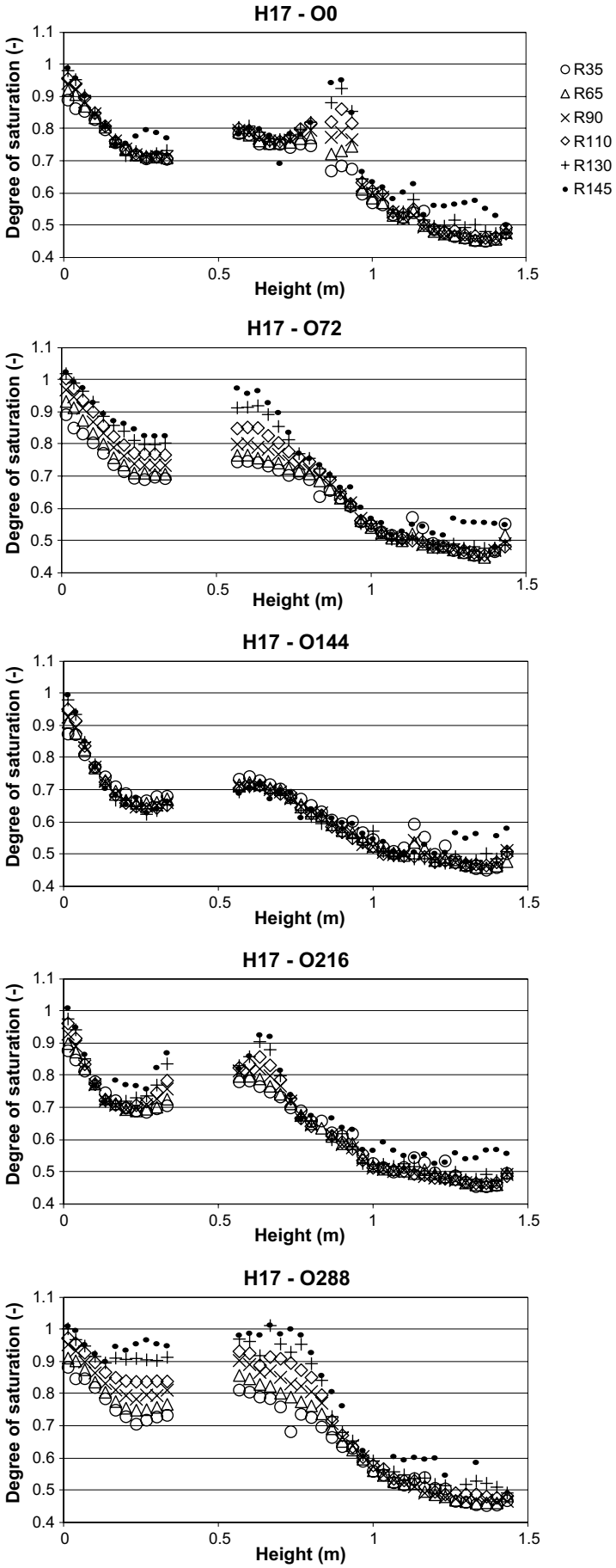

Figure G-3. *Axial distributions of degree of saturation in different directions in Hole 17.*

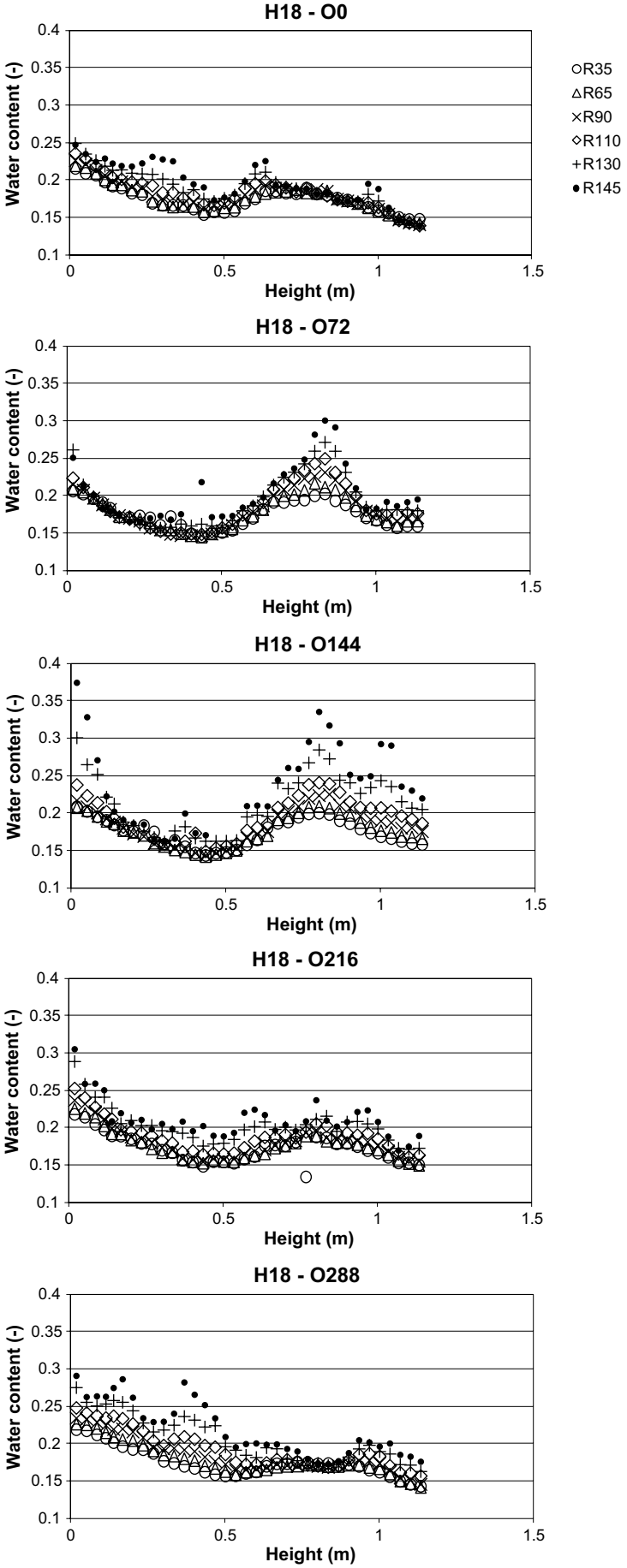

Figure G-4. *Axial distributions of water content in different directions in Hole 18.*

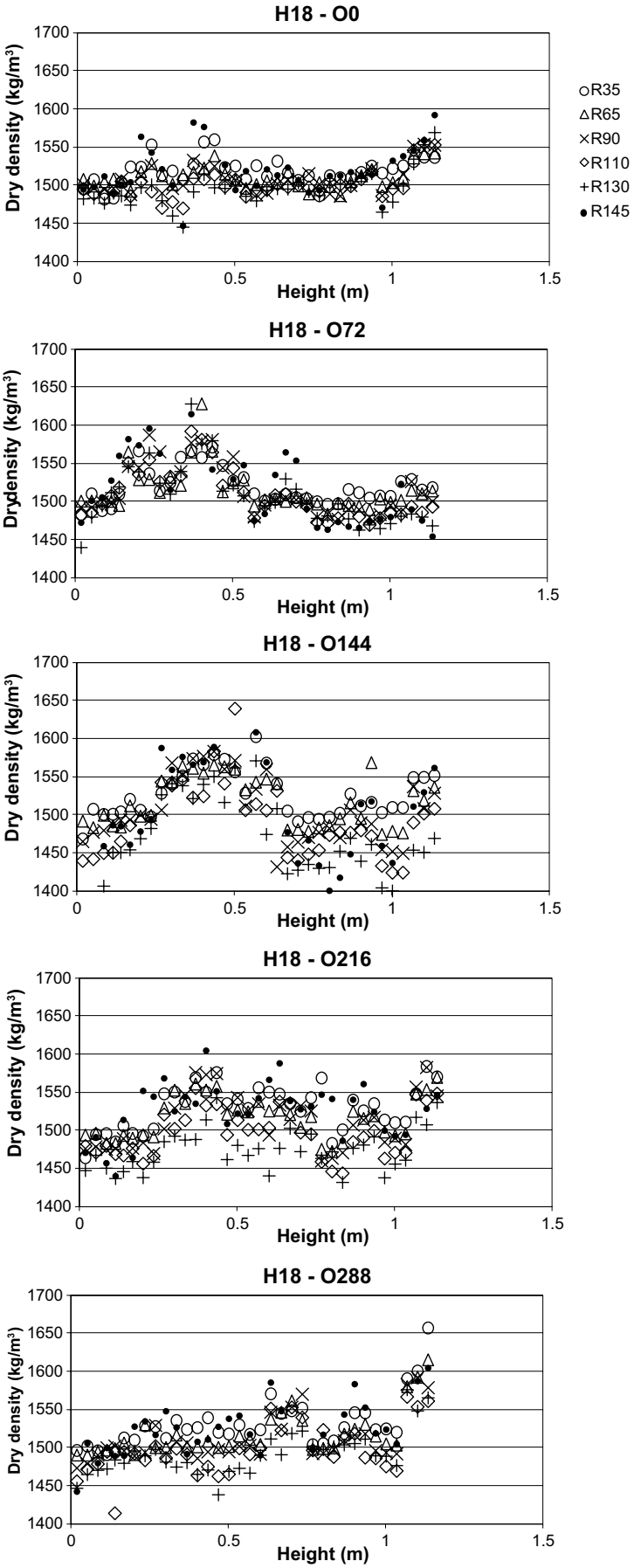

Figure G-5 . *Axial distributions of dry density in different directions in Hole 18.*

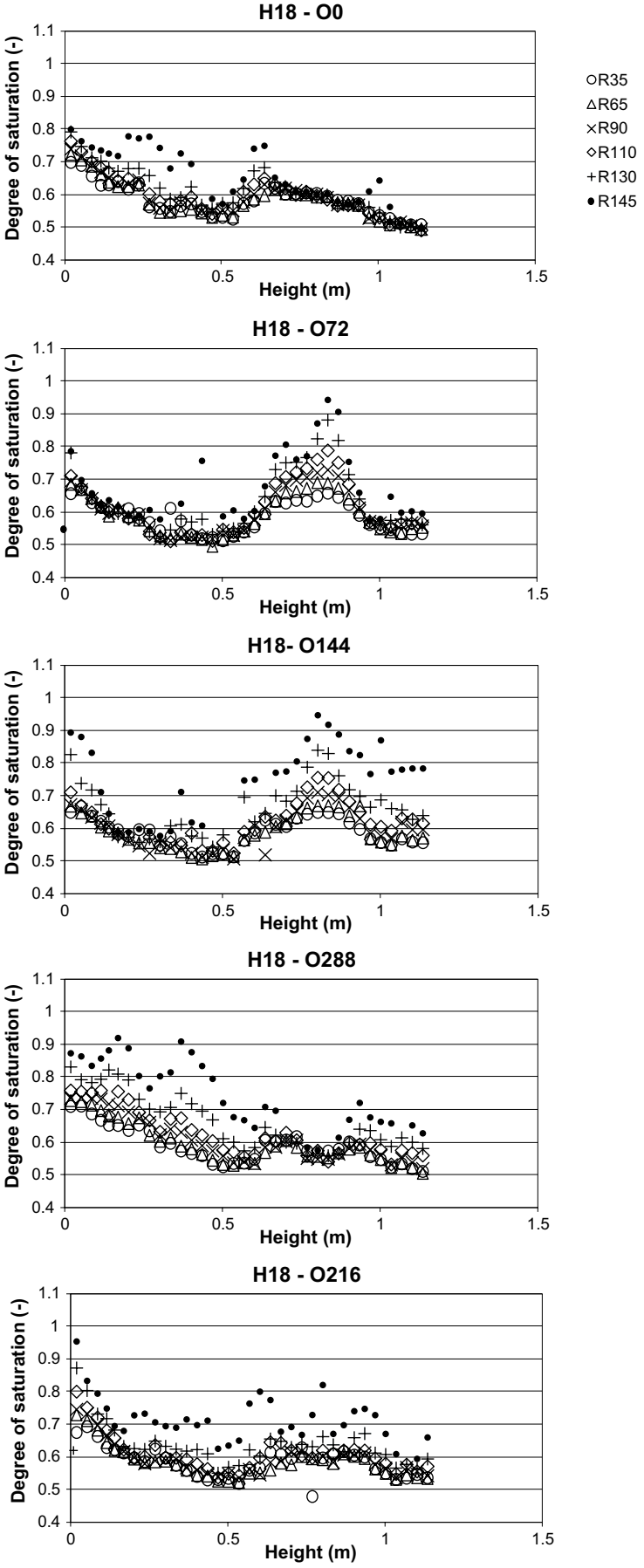

Figure G-6 . *Axial distributions of degree of saturation in different directions in Hole 18.*

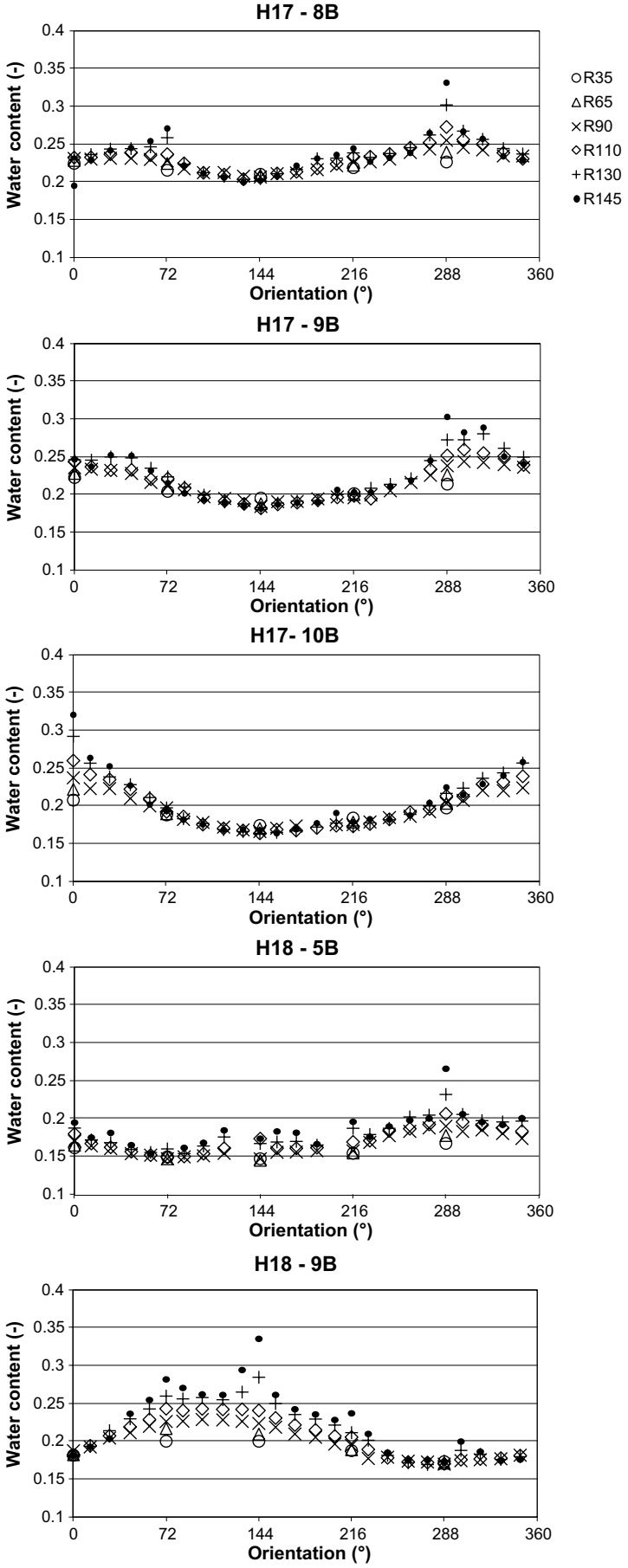

Figure G-7. *Tangential distributions of water content in different sections in Hole 17 and Hole 18.*

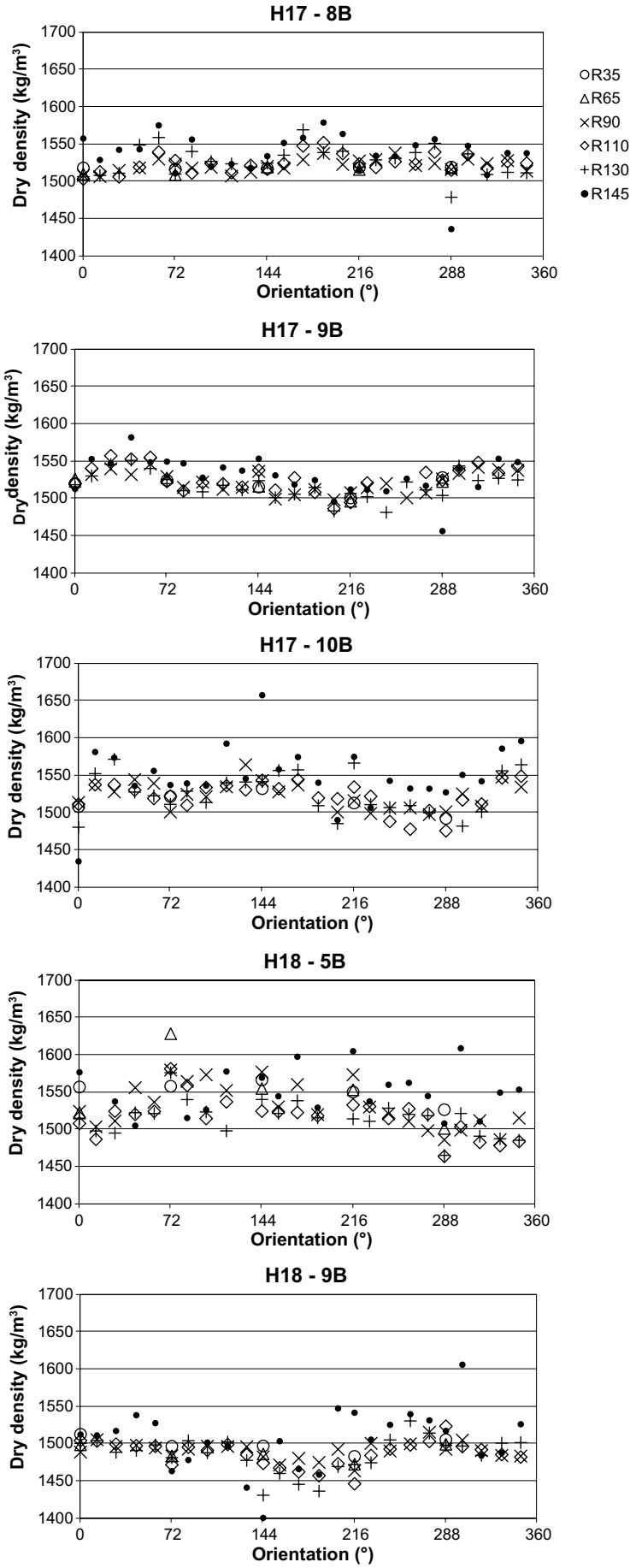

Figure G-8 . *Tangential distributions of dry density in different sections in Hole 17 and Hole 18.*

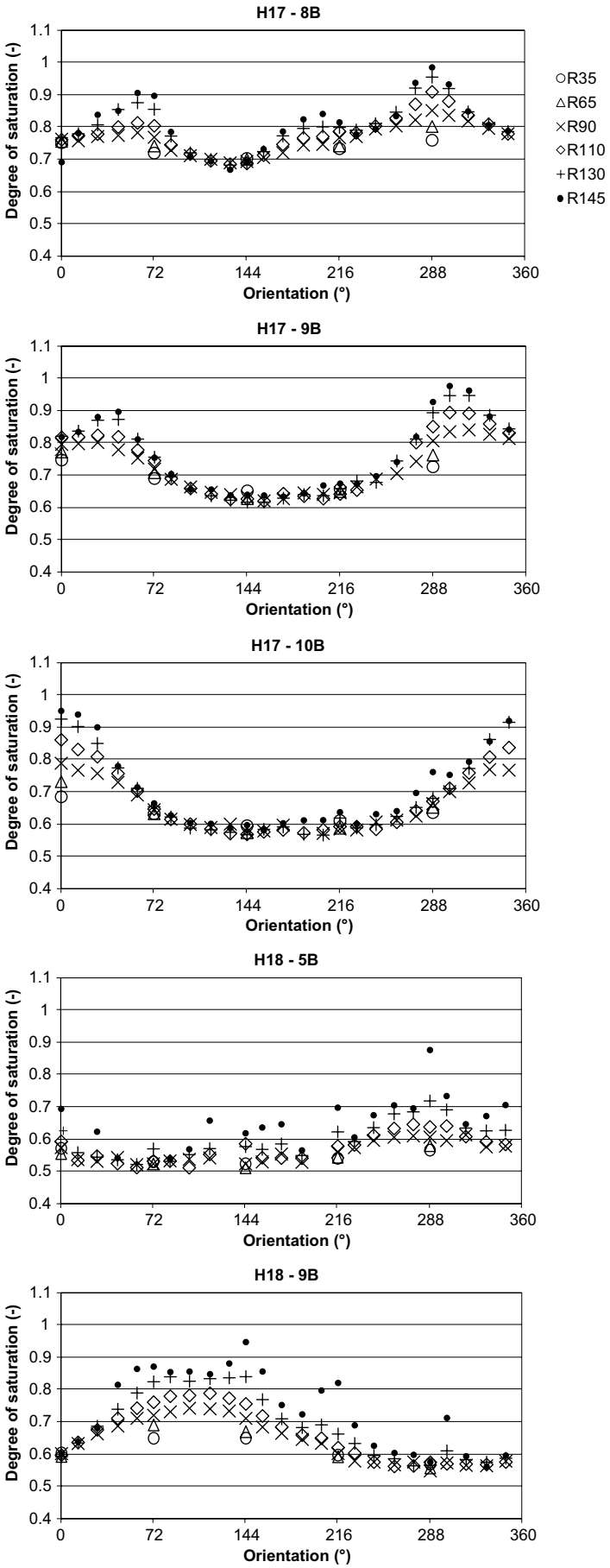

Figure G-9 . *Tangential distributions of degree of saturation in different sections in Hole 17 and Hole 18.*